Impact of Confined Extension on the Failure Envelope of Intact Low-Porosity Rock

by

Shantanu Patel

A thesis submitted in partial fulfillment of the requirements for the degree .of

Doctor of Philosophy

in

Geotechnical Engineering

Department of Civil and Environmental Engineering
University of Alberta

Abstract

A failure envelope that ignores the intermediate principal stress (σ_2) is typically adequate for the design of rock structures. To obtain the complete envelope, the rock cylinders should be tested using confined compression (CC) as well as confined extension (CE) tests. While CC tests are common, CE tests are rarely carried out. Current techniques available to test rocks under CE conditions require shaping the cylindrical specimens to a dog-bone geometry. The limited data available in the literature indicates that the results from these dog-boned shaped tests produces strengths that are considerably greater than the confined triaxial tests carried out on traditional cylindrical specimens. Whether this increased strength is real or simply an artifact of the stress path for triaxial CE tests (σ_2=σ_1) versus conventional CC tests (σ_2=σ_3) is unknown.

This research describes a new experimental technique to test rocks under CE conditions with zero σ_2. The flattened Brazilian (FB) test was used and the σ_1 and σ_3 were calculated from the strain on the surface of the specimens. However, this required derivation of new equations for the σ_1 and σ_3 in a FB specimen considering the bi-modularity in the stress-strain equations and requires the Young's modulus (E) and Poisson's ratio (ν) in both tension and compression. The E and ν in compression can be obtained from an UCS test while the tensile E and ν values can be obtained from the direct tension test. A direct tension test is difficult to conduct, so, new experimental techniques were developed to obtain the tensile E and ν from a Brazilian test. New equations for (a) the horizontal and vertical strain values at the center and (b) horizontal and

vertical displacements on the surface in a Brazilian test were derived considering the bi-modularity in the stress-strain relations. The digital image correlation technique (DIC) and conventional strain gauges were used to extract the strain at the center of the Brazilian disks. DIC was used to monitor the displacements of different points along the horizontal and vertical diameter on the flat surface of the Brazilian disk. With the DIC technique, a spackle density of approximately 250 spackles/cm^2 was needed to accurately capture the strain and displacement pattern. The strain measured using the DIC technique was consistent with the strain measured using conventional strain gauges. The major advantage of the DIC technique is the ability to map the complete strain pattern over the surface of the Brazilian disk and quantify the uniformity of loading. The E and ν in tension obtained using the new equations were found to be in general agreement with the values obtained from the direct tension tests.

After obtaining the E and ν in compression and tension, FB samples of Lac du Bonnet granite were tested with increasing depth of flattening. With the change in flattening (1mm to 10 mm) the σ_1 was increased from 15% to 37% of its UCS. The corresponding σ_3 was found to remain in the range of Brazilian strength of the material.

The flat jointed bonded particle model from ITASCA was then used to investigate the Lac du Bonnet granite in CE for a wide range of confinements and to investigate the impact of σ_2. A methodology was developed to capture the (a) initial non-linearity commonly observed in the stress-strain curve of a UCS test, (b) the bi-modularity, (c) crack initiation stress, (d) crack damage stress, and (e) peak strength in UCS, triaxial and direct tension tests. A set of micro parameters for the numerical sample could produce the behavior observed in the laboratory tests. The code was further modified to investigate the CE tests. The failure envelope from the

numerical tests was found to align with the points from the Brazilian test and the FB tests implying a tension cut-off for the material investigated. The numerical results showed a clear influence of σ_2 on the strength in CE.

The results from the laboratory testing and numerical samples suggest that the non-linear Hoek-Brown failure criterion based on only compressive triaxial results provides a reasonable estimate of the strength in CE for Lac du Bonnet granite. But this criterion could be improved for Lac du Bonnet granite by providing a tension cut-off.

Preface

This thesis is an original intellectual product of the author, Shantanu Patel. Some parts of this work are published as:

A version of Chapter 2 has been published in the Geotechnical Testing Journal: [Patel, S. and C. Derek Martin. 2018. "Application of Digital Image Correlation Technique for Measurement of Tensile Elastic Constants in Brazilian Tests on a Bi-Modular Crystalline Rock." Geotechnical Testing Journal].

A version of Chapter 3 has been published in the journal of Rock Mechanics and Rock Engineering: [Patel, S. and C. Derek Martin. 2018. "Evaluation of Tensile Young's Modulus and Poisson's Ratio of a Bi-Modular Rock from the Displacement Measurements in a Brazilian Test." Rock Mechanics and Rock Engineering 51(2):361–73.]

A version of Chapter 4 has been submitted in the journal of Rock Mechanics and Rock Engineering: [Patel, S. and C. Derek Martin. 2018. "Application of flattened Brazilian test to investigate rocks under confined extension." Rock Mechanics and Rock Engineering (manuscript accepted)]

A version of Chapter has been accepted in 52nd US Rock Mechanics/Geomechanics Symposium (ARMA): [Patel, S. and C. D. Martin. 2018. "Simulating Bi-Modularity in Crystalline Rock Using Discrete Element Modelling." 52nd US Rock Mechanics/Geomechanics Symposium, 17-20 June 2018]

Dr. C. Derek Martin was the supervisory author on this work and was involved throughout the research in concept formation and manuscript edits.

Acknowledgements

I would like to thank my supervisor, Dr. C. Derek Martin for providing me the opportunity to conduct this research. His immense knowledge in the field of rock mechanics provided me suggestions, whenever I was unsure about the reason behind a problem. His guidance helped me in all the time of research and writing of this thesis.

I would like to thank the rest of my supervisory committee: Dr. Rick Chalaturnyk and Dr. Timothy G. Joseph for their insightful comments and the questions which helped me to widen my research from various perspectives. I am also grateful to my examiners: Dr. Michael Hendry, Dr. Ben Jar and Dr. Doug Stead for their precious time, comments and suggestions.

I acknowledge the Swedish Nuclear Fuel and Waste Management Co. (SKB) Sweden, the Canadian Nuclear Waste Management Organization (NWMO), and the Natural Sciences and Engineering Research Council of Canada (NSERC) who provided funding for this work.

I also wish to thank the following people for their help during the research:

Dr. Timothy G. Joseph for providing me the setup to conduct the laboratory testing and carry out the DIC analysis.

Dr. David Potyondy for his suggestions on the discrete element modelling.

My friend Dr. Yao Tang for the discussions on numerical simulations.

The technical staffs at the University of Alberta: Ms. Christine Hereygers, Mr. Randolf Kofman, Mr. Mark Labbe, Mr. Roger Marchand, Mr. Greg Miller, and Mr. Lucas Duerksen for helping me in sample preparation and conducting the laboratory testing.

Technical support staff at the Correlated Solutions in making the spackle pattern in the samples for DIC analysis.

I would like to thank my parents Ms. Nirati and Mr. Karunakar Patel; my wife Madhumita and our daughter Aasmi in all sincerity. Without their support the thesis could not have happened.

Contents

List of Figures

List of Tables

List of Symbols

A Cartesian coordinate system is used. The center of the Brazilian/ flattened Brazilian disk coincides with the origin, O, of the Cartesian system.

OB, horizontal axis of reference,

OE, vertical axis of reference,

P, load along the vertical diameter,

D, diameter of the disk,

t, thickness of the disk,

x, distance from the center of the disk along the horizontal diameter AB,

y, distance from the center of the disk along the vertical diameter EF,

σ_t, horizontal tensile stress at the center of the disk,

σ_c, vertical compressive stress at the center of the disk,

σ_{xx}, stress in x-direction,

σ_{yy}, stress in y-direction,

σ_{zz}, stress in z-direction,

ε_{xx}, strain in x-direction,

ε_{yy}, strain in y-direction,

ν_c, Poisson's ratio in compression,

ν_t, Poisson's ratio in tension,

E_c, Young's modulus in compression,

E_t, Young's modulus in tension,

m_x, slope of linear fit for ε_{xx} in ε_{xx} vs. P plot,

m_y, slope of linear fit for ε_{yy} in ε_{yy} vs. P plot,

u, displacement in x-direction,

v, displacement in y-direction,

n, number of samples tested.

σ_{tb}, Brazilian strength;

d: depth of flattening;

w: the width of flattening;

σ_{TOP}= P/(t*w): applied vertical stress on the flat surface;

P_c: Point at which crack is initiated in flattened Brazilian test;

x_c: the distance from center along the horizontal diameter, AB, at which the crack initiates;

σ_1, σ_1, σ_1: major, intermediate and minor principal stresses respectively;

σ_{BT}: Brazilian strength;

σ_{DT}: direct tensile strength;

CI= Crack initiation

CD= Crack damage

DT= Direct tensile test

BT= Brazilian tensile test

FB= Flattened Brazilian test

UCS= Uniaxial compressive strength

TR= Triaxial test

CE= Confined extension test

SD, standard deviation;

CoV, coefficient of variation; and

n, sample size.

Sign convention:

stress and strain values are +ve in compression;

horizontal displacement +ve towards +v x-direction; and

vertical displacement +ve towards +v y-direction.

Chapter 1:

Introduction

1.1 Problem statement

The most widely employed failure criterion for intact rock is the empirical non-linear Hoek-Brown criterion (Hoek and Brown 1980). The non-linearity of the failure envelope for intact rock is attributed to the transitioning from macroscopic tensile failure at low confining stress to macroscopic shear failure observed at high confinement (Figure 1.1). The non-linear shape of the failure envelope is most pronounced in the region of Figure 1.1 where the laboratory tests are conducted as uniaxial compression or uniaxial tension. The non-linear shape of the failure envelop in this region was first proposed by Griffith in 1924 (GrifIith 1924). Griffith suggested, based on tensile tests on glass rods, and his earlier theoretical work on tensile rupture, that the shape of the rupture envelope for brittle solids was a parabola in shear stress vs normal stress space. Griffith's proposed non-linear shape of the rupture envelope for brittle solids in compression was theoretical and despite having no reference work to intact rock, Griffith's pioneering work on energy and rupture was adopted by many researchers in rock mechanics, e.g., Hoek (1968), Fairhurst (1972), Brace (1964), Murrel (1958), Hoek and Brown (1980).

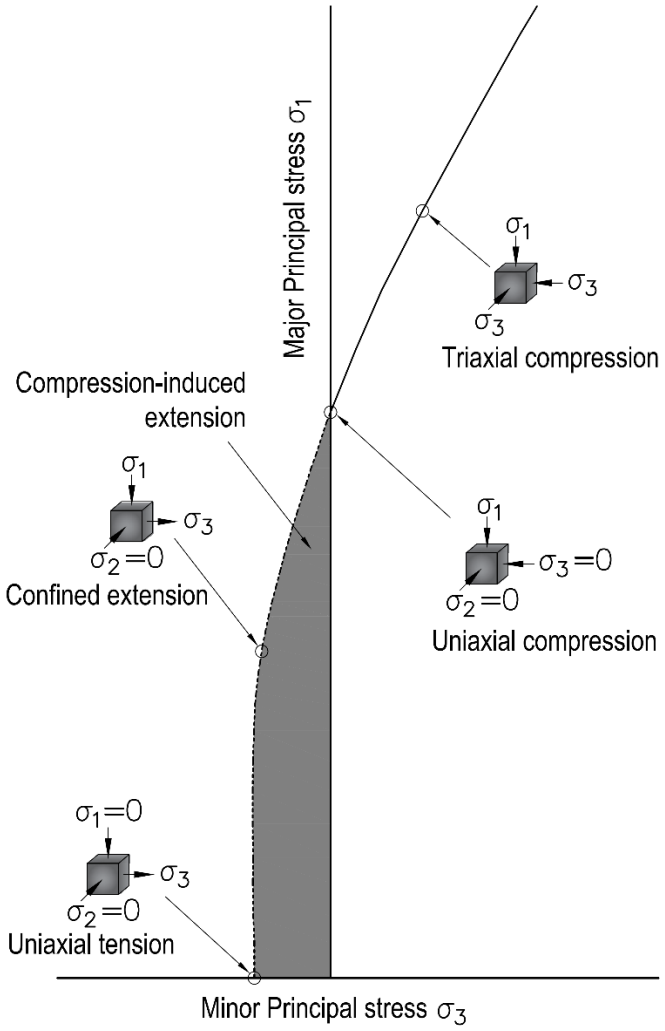

Figure 1.1: Failure envelope of a typical intact rock plotted in terms of (a) major and minor principal stresses with confined extension zone

Laboratory tests results are typically available for uniaxial compression tests (UCS), and triaxial compression tests for determining the shape of failure envelopes of different rocks in compression. However in the region of confined extension, the curve shaded region in Figure 1.1, from direct tension to uniaxial compression, limited testing has been carried out. Brace (1964) and Mogi (1967) tested a limited number of dog-bone shaped rock samples in confined extension and Mogi noted that the strength of the dog-bone samples tested in confined extension were influenced by the intermediate principal stress. More recently Ramsay and Chester (2004) using Carrara marble

samples with a modified dog-bone geometry conducted tests in the confined extension region to track the orientation of the rupture plane on a wide range of confining stresses. Their results were used by Hoek and Martin (2014) to show that in the tensile region a tension cut-off provided a better fit to the Ramsey and Chester data, than the non-linear Hoek-Brown failure envelope (Figure 1.2). This single example contradicts the long-held belief that the non-linear Griffith envelope represented the failure of rock in tension and confined extension. Cleary additional work is needed to resolve this contradiction.

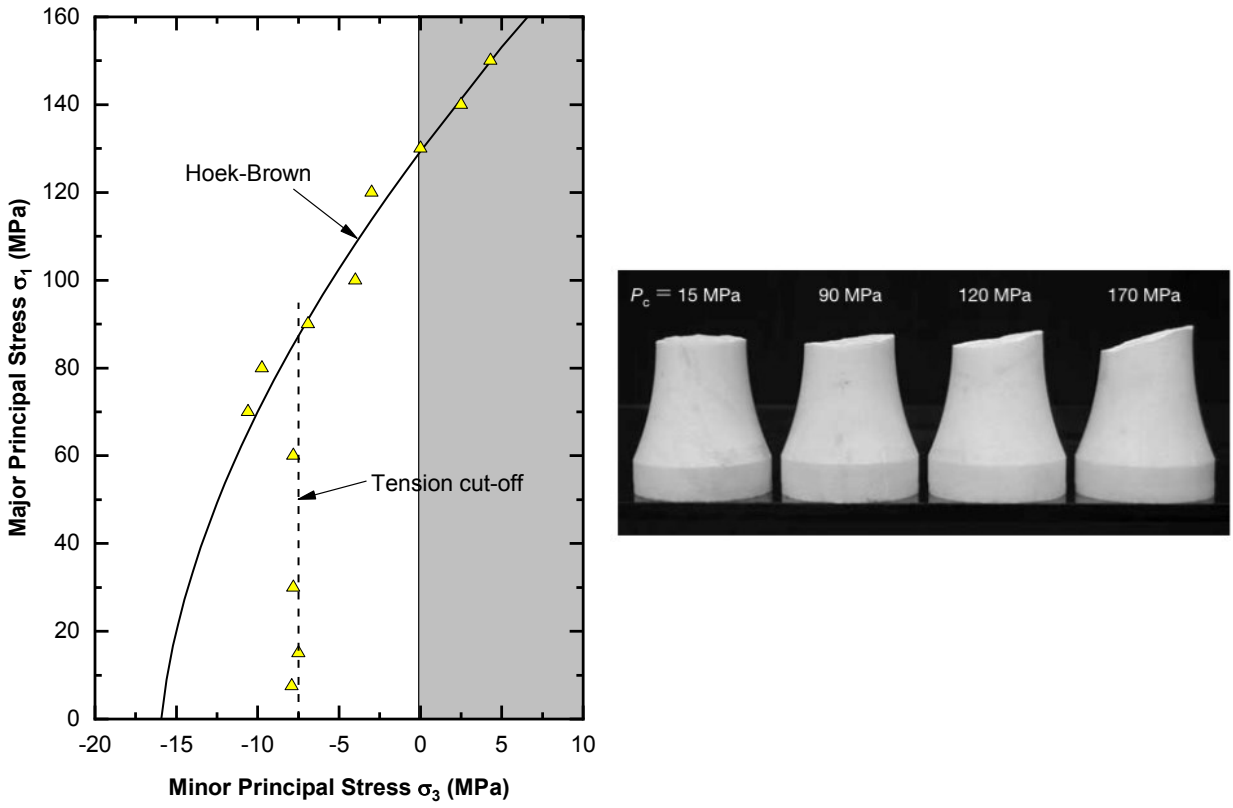

Figure 1.2: Confined extension test results for Carrera Marble (from Hoek and Martin 2014) The right Figure shows the orientation of the rupture plane in those confined extension tests (from Ramsay and Chester (2004))

1.2 Finding a Solution

The properties of Lac du Bonnet granite were extensively tested as part of Atomic Energy of Canada Limited characterization program at their Underground Research Laboratory located in Southwestern Manitoba (AECL URL). The work was carried out between 1987 and 2000 and reported in public documents. At the time of that characterization program the focus was the failure of rock in compression and only limited testing was carried out to establish tensile strength. Those results were used to establish the Hoek-Brown envelope for Lac du Bonnet Granite. While the AECL URL has been closed for a number of years core samples of Lac du Bonnet granite were available to the author. To investigate the behavior of rocks in confined extension three major steps were carried out are:

(1) development of a new experimental technique to conduct confined extension test on rock;

(2) development of a new experimental technique to obtain the tensile elastic properties of rock; and

(3) development of a methodology using a discrete element code to numerically simulate the behavior of rock in confined extension.

1.2.1 Development of a new experimental technique

The present methodology to test rock in confined extension has three main issues: (1) The dog-bone shaped rock sample is difficult to prepare, (2) laboratory testing using confined extension is difficult to conduct, and (3) there may be an impact of intermediate principal stress on the peak strength as observed by Mogi (1967). This intermediate principal stress is ignored in the Hoek-Brown criterion (Hoek and Brown 1980).

In a Brazilian test, a rock sample experiences both compressive and tensile stress at the center. If a Brazilian sample is flattened at the top and bottom, the compressive stress at the center of the specimen increases. By varying the depth of flattening the stresses at the center of the sample. can approach the stress observed in a uniaxial compressive test. Flattened Brazilian samples with different depth of flattening were investigated using the numerical code to examine the stresses change in the sample and to decide what the maximum amount of flattening needed. This also helped to decide what should be the interval of flattening and to determine the most probable location of crack initiation.

The exact location of crack initiation in a flattened Brazilian sample before the sample fails is difficult to predict in a material like rock. Both strain gauges and a digital image correlation technique, DIC (Sutton, Orteu, and Schreier (2009)) were used to establish the location of cracking and map the stress-strain behaviour of the flattened disks.

1.2.2 Development of a new experimental technique to obtain the tensile elastic properties of rock

Rocks when tested in both uniaxial compression (Bieniawski and Bernede 1979) and direct tension (ISRM 1978) show bi modularity (different Young's modulus and Poisson's ratio in compression and tension). Hondros (1959) assumed that the compressive and tensile elastic properties of concrete is the same and derived equations for the compressive Young's modulus and Poisson's ratio from the Brazilian test. Since, most rocks show bi-modularity and a Brazilian sample during testing has compression and tensile stress, the Brazilian test was used for obtaining the tensile Young's modulus and Poisson's ratio. A new set of equations was developed between the elastic properties; the compressive and tensile strain/displacements; and the sample geometry of the Brazilian test. The DIC technique was used to map the uniformity of loading and to obtain the

strain and displacement values on the surface geometry. The new derived equations were then used to obtain the tensile Young's modulus and Poisson's ratio in Lac du Bonnet granite.

1.2.3 Development of a numerical methodology to determine the confined extensional strength.

When rock engineering problems are complex, some form of numerical modelling is typically carried out to aid in finding a suiTable solution. Today, discrete element methods (DEM) are commonly used and offer many advantages over the complex constitutive models used in continuum modelling when simulating intact rock (Cundall 2015). One of the most noTable implementations of the DEM is the particle flow code in three dimensions (PFC3D) (Itasca 2015). This code is under constant improvement since it was proposed for rock by Potyondy and Cundall in 2004 (Potyondy and Cundall 2004). One of the drawbacks of the approach is the need to calibrate the micro-scale properties to provide a macro-scale response that matches the laboratory test results. Extensive calibrations were carried out to establish the behavior observed during the compression and tension testing of rocks, including initial non-linearity in a UCS test; bi-modularity and crack initiation. Once the PFC calibration results were satisfactory, the code was modified to simulate the confined extension test with stress path followed in the presented laboratory technique. The impact of the intermediate principal stress was evaluated by comparing the results with and without the intermediate principal stress. The data points obtained from the numerical results were compared with laboratory tests on Lac du Bonnet granite using the new confined extension testing technique. The results from the laboratory and the numerical investigation are then compared with the Hoek-Brown failure envelope.

1.3 Organization of the Thesis

This thesis is a paper based thesis. The chapters are organized as follows:

Chapter 2 explains the validation and application of DIC technique which was used to measure the strain and displacement values during the laboratory testing in this research.

Chapter 3 provides a new experimental technique to obtain the tensile elastic properties. For validation of the new methodology, the results are compared with the conventional direct tensile testing. The tensile and compressive elastic constants were then used for confined extension testing.

Chapter 4 describes a new experimental technique for confined extension test on rocks, which is easy to conduct at zero intermediate principal stress. Lac du Bonnet granite samples were tested in the laboratory and the results are presented.

Chapter 5 provides the results of discrete element models used for the investigation of the fracturing of rocks in the laboratory. The modification of the PFC3D code to examine the rock behavior in confined extension is presented.

Chapter 6 provides the discussion and summary of the thesis.

Chapter 2:

Validation and application of digital image correlation technique

2.1 Introduction

The unconfined compressive test (UCS) is widely accepted for determining the uniaxial compressive strength, Young's modulus and Poisson's ratio of intact rock, while the Brazilian test is used to establish the tensile strength. These tests are described in ASTM D7012 (Standard Test Methods for Compressive Strength and Elastic Moduli of Intact Rock Core Samples under Varying States of Stress and Temperatures), and ASTM D3967 (Standard Test Method for Splitting Tensile Strength of Intact Rock Core Samples). It is commonly assumed that the elastic properties of intact rock are independent of the loading path and hence that the compressive Young's modulus and tensile Young's modulus are essentially the same. This fundamental assumption is used when analyzing the stresses within a Brazilian disk. ISRM (1978) suggests the method to carry out the direct tensile test on rock. However, due to the difficulty in sample preparation and conducting the direct tensile test, the Brazilian test is typically used to obtain the tensile elastic properties (Hondros 1959, Jianhong, Wu, and Sun 2009 and Paul and Gnanendran 2016) by monitoring the deformation of the samples during loading.

A version of this chapter has been published in the Geotechnical Testing Journal:

Patel, S. and C. Derek Martin. 2018b. "Application of Digital Image Correlation Technique for Measurement of Tensile Elastic Constants in Brazilian Tests on a Bi-Modular Crystalline Rock." *Geotechnical Testing Journal*.

Digital image correlation (DIC) is a strain measurement technique that uses the principle of image matching. A high-resolution spackle pattern is applied to the region of interest in the deforming body. A single camera (in the case of 2D measurements) or multiple cameras (in the case of 3D measurements) are installed in front of the spackle pattern to continuously photograph the spackles as the object deforms. The location and relative movements of the pixels are tracked by comparing the images of the deformed sample with the reference (un-deformed) image. DIC software is used to obtain the strain from the relative displacements. Sutton, Orteu, and Schreier (2009) describe the principles behind this technique and Hijazi and Kähler (2017) discuss the effect of the imaging system components (camera, lens, image sharpness, etc.) on DIC measurements.

The DIC technique is now widely used to map strain in many engineering materials, particularly metals, during various deformation tests (Sutton et al. 2009). Also, this method appears well-suited for tracking the development of the compressive failure process in brittle rocks, from crack initiation through crack damage and strain localization. Yang et al. (2012) used this technique to study the time dependent damage and the creep behavior of natural rock salt and Hedayat and Walton (2017) used it to determine rock fracture shear stiffness. In the case of Brazilian test, this technique has been applied by Stirling, Simpson, and Davie (2013), and Belrhiti et al. (2017) for the measurement of elastic constants.

In this research, new equations have been developed to calculate the tensile Young's modulus and Poisson's ratio from the Brazilian test by considering the bi-modularity (different Young's modulus and Poisson's ratio in compression and tension) in the stress-strain equation. DIC technique is applied to Brazilian tests on Lac du Bonnet granite. The results from the Brazilian tests are compared with those obtained from direct tensile tests to verify the new methodology.

2.2 Background

Using elastic theory Timoshenko and Goodier, (1951), showed that when a Brazilian disk is loaded along its diameter, both tension and compression stress exist at the center of the sample. Figure 2.1 illustrates a Brazilian disk loaded along its vertical diameter. According to Timoshenko and Goodier, (1951) the tensile and compressive stresses at the center of the disk are given by:

$$\sigma_t = \frac{2P}{\pi Dt} \tag{2-1}$$

and

$$\sigma_c = -\frac{6P}{\pi Dt} \tag{2-2}$$

and the horizontal stress and vertical stress along the horizontal diameter AB and vertical diameter EF are given by (Hondros 1959):

(i) Horizontal diameter (AB)

$$\sigma_{xx} = \frac{2P}{\pi Dt}\left[1 - \frac{16D^2x^2}{(D^2 + 4x^2)^2}\right] \tag{2-3}$$

and

$$\sigma_{yy} = \frac{2P}{\pi Dt}\left[1 - \frac{4D^4}{(D^2 + 4x^2)^2}\right] \tag{2-4}$$

(ii) Vertical Diameter (EF)

$$\sigma_{xx} = \frac{2P}{\pi Dt} \tag{2-5}$$

and

$$\sigma_{yy} = \frac{2P}{\pi Dt}\left[1 - \frac{4D^2}{D^2 - 4y^2}\right] \tag{2-6}$$

Utilizing the fact that both tensile and compressive stresses exist in the Brazilian disk, Hondros (1959) used the Brazilian test to obtain the Poisson's ratio and Young's modulus for concrete assuming the Young's modulus values in compression and tension are same. Hondros (1959) compared the results with the values obtained from UCS testing for the same material, and found the Young's modulus values from both methods showed good statistical agreement. However, researchers have shown that many rocks display a bi-modularity between the compressive and tensile Young's modulus where the tensile Young's modulus can range between 5% and 100% of the compressive Young's modulus (Wawersik (1968), Haimson and Tharp (1974), Labuz (1985), Irani and Khan (1987), Jianhong, et al (2009), Fuenkajorn and Klanphumeesri (2011)). The effect of this bi-modularity on the interpretation of the Brazilian test is explored in the following section.

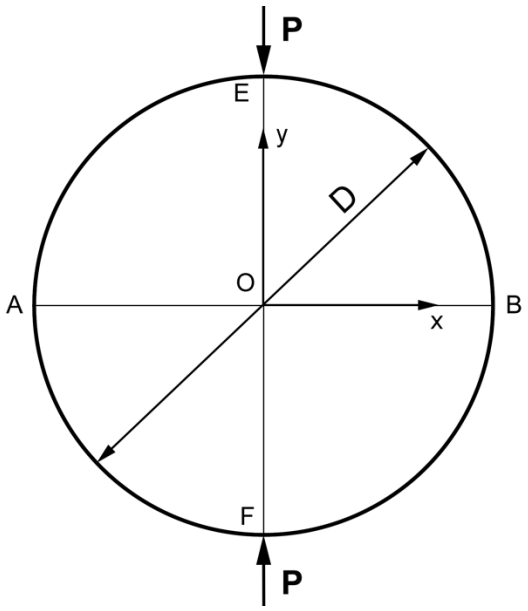

Figure 2.1: Brazilian sample loaded along its vertical diameter EF

2.2.1 *Effect of bi-modularity on the Brazilian test*

The elastic solution for the Brazilian test is derived assuming the material is homogeneous, isotropic, and linear elastic. But, a difference in compressive and tensile elastic properties in rock

makes Equations (2-1) to (2-6) invalid for the Brazilian test. Sundaram and Corrales (2008) developed a 2D finite element program to investigate the effect of bi-modularity on the Brazilian test. They found the tensile stress at the center of the disk was not in agreement with the value given by Equation (2-1), when (a) the compressive Young's modulus is different than the tensile Young's modulus and (b) values for Poisson's ratio in compression and tension are different. For a material with a tensile Young's modulus that is 50% of the compressive Young's modulus, the reduction in tensile stress at the center of the sample is approximately 10%. A change in the effective Poisson's ratio from 0.2 to 0.3 (the typical range in crystalline rock), increases the tensile stress at the center of the Brazilian sample by less than 1%. This suggests that, assuming Poisson's ratio is the same in tension and compression does not lead to significant errors in stress calculations.

Jianhong, Wu, and Sun (2009) used the Brazilian test to obtain the tensile Young's modulus in rock by monitoring the strain developed in the vertical and horizontal directions at the center of the disk. They assumed that the Poisson's ratios of rock were the same in compression and tension. However, according to Ambartsumyan (1969) and the model adopted by Sundaram and Corrales (2008) the elastic constants are related by the equation:

$$\frac{\nu_t}{E_t} = \frac{\nu_c}{E_c} \tag{2-7}$$

Hence, by Equation (2-7), if the elastic Young's modulus in tension and compression are different, the Poisson's ratio in tension and compression cannot be the same. This necessitates formulation of new equations for the tensile Young's modulus and Poisson's ratio considering the above relation between elastic constants.

2.2.2 *Calculation of Young's modulus and Poisson's ratio in tension from strain measurements*

The strain-stress relationships for a plane stress condition (σ_{zz}=0) with bi-modularity are given by:

$$\varepsilon_{xx} = \frac{\sigma_{xx}}{E_t} - C\sigma_{yy} \tag{2-8}$$

and

$$\varepsilon_{yy} = \frac{\sigma_{yy}}{E_c} - C\sigma_{xx} \tag{2-9}$$

where:

$$C = \frac{\nu_t}{E_t} = \frac{\nu_c}{E_c}$$

Taking the value of C as ν_c/E_c in both the Equations (2-8) and (2-9), the strain in x-direction and y-direction can be written as:

$$\varepsilon_{xx} = \frac{\sigma_{xx}}{E_t} - \frac{\nu_c}{E_c}\sigma_{yy} \tag{2-10}$$

and

$$\varepsilon_{yy} = \frac{\sigma_{yy}}{E_c} - \frac{\nu_c}{E_c}\sigma_{xx} \tag{2-11}$$

or

$$\frac{1}{E_c} = \frac{\varepsilon_{yy}}{\sigma_{yy} - \nu_c\sigma_{xx}} \tag{2-12}$$

Substituting the value of $1/E_c$ from Equation (2-12) in Equation (2-10), the Young's modulus in tension can be expressed as:

$$E_t = \frac{\sigma_{xx}}{\left[\varepsilon_{xx} + \left(\frac{\varepsilon_{yy}}{\sigma_{yy} - \nu_c\sigma_{xx}}\right)\nu_c\sigma_{yy}\right]} \tag{2-13}$$

Taking the value of C as ν_t/E_t in Equation (2-9), the strain in y-direction can be written as:

$$\varepsilon_{yy} = \frac{\sigma_{yy}}{E_c} - \frac{\nu_t}{E_t}\sigma_{xx} \tag{2-14}$$

or

$$\frac{\sigma_{yy}}{E_c} = \varepsilon_{yy} + \frac{\nu_t}{E_t}\sigma_{xx} \tag{2-15}$$

and substituting the value of σ_{yy}/E_c from Equation (2-15) in Equation (2-10), the Poisson's ratio in tension can be expressed as:

$$\nu_t = \frac{E_t}{\sigma_{xx}}\left[\frac{1}{\nu_c}\left(\frac{\sigma_{xx}}{E_t} - \varepsilon_{xx}\right) - \varepsilon_{yy}\right] \tag{2-16}$$

Equations (2-13) and (2-16) suggest that if the Poisson's ratio in compression is known from the UCS test, and the tensile and compressive strain values are measured at the center of a Brazilian disk, the tensile Young's modulus and the Poisson's ratio in tension can be obtained by using the stress values from Equations (2-1) and (2-2) and ignoring the small change in stress due to bi-modularity.

2.3 Material Investigated

The rock used in this study was Lac du Bonnet granite composed of biotite (~10%), quartz (~20%), perthite/microline (50-70%), and plagioclase (<10%) (Park and Piasecki 1993). The grain size for Lac du Bonnet granite varies from 2 to 6 mm. It was selected because it has been extensively tested and the results from those tests are available in the literature for comparison. Various laboratory properties found in the literature for Lac du Bonnet granite are summarized in Table 2-1.

Table 2-1: Laboratory properties of Lac du Bonnet granite (Martin 1993)

Parameter	Mean	Stdev	n
Tangent Young's modulus at 50% uniaxial compression (E_c)	69 GPa	±5.8 GPa	81
Tangent Young's modulus at 50% direct tension (E_t)	43.9 GPa	±4.9 GPa	10
Poisson's ratio in compression at 50% uniaxial compression (ν_c)	0.26	±0.04	81
Uniaxial compressive strength (UCS)	200 MPa	±22 MPa	81
Brazilian tensile strength ($\sigma_{t,b}$)	9.3 MPa	±1.3 MPa	39

2.4 Experimental Setup and Experimental Procedure

2.4.1 *Sample preparation/spackle pattern preparation*

Cores 63.4 mm in diameter were taken from Atomic Energy of Canada Limited (AECL) Underground Research Laboratory in southern Manitoba, Canada from a depth of 228 m. Ten disks were then cut from the cores using a diamond saw. These disks had a length to diameter ratio of 0.5, as suggested by ASTM D3967. The two end surfaces of the disks were then ground flat within 0.25 mm and parallel to 0.25° as per the ISRM method (ISRM 1978) using a surface grinder with a diamond wheel. Two strain measuring techniques were used (Figure 2.2a). A strain rosette with a gauge length of 6.35 mm and resistance of 350 ohms was installed at the center of one flat end of the disk as shown in Figure 2.2b. One of the strain gauges was aligned in the vertical and another in the horizontal direction; these are the directions of the principal strains.

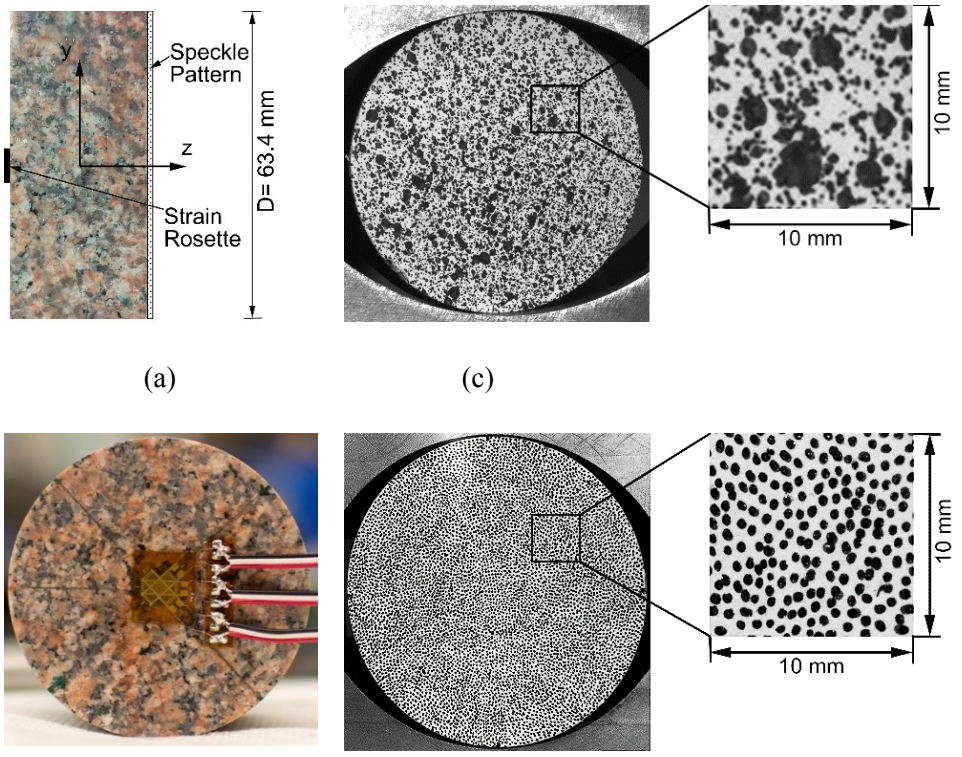

Figure 2.2: (a) Side view of sample indicating the strain rosette attached to one face and spackle pattern made on the other; (b) strain rosette attached at the center of one face; (c) spackle pattern made with spray paint (in this method it is difficult to control the size and number of spackles/cm^2); and (d) spackle pattern made with ultra-fine Sharpie® marker (about 250 spackles/cm^2, width of each spackle is about 0.5 mm)

A spackle pattern was then made on the other face of the sample (Figure 2.2c and d). There are different methods for making spackle patterns for small strain measurements (Correlated Solutions 2010a). The requirements to achieve an effective correlation in DIC are an isotropic, non-repetitive, and high contrast spackle pattern. Also, to capture the very small strain observed in a Brazilian test on rocks, a very fine spackle pattern (width of only a few pixels) is required. However, if the spackles are too small, the resolution of the camera may not be sufficient to capture the spackles during the test (aliasing effect). The ideal spackle size recommended in the Correlated Solutions manual (Correlated Solutions 2010a) is greater than 3-4 pixels. Taking these issues into

consideration, spackle patterns were created using two methods: spray paint (Figure 2.2c) and an ultra-fine Sharpie® marker (Figure 2.2d). Controlling the size of spackles was difficult with the spray paint technique and the contrast was not good; if the spackles are too big, the small strains associated with the test cannot be captured. On the other hand, the ultra-fine Sharpie® method provided consistent results (successful extraction of strain in all samples) with the required size of spackles. The average number of spackles per square centimeter using this method was about 250 and each spackle was about 0.5 mm wide.

2.4.2 *Experimental setup and testing method*

The experimental setup for the test is shown in Figure 2.3. The samples were tested in an MTS testing machine that can apply a constant strain rate to the samples. Two lenses were installed in front of the samples at a perpendicular distance of about 50 cm from the samples (as shown in Figure 2.3). A camera of resolution 2048*2048 pixels was used. The lenses used had a 90-mm fixed focal length with an aperture range of F2.8 to F32. The axes of the lenses were at an angle of about 30° from the axis of the sample. To provide sufficient light to the sample an LED light was placed in front of the sample. An LED light source was used because it has minimal thermal effect on DIC strain measurements. The cameras were connected to a computer that stored the images and ran the DIC software during the test. A multi-channel amplifier module was used to record the strain gauge data.

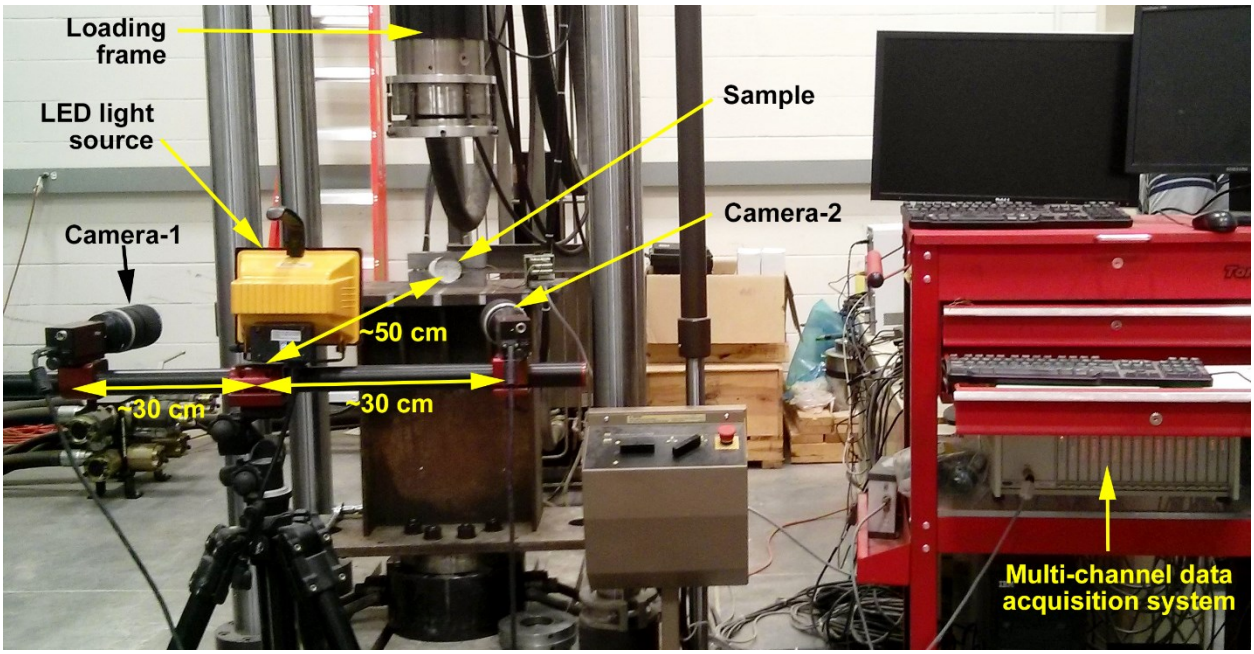

Figure 2.3: Experimental setup showing the loading frame, sample placed in the Brazilian frame, camera setup, and strain gauge data acquisition system

Samples were then placed in a Brazilian loading frame (ISRM 1978) with the vertical and horizontal strain gauges aligned in the appropriate directions. The cameras were then calibrated (Correlated Solutions 2010b) and reference images taken. The cameras were controlled by the DIC software to capture about two images per second (the maximum frequency for the setup used) throughout the test. The strain gauges were linked to the data acquisition system and the samples were loaded by applying a constant strain rate of 0.2 mm/minute until the sample failed. The samples failed in ~5 minutes, which is within the recommended time of 1-10 min as per ASTM D3967.

2.5 Results and Discussion

The average Brazilian strength as obtained from the peak load measured from the MTS testing machine for the ten samples tested was 11.2 MPa, which is similar to values reported by Martin (1993) for the medium grained Lac du Bonnet granite. The images taken by the two cameras during

the test were analyzed by comparing the displacement of pixels with respect to the reference image using three-dimensional visual image correlation software (VIC-3D, Correlated Solutions 2010b). We used three-dimensional DIC to confirm that there was no local out-of-plane displacement in the flat surface of the samples. The post-processing steps for the VIC-3D are described in the VIC-3D reference manual (Correlated Solutions 2010b).

As discussed in the VIC-3D manual, the strain calculations requires three important inputs; subset, step size and strain filter size. VIC-3D does not track the displacement of the actual spackles on the sample. It assigns a mesh of subsets or windows across the sample. The software then finds a unique point within each subset to track. The subset size is required to be greater than the largest size of the spackle on the sample. Step size (in pixels) defines how far apart the tracking points are placed in the sample. The subsets are overlapped and tracked for every step size. A step size of one-fourth the size of the subset is recommended in the VIC-3D manual. The strain values are smoothed using the filter size. The virtual size of the strain gauge in DIC is calculated as the step size multiplied by the filter size. We used a subset of 80 pixels, a step size of 20 pixels and a filter size of 9. This corresponds to a DIC virtual strain gauge length similar to that for the strain rosette (~6.35 mm).

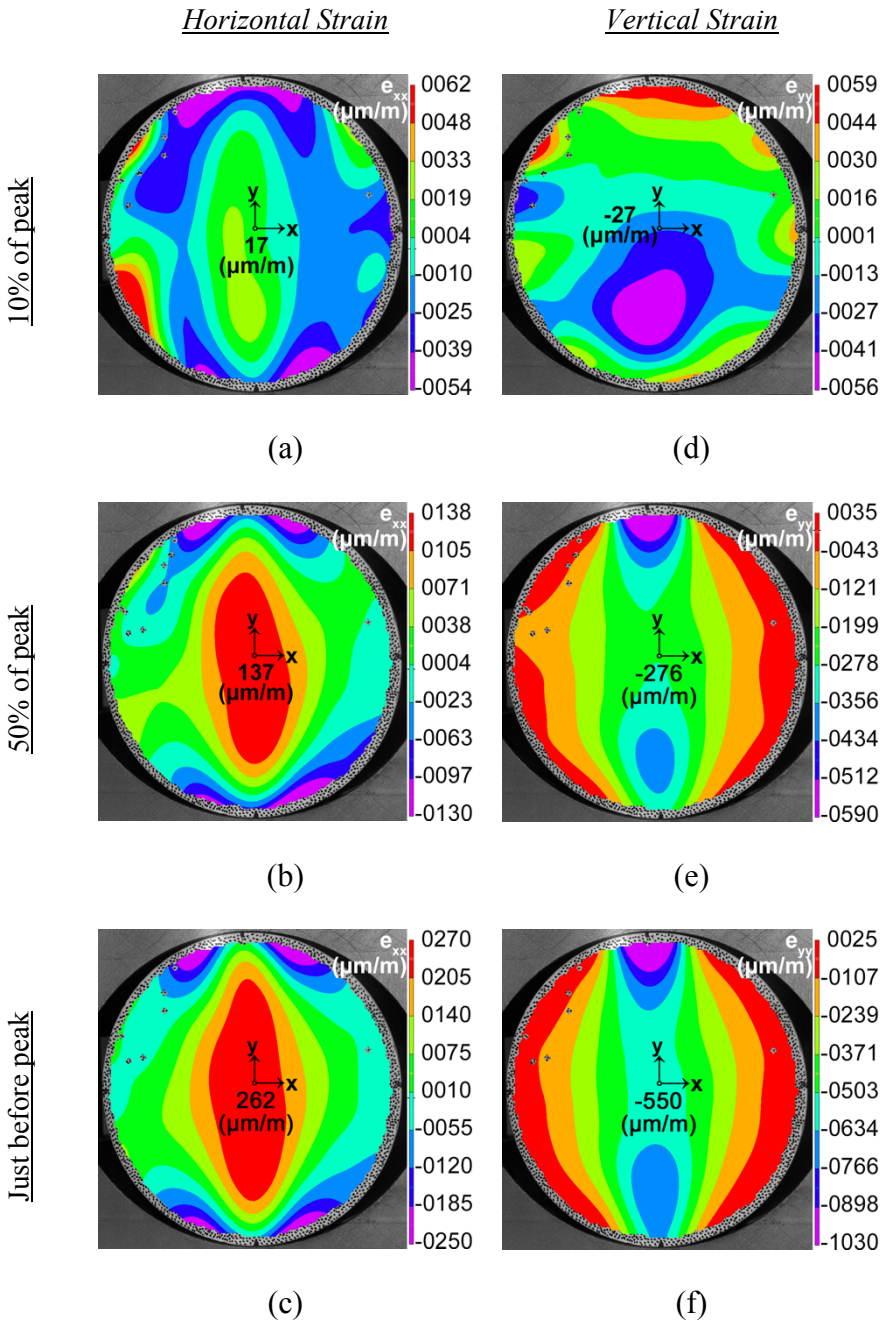

Figure 2.4: Strain contours from DIC analysis: (a), (b) and (c) are horizontal strain contours; (d), (e) and (f) are vertical strain contours. The strain is positive in tension. Refer to Figure 2.5 for loading locations on the load-strain curve.

Figure 2.4a to c show the typical development of tensile strain (horizontal strain, ε_{xx}) in the sample at different loading magnitudes. Notably, there is a tensile strain concentration at the center of the sample at all load levels shown. The tensile strain increased from 17 μm/m at 10% of peak load to a peak of 262 μm/m just before failure, at which point a crack developed at the center of the sample that eventually propagated in the vertical direction. Figure 2.4d to f show the typical development of vertical strain (ε_{yy}) in the sample. A compressive zone is evident in the central region of the Brazilian disk and the ratio of compressive to tensile strain values is consistently near two at different load levels.

2.5.1 *Comparison of DIC with strain gauge measurements*

Since the stress magnitudes in the horizontal and vertical directions on the surface of a Brazilian disk are not uniform, for a gauge length of 6.35 mm, there is a difference in the stress magnitudes between the center and end points of the strain gauges (Figure 2.2b). However, as per Equations (2-3) to (2-6) suggested by Hondros (1959), when the corresponding stresses were compared between the center and ends, the maximum difference was found to be less than 4%. Therefore, we considered that the strain values obtained from the strain rosette were the strain values at the center of the Brazilian disk.

Figure 2.5 compares the typical load-strain curves obtained from the strain gauges and the DIC method at the center of a Brazilian sample (on opposite faces). We found that when the vertical load was less than 10% of peak load, the DIC strain measured in the horizontal and vertical directions are scattered around zero. We believe that the DIC system used did not have the capacity to capture these very low strain values. However, at loads between 10% of the peak and the yield point, both measurement systems provide load-strain curves with similar slopes. The slope values

obtained from two methods for horizontal and vertical stain plots are compared in Table 2-2. The ratio of lateral (ε_{xx}) to axial (ε_{yy}) strain at 50% of the peak load was ~0.6 in both measurement systems, which is very high compared to the Poisson's ratio obtained from the UCS test (0.26). This is because the loading applied at the center of a cylindrical UCS test is uniaxial while the loading at the center of a Brazilian test is bi-axial. Hence, the ratio of the lateral to axial strain in the Brazilian test is not the Poisson's ratio.

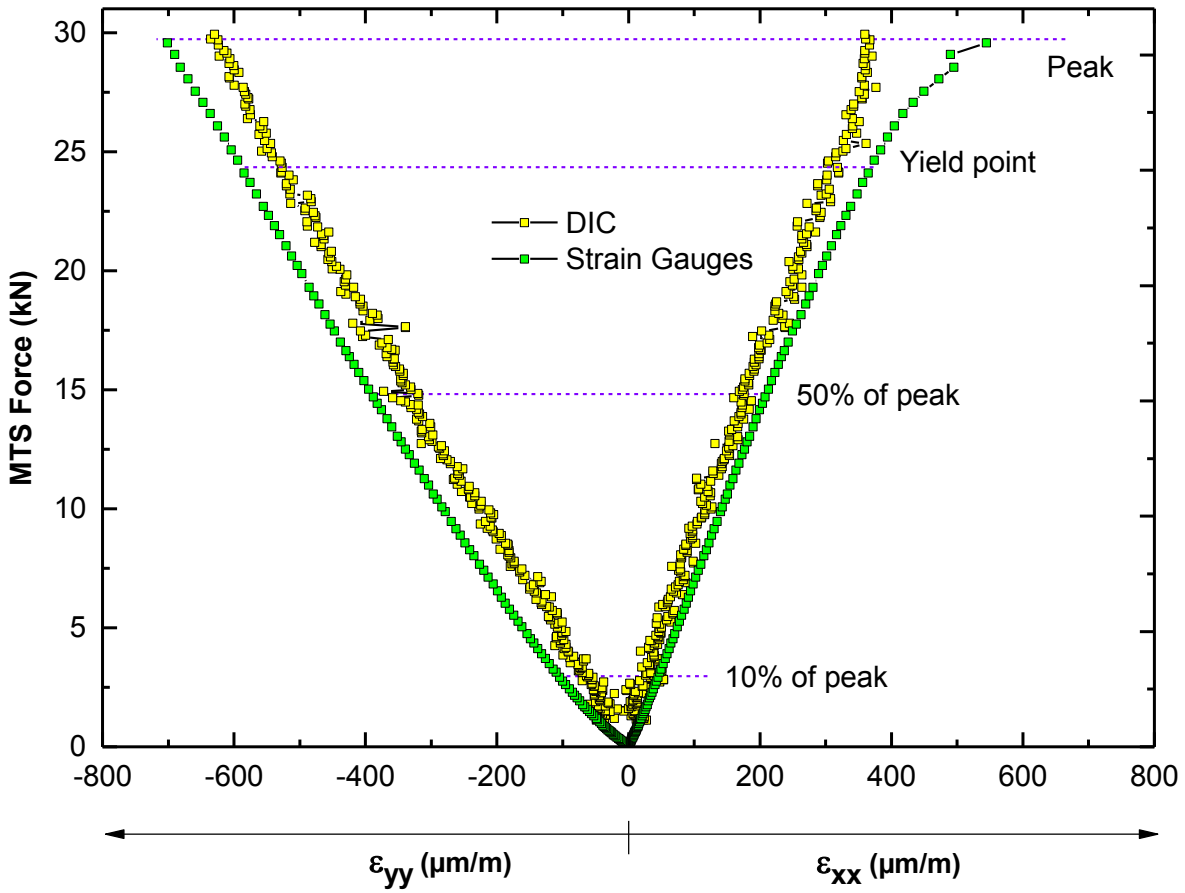

Figure 2.5: Comparison of load-strain plots obtained from the DIC technique and strain gauge measurements. The strain values were extracted from the centers of opposite faces of the Brazilian disk. The percentage shown indicates the load level at which strain in the x- and y-directions are compared in Figure 2.4, Figure 2.6 and Figure 2.7.

2.5.2 *Comparison of DIC measurements with the elastic solution*

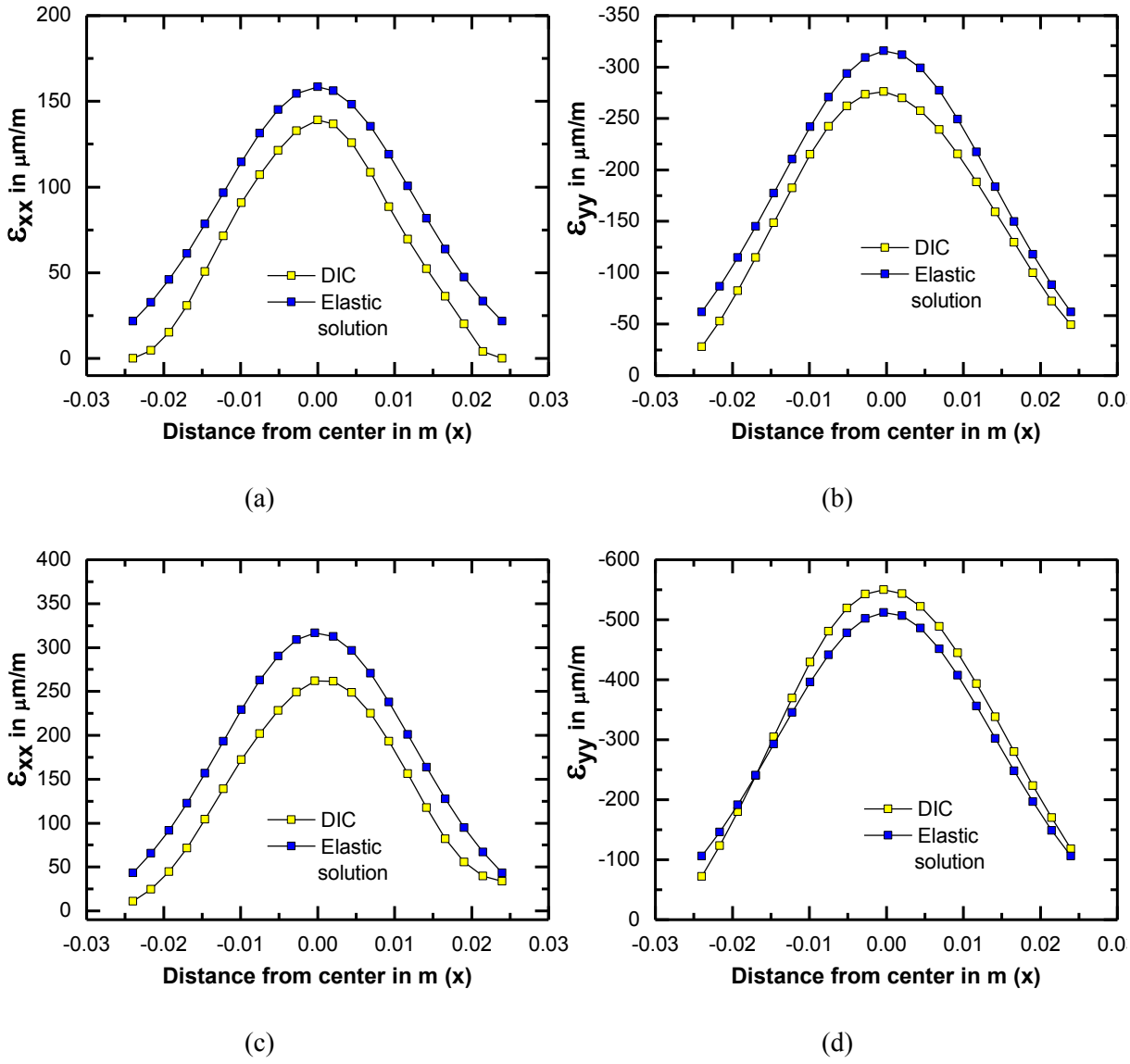

Figure 2.6: Comparison of horizontal and vertical strain vs. distance from the center of the disk along AB (Figure 2.1) obtained from the DIC method and the elastic solutions: (a) ε_{xx} at 50% of peak load (b) ε_{yy} at 50% of peak load (c) ε_{xx} at peak load (d) ε_{yy} at peak load

Horizontal and vertical strain data were extracted along the horizontal diametrical line (diameter AB, Figure 2.1) at 21 equally spaced points from the VIC-3D. These values were then compared with the elastic solutions. The strain values (ε_{xx} and ε_{yy}) for the elastic solution were calculated using Equations (2-8) and (2-9) using the Young's modulus and Poisson's ratio value from the

DIC measurements (Table 2-2). Figure 2.6a and b compare the strain values in x- and y-direction (ε_{xx} and ε_{yy}) along the diameter AB when the load is 50% of the peak load and Figure 2.6c and d compare just before the peak point (refer to Figure 2.5). The results obtained from VIC-3D are in good agreement with those from the closed form elastic solution. The shape of the curves obtained using both methods are very much comparable while there is a small difference in the horizontal (ε_{xx}) and vertical (ε_{yy}) strain values (12.1% and 12.5% at the center for 50% of peak load for ε_{xx} and ε_{yy} respectively). The corresponding difference in the case of peak load (Figure 2.6c and d) is 17.4% and 13.4% respectively. These differences are in the range of values reported by Hondros (1959). There is always an error calculating the strain at the edges of the spackle pattern using the DIC method. So, in Figure 2.6a to d the results are given from the centre to ~0.4D away on both sides of the sample (-24 mm to 24 mm).

2.5.3 *Calculation of Young's modulus and Poisson's ratio in tension*

Bieniawski and Bernede (1979) suggests that Young's Modulus and the Poisson's ratio for a sample loaded in compression should be determined at 50% of the peak load. This approach was used to determine the tensile Young's modulus and Poisson's ratio from the strain gauge and DIC. One of the issues with this approach is the data range that should be considered for the Young's modulus calculations. This is particularly relevant when data acquisition systems use a fast sampling rate and when the load-strain curves are not linear. Figure 2.7a shows the load-strain plot from the DIC method with 20% of the data above and below 50% of peak load considered. Figure 2.7b shows the effect of increasing the data range above and below 50% of the peak load to establish the slope of the best fit line. When only 5% of the data is considered, the slope of the best fit line is low and gradually increases as the data range is increased. When more than 40% of the data range is considered, the slope of both the vertical and axial and lateral response is

essentially constant. Consequently, for all Young's modulus calculations a 40% range was used for providing the best linear fit. This method of choosing the data range is specific to the material tested and the strain measurement system used.

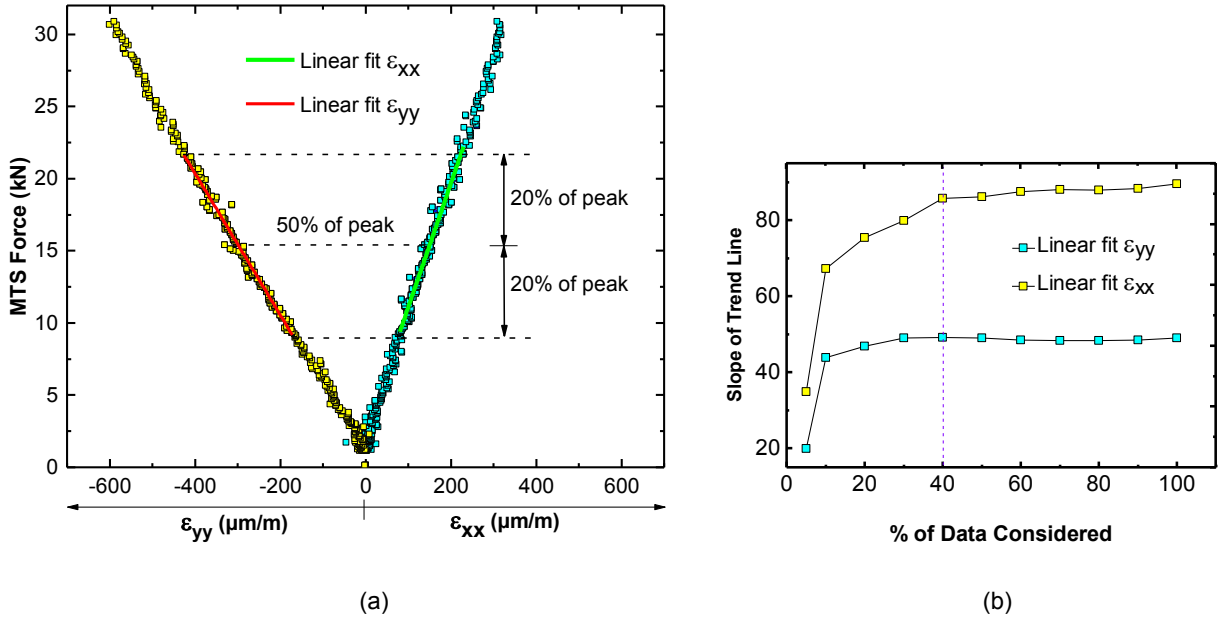

Figure 2.7: (a) Load vs. strain plot obtained from data from the DIC technique. The tensile Young's modulus was obtained from a linear fit of the data at 50% of peak load. The percentage of load indicates the range of data points used. (b) Curves showing the effect of data range considered above and below 50% of peak load on the measured slope of trend lines in (a).

Instead of using the absolute values of strain for Young's modulus calculations (i.e. remove the initial non-linearity), the slopes for the linear fit for ε_{xx} and ε_{yy} are used to calculate the strain values (ε_{xx} and ε_{yy}) at 50% of the peak load using the relations:

$$\varepsilon_{xx} = \text{slope of linear fit for } \varepsilon_{xx} \times \mathrm{P}/2$$

$$\varepsilon_{yy} = \text{slope of linear fit for } \varepsilon_{xx} \times \mathrm{P}/2$$

where, P is the peak load. The stress values (σ_{xx} and σ_{yy}) at 50% of peak load were calculated using Equations (2-1) and (2-2). The Young's modulus and Poisson's ratio in tension were then obtained by substituting the stresses (σ_{xx} and σ_{yy}), strain (ε_{xx} and ε_{yy}) values and Poisson's ratio in

compression from Table 2-1 in Equations (2-13) and (2-16). The results are presented in Table 2-2.

Table 2-2: Results of the Brazilian tests from DIC and strain gauge measurements at 50% of peak load

Sample	P (kN)	DIC[ab]						Strain Gauge[b]					
		m_x	m_y	ε_{xx}	ε_{yy}	E_t	ν_t	m_x	m_y	ε_{xx}	ε_{yy}	E_t	ν_t
1	14.7	0.08	-0.07	183.3	-225.7	46.5	0.14	0.09	-0.07	157.0	-213.8	45.8	0.16
2	13.9	-	-	-	-	-	-	0.07	-0.05	228.2	-322.8	39.6	0.17
3	16.0	0.07	-0.05	226.9	-300.6	38.7	0.15	0.06	-0.04	242.6	-348.5	34.4	0.17
4	15.7	0.10	-0.05	160.5	-319.6	65.4	0.30	0.08	-0.04	193.1	-404.8	62.3	0.34
5	15.4	0.07	-0.05	212.5	-326.6	40.7	0.19	0.07	-0.05	223.8	-325.8	37.3	0.18
6	15.3	0.09	-0.05	171.0	-310.4	54.9	0.26	0.07	-0.04	223.8	-401.6	41.6	0.25
7	15.6	0.08	-0.05	198.0	-322.2	47.3	0.21	0.08	-0.05	202.7	-352.8	49.3	0.24
8	17.1	-	-	-	-	-	-	0.08	-0.06	225.9	-307.6	39.3	0.16
9	14.0	0.08	-0.05	174.9	-282.9	47.2	0.21	0.08	-0.05	208.4	-308.0	42.7	0.18
10	16.2	0.06	-0.03	270.3	-490.0	37.7	0.26	0.07	-0.04	207.1	-331.9	39.5	0.21
Mean	-	0.08	-0.05	199.2	-345.7	47.3	0.22	0.07	-0.05	211.3	-331.8	43.2	0.21
SD	-	0.01	0.01	34.0	65.4	8.6	0.05	0.01	0.01	22.7	51.1	7.5	0.05
CoV (%)	-	15.1	12.7	17.1	18.9	18.3	23.8	9.2	17.1	10.8	15.4	17.4	25.4

[a] DIC results for the two samples were ignored because the spackle patterns were not proper (large spackles, Figure 2.2c) to capture the strain in the samples accurately.

[b] Units: m_x and m_y in $*10^{-6}$ kN, ε_{xx} and ε_{yy} in μm/m, E_t in GPa

The average tensile Young's modulus values obtained at 50% of peak load from the strain gauge measurements and the DIC measurements are 43.2 GPa and 47.3 GPa, respectively. These values are close to the historic data (43.9 GPa) provided in Table 2-1 from direct tension tests on 'dog-bone' samples. However, for such a low value of strain (average ε_{xx} ~0.02% and ε_{yy} ~0.033%) at 50% of peak load, we believe that, strain gauge measurement is more reliable compared to the DIC method. This is in agreement with the findings of Hijazi and Kähler (2017) that when using DIC, errors may be expected when measuring very small strains. The average values of Poisson's ratio in tension obtained from the DIC and strain gauge method are 0.22 and 0.21 respectively.

The Young's modulus of Lac du Bonnet granite from uniaxial compression tests taken at 50% of the peak load is 69 GPa (Table 2-1). The tensile Young's modulus obtained from the DIC data and the strain gauge data is 68.5% and 62.6% of the compressive Young's modulus values respectively. This finding is in keep with the findings from Martin (1993). In graphical form, the Young's modulus values obtained using different methods are compared in Figure 2.8.

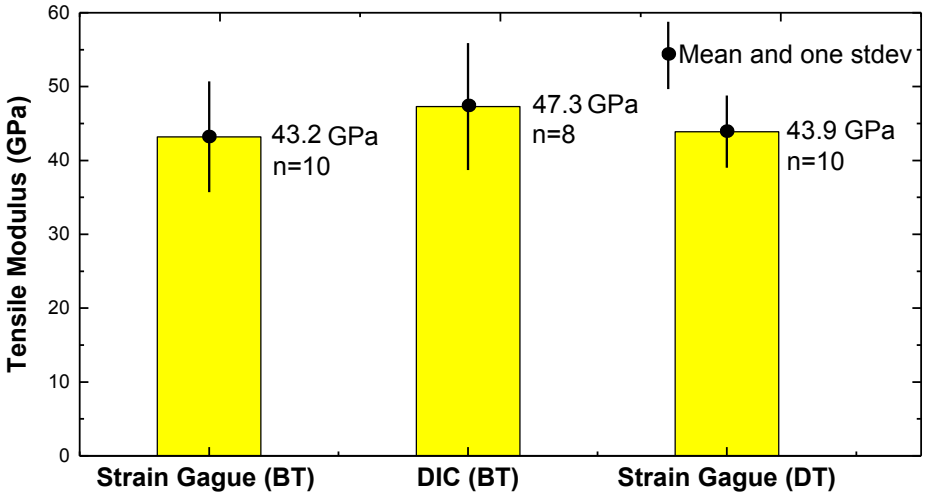

Figure 2.8: Comparison of average tensile Young's modulus values obtained from (i) strain gauge measurements on the Brazilian test (ii) DIC measurements on the Brazilian test and (iii) strain gauge measurements on the direct tension test (BT= Brazilian Test and DT= Direct Tension Test).

2.6 Summary

Hondros (1959) suggested a method to evaluate Poisson's ratio and Young's modulus from the Brazilian test assuming the elastic constants are the same in compression and tension. In this study, the bi-modular relation between the elastic constants (as suggested by Ambartsumyan 1969 and Sundaram and Corrales 2008) was applied to the equations for the Brazilian test to derive new equations for the Young's modulus and Poisson's ratio in tension. The DIC technique was used to verify the uniformity of loading and to obtain the strain values in the sample during loading. The results obtained from the DIC method were also compared with the conventional strain gauge

measurements and the results obtained from direct tension tests on dog-bone shaped Lac-du-Bonnet granite samples. The results from this study lead to the following conclusions:

- When the vertical load is greater than 10% of peak, the DIC system used for the study was found to be capable of measuring the <0.1% strain values observed in the crystalline rock before tensile fracturing. For the rock tested, a spackle pattern with a density of ~250 spackles/cm^2 made using an ultra-fine Sharpie® was suiTable for capturing the strain distribution over the entire disk surface.
- We observed that the load-strain plots obtained from the strain gauges are smoother (high R-squared value for a linear fit) compared to that from the DIC measurements. However, the average slopes of the stress-strain response at 50% of peak using the data from the DIC method were in agreement with those obtained from the strain gauges.
- The DIC strain values along a horizontal line at the midheight of the disk were found to be similar to those from the elastic solution. The shape of the curves obtained from the two methods matched and the difference in elastic strain magnitudes was less than 12.5%.
- The average value of Poisson's ratio in tension obtained from the DIC data (0.22) and the strain gauge data (0.21) were found to be less than the Poisson's ratio in compression (0.26) which was measured from the UCS test.
- The difference in average elastic tensile Young's modulus obtained from the DIC data (47.3 GPa) and strain gauge data (43.2 GPa) using Brazilian tests is less than 8% of the value (43.9 GPa) from direct tensile tests on dog-bone shaped sample. The coefficient of variation for the tensile Young's modulus obtained from DIC data (18.3%) was similar to that obtained using strain gauge data (17.4%) and as observed by Hondros (1959) for concrete.

Chapter 3:

Evaluation of tensile Young's modulus and Poisson's ratio of a bi-modular rock from the displacement measurements in a Brazilian test

3.1 Introduction

It is commonly assumed that the modulus of rocks is independent of the loading path and the compressive modulus and tensile modulus are essentially the same. Bieniawski and Bernede, (1979) described the ISRM Suggested Method for obtaining the deformability of rock materials in uniaxial compression. When researchers (Wawersik 1968, Haimson and Tharp 1974, Irani and Khan 1987 and Fuenkajorn and Klanphumeesri 2011) obtained the elastic modulus in tension from the direct tensile test (ISRM 1978) they observed that the compressive elastic modulus was always greater than the tensile modulus. This difference in tensile and compressive modulus was initially observed using different samples. Fairhurst (1961) using 3 point bending tests of granite beams observed on the same beam that the tensile modulus was about 80% of the compressive modulus.

A version of this chapter has been published in the journal of Rock Mechanics and Rock Engineering:

Patel, S. and C. Derek Martin. 2018. "Evaluation of Tensile Young's Modulus and Poisson's Ratio of a Bi-Modular Rock from the Displacement Measurements in a Brazilian Test." *Rock Mechanics and Rock Engineering* 51(2):361–73.

Ye, Wu, and Sun (2009) and Ye et al. (2012) derived equations for the tensile Young's modulus from the Brazilian test assuming the Poisson's ratio in tension and compression is the same. In this research, we extend the work of Ye et al (2012) and describe a new methodology to obtain the tensile elastic modulus and Poisson's ratio from the Brazilian test. New equations for the displacement in horizontal and vertical directions of the points on the flat surface of a Brazilian test are derived by incorporating the bi-modular relations between the elastic constants (E_c, E_t, ν_c and ν_t). We tested Brazilian samples of Lac-du-Bonnet granite and using the derived displacement equations, estimated the tensile elastic modulus and Poisson's ratio. These values are then compared with the results from direct tension tests using dog-bone shaped Lac-du-Bonnet granite samples.

3.2 Background

A direct method for measuring the tensile Young's modulus and Poisson's ratio in rock is the direct tension test (ISRM 1978). While this method provides direct results, sample preparation and test configuration can be challenging. The Brazilian test was introduced in 1943 (Fairbairn and Ulm 2002) to overcome the issues associated with the direct tension test. Today, the Brazilian test is typically used in practice for determining the rock tensile strength (ISRM 1978 and ASTM 2008). Hondros (1959) used this test to estimate the elastic compressive modulus and Poisson's ratio in concrete. He assumed the Young's modulus and Poisson's ratio of concrete in compression to be same as that in tension and derived the following equations for the Poisson's ratio (ν) and Young's modulus (E) (relating to the central strains and load applied, Figure 3.1):

$$\nu = -\frac{3\varepsilon_{yy} + \varepsilon_{xx}}{3\varepsilon_{xx} + \varepsilon_{yy}} \tag{3-1}$$

and

$$E = \frac{2P(1-\nu^2)}{\pi Dt\left(\varepsilon_{xx} + \nu\varepsilon_{yy}\right)} \tag{3-2}$$

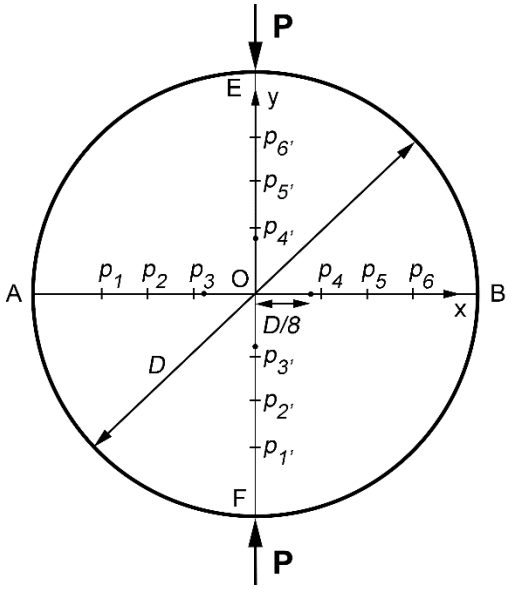

Figure 3.1: Brazilian sample with reference points for displacement measurements

Hondros (1959) compared the results from the Brazilian tests with the unconfined compression test on concrete and found a good match. However, the limited data found in the literature where both compressive and tensile elastic moduli are available indicate that the compressive modulus is always more than the tensile modulus Table 3-1.

Table 3-1: Tensile (E_t) and compressive (E_c) modulus values of some rocks from the literature.

Rock Type	E_t (GPa)	E_c (GPa)	E_t/E_c (%)
Tennessee Marble I[a]	42.7	53.8	79.5
Tennessee Marble II[a]	56.5	71.7	78.8
Georgia Marble[b]	23.4	42.1	55.7
Tennessee Marble[b]	53.1	76.5	69.4
Russian Marble[b]	9.0	20.7	43.3
Marble[d]	66.8	76.9	86.9
Saraburi Marble[e]	34.4	41.7	82.6
Granite[f]	55.2	68.9	80.0
Charcoal Grey Granite[a]	37.9	48.3	78.6
Westerly Granite[b]	17.2	72.4	23.8
Granite[c]	46.1	59.6	77.3
Granite[d]	14.0	20.3	69.0
Austin Limestone[b]	11.7	15.9	73.9
Carthage Limestone[b]	35.2	63.4	55.4
Indiana Limestone[b]	11.0	26.9	41.0
Limestone[d]	43.3	57.7	75.0
Saraburi Limestone[e]	26.1	37.2	70.3
Arizona Sandstone[b]	11.7	45.5	25.8
Berea Sandstone[b]	4.1	23.4	17.6
Millsap Sandstone[b]	0.7	13.1	5.3
Tennessee Sandstone[b]	1.4	16.5	8.3
Russian Sandstone[b]	11.7	57.2	20.5
Sandstone[d]	7.1	10.0	71.0
Phu Phan Sandstone[e]	6.7	16.2	41.5

[a]Wawersik 1968, [b]Haimson and Tharp 1974, [c]Irani and Khan 1987, [d]Jianhong, Wu, and Sun 2009, [e]Fuenkajorn and Klanphumeesri 2011, [f]Fairhurst 1961

Considering the difference in the elastic moduli and Poisson's ratios in compression and tension (bi-modularity) in rock, Sundaram and Corrales (1980) investigated the validity of the Brazilian stress equations given in ISRM (1978) and ASTM (2008) using a numerical model. They used bi-modular relations between the elastic constants (Equation (3-5)) as suggested by Ambartsumyan (1969) for their numerical model. Sundaram and Corrales (1980) found out that the difference in

the elastic moduli was around 10% difference when tensile modulus was 50% of compressive modulus, while the difference in Poisson's ratio was less than 1.3% for the ranges of Poisson's ratio found in rocks on the stress values in a Brazilian test. However, when the elastic moduli and Poisson's ratios in compression and in tension are different, the stress-strain relationships used by Hondros (1959) and given in Equations 3-1 and 3-2, are no more applicable.

Patel and Martin (2018a) incorporated the bi-modularity in the Brazilian test relations as suggested by Ambartsumyan (1969) and developed new equations for the elastic tensile modulus and Poisson's ratios (relating to the compressive and tensile strain values at the center 'O' of the Brazilian disk, Figure 3.1). They found out that the tensile elastic constants obtained from the Brazilian test on Lac-du-Bonnet granite using the strain measurements at the center of the Brazilian disk are comparable to the values obtained from the direct tensile test on Lac-du-Bonnet granite. However, Fairhurst (1961) suggested that when using the strain measurement technique to determine the elastic constants, the strain measured in a localized area, such as at the center of the Brazilian disk, is a disadvantage and can be applied to the fine grain rocks or when large diameter rock cores are available.

To remove the effect of strain localization at the disk centre, Ye et al. (2012) used the displacements measured during the Brazilian test to estimate the compressive and tensile modulus in rock. In this method, the displacements are measured at different locations along the horizontal and vertical diameter of a Brazilian disk (Figure 3.1). Such large-scale measurements average the response of different minerals present in a rock and minimize the possibility of local effects. However, Ye et al. (2012) assumed that the Poisson's ratio in compression and tension were the same for the Brazilian stress-strain equations. This limitation can be removed using the approach described in the next section.

3.2.1 *Calculation of Young's modulus and Poisson's ratio in tension from deformation measurements*

The displacements of the points on the surface of a Brazilian disk (Figure 3.1) are functions of the load applied *(P)*, the *x* and *y* co-ordinate of the point and the elastic parameters (E_c, E_t, ν_c and ν_t). The horizontal displacement *u(x)* long the horizontal diameter AB and vertical displacement, *v(y)*, along the vertical diameter EF (Figure 3.1) are given by:

$$u(x) = \frac{2P}{\pi t}\left[\left(\frac{x}{D} - tan^{-1}\frac{2x}{D}\right)\left(\frac{1}{E_t} - \frac{\nu_c}{E_c}\right) + \frac{2Dx}{4x^2 + D^2}\left(\frac{1}{E_t} + \frac{\nu_c}{E_c}\right)\right] \tag{3-3}$$

$$v(y) = \frac{2P}{\pi t}\left[\frac{1}{E_c} ln\frac{D + 2y}{D - 2y} + \frac{y}{DE_c}(\nu_c - 1)\right] \tag{3-4}$$

(the derivation of these equations are given in Appendix A).

At a particular value of *P* during a Brazilian test, the horizontal/vertical displacements along the horizontal and vertical diameter can be measured. Now, there are only three unknowns in the displacement equations, E_c, E_t and ν_c. Substituting the value of E_c from Equation (3-4) and ν_c from the uniaxial compressive test in Equation (3-3) the value of E_t can be obtained. The value of ν_t can be calculated from the relation between the elastic constants (Ambartsumyan 1969 and Sundaram and Corrales 2008)

$$\frac{\nu_t}{E_t} = \frac{\nu_c}{E_c} \tag{3-5}$$

What remains is finding a suiTable technique for measuring the displacement during testing.

3.2.2 *Displacement measurement using the DIC technique*

The digital image correlation (DIC) is a non-contacting technique that captures the images of a deforming object, stores the images in a digital format and analyzes them to obtain the shape,

displacement and strain in the object. A single camera or multiple cameras are used to capture the two dimensional and three dimensional deformation patterns, respectively. To get good resolution pictures taken by DIC cameras high contrast black spackles are made on a white layer of paint on the surface of the specimen (Figure 3.2c). Cameras are then installed in front of the specimen (Figure 3.3) to take pictures continuously during the test. The pictures are stored in a computer and later analysed using specialized software. The software compares the deformed pictures with the reference picture (un-deformed) to obtain the shape, deformation and motion. The details of this technique is described by Sutton, Orteu, and Schreier (2009). Stirling, Simpson, and Davie (2013), Belrhiti et al. (2017) and Patel and Martin (2018a) used the technique to measure the elastic constant from the Brazilian test.

3.3 Material investigated

For this research, we selected one of the extensively tested crystalline rock, Lac-du-Bonnet granite. The results of the tests for Lac-du-Bonnet granite are available in Martin 1993. We took 63.4 mm diameter cores of the rock from the 228 m level of the Atomic Energy of Canada Limited (AECL) Underground Research Laboratory in southern Manitoba, Canada. The rock core was relatively homogeneous, isotropic. The mineral contents of the rock are: biotite (~10%), quartz (~20%), perthite/microline (50-70%), and plagioclase (<10%) (Park and Piasecki 1993). The grain size for Lac-du-Bonnet granite varies from 2 to 6 mm. The density of the rock is 2630 kg/m^3 while the p-wave velocity is around 3100 m/s (Collins 1997). Table 3-2 summarizes the relevant laboratory properties of the rock used for this study.

Table 3-2: Relevant laboratory properties of Lac-du-Bonnet granite for the study from literature (Martin 1993)

Parameter	Mean	Stdev	n
Density	2630 kg/m^3	±10 kg/m^3	-
Tangent Young's modulus at 50% uniaxial compression (E_c)	69 GPa	±5.8 GPa	81
Tangent Young's modulus at 50% direct tension (E_t)	43.9 GPa	±4.9 GPa	10
Poisson's ratio in compression at 50% uniaxial compression (ν_c)	0.26	±0.04	81
Uniaxial compressive strength (UCS)	200 MPa	±22 MPa	81
Brazilian tensile strength (σ_{tb})	9.3 MPa	±1.3 MPa	39

3.4 Experimental setup and experimental procedure

3.4.1 *Sample preparation*

We diamond sawed the Lac-du-Bonnet granite cores (63.4 mm diameter) taken from the underground research laboratory in disk shape with thickness to diameter ratio of about 0.5 as suggested by ISRM 1978 and ASTM D3967. We ground the two end surfaces of the disks using a diamond wheel to be parallel within 0.25^0 and flat within 0.25 mm as per the ISRM method (ISRM 1978).

For the displacement measurements using DIC technique, we made a spackle pattern on one flat face of the disk by putting black spackles using ultra-fine Sharpie® marker on a white layer of spray paint (Figure 3.2c). The average number of spackles per square centimeter were around 240 with average diameter of the spackle around 0.5 mm. The detailed procedure of making spackle pattern on the specimen is described in CorelatedSolutions (2010a).

A strain rosette (gauge length of 6.35 mm and resistance of 350 ohm) was installed at the center of the other face of the disk as shown in Figure 3.2a and b. These strain gauges were used to compare the strain along the horizontal and vertical direction at the center of the disk with the corresponding values obtained from the DIC method on the opposite disk face.

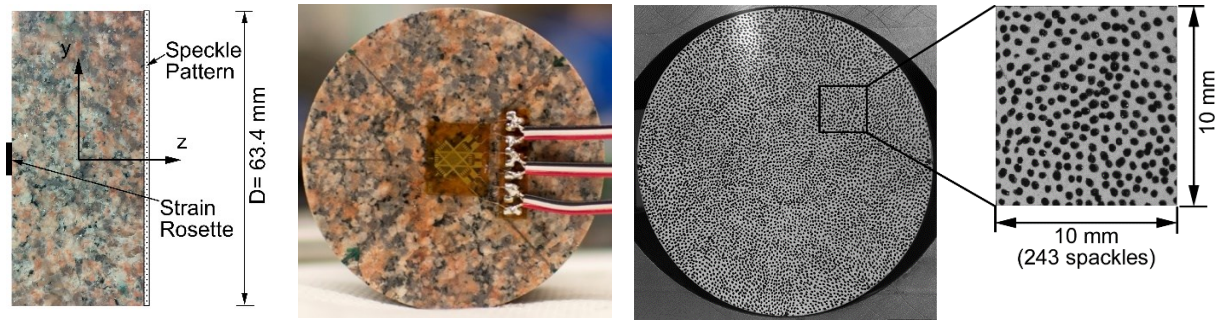

(a) (b) (c)

Figure 3.2: (a) Side view of sample showing the strain rosette and the spackle pattern made on two faces; (b) strain rosette attached at the center of one face; and (c) spackle pattern made with ultra-fine Sharpie® marker for the DIC measurements

3.4.2 *Experimental setup and testing method*

Figure 3.3 shows the experimental set up for the Brazilian test. We used a MTS testing machine to apply a constant strain rate to the samples. The specimens were placed in a Brazilian frame (ISRM 1978) with the spackle pattern on the front and strain gages on the back of the sample. The strain gages were attached to a data acquisition system. Two cameras with 90-mm fixed focal length and an aperture range of F2.8 to F32 were placed at the front of the specimen as shown in Figure 3.3. The cameras were at a perpendicular distance of about 0.5 m from the specimen and at an offset of about 0.3 m from the axis of specimen. Setting up the camera are described in CorelatedSolutions (2010b). To store the images and operate the DIC software the two cameras were connected to a computer. This computer was later used to analyze the data using DIC software.

Reference images were taken at no load and the cameras were set to take two images of the sample per second during the test. The samples were then loaded at a constant displacement rate of 0.2 mm/min. This failed the samples in around 5 minute which is within the recommended time of 1-10 minute as per ASTM D3967.

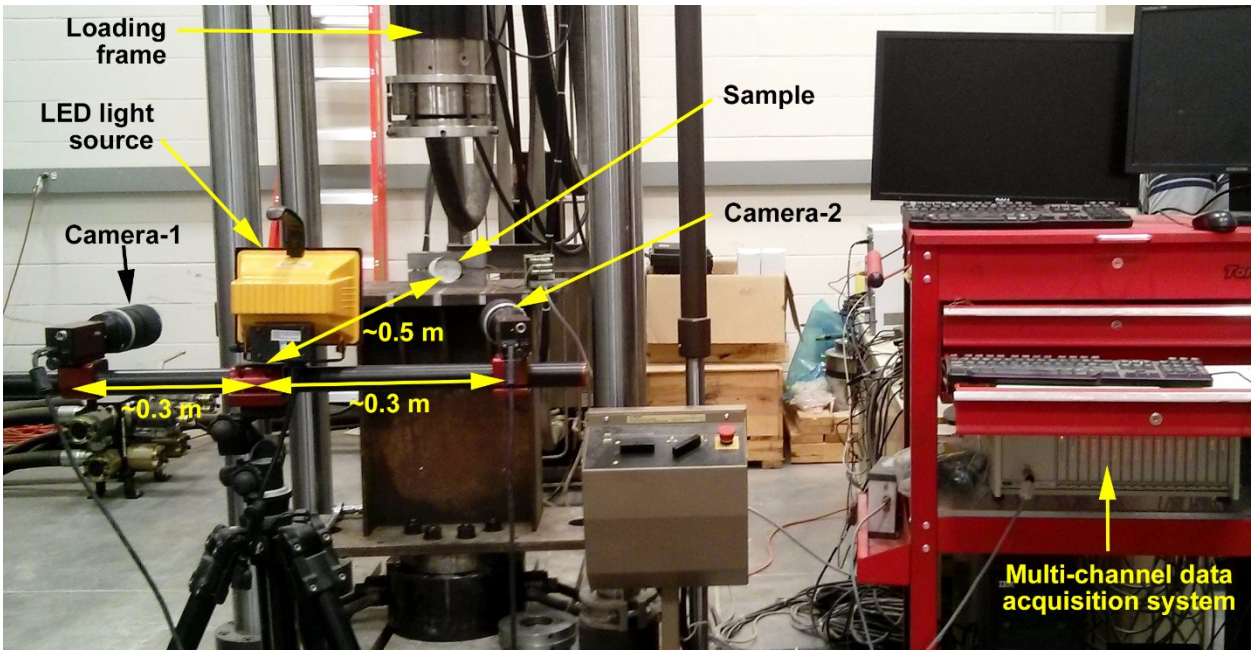

Figure 3.3: Experimental setup for the Brazilian test and the digital image correlation (DIC) system

3.5 Results and discussion

The images taken by the cameras during the Brazilian tests were analyzed using the DIC software to extract the strain at the center of the specimen and the displacement along the horizontal and vertical diameter. Data extraction procedures in DIC are described in the CorelatedSolutions (2010b) manual. Both the DIC and the strain-gauge data were analyzed using the horizontal and vertical stain (ε_{xx} and ε_{yy}) versus load (P) at the center of the Brazilian disk. Table 3-3 compares the slope of the ε_{xx} and ε_{yy} versus P plots at 50% of peak load (in the linear part of strain-load plot). The average slope values for five samples using the DIC data are 0.078 and -0.050 for ε_{xx} and ε_{yy} respectively and that from the strain gauge measurements are 0.072 and -0.046. The difference between these two methods are less than 10%.

Table 3-3: Comparison of slopes of strain (ε_{xx} and ε_{yy}) vs load (P) plots obtained from DIC method and strain gauge (SG) measurements at 50% of peak load

Slope	DIC		Strain gauge	
	ε_{xx} vs P	εyy vs P	ε_{xx} vs P	ε_{yy} vs P
Average (*10^{-6} kN)	0.078	-0.050	0.072	-0.046
SD (*10^{-6} kN)	0.007	0.002	0.006	0.005
CoV (%)	9.4	4.6	8.7	11.4

Figure 3.4 shows the horizontal (u) and vertical (v) displacement contours obtained from the DIC method at 50%, 75% of the peak load and at the peak load during the Brazilian test. The displacements at the symmetrical points P_2 vs P_5 and $P_{2'}$ vs $P_{5'}$ (Figure 3.1) are compared. For the Lac-du-Bonnet granite tested the displacement values at these mid points are very low (average value of 0.0018 mm for u and of 0.0049 mm for v at 50% of peak load). The values of u and v at the symmetrical points was found to be very similar (u for P_2=-0.0019 mm and P_5=0.0017 mm whereas for v at $P_{2'}$=-0.0047 mm and $P_{5'}$=0.0052 mm at 50% of peak load).

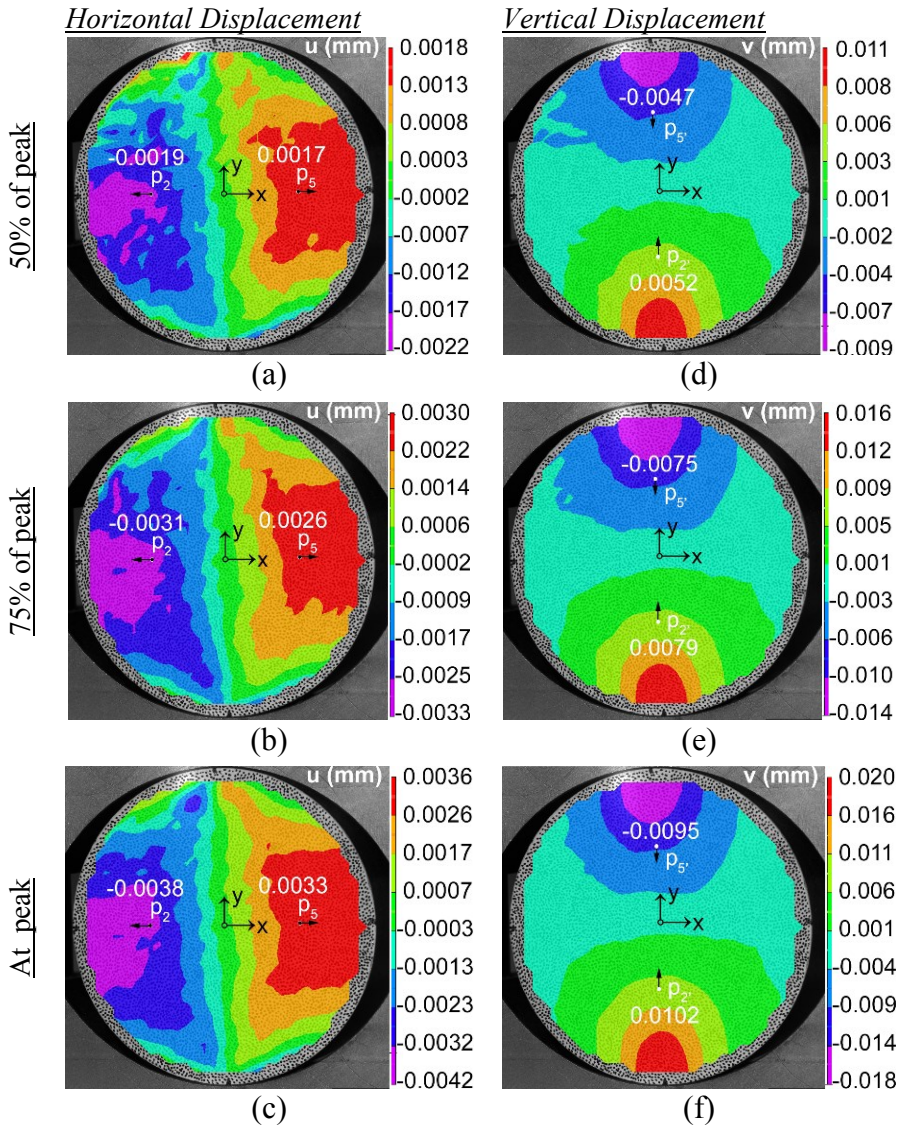

Figure 3.4: Displacement contours from the DIC technique. (a), (b) and (c) horizontal displacement (u) contours at 50%, 75% and at peak respectively. (d), (e) and (f) vertical displacement (v) contours at 50%, 75% and at peak respectively (displacement scales are different for each Figures; x-displacement is +ve towards right and y-displacement is +ve towards upward direction).

In addition, the displacement values along the diameters AB and EF were extracted at 21 equally spaced points using the DIC software Figure 3.5a shows the horizontal displacement (u) and Figure 3.5b shows the vertical displacement (v) with increasing applied load (P) along AB and EF respectively. As shown in Figure 3.5, these values were found to be essentially symmetrical about the center. However, as the displacement values near the center reflect the tensile and compressive Young's moduli of localized mineral grains, we considered the points P1 to P6 and P1' to P6' after a distance D/8 from the center of the disk as shown in Figure 3.1.

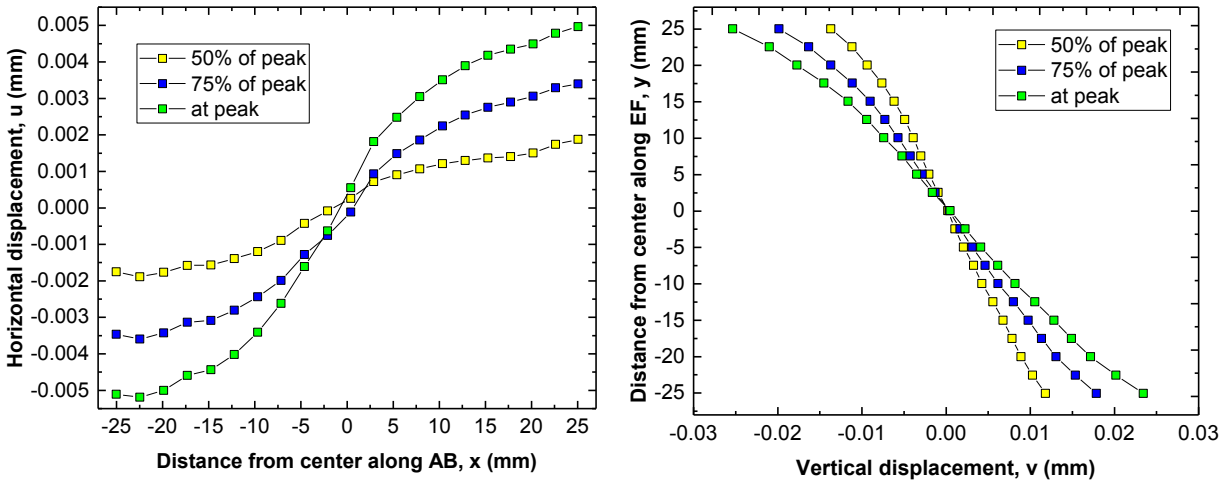

(a) (b)

Figure 3.5: (a) Horizontal displacement (u(x)) vs distance from the center (x) along the horizontal diameter AB at different load levels (b) vertical displacement (v(y)) vs distance from the center (y) along the vertical diameter EF at different load levels

The typical horizontal displacements at the six points (P_1, P_2, P_3, P_4, P_5 and P_6, Figure 3.1) along the horizontal diameter AB with the increase in diametrical load (P) are shown in Figure 3.6a whereas the vertical displacements at the points ($P_{1'}$, $P_{2'}$, $P_{3'}$, $P_{4'}$, $P_{5'}$ and $P_{6'}$) along the vertical diameter EF with increase in load (P) are shown in Figure 3.6b. The slope of these curves (at 50% of load) is less when the point is far from the center (example: slope for P_1<P_3). The displacements of the symmetrical points (example: P_1 vs P_6) are found to be symmetrical. These displacement

curves were than used to calculate the Young's modulus and Poisson's ratio of Lac-du-Bonnet granite.

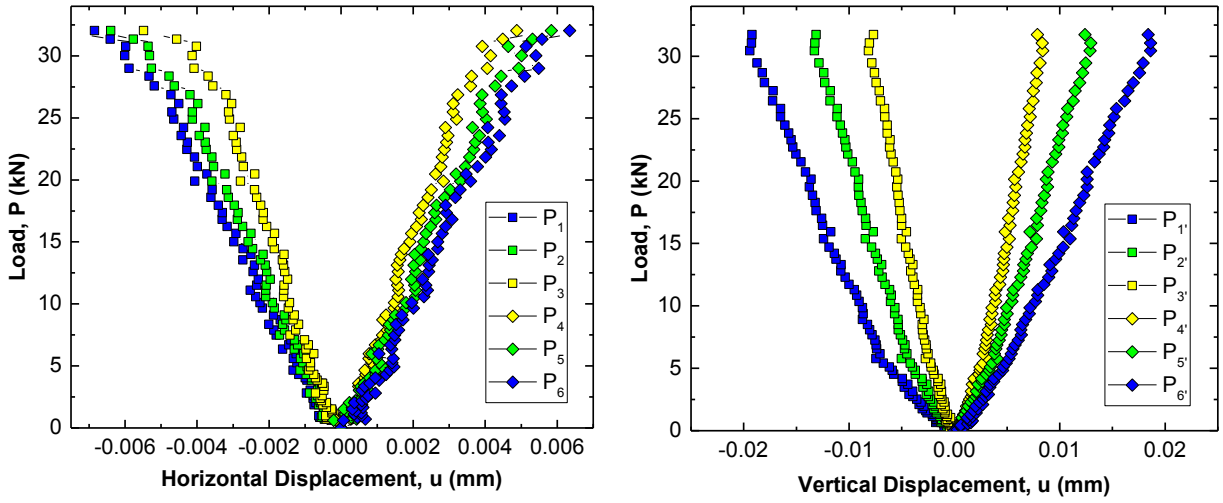

(a) (b)

Figure 3.6: (a) Horizontal displacement vs load at points P_1 to P_6 (b) Vertical displacement vs load at points $P_{1'}$ to $P_{6'}$ (Figure 3.1)

3.5.1 *Calculation of Young's modulus and Poisson's ratio in tension*

The Equation (A-16) and (A-17), Appendix A, are used to obtain the tensile Young's modulus and Poisson's ratio for Lac-du-Bonnet granite. These equations requires the displacements values at two points, one along the horizontal diameter and another along vertical diameter. However, to get an average value for the sample, we monitored the displacement of twelve points (P_1 to P_6 and $P_{1'}$ to $P_{6'}$, Figure 3.1) along the horizontal and vertical diameter. Three average values of the horizontal displacements for the symmetrical points (P_1 and P_6; P_2 and P_5; P_3 and P_4) and three average values of vertical displacements for the symmetrical points ($P_{1'}$ and $P_{6'}$; $P_{2'}$ and $P_{5'}$; $P_{3'}$ and $P_{4'}$) were calculated. This provided three sets of data points for each sample (average of (P_1 and P_6) vs average of ($P_{1'}$ and $P_{6'}$); average of (P_2 and P_5) vs average of ($P_{2'}$ and $P_{5'}$); and average of (P_3 and P_4) vs average of ($P_{3'}$ and $P_{4'}$)) for tensile Young's modulus and Poisson's ratio calculations.

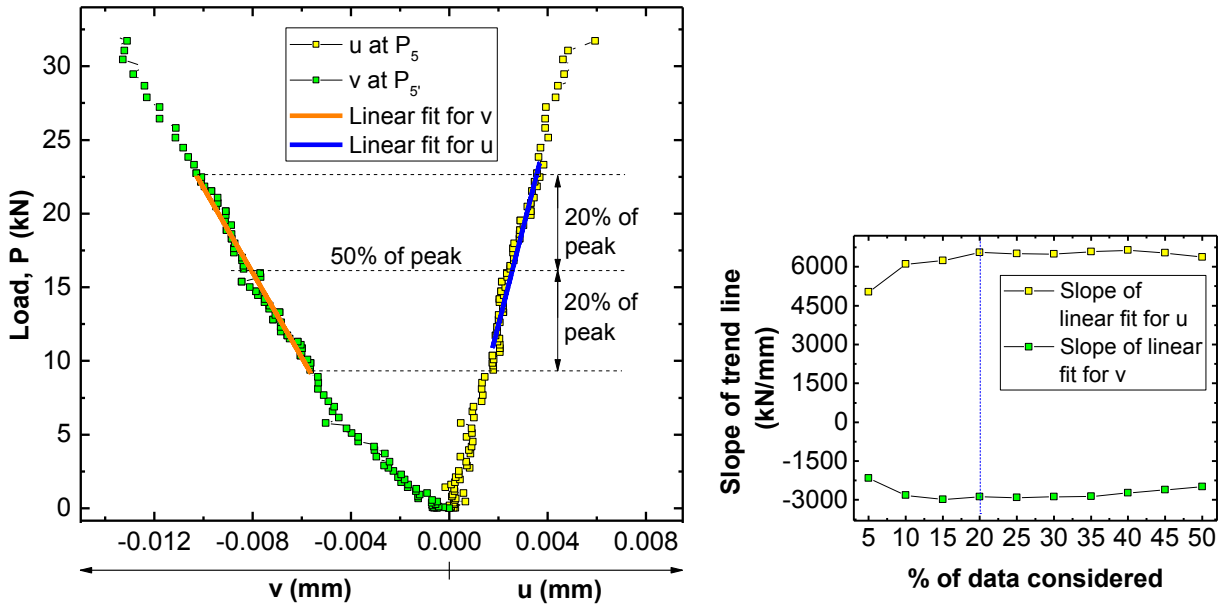

(a) (b)

Figure 3.7: (a) Typical displacement vs load plot at P_5 and $P_{5'}$ (Figure 3.1) and the data range considered for modulus and Poisson's ratio calculation (b) Percentage of data considered vs the slope of trend line for displacement-load plot

The typical horizontal displacements at P_5 vs the diametrical load and the vertical displacement at $P_{5'}$ vs the diametrical load are shown in Figure 3.7a. The slope of the vertical displacement-load curve changes with load, which is commonly observed when testing rocks in compression. The ISRM method (1979) suggests measuring the tangent Young's modulus at 50 percent stress level of the ultimate load in the uniaxial compression test. We adopted the same principle for our Brazilian test. Another issue in elastic constants calculation is the range of data to be considered to obtain the slope of the curve at 50% of peak load. Figure 3.7b shows the slope of the trend line versus percentage of data considered for the linear fit for u and v. The slope of the trend lines become constant when the number of data points used to establish the trend is greater than 20%. This constraint was used for analyzing all test results. The Young's modulus and Poisson's ratio in tension were calculated from the slope of the trend lines (m_x and m_y). The input and calculated values for one sample are tabulated in Table A.1 and Appendix A. The final results for the five

samples are presented in Table 2-2 (average of three sets of data for each sample). The average value of the tensile Young's modulus, tensile Poisson's ratio and compressive Young's modulus from the five samples tested are 42.4 GPa, 0.17 and 64.8 GPa with coefficient of variation of 11.9%, 13% and 4.1% respectively. This tensile Young's modulus is close to the value found from the direct tension test (43.9 GPa, Table 2) and also from the strain gauge measurements at the center of the Brazilian sample (43.2 GPa,). The compressive Young's modulus found from this test (64.8 GPa) is close to the value from the UCS test (69 GPa, Table 2). These co-efficient of variations are found to be of similar order reported by (Hondros 1959) for the concrete he tested.

Table 3-4: Results of the Brazilian tests

Sample	**σ_{tb} (MPa)**	**E_t (GPa)**	**E_c (GPa)**	**ν_t**
1	12.0	40.3	64.6	0.16
2	10.9	40.0	62.2	0.17
3	11.4	50.3	63.0	0.21
4	12.0	44.3	69.1	0.17
5	11.5	37.2	65.3	0.15
Mean	*11.6*	*42.4*	*64.8*	0.17
SD	*0.4*	*5.1*	*2.7*	*0.02*
CoV (%)	*3.8*	*11.9*	*4.1*	*13.0*

3.6 Summary

In this study, we used the Brazilian test to obtain the tensile Young's modulus and Poisson's ratio for Lac-du-Bonnet granite. We incorporated the bi-modularity relation between the elastic constants (E_c, E_t, ν_c and ν_t) in the stress-strain equations of a Brazilian test. New equations were derived to obtain the tensile elastic constants from the displacement measurements along the vertical and horizontal diameter of the Brazilian disk. The DIC technique was used to monitor the displacements on the flat surface of Brazilian disks. When we compared the results from the Brazilian tests with the direct tensile test results on dog-bone shaped samples, we found there is good agreement. The tensile modulus was found to be 65.4% of the compressive modulus from the Brazilian test where as it was 64% from the direct tensile test. These values are in the similar order found in the literature for granite (Table 3-1). The co-efficient of variation in the Brazilian method was 11.9% while from the direct tensile test is 11.2%. The reasons for this bi-modularity in rock is under investigation.

Chapter 4:

Application of flattened Brazilian test to investigate rocks under confined extension

4.1 Introduction

One of the most widely used failure criterion for rock mechanics applications is the two dimensional Hoek-Brown failure criterion (Hoek and Brown 1980). To obtain the two-dimensional Hoek-Brown failure envelope of a rock, the rock is typically tested with uniaxial compression and triaxial compression boundary conditions. These boundary conditions and stress paths taken during the tests are shown in principal stress (σ_1, σ_3) space in Figure 4.1. For these test configurations the boundary conditions are uniform in that the applied stresses are compressive and at failure the stress magnitudes are simply taken from those applied boundary conditions. The curved linkage from the compressive strength to the uniaxial tensile strength in the Hoek-Brown failure criterion in Figure 4.1 is empirical but guided by the Griffith theory of rupture (Hoek and Brown 1980). During the development of the Hoek-Brown failure criterion this region from compression to tension, i.e., confined extension, received little attention, although the ratio of uniaxial compressive strength to uniaxial tensile controls the curvature of the failure criterion in this region of confined extension (Hoek and Martin 2014a).

A version of this chapter has been submitted to the journal of Rock Mechanics and Rock Engineering:

Patel, S. and C. Derek Martin. 2018. "Application of flattened Brazilian test to investigate rocks under confined extension." Rock Mechanics and Rock Engineering. (Accepted)

The region of confined extension in Figure 4.1, was investigated by Brace (1964) using dog-bone shaped specimens Figure 4.2. In the methodology adopted by Brace (1964), the specimens are compressed to a predetermined hydrostatic stress so that $\sigma_1=\sigma_2=\sigma_3$. The specimen is then brought to failure by decreasing the axial stress such that this confined extension stress state can produce tensile rupture. This stress path is shown in Figure 4.1 (path-4) along with the stress paths for the conventional tests. What is immediately obvious is that the confined extension test uses a specimen geometry and stress path that is completely different to the conventional compression tests from which the Hoek-Brown parameters are determined. A consequence of this approach is that the stress state at failure cannot be measured directly but must be calculated based on the specimen shape and boundary conditions. Hence the tests on dog-bone shaped specimen to evaluate the Hoek-Brown failure criterion in the confined extension region, may not be valid. An alternative to the confined extension tests is the Brazilian test (ASTM 2008 and ISRM 1978) which maintains the confined extension stress state to induce tensile rupture but maintains a stress path that is more aligned with the conventional stress path for compression tests Figure 4.1. Despite the similarity to the compression stress path the Brazilian test still requires the calculation of the tensile strength at rupture.

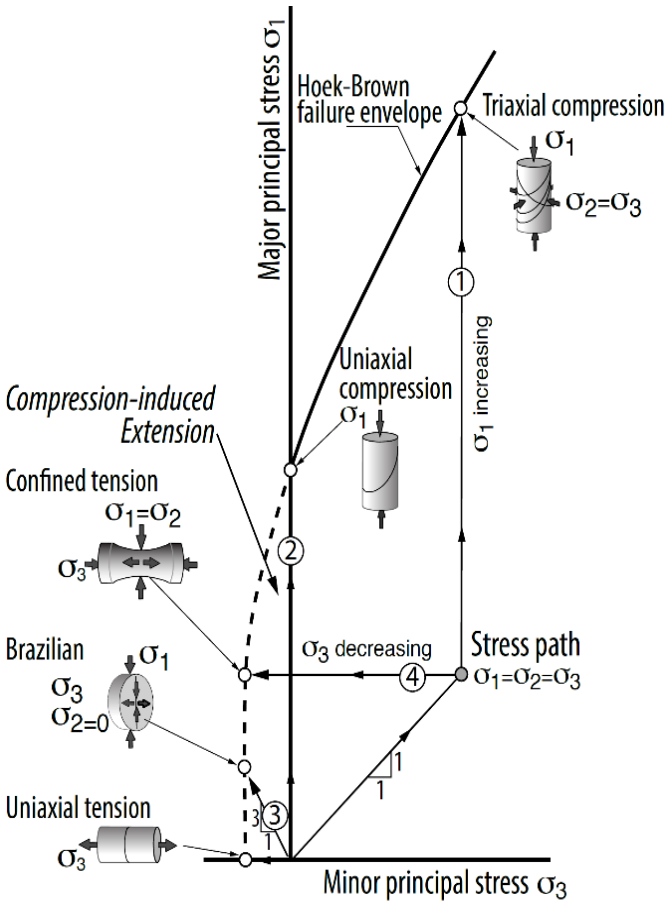

Figure 4.1: Failure envelope of a typical intact rock plotted in terms of major and minor principal stresses with confined extension region and location of Brazilian point (confined extension shown as dashed line)

Timoshenko and Goodier (1951) showed that the Brazilian test induces a compression-induced tensile stress state ($\sigma_1=3\sigma_3$, $\sigma_2=0$). This stress state can be modified by changing the shape of the Brazilian disk. In this paper we review the limited confined extension test results available in the literature. We then describe the modified Brazilian testing configuration and present the methodology for interpreting the test results. Both the results on dog-bone shaped specimens and the modified Brazilian specimens are compared to the Hoek-Brown failure criterion for this region of confined extension.

4.2 Background

4.2.1 *Dog-bone shaped specimens*

Dog-bone shaped specimens of rocks used by Brace (1964) for the confined extension test is shown in Figure 4.2a. The applied axial compressive force (F) generated an axial compression in the throat portion of the specimen while confining pressure (P′), generated an axial tension due to the curve shape of the specimen. The total axial stress (C) in the throat portion of the specimen is given by the equation,

$$C = \frac{F}{A_t} + \frac{P'(A_h - A_t)}{A_t} \tag{4-1}$$

Where,

C= axial stress (+ve in tension),

F= axial force (-ve F acts towards specimen),

P′= confining pressure (+ve),

A_h= head area, and

A_t= throat area.

Initially, a hydrostatic stress field is generated in the central part of the specimen by gradually increasing both the confining pressure (P') and vertical compressive load (F). Then, keeping the confining pressure (P') constant, the axial load is gradually reduced until the specimen fails. To test rocks under different confined extension conditions, Brace (1964) loaded the specimens to different values of confining pressure P′ (with corresponding increase in axial compression). The axial loading to the specimen was always compressive during the tests. The stress state in an element in the central region of a specimen at failure is shown in Figure 4.2a where the major and intermediate stress are same and compressive while the minor principal stress is tensile. Brace

(1964) tested 25.4-mm diameter (12.7-mm diameter at throat) specimens of Webatuck dolomite, Blair dolomite, Frederick diabase, Cheshire quartzite and Westerly granite.

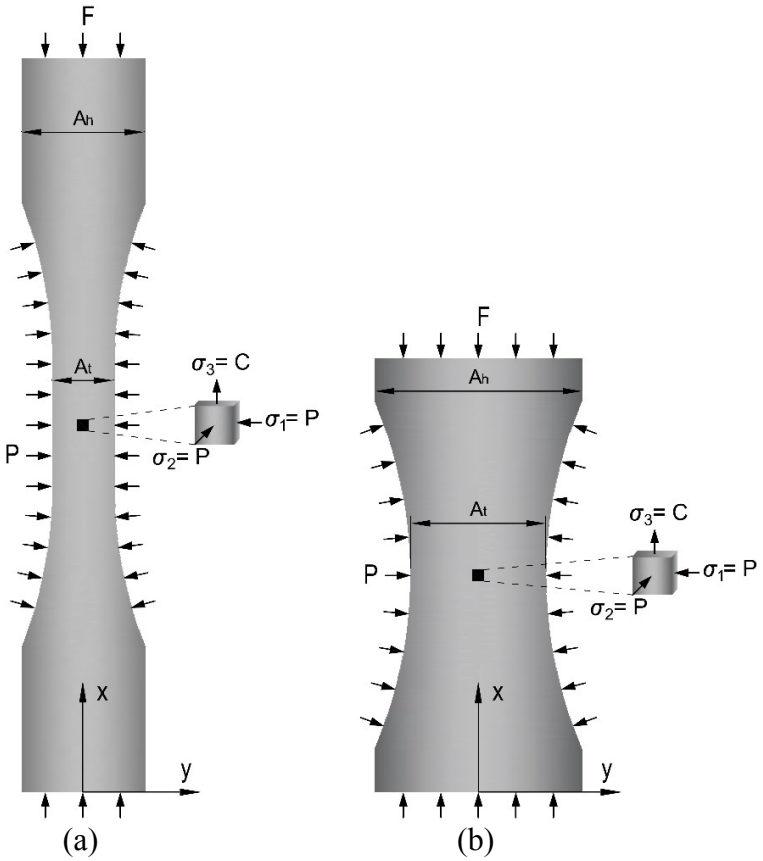

Figure 4.2: Dog-bone shaped specimen used by (a) Brace (1964) and (b) Ramsey and Chester (2004) for conducting confined extension test and the stress state of an element at the throat part of the specimen

Hoek and Brown (1980) assumed that the intermediate principal stress (σ_2) had minor impact on the Hoek-Brown failure envelope of rocks and used the results from Brace (1964) to obtain the corresponding envelope for five rock types. The test results from Brace (1964) along with the corresponding Hoek-Brown envelopes are shown in Figure 4.3. Inspection of Figure 4.3 shows a general lack of agreement between the data from Brace and the Hoek-Brown failure envelope as the number of data points is limited. Hence it is uncertain if shape of the Hoek-Brown failure envelopes in the confined extension region is valid.

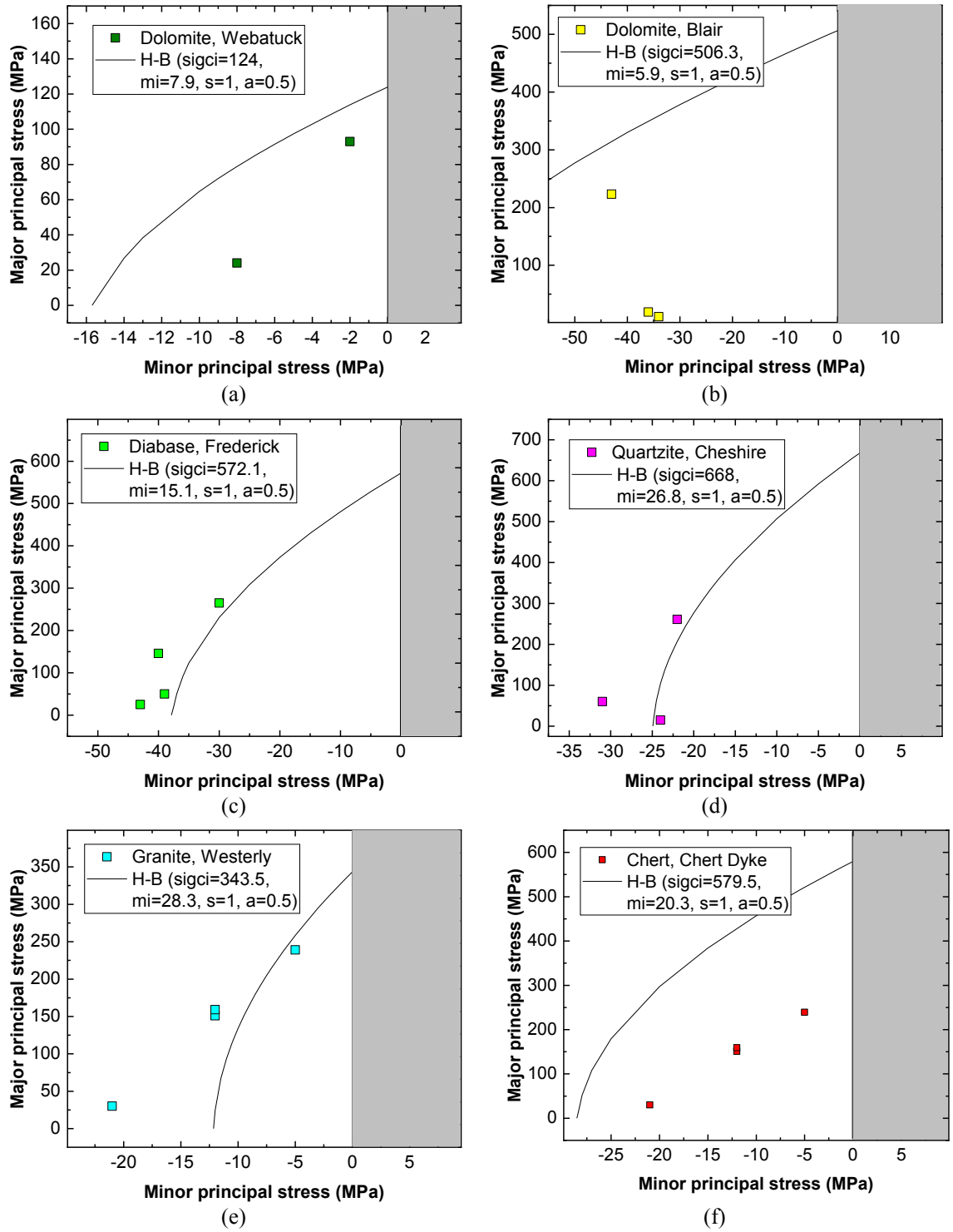

Figure 4.3: Brace (1964) confined extension test results on (a) Webatuck dolomite; (b) Blair dolomite; (c) Frederick diabase; (d) Cheshire quartzite; (e) Westerly granite; and by Hoek on (f) Chert, Chert dyke (Hoek and Brown 1980). The Hoek and Brown (H-B) parameters are taken from Hoek and Brown (1980).

Mogi (1967) carried out similar tests to those of Brace on Dunham dolomite, Westerly granite and Solenhofen limestone. To produce a dog-bone shaped specimen, Mogi put epoxy at the two ends of a cylindrical specimen, instead of grinding the central part as carried out by Brace (1964). Mogi (1967) tested 2.3 cm to 2.54 cm diameter and 5 cm long specimens. He then compared the results of confined extension tests with conventional triaxial tests on 1.6 cm diameter and 5 cm long specimens. Mogi (1967) observed that for Dunham dolomite and Westerly granite, the peak strength in case of confined extension conditions are 30-50% higher than the corresponding triaxial test. Although the effect of intermediate principal impact was less in Solenhofen limestone. Figure 4.2b). This reduced the bending effect in the specimen geometry used by Brace (1964) which was due to the high ratio of length to diameter of the specimen (12:1 at throat). However, this modification resulted in only a very narrow section of the specimen at the midpoint being subjected to uniform stresses. Ramsey and Chester (2004) tested Cararra marble by following the same stress path used by Brace (1964). Figure 4.4a shows Ramsey and Chester (2004) experimental results along with the results from direct tension, uniaxial compressive strength (UCS) and triaxial compression tests (Ramsey 2003). Bobich (2005) conducted a simliar set of of confined extension tests on Berea Sandstone using the same specimen geometry and test procedure developed by Ramsey and Chester (2004), as well as conventional laboratory tests. Figure 4.4b shows the results for Berea sandstone. Also shown in Figure 4.4 is the Hoek-Brown failure envelopes for intact Carrara marble and Berea Sandstone. The Hoek-Brown parameters were determined from conventional Triaxial and uniaxial laboratory tests.

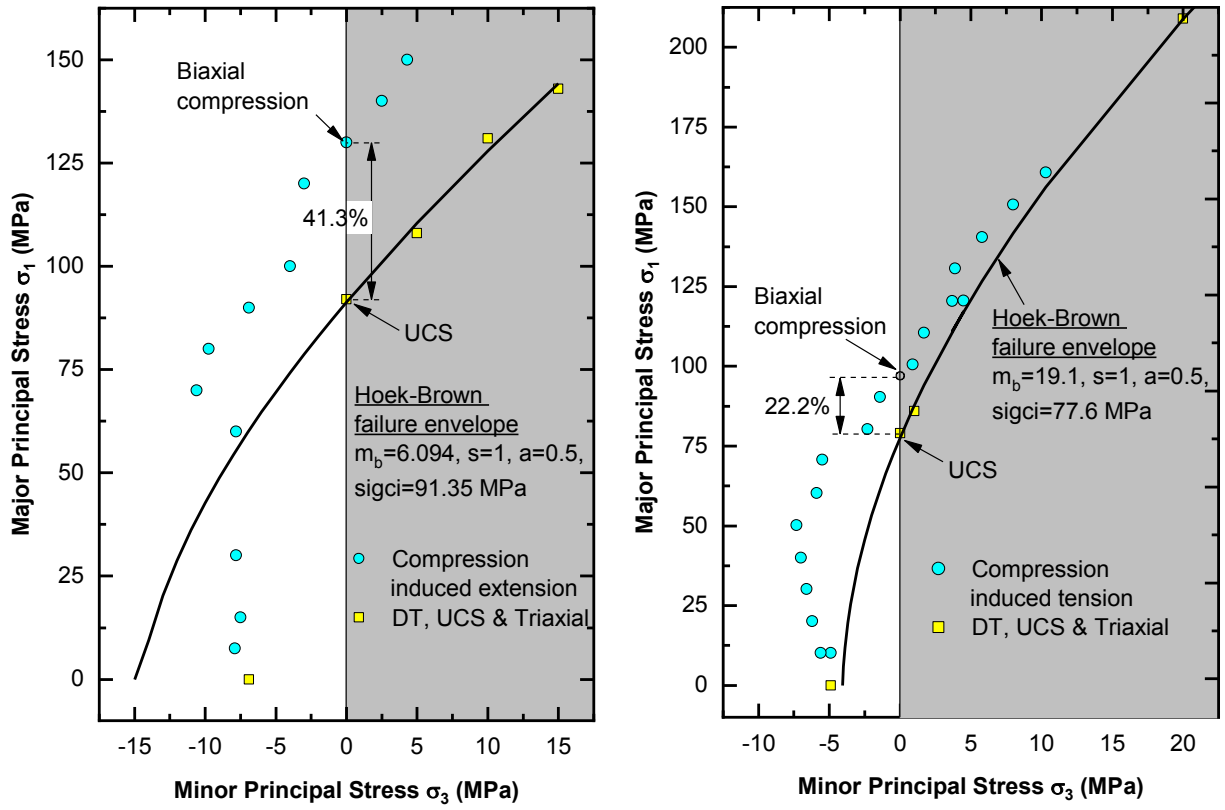

Figure 4.4: Results of direct tension (DT), uniaxial compression strength (UCS), triaxial compression and confined extension test and the Hoek-Brown failure envelopes for (a) Carrara Marble (Ramsey 2003) and (b) Berea sandstone (Bobich 2005). Biaxial strength of Berea sandstone is calculated using interpolation.

We carried out an elastic, axisymmetrical analysis of the specimen geometry used by Ramsey and Chester (2004) and Brace (1964) using the finite difference code FLAC2D (ITASCA 2011). We considered a confining pressure of 60 MPa and a vertical stress to produce an axial tensile stress of -7.8 MPa in the specimens (one of the loading case for Ramsey and Chester (2004)). The corresponding vertical stress for the two specimen geometries were calculated using the Equation 4.1.

Figure 4.5a-d shows the horizontal and vertical stress contours for the two cases. The horizontal stresses ($\sigma_{xx}=\sigma_1=\sigma_2$, Figure 4.5a) and the vertical tensile stress ($\sigma_{yy}=\sigma_3$, Figure 4.5b) was found to be uniform for the geometry used by Brace (1964). However, for the Ramsey (2003) specimen, between the center and at the boundary, there is a difference of 5.3% in compressive stress (56.8 MPa versus 60 MPa, Figure 4.5c) and 280% in tensile stress (-3.5 vs -13.3 MPa, Figure 4.5d). The point at which the tensile stress is -8.7 MPa in the Ramsey and Chester (2004) specimen is shown in Figure 4.5d.

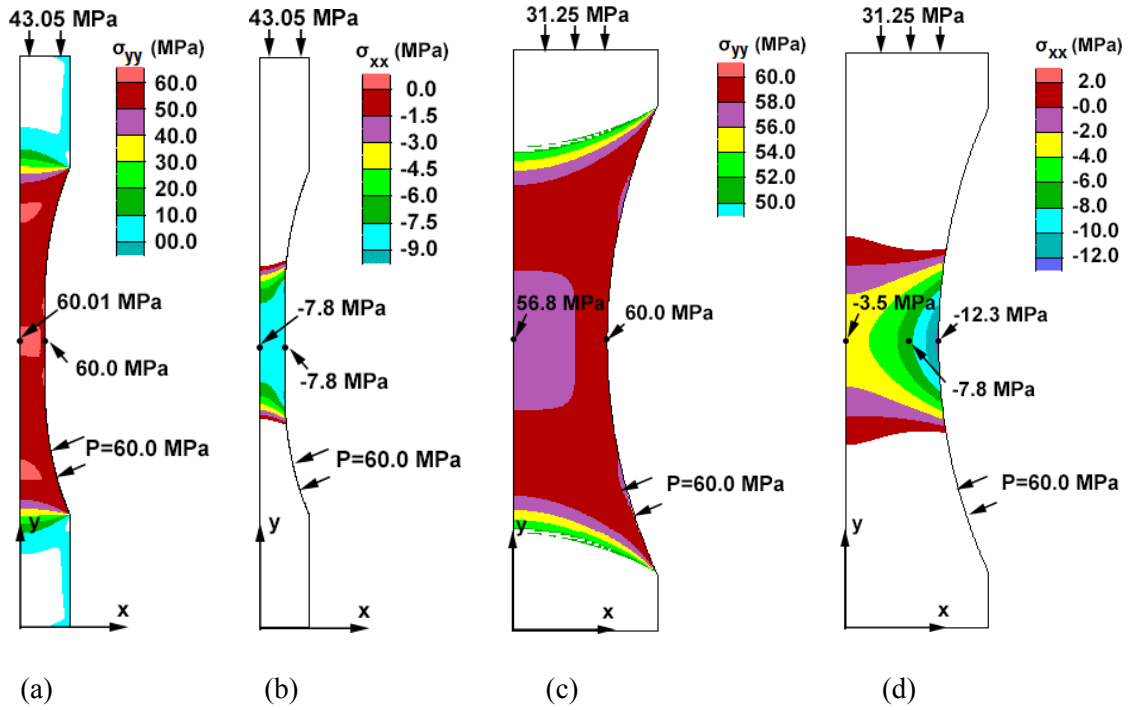

Figure 4.5: Horizontal and vertical stress contours for axisymmetrical elastic FLAC2D analysis for the specimens used by Brace (1964) and Ramsey and Chester (2004). (a) Horizontal stress contours Brace (1964); (b) vertical stress contours Brace (1964); (c) horizontal stress contours Ramsey and Chester (2004); and (d) vertical stress contours Ramsey and Chester (2004). Both specimens were subjected to a confining pressure (P) of 60 MPa (note that the vertical pressure applied to the two specimens are different to produce a vertical tensile stress of -7.8 MPa at center).

Inspection of the testing and numerical results from Ramsey and Chester (2004) and Bobich (2005) studies highlight the following:

(1) the Hoek-Brown failure envelopes obtained from the UCS and Triaxial tests for Carrara marble and Berea sandstone do not pass through most of the data points obtained from the experimental results on confined extension,

(2) the biaxial compressive strength ($\sigma_1=\sigma_2=130$MPa,$\sigma_3=0$) obtained by Ramsey and Chester (2004) for Carrara marble is 41.3% higher than the uniaxial compressive strength (92MPa),

(3) the biaxial compressive strength ($\sigma_1=\sigma_2=96.5$MPa (interpolated from two nearest data points),$\sigma_3=0$) obtained by Bobich (2005) for Berea sandstone is 22.2% higher than the uniaxial compressive strength (79 MPa), and

(4) the specimen geometry used produces a highly non uniform tensile stress in the central part of the specimen and the specimen failure initiates at a different stress condition than that calculated using Equation (4-1) (Maximum tensile stress (σ_3)=-12.3 MPa, Figure 4.5d versus σ_3=-7.8 MPa as per the Equation (4-1)).

The results from the Brace (1964), Mogi (1967), Ramsey and Chester (2004) and Bobich (2005), all suggest that the shape of the failure envelope for the dog-boned shaped samples tested used in the region of confined extension varies significantly from the curvature proposed by the Hoek-Brown criterion. Even if the magnitudes of the Ramsey and Chester (2004) and Bobich (2005) are discounted, for the reasons noted above, it is likely that the shape of the envelop is valid. It would appear that either the influence of the intermediate principal stress and/or the stress path shown in Figure 4.1 may be causing this difference.

4.2.2 *Confined Brazilian Tests*

Jaeger and Hoskins (1966) conducted confined extension tests on Bowral trachyte, Gosford sandstone and Carrara marble by modifying the conventional Brazilian test. They put copper jacketed 5 cm diameter Brazilian specimens in an ordinary triaxial cell and applied all around confining pressure ($\sigma_1=\sigma_2=\sigma_3$). They then failed the specimen by applying an additional external diametrical load such that $\sigma_1>\sigma_2=\sigma_3$, while at the center of the sample $\sigma_1>\sigma_2>\sigma_3$. Jaeger and Hoskins (1966) tested Carrara marble, Gosford sandstone and Bowral trachyte for a wide range of minor principal stresses (tensile to compressive) and compared the results with the results from conventional triaxial tests. They concluded that the value of the intermediate principal stress affects the peak strength of the material. The results of their confined Brazilian and triaxial tests are shown in Figure 4.6. Again, as observed with the dog-boned shaped samples, the Hoek-Brown failure envelope obtained from the triaxial tests are not in agreement with the data obtained in the confined extension region and underestimates the biaxial compressive strength.

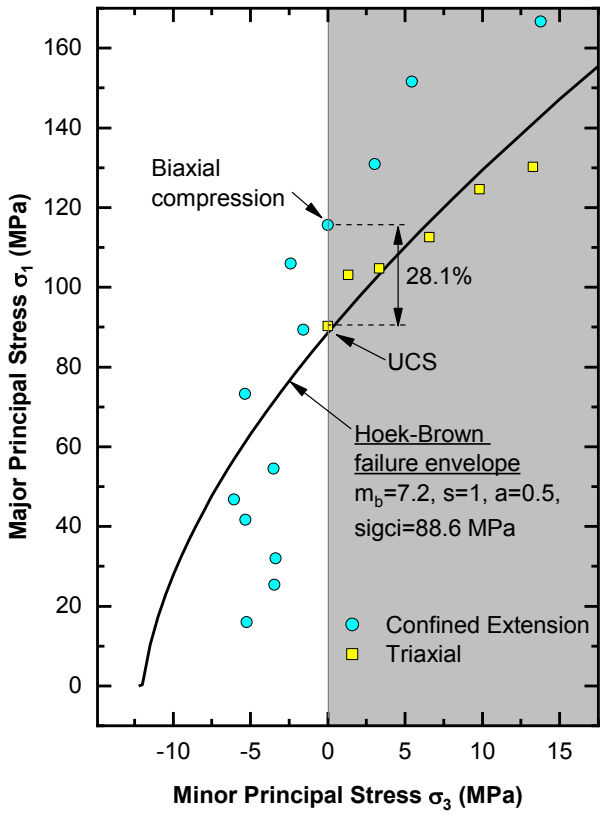

(a)

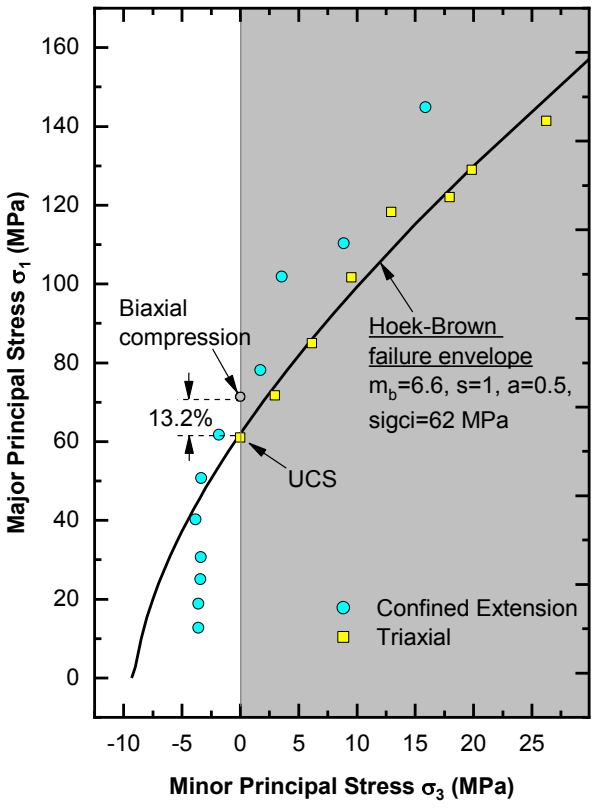

(b)

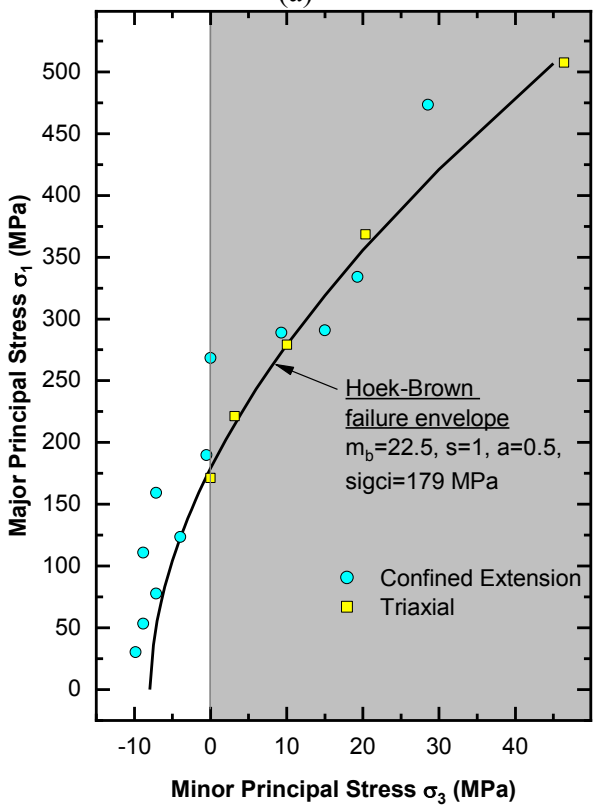

(c)

Figure 4.6: Results of confined Brazilian test from Jaeger and Hoskins (1966) ; triaxial compression test; and the Hoek-Brown failure envelopes for (a) Carrara marble (b) Gosford sandstone and (c) Bowral trachyte. Biaxial strength of Gosford sandstone is calculated using interpolation.

4.2.3 *Summary*

Notwithstanding the challenges with interpreting the results from Ramsey and Chester (2004) and Bobich (2005), inspection of the data from Brace (1964), Jaeger and Hoskins (1966) and Mogi (1967) obtained from the confined extension tests suggests that the intermediate principal stress when greater than the minimum stress ($\sigma_2 > \sigma_3$) may increase the peak strength in the confined extension region. In other words, the data points obtained from those tests in the confined extension region may not be the critical data points when comparing to the two-dimensional Hoek-Brown failure envelope.

The following sections discuss the new methodology adopted to conduct confined extension tests in rocks with zero intermediate principal stress (σ_1=compressive, σ_3=tensile, σ_2=0).

4.3 Flattened Brazilian Test

The Brazilian test (ASTM 2008 and ISRM 1978), as an indirect method to obtain the tensile strength of rock. As per the elastic theory, at the center of a Brazilian specimen, the magnitude of the vertical stress (σ_{yy}, compressive) is always three times the horizontal stress (σ_{xx}, tensile). If the Brazilian specimen is flattened and loaded along the flat ends (Figure 4.7), the stress conditions at which the fracturing will begin in the critical location in the sample will change. By the gradual increase in depth of flattening, the vertical compressive stress in the specimen can simultaneously be increased. The stress state at a critical location, P_c, on the surface of a flattened Brazilian specimen along the horizontal diameter AB is shown in Figure 4.7. The three major principal stress directions are in vertical ($\sigma_{yy}=\sigma_1$= compressive), out of plane ($\sigma_{zz}=\sigma_2=0$) and horizontal ($\sigma_{xx}=\sigma_3$= tensile) directions. This test was used by Wang and Xing (1999) to determine the

fracture toughness in rocks. However, when the depth of flattening in a flattened Brazilian test is increased, the stresses at the point where the fracturing begins have never been explored.

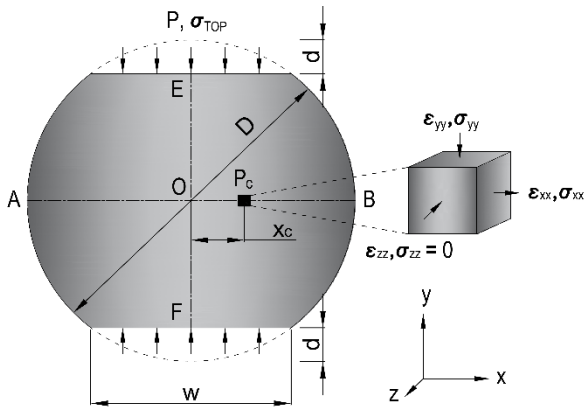

Figure 4.7: Flattened Brazilian specimen showing stress state for a critical element on the surface along the mid height of the specimen.

4.4 Numerical modelling of Flattened Brazilian specimen

To understand the stress state and determine the most critical location in a flattened Brazilian specimen, we modelled the test using the three dimensional finite difference code FLAC3D (ITASCA 2013). We considered 63.4 mm diameter Lac du Bonnet granite numerical specimens with two depths of flattening (1 mm and 8 mm). The diameter to thickness ratio of two, as suggested in ISRM suggested method for Brazilian test (ISRM 1978) were used. The models used were elastic with Young's modulus of 53.6 GPa and Poisson's ratio equal to 0.17 (average value for Lac du Bonnet granite, Table 4-1)

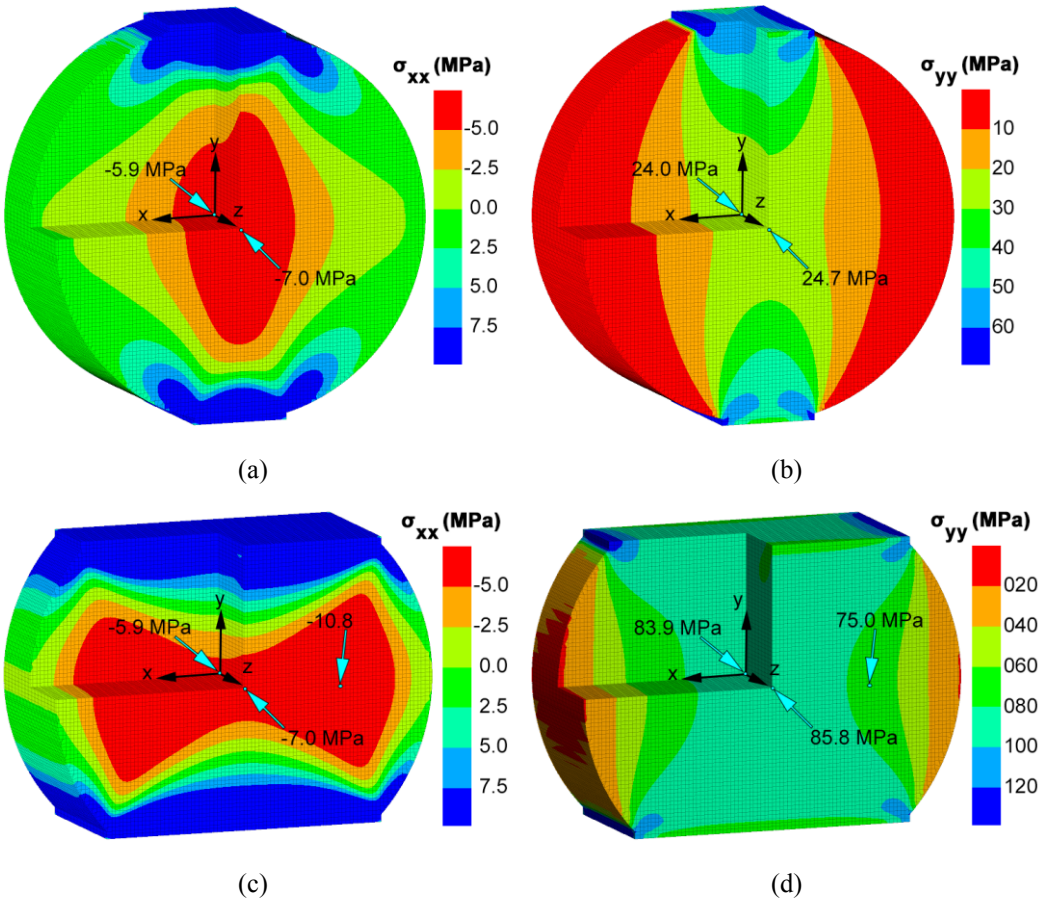

Figure 4.8: Results of FLAC3D analysis on flattened Brazilian disks (a) stress contours in x-direction, σ_{xx}, for depth of flattening 1 mm (b) stress contours in y-direction, σ_{yy}, for depth of flattening 1 mm (c) stress contours in x-direction, σ_{xx}, for depth of flattening 8 mm (d) stress contours in y-direction, σ_{yy}, for depth of flattening 8 mm

Figure 4.8a-d shows the vertical and horizontal stress contours (which are the principal stress contours) obtained when the flattened Brazilian specimens are loaded vertically at the flat ends (Figure 4.7). We gradually increased the loads until the horizontal tensile stress at the centers (Figure 4.8a and c) reach a tensile stress of 7 MPa. Then we investigated both compressive and tensile stress state at different locations in the specimen.

The findings from the numerical investigations are: (a) the tensile and compressive stress magnitudes are highest on the surface of the specimen, i.e., the critical location at which the crack will initiate is on the surface of the specimen; (b) when the depth of flattening is increased from 1 mm to 8 mm the corresponding central compressive stress, $\sigma_{yy,}$ increased from 24.7 MPa to 85.8 MPa; and (c) when the depth of flattening is 8 mm the location of highest tensile stress shifts towards the edges of the specimen.

4.5 Strain measurement in flattened Brazilian test (DIC)

From the three-dimensional elastic analysis of the flattened Brazilian test, we concluded that the most critical stress location is on the surface of a specimen. However, it is not possible to know the principal stresses (σ_1 and σ_3) at the critical locations directly. In this study, we used the principal strain values measured on the specimen and the elastic properties (Young's moduli and Poisson's ratios) to obtain the corresponding principal stresses (described in the next section).

The most popular way to obtain the strain in rock testing is using the strain gauges. However, in case of the flattened Brazilian tests, obtaining the principal strain values using the strain gauges is difficult because the exact location of the fracture initiation point is unknown. On the other hand, the digital image correlation (DIC) technique (described by Sutton, Orteu, and Schreier (2009) and

CorelatedSolutions (2010b), the strain values can be obtained throughout the surface of a deforming specimen.

4.6 Bi-modular stress-strain relations for flattened Brazilian test

Most of the rocks show some degree of bi-modular behaviour whereby the Young's modulus and Poisson's ratio in compression is not the same in tension (Patel and Martin 2018c). As per Ambartsumyan (1969) and Sundaram and Corrales (1980), the stress-strain equations for a modified Brazilian test with bi-modularity can be written as:

$$\varepsilon_{xx} = \frac{\sigma_{xx}}{E_t} - C\sigma_{yy} \tag{4-2}$$

and

$$\varepsilon_{yy} = \frac{\sigma_{yy}}{E_c} - C\sigma_{xx} \tag{4-3}$$

where:

$$C = \frac{\nu_t}{E_t} = \frac{\nu_c}{E_c} \tag{4-4}$$

Considering

$$C = \frac{\nu_c}{E_c}$$

for both the equations (4-2) and (4-3), the horizontal stress and the vertical stresses can be written as:

$$\sigma_{xx} = \frac{\varepsilon_{xx} + \nu_c \varepsilon_{yy}}{\frac{1}{E_t} - \frac{{\nu_c}^2}{E_c}} \tag{4-5}$$

$$\sigma_{yy} = \frac{\varepsilon_{xx} + \frac{\varepsilon_{yy} E_c}{\nu_c E_t}}{\frac{1}{\nu_c E_t} - \frac{\nu_c}{E_c}} \tag{4-6}$$

So, if the elastic properties (E_c, E_t and ν_c) of a rock is known and the principal (compressive and tensile) strain are measured during the flattened Brazilian test, the corresponding principal stresses can be calculated using equations (4-5) and (4-6).

4.7 Material investigated

We tested 63.4 mm diameter specimens of Lac du Bonnet taken at a depth of 228 m from an underground research laboratory in southern Manitoba, Canada. Lac du Bonnet Granite is a crystalline rock with the grainsize varying from 3 mm to 7 mm with perthite/microline (50-70%), quartz (~20%), biotite (~10%), and plagioclase (<10%) (Park and Piasecki 1993). The density of the rock is 2630 kg/m^3 and the p-wave velocity is about 6096 m/s (Lau and Jackson 1992). Other material properties of Lac du Bonnet granite related to this study are summarized in Table 4-1.

Table 4-1: Laboratory properties of Lac du Bonnet Granite*

Parameter	Mean	Stdev	n
Uniaxial compressive strength (UCS) [a]	220 MPa	±22 MPa	81
Brazilian Tensile Strength (σ_{BT}) [b]	11.6 MPa	±0.4 MPa	5
Brazilian vs direct tensile strength ratio (σ_{BT}/ σ_{DT}) [a]	1.35	-	-
Compressive tangent Young's modulus (50%) from Brazilian test (E_c)[b]	64.8 GPa	±2.7 GPa	5
Tensile tangent Young's modulus 50% from Brazilian test (E_t) [b]	42.4 GPa	±5.1 GPa	5
Poisson's ratio in compression at 50% of UCS (ν_c)[a]	0.26	±0.04	81
Hoek Brown constant m_i[c]	32.4	-	-

[a] Martin 1993, [b] Patel and Martin (2018a), and [c] Hoek and Martin 2014

*Lac du Bonnet granite has not been tested in confined extension condition

4.8 Experimental setup and experimental procedure

4.8.1 *Specimen preparation*

There is no ISRM or ASTM standard for a flattened Brazilian test on rock. So, we used the standard for the Brazilian test (ISRM 1978 and ASTM 2008) for our study. We flattened the 63.4 mm diameter rock core with a diamond saw to achieve a diameter to thickness ratio about 0.5. Then we ground the top and bottom of the disk using a surface grinder with a diamond wheel to produce different depths of flattening as shown in Figure 4.9 (1 mm, 4 mm, 6 mm, 8 mm and 10 mm).

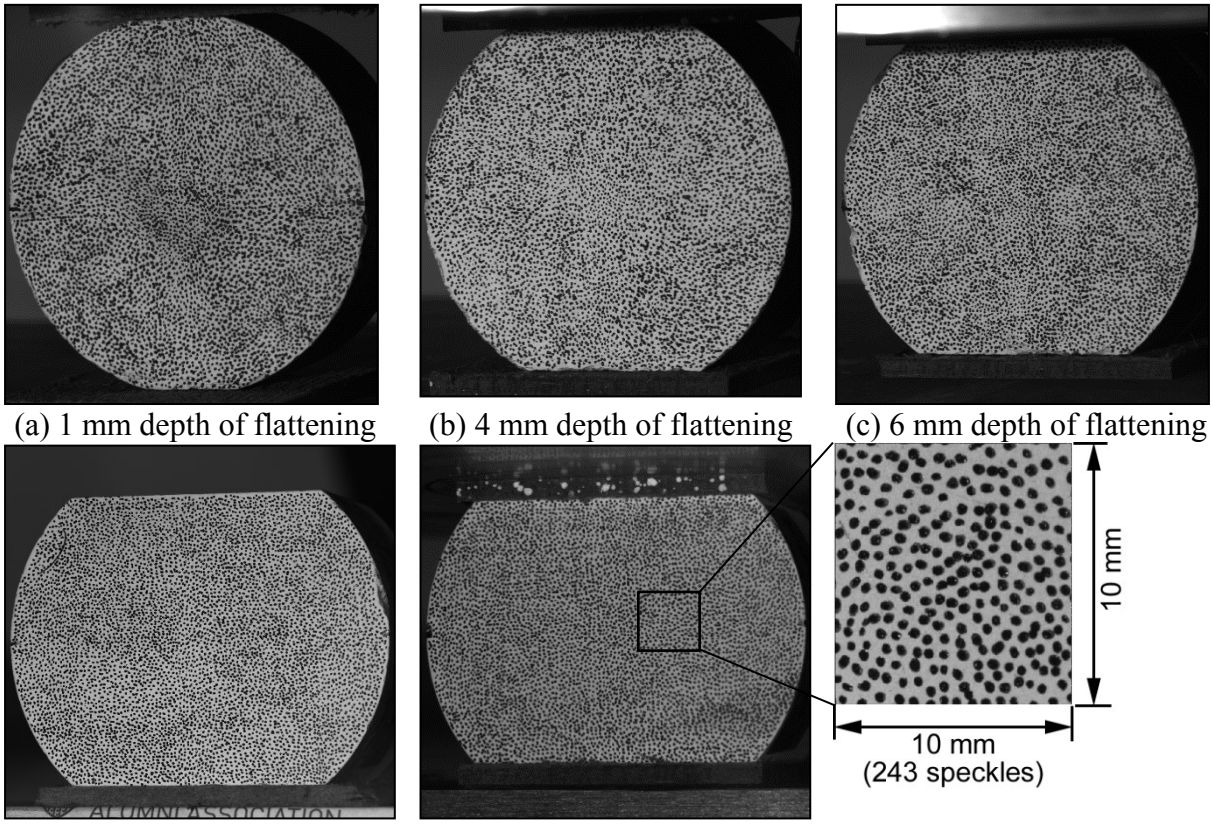

(a) 1 mm depth of flattening (b) 4 mm depth of flattening (c) 6 mm depth of flattening

(d) 8 mm depth of flattening (e) 10 mm depth of flattening

Figure 4.9: Flattened Brazilian specimens and spackle pattern made for DIC measurements. Average spackle diameter ~0.5 mm.

For the DIC measurements, we put a thin layer of white paint on one flat surface and created a spackle pattern using an ultra fine black fine Sharpie® marker (Figure 4.9). The procedure to make

spackle pattern for DIC measurements are described in CorelatedSolutions (2010a). The diameter of the spackles were around 0.5 mm with a spackle density of about 243 spackles/cm^2. Such a high density of small spackles were required for this study because the range of strain of interest was small (less than 500 micro strain).

4.8.2 *Experimental setup and testing method*

We used a MTS testing machine to test the flattened Brazilian specimens. The experimental setup for the test is shown in Figure 4.10. For the DIC measurements, two cameras were placed in front of the specimen at a distance of about 50 cm inclined at angle 30 degree with the axis of the specimen. The lenses used were fixed focal length (90mm) with an aperture range F2.8 to F32. The resolution of the camera was 2048*2048 pixels. An LED light source was used to provide good lighting condition with minimal thermal impact on DIC strain measurements (CorelatedSolutions 2010b). The two cameras were connected to a computer to take pictures during the test, store the pictures, and analyze them after the tests. The DIC software VIC3D (CorelatedSolutions 2010b) was used to perform these tasks. The DIC procedures are described in the software manual (CorelatedSolutions 2010b).

Reference pictures (at zero load) were then taken to compare with the deformed images. DIC software was used to control the camera to take two pictures per second throughout the test. The specimens were then loaded by moving the top platen with a constant rate of 0.2 mm/min. This failed the specimens within 1-10 minute as per the Brazilian test recommendations (ISRM 1978 and ASTM 2008).

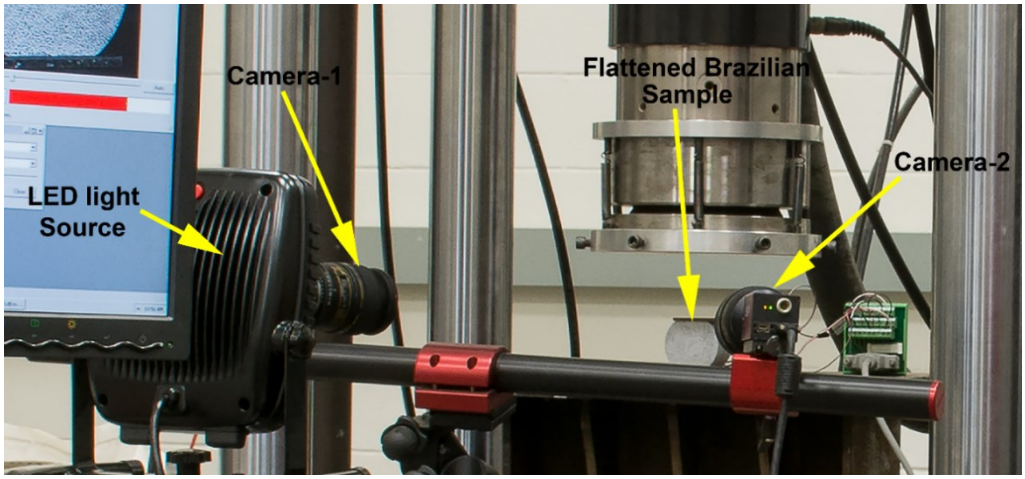

Figure 4.10: Experimental setup showing the loading frame, flattened Brazilian specimen and the DIC setup

4.9 Results

We tested five depths of flattening (1 mm, 4 mm, 6 mm, 8 mm and 10 mm, Figure 4.9) and five specimens for each depth of flattening. Pictures taken by the two cameras during the tests were analysed using the DIC software VIC3D. The post processing procedure for VIC3D is described in the VIC3D manual (CorelatedSolutions 2010b).

Figure 4.11 shows the typical horizontal and vertical strain (tensile negative and compressive positive) developed on the surface of the specimen with 4 mm depth of flattening during a flattened Brazilian test at different load levels (contours for other depths of flattening are shown in Figure B.8; Figure B.10; Figure B.12 and Figure B.14) . Figure 4.11a to d are horizontal strain contours and Figure 4.11e to h are vertical strain contours. The strain pattern obtained from DIC measurements were found to be similar to the horizontal and vertical stress contours obtained from the FLAC3D elastic analysis. Tensile strain concentration occurs at a critical point, Pc, at the mid height of the specimens. At the yield point (Figure 4.13), a vertical macro (visible) crack of finite length as shown in Figure 4.12 was initiated at point Pc. The horizontal and vertical strain in the

specimen at which the crack initiated were -509 μm/m and 994 μm/m respectively (Figure 4.11b and f). The crack then gradually grew in vertical direction with the increase in the vertical load on the specimen. The specimens ultimately failed completely at the peak with multiple vertical cracks (similar to axial splitting commonly observed in a uniaxial compression test test). We observed similar contour patterns and failure mode in all tests regardless of the depth of the flattening.

Figure 4.11: Typical strain contours obtained from the DIC analysis at different load levels (depth of flattening 4mm, see Figure 4.13 for the load levels). (a), (b), (c) and (d) Horizontal strain (ε_{xx}) at 50% of yield, at yield, between yield and peak and at peak respectively. (e), (f), (g) and (h) Vertical strain (ε_{yy}) at 50% of yield, at yield, between yield and peak and at peak respectively.

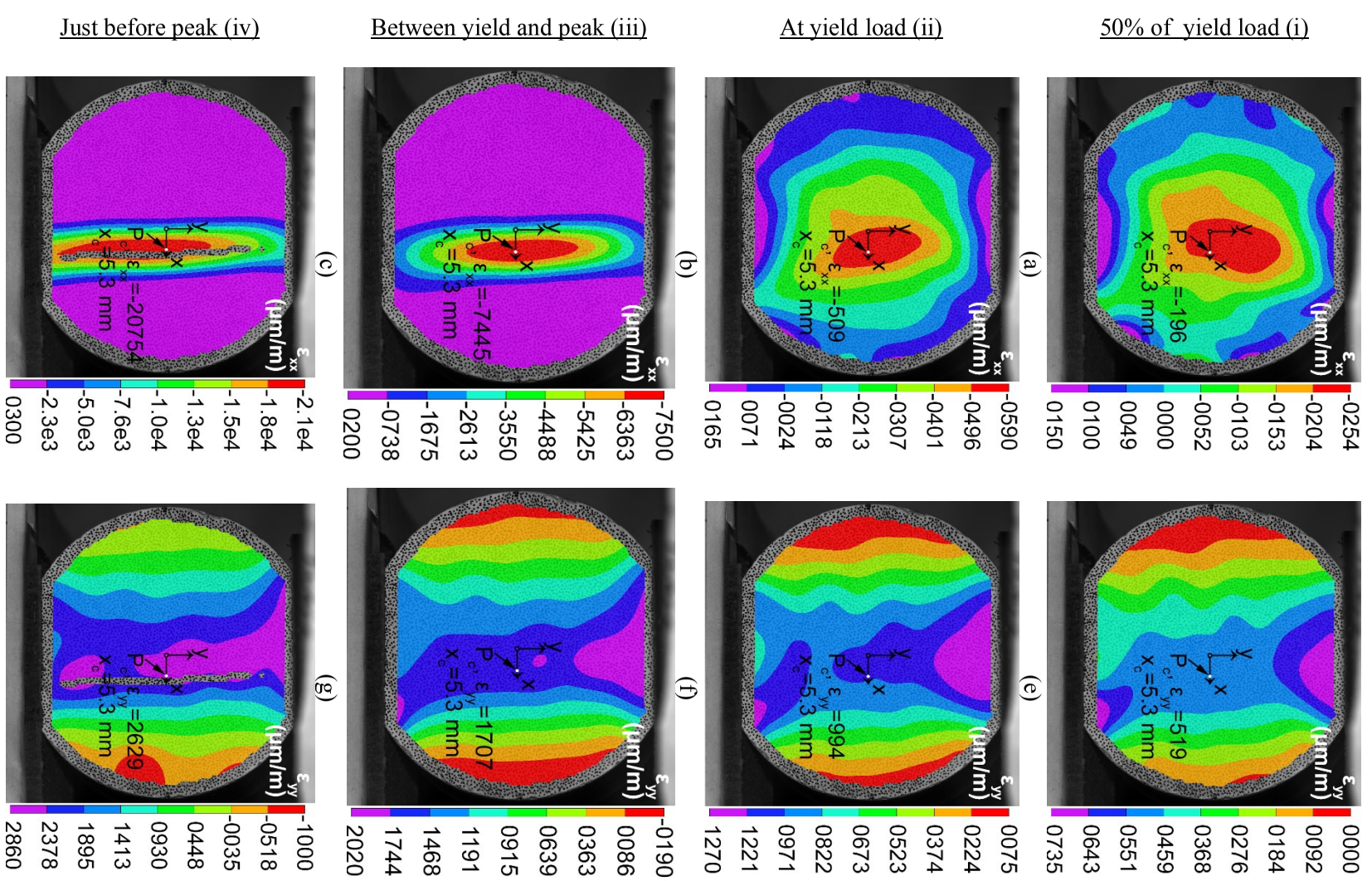

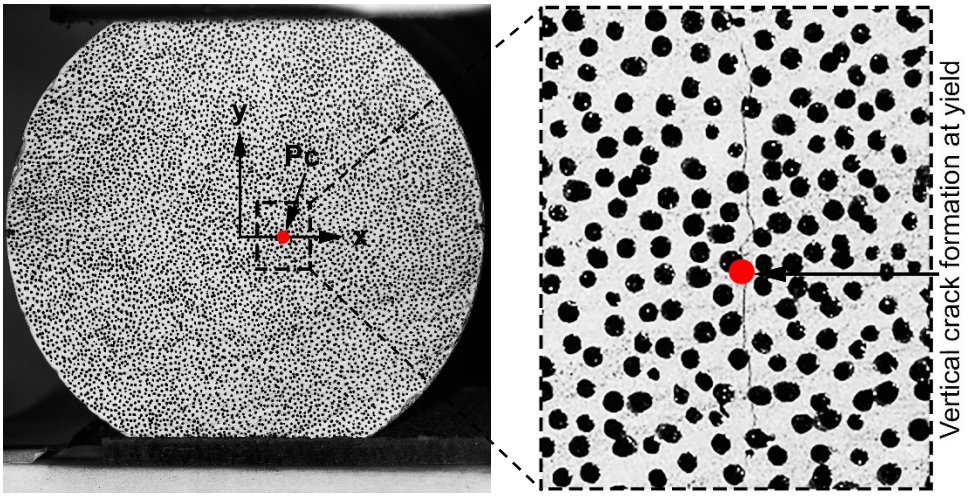

Figure 4.12: Typical vertical crack initiation at the critical point, Pc, in a flattened Brazilian specimen at the yield point (Figure 4.13)

Load versus horizontal (tensile) and vertical (compressive) strain data were then extracted for each specimen at the critical point, P_c, using the DIC software. A typical load (P) vs strain in horizontal (ε_{xx}) and vertical (ε_{yy}) directions at the critical point P_c, for a sample with 4 mm depth of flattening, is shown in Figure 4.13 (typical plots for other depths of flattening are shown in Figure B.7; Figure B.9; Figure B.11 and Figure B.13). The Load-strain plot remained linear until the yield point and then the slope of load versus horizontal strain decreased sharply. We interpret this change in behaviour as the generation of a crack as shown in Figure 2.12. The formation of this crack is the initiation of the failure process. As the load increases the crack continues to grow in the vertical direction until the strength peak is reached Figure 4.13. The critical horizontal and vertical strain values at which the initiation of the vertical crack formed were used to determine the corresponding values of principal stresses.

(a)

(b)

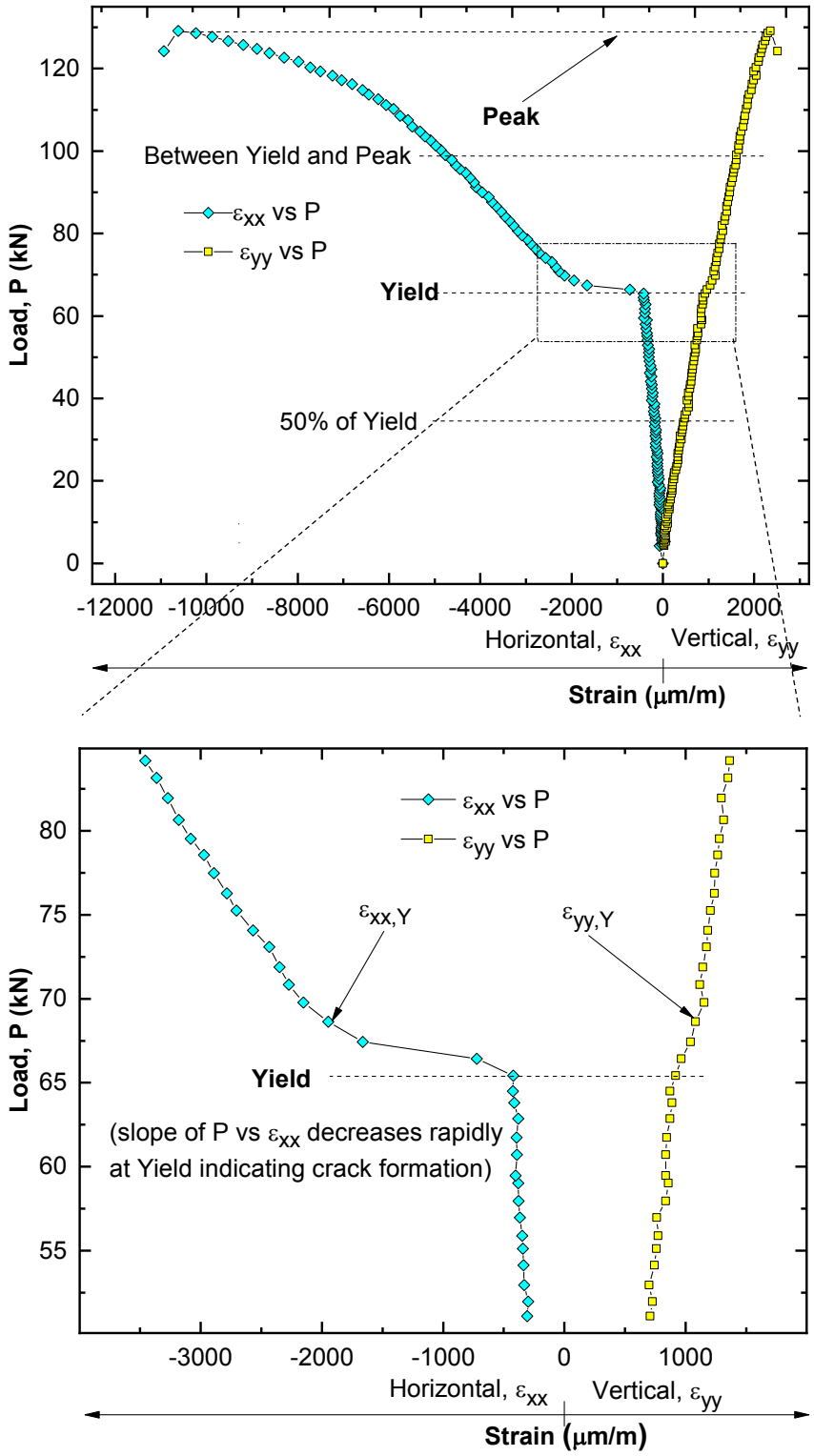

Figure 4.13: Typical load strain plot obtained from DIC measurements (depth of flattening 4mm). (a) Complete strain-load plot showing yield and peak and other load levels at which strain values are compared in Figure 4.11 (b) Zoomed portion of the plot near the yield.

The major and minor principal stresses for the flattened Brazilian test at different depths of flattening were calculated using the Equations (4-5) and (4-6). The elastic constants (compressive Young's modulus, tensile Young's modulus and the compressive Poisson's ratio) were taken from Table 4-1 and the yield horizontal ($\varepsilon_{xx,Y}$, tensile) and vertical ($\varepsilon_{yy,Y}$, compressive) strain values were taken from the respective load vs strain plots as shown in Figure 4.13. The dimensions, load values obtained from the MTS testing machine, strain values from the DIC analysis and principal stresses calculated for all the specimens are presented in Table B-2 to Table B-7. The average results and standard deviations for each depth of flattening are given in graphical form in Figure 4.14.

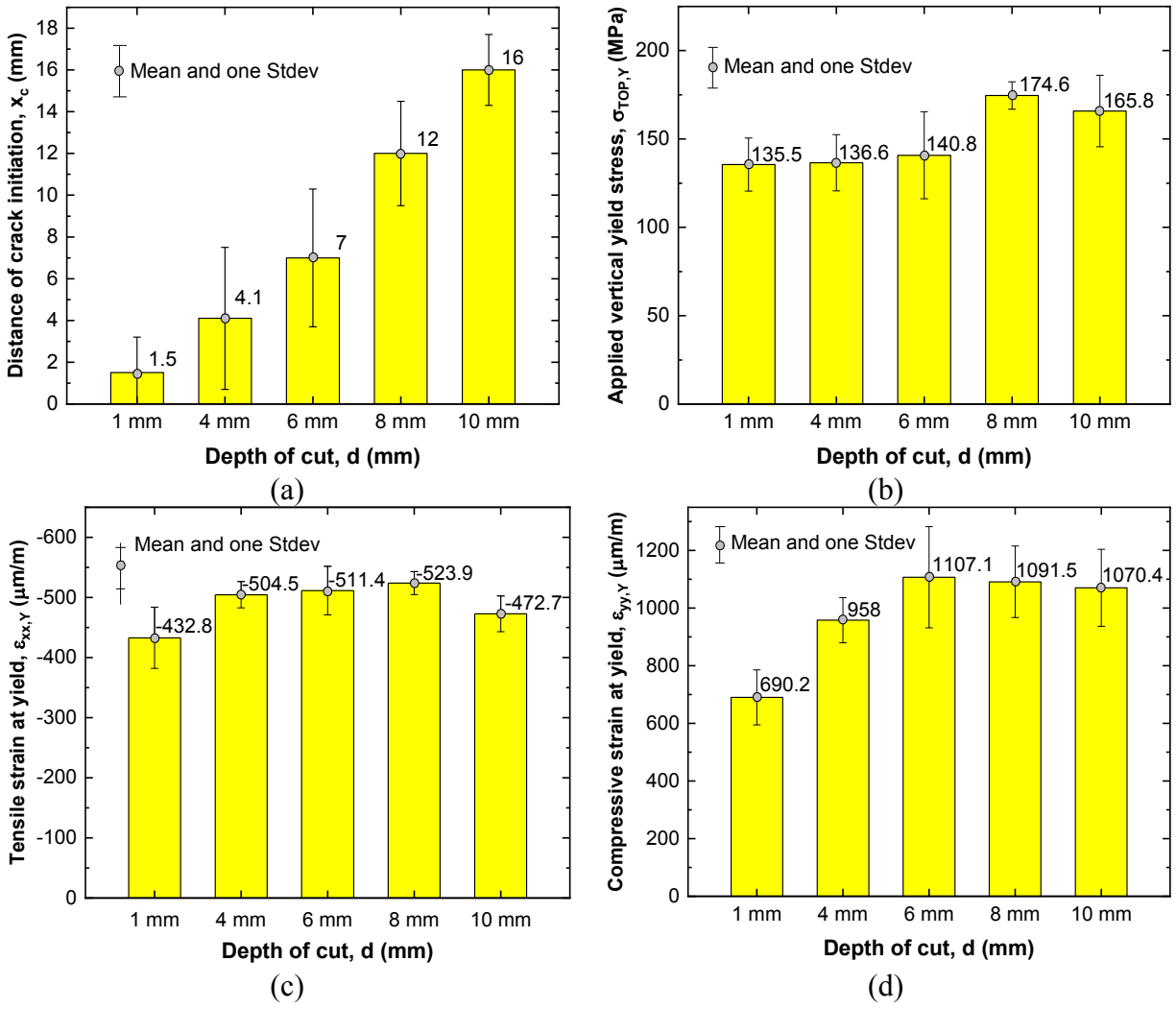

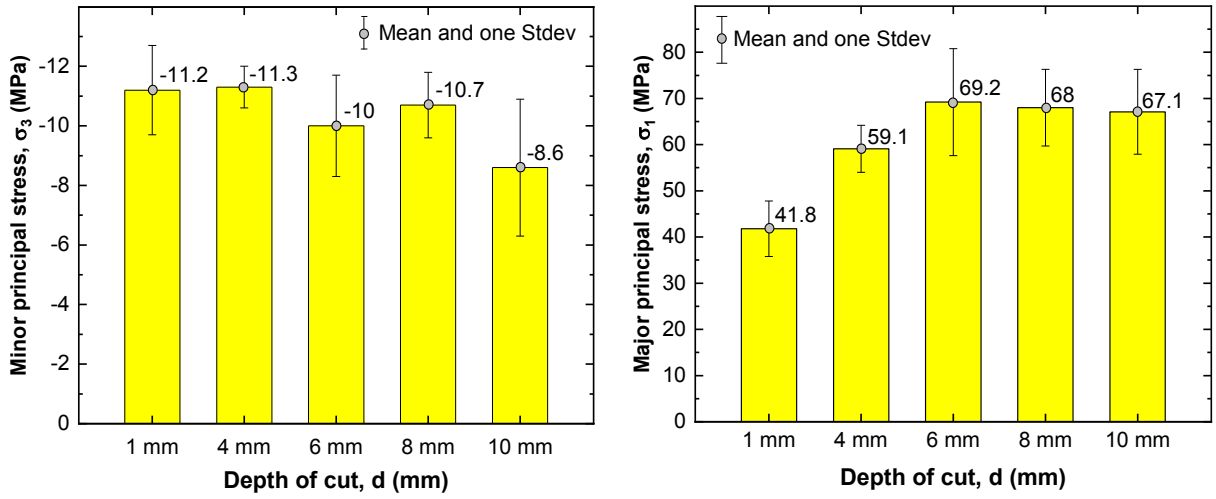

Figure 4.14: Mean and standard deviation of the results obtained for the confined extension test on Lac du Bonnet granite (a) crack initiation distance from centre, x_c (b) applied vertical yield stress on the flat surface, $\sigma_{TOP,Y}$ (c) principal tensile strain at yield, $\varepsilon_{xx,Y}$ (d) principal compressive strain at yield, $\varepsilon_{yy,Y}$ (e) principal tensile stress at yield, σ_3 and (f) principal compressive stress at yield, σ_1. Number of specimens tested for each depth of flattening is five. Refer Figure 4.7 and Figure 4.13 for the symbols used and load levels.

The important observations from the flattened Brazilian tests are:

- When the depth of flattening is 1 mm, the crack initiates along the horizontal diameter close to the center of the specimen. As predicted by the numerical analysis, with the increase in depth of flattening the crack initiation point (x_c) shifts towards the edge of the specimen, the maximum distance being 16 mm for 10 mm depth of flattening (radius of specimen is 31.7 mm). The coefficient of variation for the location of crack formation is very high (maximum 110.3% for 1 mm depth of flattening, Table A6) suggesting that it is difficult to predict it. It also confirms the importance of using the DIC technique for identifying the location of crack initiation.
- With the increase in depth of flattening, there is a slight increase in the vertical stress on the top of the specimens (135.5 MPa to 174.6 MPa) at which the first crack initiates.

- The major principal stress (σ_1) at the location of crack initiation increases from 41.8 MPa to 69.2 MPa when the depth of flattening is increased. However, the difference in major principal stress for 6 mm, 8 mm and 10 mm depths of flattening is within 3%.
- The average value of tensile stress at the crack initiation is about -10.4 MPa with coefficient of variation of 14%. This value is close to the Brazilian strength of Lac du Bonnet granite (-11.6 MPa).

4.10 Discussion

It is now widely recognized that the failure process in rock when loaded in uniaxial and triaxial compression is initiated by the onset of cracking with the cracks growing in the general direction of the applied load and normal to the plane of the minimum stress (Nicksiar and Martin 2013). This is also true in a traditional Brazilian test and the flattened Brazilian tests and recorded by the DIC images (see Figure 4.12). As shown in Figure 4.13, the onset of fracture initiation does not mean immediate failure, and the specimen requires additional loading to achieve complete rupture of the specimen. This phenomenon is characteristic of confined extension. However, when a rock specimen is loaded in uniaxial tension, the load at which cracking initiates and the uniaxial tensile strength is very similar (Hoek and Martin 2014a).

The strain associated with the onset of crack initiation (CI) from the uniaxial tension, Brazilian, flattened Brazilian, uniaxial compression and triaxial compression are compiled in Figure 4.15. Figure 4.15 clearly shows that the uniaxial tension test has the lowest strain required for fracture initiation. For confined extension, with the gradual increase in confinement for the Brazilian and flattened Brazilian, the crack initiation strain increases. In the compression side, at low confinement crack initiation occurs at a stress level of around 40-50% of the peak load which is consistent with the findings by Nicksiar and Martin (2012) for low porosity crystalline rock. It is

clear from Figure 4.15 that strain associated with crack initiation is a function of the stress path and the confining stress.

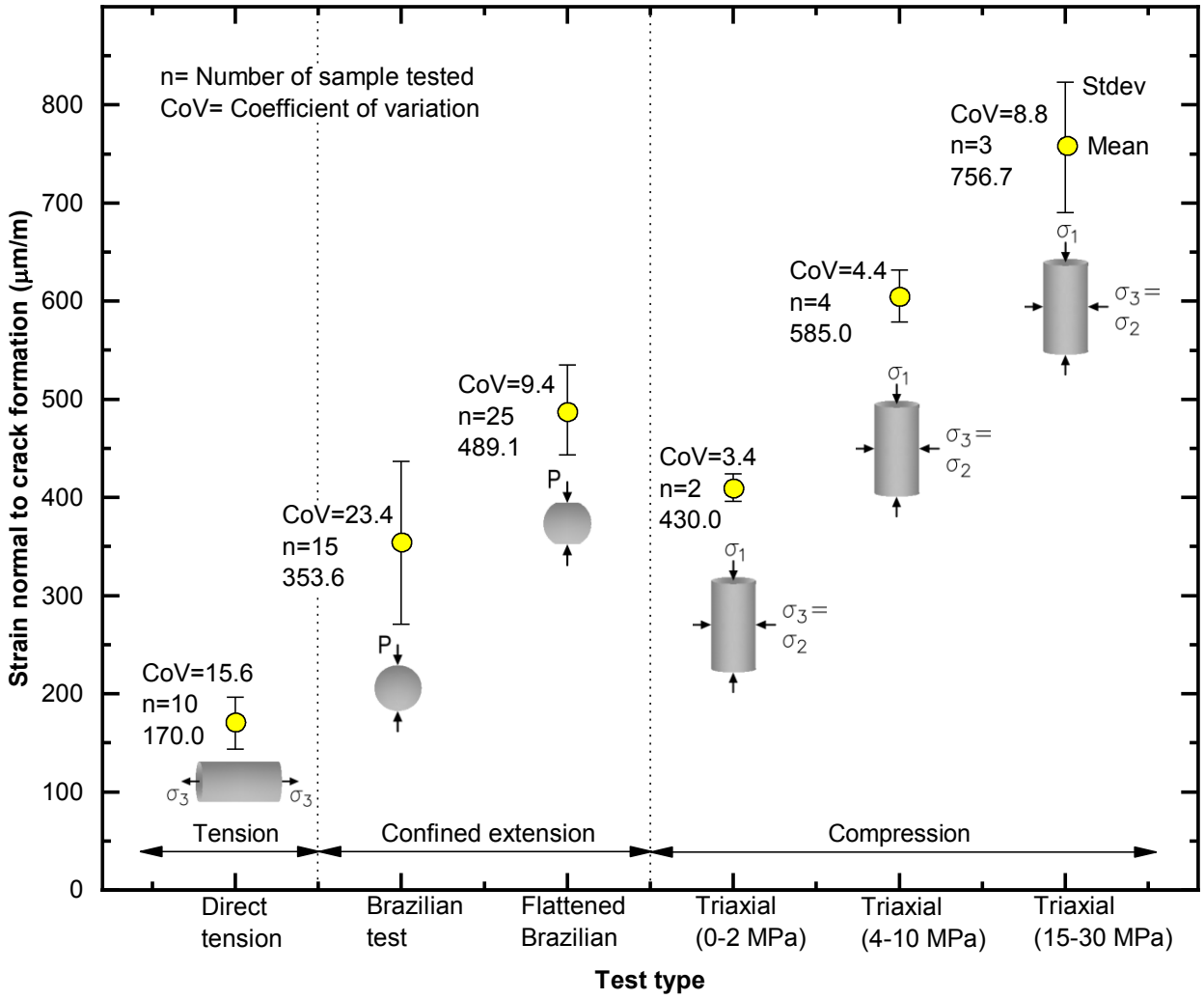

Figure 4.15: Comparison of strain normal to crack formation for direct tension, Brazilian, UCS and triaxial tests (Lau and Jackson 1992) with that measured in Flattened Brazilian tests on Lac du Bonnet granite.

The average value of major and minor principal stress obtained for different depths of flattening from the flattened Brazilian tests are plotted in Figure 4.16. As expected, there is a gradual increase in the applied σ_1 values as the depth of the flattening increases, reflecting the increase in confined extension. The Brazilian and direct tension for Lac du Bonnet is also shown on Figure 15. It is

well known that the tensile strength form a direct tension test is approximately 80% of the Brazilian Strength and hence plots to the left of the direct tensile strength. The Hoek and Brown failure envelope obtained from the uniaxial and triaxial compression tests plot to the right of the confined extension results. As noted by Hoek and Martin (2014) the curvature of the Hoek-Brown envelope may not be correct for this region, but the envelope does provide a reasonable estimate for this confined extension region even when only using the results from compression tests. The fit could certainly be improved if the tensile strength data was also used for establishing the Hoek-Brown envelope.

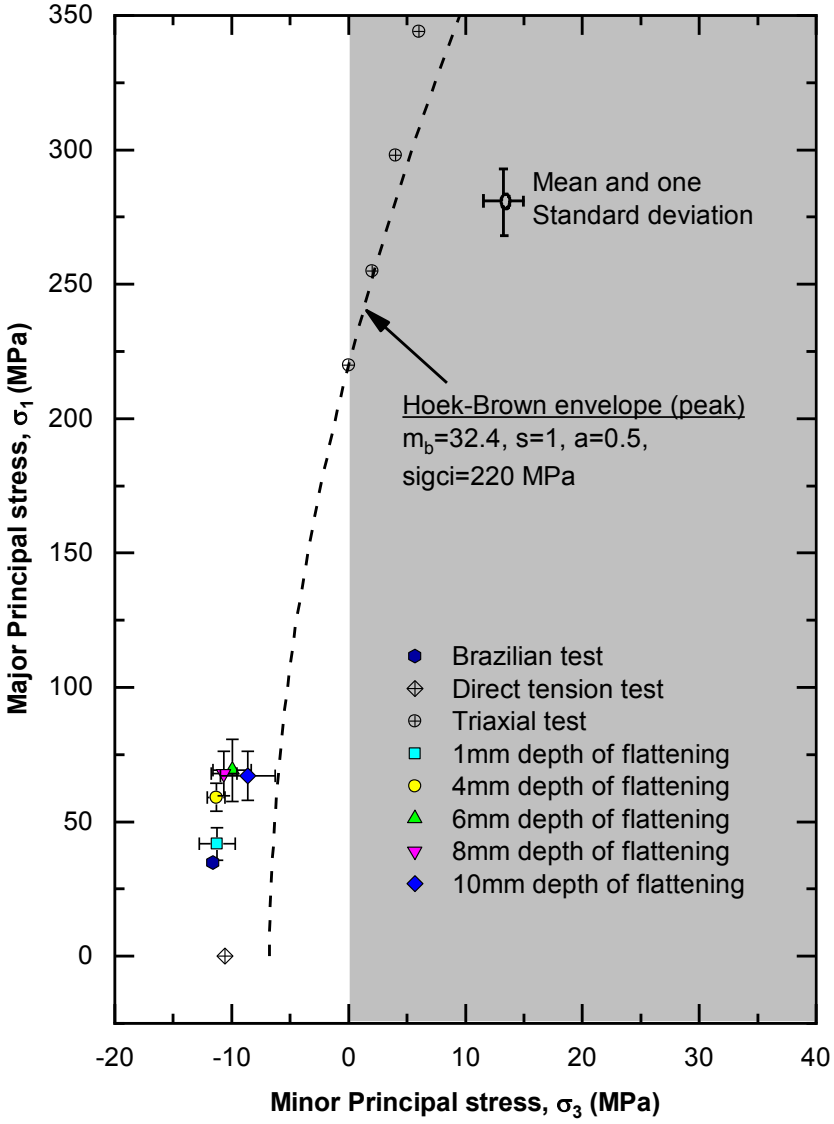

Figure 4.16: Results of Brazilian, Flattened Brazilian tests on Lac du Bonnet granite.

4.11 Summary

In this study, we used the flattened Brazilian test to understand the confined extension behavior of Lac du Bonnet granite. A methodology was developed that increased the confinement around the tensile stresses using a flattened Brazilian disk. DIC technique was employed to track the location of the macro crack initiation and to measure the strain values on the surface of the specimens during the tests. We derived stress-strain equations by considering the bi-modular relations between the elastic constants. We tested modified Brazilian specimens of Lac du Bonnet granite with increasing depth of flattening. By doing so, we could increase the major principal stress from about 33 MPa (that is the theoretical value of major principal stress for Brazilian test) to 69.2 MPa at 6 mm depth of flattening. Beyond a depth of flattening of 6 mm the increase in the major principal stress is minor. For the six depths of flattening tested, we found out that cracking initiates when the tensile strain reaches around -489 μm/m. Because the present methodology only provided major principal stresses up to approximately 30% of the uniaxial compressive strength, uncertainty remains for the confined extension region above those values. While the dog-boned confined extension test remains attractive, the effects of the stress path and specimen geometry need to be resolved. An alternative may be a confined Brazilian test as proposed by Jaeger and Hoskins (1966).

The stress path used to establish the strength of intact rock plays a major role in the approach used to develop a failure envelope. The Hoek-Brown failure criterion was developed for the complete stress region from uniaxial tension to triaxial compression. The criterion is calibrated using only laboratory results from the compression tests. The confined extension results reviewed in this paper does not support the shape of the current Hoek-Brown criterion in this region. The limited

testing carried out in this program for Lac du Bonnet granite also supports this finding. For Lac du Bonnet granite the Hoek-Brown envelop underestimates the confined tensile strength, but is likely adequate for most rock engineering applications. The fit for the Hoek-Brown envelope in the confined extension region should be improved by including tensile strength in the fitting data or possibly providing a tension cut-off as proposed by Hoek and Martin (2104). Such a change would require more supporting test results.

Chapter 5:

Investigation of the confined extension behavior of low-porosity rock using the flat jointed bonded particle model

5.1 Introduction

To obtain the design parameters of a rock from the laboratory testing, the rock should be tested under similar sets of boundary conditions as those expected in the field (Brady and Brown 2004). The complexity of testing rock under all boundary conditions has led to the application of simplified two dimensional failure envelopes such as the non-linear Hoek-Brown (Hoek and Brown 1980) and the linear Mohr-Coulomb failure criterion. Of these two criteria the empirical Hoek-brown criterion is widely used in practice. Hoek and Brown (1980) suggested that the parameters for their criterion should be obtained from triaxial compression data. They assumed, based on limited laboratory data that their criterion could be extrapolated to the region of confined extension and direct tension with adequate accuracy.

A version of this chapter has been accepted in 52nd US Rock Mechanics/Geomechanics Symposium (ARMA):

Patel, S. and C. D. Martin. 2018. "Simulating Bi-Modularity in Crystalline Rock Using Discrete Element Modelling." *52nd US Rock Mechanics/Geomechanics Symposium*, 17-20 June 2018

And two journal manuscripts are under preparation:

Patel, S. and CD Martin. 2018. "Investigation of laboratory response observed in rocks using the flat jointed bonded particle model." *(Under Preparation)*.

Patel, S. and CD Martin. 2018. "Investigation of Confined Extension Behavior of Rock Using Flat Jointed Bonded Particle Model." *(Under Preparation)*.

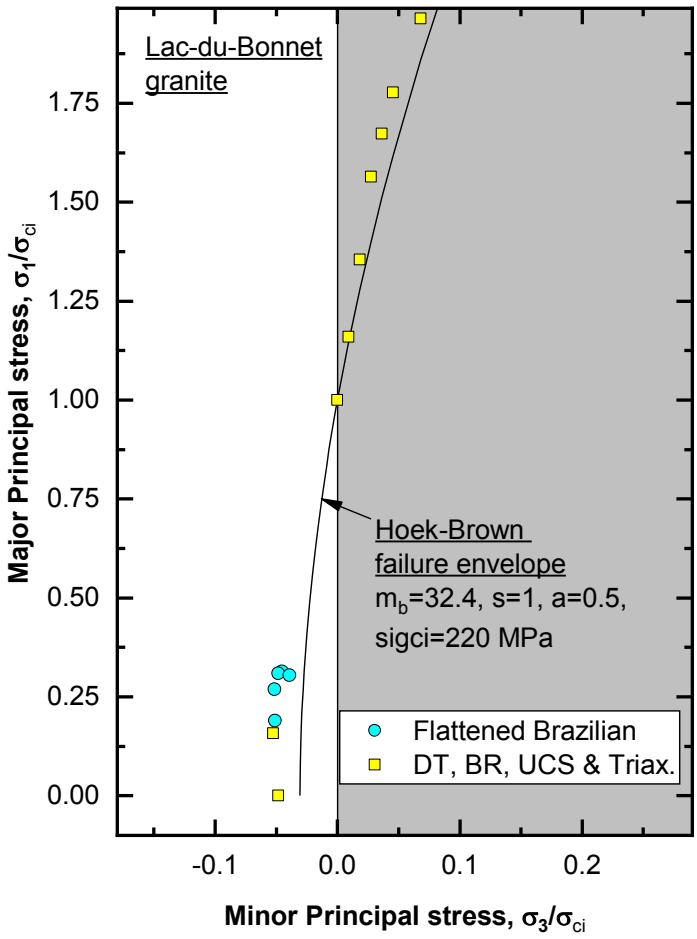

Figure 5.1: Laboratory test results and failure envelope for Lac-du-Bonnet granite (Patel and Martin 2018b). The flattened Brazilian results are the average for 5 depth of flattening (5 samples for each depth of flattening)

The data available in the literature in the region of confined extension is very limited. Patel and Martin (2018b) reviewed the limited data available from confined extension tests and found that there is a clear impact of intermediate principal stress (σ_2) on the peak strength. Patel and Martin (2018b) conducted confined extension tests on Lac du Bonnet granite using the flattened Brazilian test where the intermediate principal stress is zero (Figure 5.1). Because of the difficulty of conducting confined extension tests at high compressive stresses a numerical flat jointed (FJ) bonded particle model is used in this chapter to investigate rock behavior in confined extension.

To undertake this task, we: (a) modified the code (PFC3D, Potyondy 2012) to carry out the confined extension tests using FJ bonded particle model and various confined extension stress paths; (b) validated the laboratory results on Lac du Bonnet granite using the UCS/σt ratio, the crack closure stress, the crack initiation stress, the crack damage stress, and the bi-modularity; and (c) determined the failure envelope of Lac du Bonnet in confined extension and investigated the impact of intermediate principal stress in confined extension.

5.2 Background

5.2.1 *Compressive and tensile failure in rock*

The ISRM suggested method (Bieniawski and Bernede 1979) describes the methodology to conduct the UCS test on rock while the ISRM suggested method (ISRM 1978) describes the methodology to conduct the direct tension test. Unlike metals, the ratio between the UCS and direct tension strength of rock is typically greater than 10 (Hoek 1966). The brittle fracture of rock under tension and compression was first studied by Hoek and Bieniawski (1965) and Bieniawski (1967a, b, c). The tensile cracking in a rock sample during the direct tension test starts close to the peak while in an UCS test it gradually develops from approximately the beginning of the test (at the grain boundary where there is a critical stress concentration). Hence, rock during compressive failure in the laboratory passes through different stages, which are crack closure, crack initiation, crack damage and peak stress (Martin and Chandler 1994). A typical stress-strain curve in an UCS test is shown in Figure 5.2.

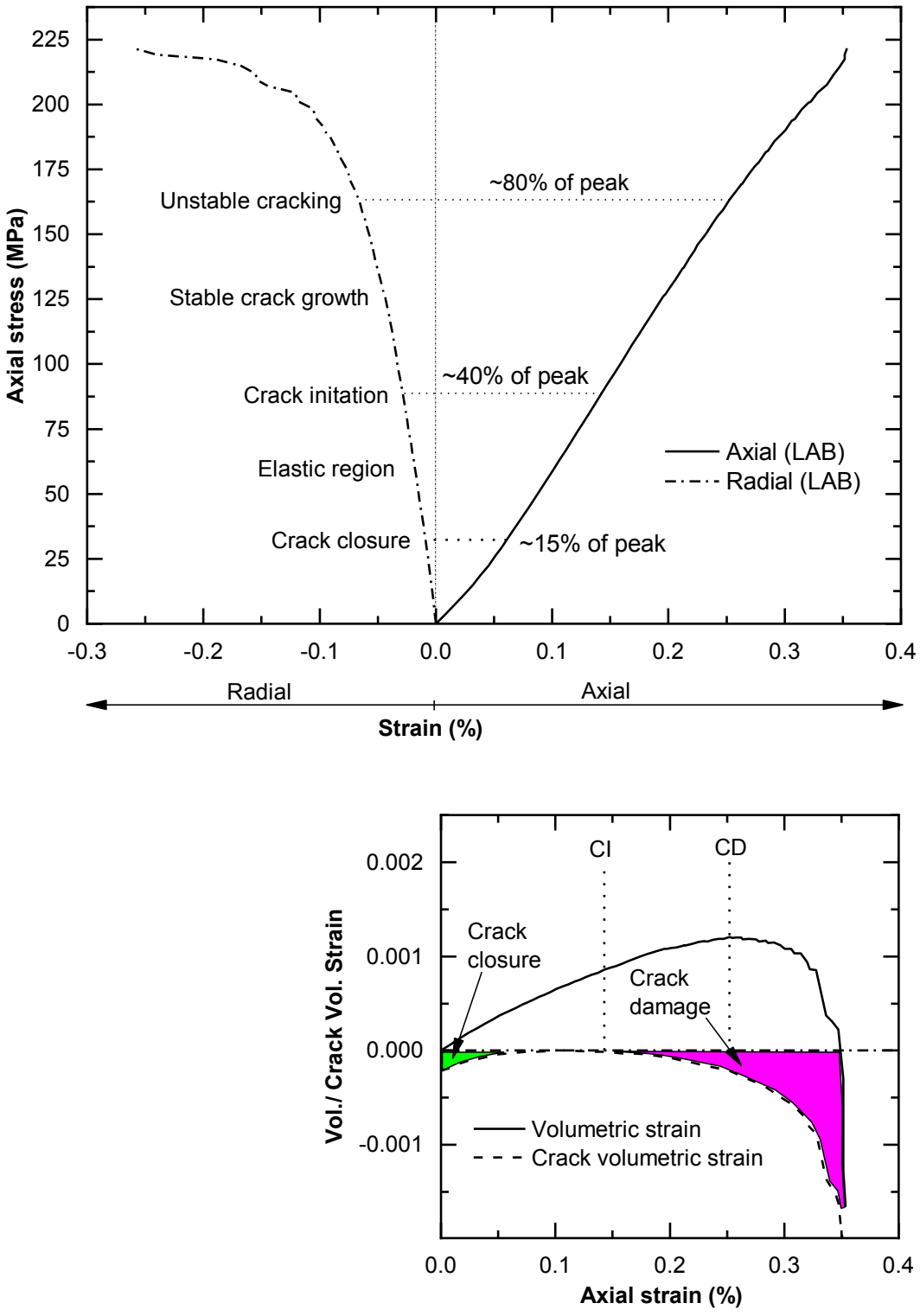

Figure 5.2: A typical stress-strain curve obtained for Lac du Bonnet granite (Lau and Jackson 1992). The volumetric and crack volumetric strain are calculated using equations (5-8) and (5-9) (Martin 1993).

5.2.2 *Flat jointed bonded particle model*

The latest development in bonded particle modelling to simulate rock behavior is the flat joint (FJ) model proposed by Potyondy (2012). As shown in Figure 5.3a, in a FJ model, the mineral grains are represented by rigid spheres and the contacts by disk shaped FJs. The FJ contacts are further discretized along radial and tangential directions as shown in Figure 5.3b. Each discretized element in FJ fails separately when either the tensile or shear stress exceeds its strength. This allows a partially fractured FJ in the model to carry the moment, which is essential to produce the high ratio of UCS to tensile strength typically found in crystalline rocks. The high ratio of UCS to direct tensile strength was not possible to achieve using the previous parallel bonded particle model (Potyondy and Cundall 2004) first proposed for rock modelling (Potyondy 2012). However, to capture the progressive fracturing observed in a laboratory UCS test and described by Martin and Chandler (1994) still remains a challenge using the FJ model. The physics behind the FJ bonded particle model is described by Potyondy (2012).

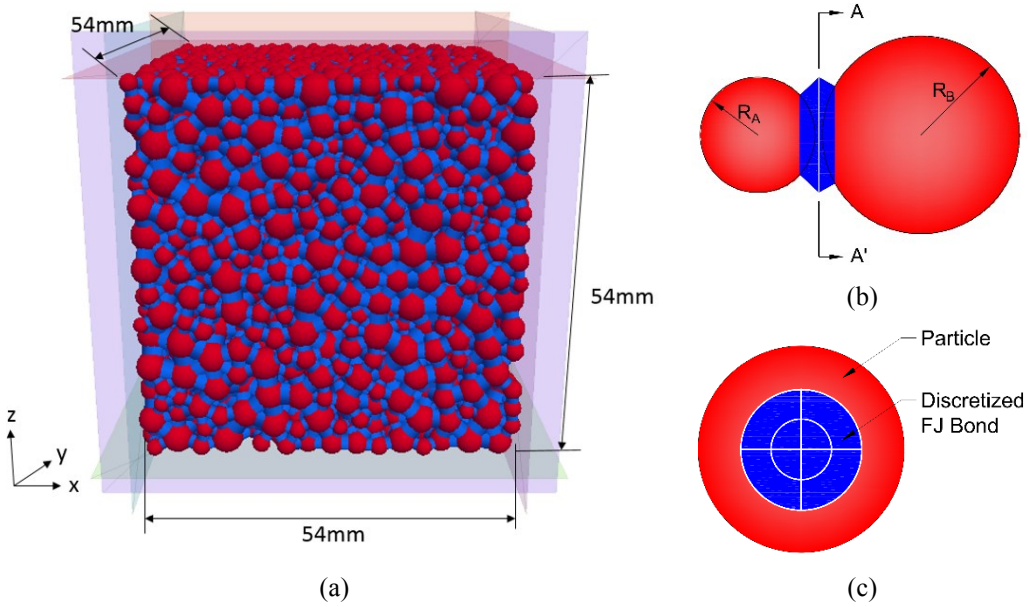

Figure 5.3: (a) PFC3D FJ contact model with 3618 grains and 19511 FJ contacts (b) grains represented by the spheres and force of attraction between the grains by FJ bond and (c) the discretized FJ contact between the grains, each FJ contact is divided in 8 FJ elements.

Table 5-1. List of micro properties obtained after calibration. These parameters are described by Potyondy (2017)

Parameter	Value
Associated with particle size distribution:	
Minimum particle diameter (R_{min})	2.2 mm
Particle-size ratio (R_{max}/R_{min})	2.3
Associated with material genesis:	
Width of sample (W)	54 mm
Height width ratio (H/W)	1
Associated with Flat-jointed material group:	
fjm_igap (installation gap):	1.31 mm
fjm_B_frac (bonded fraction):	0.65
fjm_G_frac (gapped fraction):	0.35
fjm_S_frac (slit fraction, derived):	0
fjm_G_m (initial surface-gap distribution, mean):	0.002mm
fjm_G_sd (initial surface-gap distribution, standard deviation):	0
fjm_Nr (elements in radial direc.)	1
fjm_Nal (elements in circumferential direc.)	3
fjm_rmulCode (radius-multiplier code): 0 (fixed)	0
fjm_rmulVal (radius-multiplier value):	0.577
fjm_emod (effective modulus):	149 GPa
fjm_krat (stiffness ratio):	1.6
fjm_fric (friction coefficient):	1.38
fjm_ten_m (tensile-strength distribution, mean):	44.5 MPa
fjm_ten_sd (tensile-strength distribution, standard deviation):	0
fjm_coh_m (cohesion distribution, mean):	250 MPa
fjm_coh_sd (cohesion distribution, standard deviation):	0
fjm_fa (friction angle [degrees]):	43.2
Associated with Linear material group:	
lnm_emod (effective modulus):	149 GPa
lnm_krat (stiffness ratio):	1.6
lnm_fric (friction coefficient):	1.1

The parameters used for the grains (spheres) and contacts are described in the material modelling support manual (Potyondy 2017) and are listed in

Table 5-1. These are micro parameters and are impossible to determine directly from laboratory tests. These parameters are obtained by the calibration of macro-parameters such as tensile strength, UCS, triaxial strength, Young's modulus and Poisson's ratio obtained from the laboratory tests. An iterative method is used to find a set of parameters with which the model can produce the properties obtained by the traditional testing in the laboratory. However, as shown in

Table 5-1, this set of micro-parameters contains 18 parameters for FJs and these need to be calibrated simultaneously. The methodology used to select these parameters is described in the following sections including how the (a) crack closure; (b) crack initiation; (c) crack damage; and (d) bi-modularity (different Young's modulus and Poisson's ratio in compression and tension) can be captured using the FJ bonded particle model.

5.3 Calibration to Lac du Bonnet granite

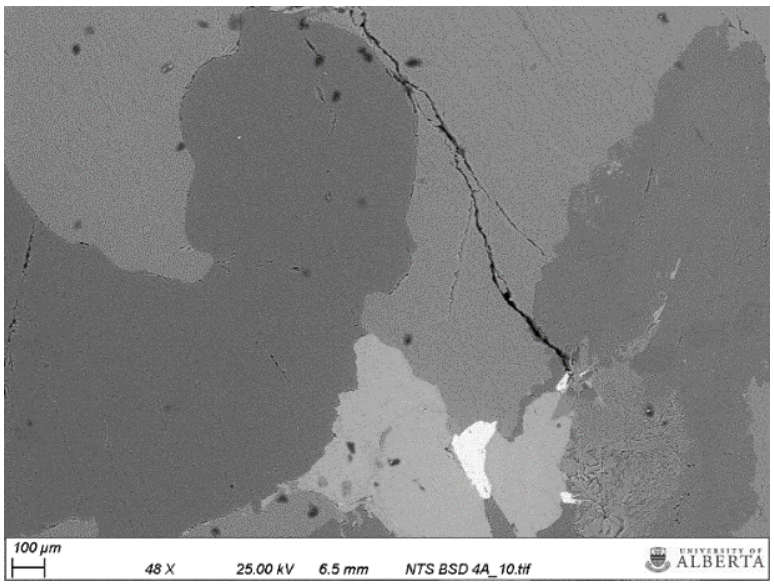

Figure 5.4: SEM image of an intact Lac du Bonnet granite sample showing complex mineral grains and stress released micro fractures

For our study, we used Lac du Bonnet granite, a crystalline rock with the grain size varying between 3 mm to 7 mm (Martin 1993). The uniaxial compressive strength of Lac du Bonnet granite is approximately 220 MPa, and the CI stress is approximately 40% of the UCS. The ratio between the Et and the Ec for Lac du Bonnet granite is around 0.65. The complex shaped mineral grains with stress released induced micro fractures present in an intact sample of Lac du Bonnet granite is shown in Figure 5.4. The laboratory properties of Lac du Bonnet granite are presented in Table 5-5 and Table 5-6.

5.4 Guideline for choosing micro parameters for FJ analysis

5.4.1 *Grain size and grain size distribution*

One of the most important issues to consider in particle modelling is the rock microstructure. As shown in Figure 5.4, the shape of the grains in a rock is very complex and it is impossible to make a numerical rock sample with similar shape of mineral grains in a real rock. Also, there are different types of mineral grains present in a rock (Lac du Bonnet granite contains four types of mineral grains) which will have their own set of micro parameters. The interfaces at grain-grain contact properties between one combinations of mineral grains will be different from another combination. So, if all grains and their interfaces are considered separately, it will increase the total number of micro parameters required to capture the macro response of rock. To simplify the model, in this research, one type of grain with an average of the material properties of all grains is used to simulate the four types of mineral grains present in Lac-du-Bonnet granite.

The grain size in Lac-du-Bonnet granite varies from 3 mm to 7 mm (Martin 1993), the ratio between the largest and smallest particle being 2.3. A similar distribution of grain size was considered for the numerical sample with a minimum particle size of 2.2 mm. As suggested by

Brown (1981), the width of the rock sample should be at least 10 times the largest mineral grain present in the rock. Similarly, the ISRM Suggested Method for obtaining the deformability of rock materials in uniaxial compression (Bieniawski and Bernede, 1979) recommends the diameter of the sample should be at least NX (54 mm) size. The maximum diameter of the grains used in the study is 5.06 mm. To meet both of the above conditions, an average of 15 particles along the diameter (resolution=15) is required.

5.4.2 *Sample dimensions*

To reduce the confining effect of steel end platens with frictional contacts, the ISRM Suggested Method for obtaining the deformability of rock materials in uniaxial compression (Bieniawski and Bernede, 1979), recommends a length to diameter (L/D) ratio of 2.5-3. However, in the PFC model the top and bottom loading platens (walls) are frictionless and a L/D=1.0 was found to provide similar results to the L/D=2.0 model saving considerable run time. When a model with L/D=1.0 was compared with L/D=2.0 with same set of micro parameters, the model was only 7% less in direct tensile strength and 6% more in UCS.

5.4.3 *Modulus and stiffness ratio of particles and FJs*

The modulus and the ratio between the normal and shear stiffness of the particle and the FJs, are the parameters which affects the macro-scale Young's modulus and Poisson's ratio of the numerical sample. Ideally these values should be different for the particles and the FJs with the particle values being greater. Also, the values in compression and tension of the modulus and stiffness ratio should be different. However, for simplicity the behavior in compression and tension and for the particle and the bonds were initially considered the same. Potyondy (2012) suggested the kn/ks stiffness ratio should be 1.66. When this ratio increases, the sample expansion increases

laterally increasing the Poisson's ratio. It also increases the compression-induced extensile stress between the mineral grains causing early tensile failure in the material. The initial modulus value of the particles can be considered the same as the modulus of rock (70 GPa, Table 5-5) for calibration. This will produce either a higher or a lower macro Young's modulus which can be adjusted to match the laboratory Young's modulus of the rock. The relation between the macro and micro modulus was found to be linear.

5.4.4 *Friction angle*

The friction angle of the numerical sample impacts the crack damage stress, the peak strength and the shape of the stress-strain curve after the crack damage point in the UCS and triaxial tests. As a starting value for calibration, the program RocLab (RocLab 2008) was used to obtain an approximate friction angle using the triaxial test results as input. The friction angle was then adjusted to provide the best match with the UCS and low confinement triaxial results from the laboratory. Figure C.15 shows the impact of friction angle on the failure envelope.

5.4.5 *FJ Contact type*

When two grain boundaries in a rock are close to each other, they can be either bonded or a broken contact with no cohesion. There can also be a gap between two neighboring interface due to tensile failure during stress relaxation or unloading. However, in this study, it was assumed that if the interfaces are in contact they are bonded (no broken contact). The gapped contact during an UCS test in a real/numerical rock sample closes with application of gradual loading. This produces non-linearity in the initial part of stress-strain curve in an UCS test. The procedure to obtain the initial gap in the numerical sample is described in Section 5.7.

5.4.6 *FJ discretization*

The most important change in the FJ bonded particle model compared to the previous parallel bonded model is that the grain interfaces are discretized (as shown in Figure 5.3b). This allows the interfaces to progressively fail and retain some moment resistance until complete rupture of the contact. However, with the increase in the FJ discretization the run time for the model increases, especially after the formation of cracks in the model. The analysis in this research was started with the minimum discretization of 1node in the radial and 3 nodes in the tangential direction. This discretization can be increased to match the macro response of the rock.

5.4.7 *Radius of FJ between mineral grains*

The FJ bonded particle model requires the radius of the FJs as an input. The radius of a FJ in the numerical sample depends upon the radius of the contacting particles and is given by Equation (5-1) below:

$$R_{FJ} = \lambda \times \text{Minimum}(R_1, R_2) \quad (5\text{-}1)$$

Where, R_1= radius of first particle, R_2= radius of second particle and λ is a constant called the radius multiplication factor.

With an increase in the value of radius multiplication factor, the void between the grains decrease and the strength of the numerical sample increases. However, there must be a limit to the radius multiplication factor. Figure 5.5a shows three particles with different radii in contact. If a radius multiplication factor of one is chosen, the three FJs (FJ_1, FJ_2 and FJ_3) will intersect at point D. This will produce an invalid micro structure as described in the software material modelling support manual (Potyondy 2017). There will be many combinations of particles of different radius that will be present in the model but the critical radius multiplication factor will occur when three particles

of same radius will be in contact (as shown in Figure 5.5b). To obtain the maximum multiplication factor, three particles with minimum particle radius (R_{min}) was used (see Figure 5.5b). To avoid invalid micro structure, the radius of the FJs in Figure 5.5b must be less than the distance DE which can be calculated using the equilateral triangle ABC in Figure 5.5b:

$$\mathrm{DE} = \frac{1}{3}\mathrm{AE}$$

$$\Rightarrow \mathrm{DE} = \frac{1}{3}\mathrm{AC} \times \sin 60$$

$$\Rightarrow \mathrm{DE} = \frac{1}{3} 2 \times \mathrm{r} \times \frac{\sqrt{3}}{2}$$

$$\Rightarrow \mathrm{DE} = 0.5774\mathrm{R}_{\mathrm{min}} \qquad (5\text{-}2)$$

Consequently, a radius multiplication of 0.577 was used for this study.

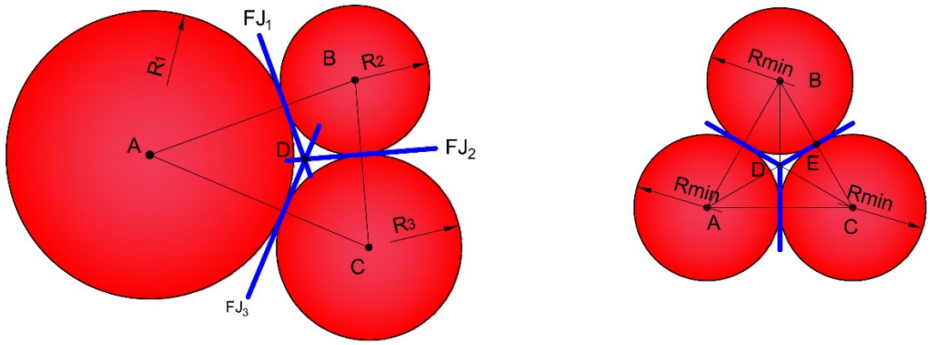

(a) (b)

Figure 5.5: (a) Invalid microstructure produced (FJs are intersecting) when a radius multiplication factor of one was used (b) FJ with the maximum radius multiplication factor (0.577).

5.4.8 *Grain interaction range*

In the FJ bonded particle model the particles are represented by rigid spheres. To create the numerical rock sample the spheres are generated in a confined volume surrounded by rigid walls (as shown in Figure 5.3). To make a compacted structure with a low porosity an all-around confinement is provided to the numerical specimen. FJs are then installed at the grain-grain

contacts. Figure 5.6 shows the change in porosity by the gradual application of 10 MPa confinement to the numerical sample. The porosity achieved at the end of confinement was ~0.35. The average number of contacts per particle was found to be 2.49 (3618 particle and 9009 FJs). The porosity does not include a contribution from the FJs volume, however as shown in Figure 5.7a there are voids between the neighboring particles (shown in dotted lines). Figure 5.7b shows, when an axial compressive load is applied to the specimen, cracks form in the sample very early (yellow lines, less than 10% of peak). With the voids present in the sample it was not possible to match the stress-strain curve observed in the laboratory. To avoid this the software allows a bond to form between neighboring particles even if they are not touching (installation gap, Potyondy 2017). If the gap between two particles is less than the installation gap, a FJ will be formed at the mid-point between the two particles. However, the gaps between different locations are different. Ideally the program should identify the voids inside the sample and install the FJs. This option is not available with the present version of the program. So, the following procedures were adopted to mitigate this.

(a) As shown in Figure 5.8, the most critical combination for the installation gap occurs when five particles with minimum particle radius (Rmin,
(b) Table 5-1) combine together as shown in Figure 5.8.
(c) In Figure 5.8a, the centers of particles A, B and C form an equilateral triangle while the particles D and E fit perfectly in the space between A, B and C so that the distance between particles D and E (=2*FH) is minimum.
(d) The maximum installation gap in the sample must be less than twice the distance between the points F and H. if it is more than two times FH it will form a bond between the particles D and E. this will produce an invalid micro structure.

(e) The distance FH can be calculated as AB=BD=AD=2Rmin (Figure 5.8c)

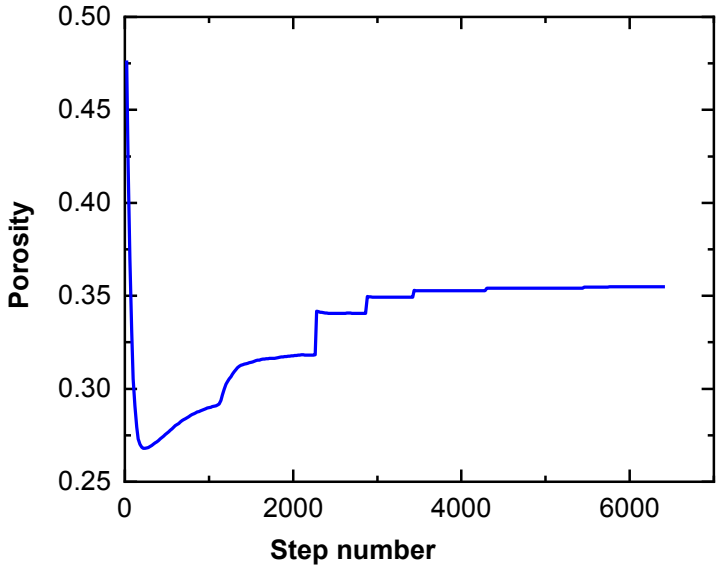

Figure 5.6: Change in porosity with time steps of numerical sample during material generation in PFC3D

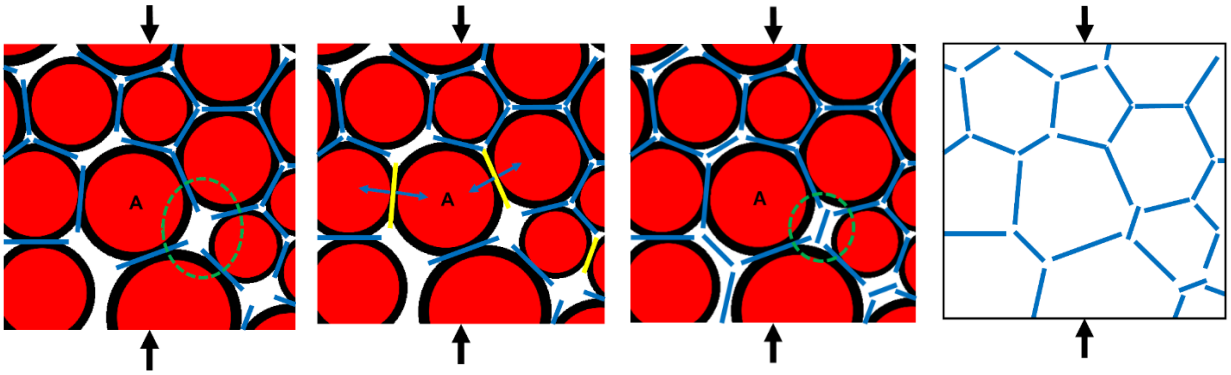

Figure 5.7: (a) Part of numerical sample showing particles (red circles), FJs (blue lines) and void shown in dotted line; (b) yellow lines representing tensile fracture near the voids; (c) FJ created in the model (inside dotted circle) even if the neighboring particles are not touching; and (d) a complex mineral grain structure produced with circular mineral grains. Note: the Figures are produced using the two dimensional code (PFC2D) for clarity.

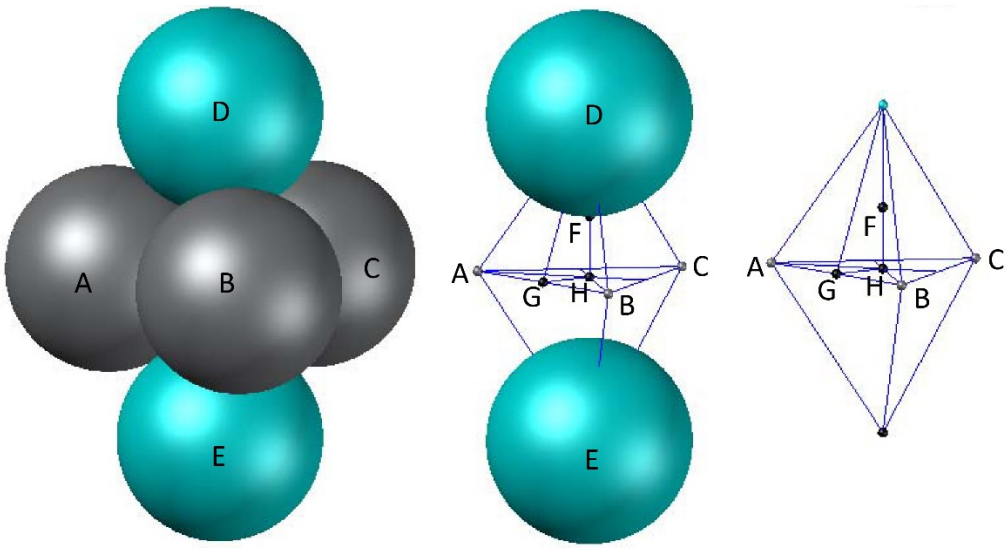

(a) (b) (c)

Figure 5.8: Showing steps for calculation of interaction range for PFC3D (a) five particles with minimum particle radius touching each other (except D and E), centers of the particles A, B, and C form an equilateral triangle; (b) minimum possible gap between particles D and E (c) maximum permissible gap must be less than two times FH

$$DG = \sqrt{BD^2 - BG^2} \tag{5-3}$$

$$\Rightarrow DG = \sqrt{BD^2 - (AB/2)^2}$$

$$\Rightarrow DG = \sqrt{(2 \times R_{min})^2 - (2 \times R_{min}/2)^2}$$

$$\Rightarrow DG = \sqrt{3} R_{min} \tag{5-4}$$

$$GH = \frac{1}{3} CG = \frac{2}{3} R_{min} \tag{5-5}$$

$$DH = \sqrt{DG^2 - GH^2}$$

$$\Rightarrow DH = \sqrt{3 \times {R_{min}}^2 - \frac{4}{9} {R_{min}}^2}$$

$$\Rightarrow DH = \frac{\sqrt{23}}{3} R_{min} \tag{5-6}$$

$$FH = DH - DF$$

$$\Rightarrow FH = \frac{\sqrt{23}}{3} R_{min} - R_{min}$$

$$\Rightarrow FH \sim 0.6 \times R_{min} \quad (5\text{-}7)$$

Hence, the installation gap was varied from zero to 2*FH ($1.2 \times R_{min}$) providing better agreement with the stress-strain response.

5.4.9 *FJ tensile strength and cohesion*

The macro tensile strength of the numerical sample is directly proportional to the micro tensile strength of the FJs. So, the micro tensile strength of the FJ can be assumed as the tensile strength of the rock (10.6 MPa, Table 5-5) and then gradually adjusted to match the peak tensile strength.

The FJ cohesion impacts the crack damage stress and the peak strength in an UCS and triaxial tests. For a particular value of friction angle the FJ cohesion is calibrated by matching the crack damage and the peak strengths. Figure C.15 shows the relation between the friction and cohesion to produce same value of UCS.

5.5 Steps for calibration

A micro parameter can have a minor or major impact on the macro response of the numerical model. A parametric study was carried out for all the micro parameters listed in

Table 5-1. The results, i.e. the macro parameters obtained by changing the micro parameters were then examined. For example the micro cohesion (fjm_coh) as shown in Figure 5.9 has a major impact on the UCS and crack damage stress; minor impact on crack initiation stress; but negligible impact on Young's modulus, Poisson's ratio and direct tensile strength. The result of the parametric study is summarized in Table 5-2 and Table 5-3 below. Steps to follow for an efficient

and logical calibration are given in Figure 5.10. These steps were used to calibrate the Lac du Bonnet granite properties obtained in the laboratory.

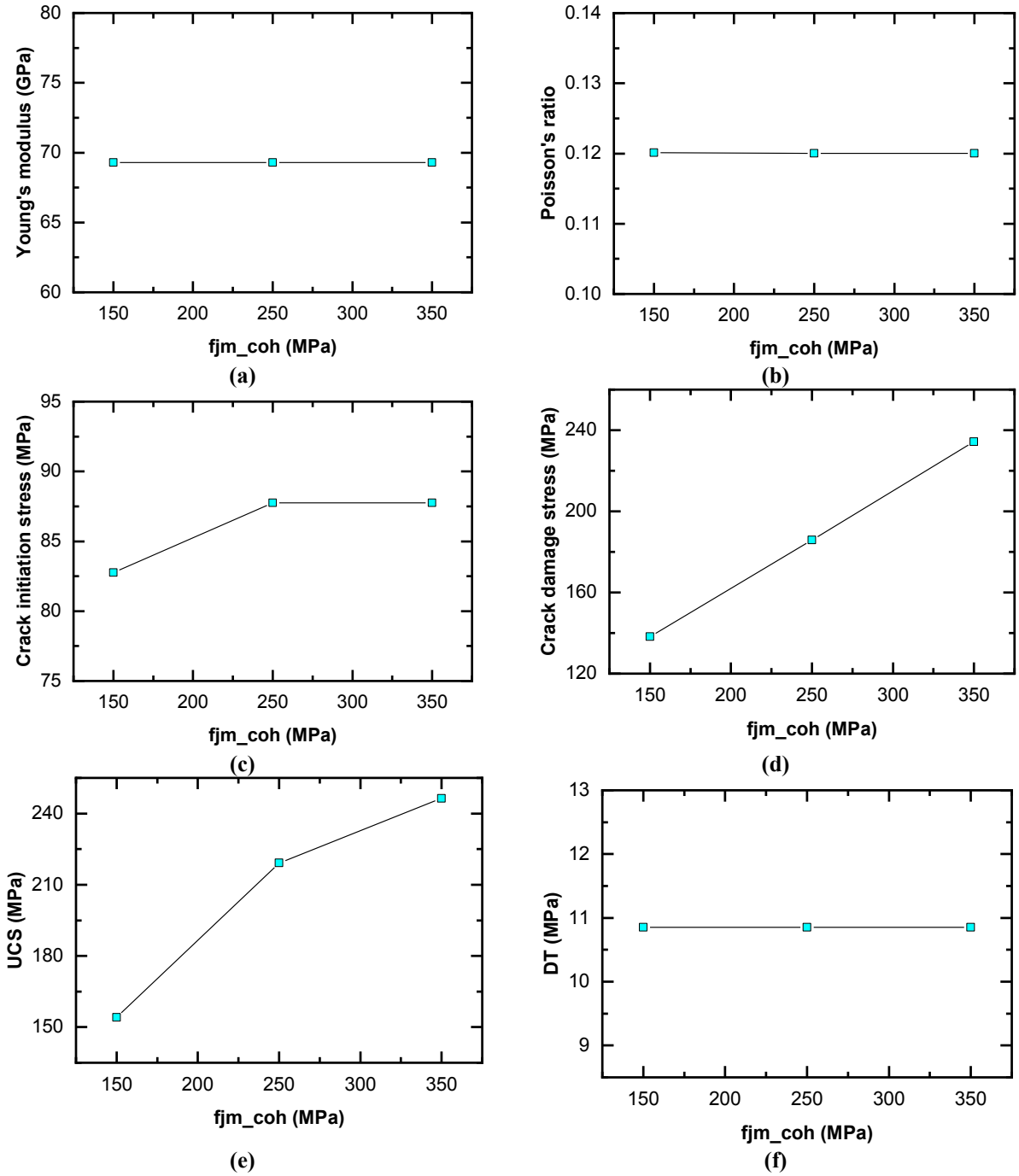

Figure 5.9: Results of calibration in PFC3D: effect of the change in Flat-Joint cohesion on macro parameters (a) on Young's modulus (b) Poisson's ratio (c) crack initiation stress (d) crack damage stress (e) UCS and (f) direct tension

Table 5-2: Results of calibration in PFC3D: summary of parametric study on micro parameters. The parameters are defined in (Potyondy 2017).

	Micro Parameters	Impact on macro parameters
1.	Krat Ball	Minimal impact on all
2.	Ball E	Minimal impact on all
3.	E of FJ	The modulus of material increase almost linearly with increase in modulus of FJ.
4.	FJ Krat	All values except ν decrease with increase in FJ modulus ratio. ν increases with increase in FJ Krat.
5.	FJ radius-multiplier	All values decrease with decrease in λ.
6.	Ball friction angle	Impacts the post peak response in UCS and triaxial
7.	FJ Cohesion	σ_t, σ_{ci}, E, ν remain constant. UCS and σ_{cd} increase. σ_1 increases.
8.	FJ Friction co-eff	UCS, σ_{ci}, E, ν and σ_t remain constant. Only σ_1 increases.
9.	FJ Tensile strength	σ_t, σ_{ci} and UCS increase while ν decreases. E increases slightly.
10.	FJ Friction angle	σ_1 increases with increase in friction angle. There is a slight increase in UCS.
11.	Insitu stress	Minimal impact on all
12.	Nr and Na	Minimal impact on all

* σ_1= peak strength in triaxial test

Table 5-3: Results of calibration in PFC3D: Effect of micro parameters on macro parameters

	Macro Parameters	Affected By
1.	UCS	FJ Krat(-), FJ Coh(+), FJ Fri Ang (+)
2.	σ_{CI}	FJ Krat(-), FJ Ten Str (+)
3.	σ_{CD}	FJ Krat(-), FJ coh, FJ fric
4.	E	E FJ (+), FJ Krat (-)
5.	ν	FJ Krat (+), FJ Ten Str (-), FJ Coh (+)
6.	σ_t	FJ Krat (-), FJ Ten Str (+)
7.	σ_1	FJ Coh (+), FJ Fri Ang (+), FJ Fr Co (+)

* + increases, - decreases

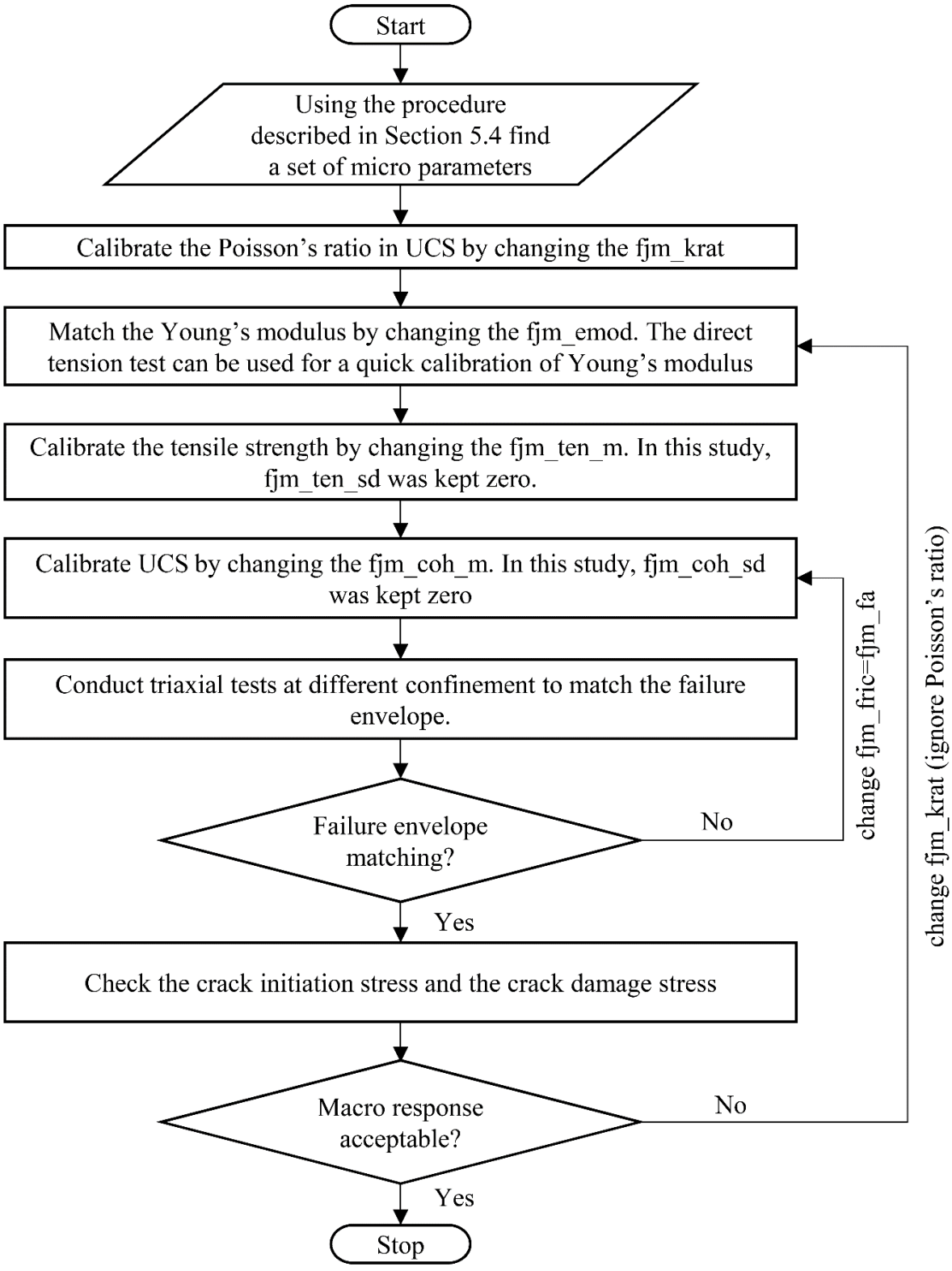

Figure 5.10: Results of calibration in PFC3D: Steps for calibrating laboratory results: UCS, direct tensile test and triaxial test (Note: Additional steps were taken to capture initial non-linearity in UCS test and bi-modularity)

5.6 Obtaining the macro parameters from the numerical tests

The PFC3D uses two schemes to obtain the stresses and strains in a numerical sample: (1) wall based and (2) measurement based (Potyondy 2017). In a wall based measurement when using a wall as a loading platen in an UCS test it calculates the total force applied by the particles touching the wall and divides it by the total area of the wall. Similarly, the strain is calculated from the change in distance between two walls and the initial distance. When using the measurement based approach, PFC considers a measurement sphere (with a given center and radius) inside the numerical sample. PFC than calculates the strain and stress from the contact forces between the grains and FJs in different directions within the sphere. A small difference (around 10% in UCS) was found between the two measurement schemes which is due to the fact that the wall based measurement calculates the stress on the surface while the measurement sphere is inside the sample. The stress and strain values in a numerical sample can be obtained by both techniques in an UCS test while it can be only obtained from the measurement sphere in a direct tension test. So, for uniformity the measurement sphere technique was chosen for calibrating all parameters.

5.6.1 *Elastic parameters*

As described in Section 5.2.1, the stress-strain curve in an UCS test has 5 distinct stages. The elastic parameters (Young's modulus and Poisson's ratio) of the numerical sample must be obtained when the material behaves elastically, i.e., between the crack-closure stress and the crack-initiation stress. The stress-strain plot in direct tension does not show these 5 distinct stages nor the non-linear crack closure stage. Hence, the Young's modulus in tension was obtained over the linear region at approximately 50% of the peak strength.

5.6.2 *Crack initiation and crack damage stress in compression*

Similar to the elliptical micro flaw in a brittle material considered by Griffith (Griffith 1921), the PFC3D model contains voids between the mineral grains as shown in Figure 5.7a. At the tip of these voids, tensile stress concentration occurs with the application of an external compressive stress. Tensile crack occurs in these critical locations when the tensile stress exceeds the tensile strength of the bonds. Griffith theory on compressive failure of brittle material suggests that the tensile cracks at rupture should form at a compressive stress magnitude of eight times the tensile strength of the material (Griflith, 1924). However, it is highly unlikely that in a heterogeneous material with complex mineral grains like rock, the tensile stress around the void/flaw will be uniform throughout the heterogeneous sample at a particular value of compressive stress. It is likely that at a few void tips the critical tensile stress occurs much earlier than the theory proposed by Griffith. Figure 5.26 shows the number of cracks generated in the PFC sample with increase in the axial load. The first crack forms in the sample at an axial load of about 30 MPa. However this cannot be defined as the crack initiation stress in the material. Martin (1993), argued that the best approach to obtain the crack initiation stress in a rock with a high amount of initial micro fracture, is from the plot between the crack volumetric strain versus the axial strain plot. The crack volumetric strain is obtained by subtracting the elastic volumetric strain in the sample (Equation (5-9) from the total volumetric strain (5-8).

Total volumetric strain=

$$\frac{\Delta V}{V_{total}} = \varepsilon_a + 2 \times \varepsilon_r \tag{5-8}$$

Elastic volumetric strain for a uniaxial test=

$$\frac{\Delta V}{V_{elastic}} = \frac{1-2\nu}{E}(\sigma_1) \quad (5\text{-}9)$$

The crack initiation stress is then defined as the point where the crack volumetric strain versus the axial strain plot changes its direction after crack closure stress.

Different methods to determine the crack initiation stress from the stress-strain curve of an UCS test were reviewed by Nicksiar and Martin (2013). They concluded that statistically all methods reviewed gave similar results. In this study the crack volumetric strain method (Martin and Chandler 1994) was used to obtain the crack initiation stress.

The crack damage stress is the stress where the volumetric strain reversal (Martin 1993) occurs in an UCS test. A volumetric strain versus the axial strain for a numerical sample is shown in Figure 5.22.

5.7 Capturing the initial non-linear stress-strain response in a UCS test

Most rocks tested in uniaxial compression show an initial non-linear response between the axial stress and axial strain (Martin 1993). This is mainly due to the stress released micro fracture generated during the coring process. Figure 5.11 shows the axial stress-strain curves for two Lac du Bonnet granite samples cored from two depths from an underground research laboratory in southern Manitoba, Canada (240m depth and 420m depth). When the sample is taken from a greater depth, i.e., at higher in situ stress magnitudes, the micro fractures present in the sample increases. The increase in the volume of stress-released micro cracks increased the non-linearity in the stress-strain response, decreased the UCS from 221.7 MPa to 161.6 MPa and decreased the Young's modulus from 70.5 GPa to 62 GPa. This change in stress-strain response and properties caused by increasing the micro crack volume is examined in this study.

With the application of axial load during an UCS test the gaps between the fractured grains gradually close and the grains again come into contact. This increases the Young's modulus of the material gradually producing non-linearity. To capture this behavior in FJ bonded particle model, the following procedure was adopted:

(a) As shown in Figure 5.12a straight line AB was drawn along the straight part of the stress-strain curve.

(b) The point at which the line AB meets the horizontal axis is the gapped strain (ε_g) in the sample due to the micro crack closure.

(c) In the numerical sample, ε_g is a function of (i) the percentage of micro fractures present (p), (ii) the initial gap (iii) length of the specimen and (iv) average number of particles along the length of the specimen. The gap can be calculated using the follow equations:

$$\varepsilon_g = \frac{\Delta L_g}{L} \tag{5-10}$$

$$\Rightarrow \Delta L_g = \varepsilon_g L$$

Where,

ΔL_g=change in length of the sample due to gap closure

Also, ΔL_g can be written as:

ΔL_g

$=$ gap between the two interfaces of a FJ

$\times$ average number particle along the length of sample having gap

(see Figure 5.12b, the FJ with gap are marked in red)

$$\Rightarrow \Delta L_g = G \times \left((n-1) \times p/100\right) \tag{5-11}$$

Where,

G= gap between the two interfaces of a FJ,

n=average number of particles along the length of the sample,

p= percentage of micro fractures in the sample. Note: if there are n particles along the length of samples, there are n-1 FJs (see Figure 5.12b)

So, the gap G can be found from

$$G = \frac{\varepsilon_g L}{(n-1) \times (p/100)} \tag{5-12}$$

From the Equation (5-12), the micro fracture gap can be calculated. This gap can be taken as an initial value and gradually increased or decreased to match the non-linear part of the stress-strain curve in UCS.

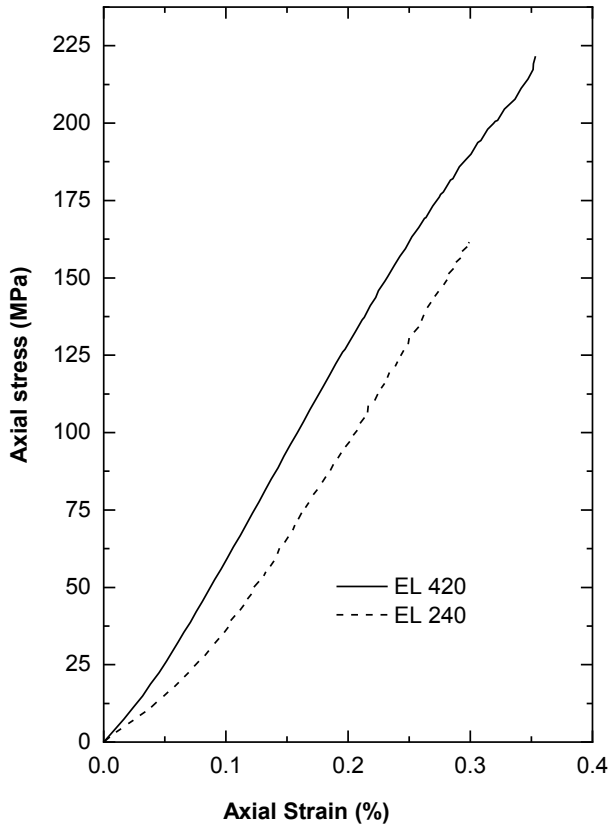

Figure 5.11: Laboratory stress-strain curve obtained from UCS test for Lac du Bonnet granite samples taken from two stress levels, EL 240 and EL 420 (Martin 1993)

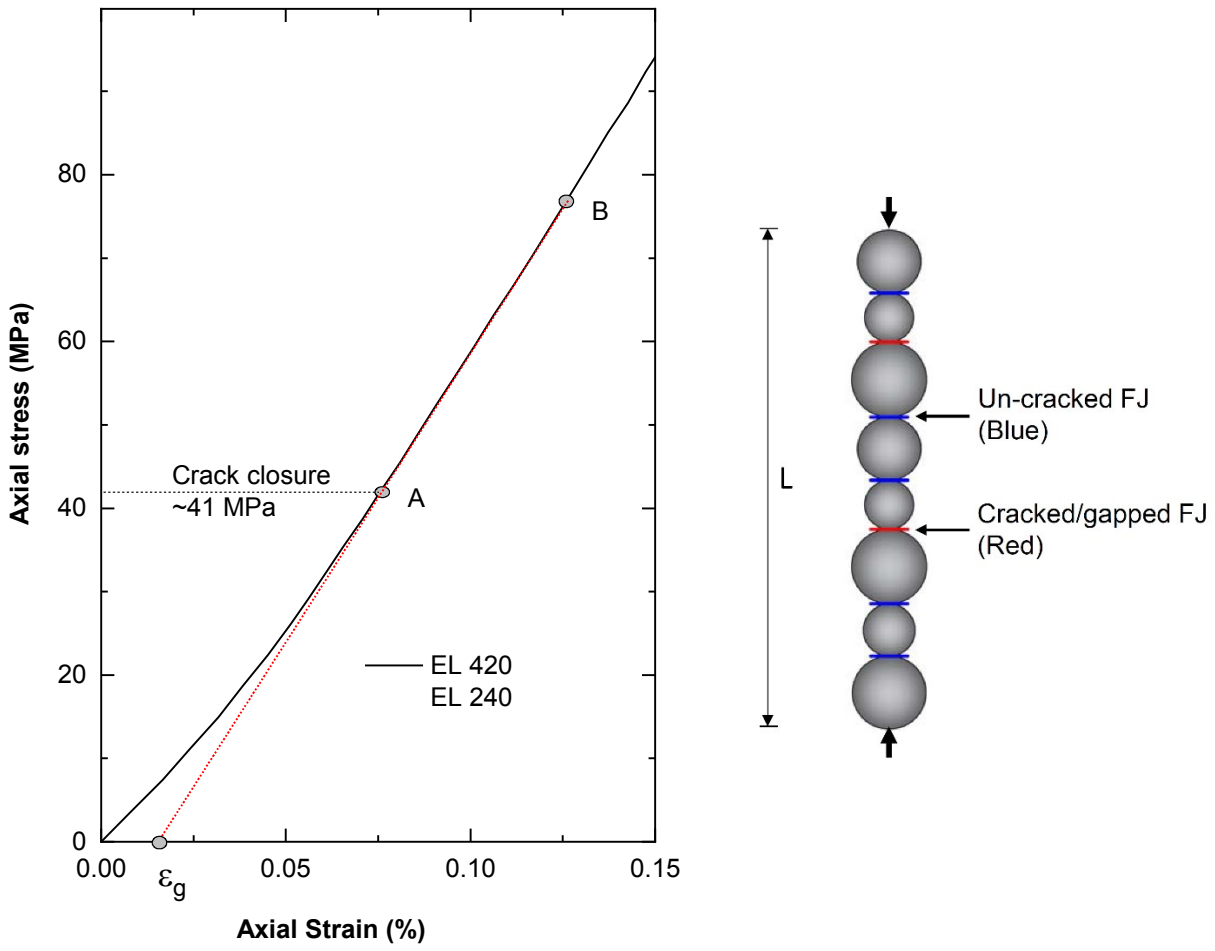

(a) **(b)**

Figure 5.12: (a) Gap induced strain (ε_g) used to calibrate the non-linear stress-strain response observe during UCS test for Lac du Bonnet granite sample (line AB is extended from the linear part of stress-strain curve) (b) spherical particle representing the grains and FJs by lines (blue is un-fractured and red is fractured) in PFC3D sample. The gap between the fractured (red) FJs will close when axial compressive load is applied to the sample. For clarity few grains are shown along the length of the sample.

5.8 Capturing the bi-modularity of rock

Rock when tested in compression and tension shows different Young's modulus and Poisson's ratio (bi-modularity). Patel and Martin (2018c) compiled the values of tensile Young's modulus (E_t) and compressive Young's modulus (E_c) for different rock types found in the literature. The mean and standard deviation of the ratio between E_t and E_c is shown in Figure 5.13. As can be observed from Figure 5.13, the E_t is always less than 1.0 (mean varies from 0.27 to 0.72). This is true irrespective of the grain size. However, for the fine grained rock the ratio is close to one. For Lac du Bonnet granite the ratio of E_t/E_c value is 0.65.

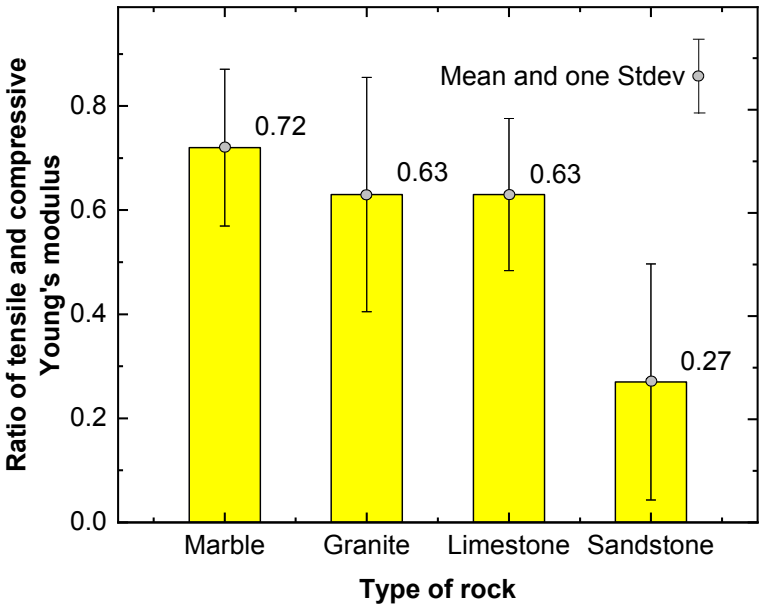

Figure 5.13: Ratio of tensile (E_t) and compressive (E_c) Young's modulus of some rocks from the literature (Patel and Martin 2018c)

The FJ bonded particle model was used to investigate the bi-modularity observed in Lac du Bonnet granite. The micro parameters of the model were obtained from the calibration of macro parameters from the laboratory tests. The stress-strain plot obtained from the UCS test and direct tension test for the numerical sample and the comparison with laboratory results is shown in Figure 5.14. For the UCS test in PFC3D, we found a good agreement with the modulus of the laboratory

data while the slope of the stress-strain plot in direct tension test from laboratory tests has a lower value than the PFC3D sample. The macro parameters obtained from PFC3D are compared with the laboratory results in Table 5-4. The strength values and the Ec was found to be within 3% of the lab results. While the PFC3D did not show any bi-modularity (Et/Ec~1.0). The impact of micro properties on bi-modularity is examined in the next section. The micro rock parameters examined are: (a) the grain size (fine versus coarse) (b) the grain size distribution (heterogeneous versus uniform) and (c) micro fractures present in the rocks.

Table 5-4: Comparison of macro properties obtained from Laboratory testing and PFC3D (using the micro properties from Table C-8)

	σ_t (MPa)	UCS (MPa)	E_c (GPa)	E_t (GPa)	E_t/E_c
Lab	10.6	224.4	70.5	45.8	0.65
PFC3D	10.6	226.2	72.4	71.7	0.99

5.8.1 *Grain size*

The increase in rock strength with the decrease in grain size was reported by Brace (1961) and Fredrich et al. (1990). As shown in Table 5-4, the ratio Et/Ec is close to 1.0. So, keeping all other the micro parameters in the previous case the same, the average number of particles along the diameter was increased from 15 to 25 decreasing the particle size. The results of the study are shown in Figure 5.15. This increased the UCS value by 9.8% but the change in tensile strength is less than 1%. No change in the ratio Et/Ec was observed.

5.8.2 *Grain size distribution*

The Grain Based Modelling by Lan, Martin, and Hu (2010) showed that grain size heterogeneity has the highest impact on the strength parameters. Figure 5.16 compares the result with maximum to minimum particle radius (R_{max}/R_{min}) of 2.3 with R_{max}/R_{min}=1.0. With the decrease in the R_{max}/R_{min} value (material becoming more uniform) the strength of the material increases. As the

grain size distribution changes from heterogeneous to uniform, the UCS of the rock is increased by 107.6% and the tensile strength by 39.6%. The Ec value for uniform particles was found to be 103.4 GPa while for the rock with R_{max}/R_{min}=2.3 it was 72.4 GPa. However, for both the cases the E_t/E_c value is close to 1.0 suggesting grain size distribution has also no impact on the bi-modularity.

5.8.3 *Micro fracturing*

The model shown in Figure 5.3 has 19511 FJ contacts (58533 FJ elements). Micro fractures were inserted in the model by assigning 10 percent of the FJ as broken, i.e., the FJ contacts are touching but have no tensile strength. The micro fracture percentage was then increased using increments of 5%. With the increase in micro fracture percentage, we found out that the E_t value gradually decreases. Also, the UCS and the tensile strength value of the rock are reduced. The only parameter not significantly impacted is the E_c. The results for 0% micro fracture are compared with 35% micro fractures in Figure 5.17. With the increase in micro fractures the UCS decreased from 226.2 MPa to 182 MPa while the tensile strength decreased from 10.6 MPa to 6.4 MPa. The ratio Et/Ec was found to decrease from 1.0 to 0.65 which is the Et/Ec value observed in the laboratory. In compression some of the fractures are closed and these closed fractures do not significantly reduce the value of E_c. However, in tension the fractures have no contact stiffness which reduces the value of E_t.

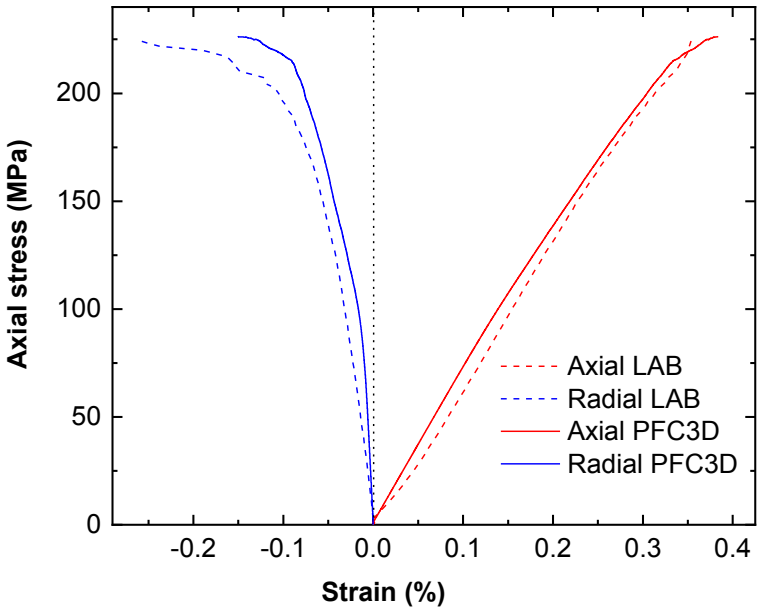

(a)

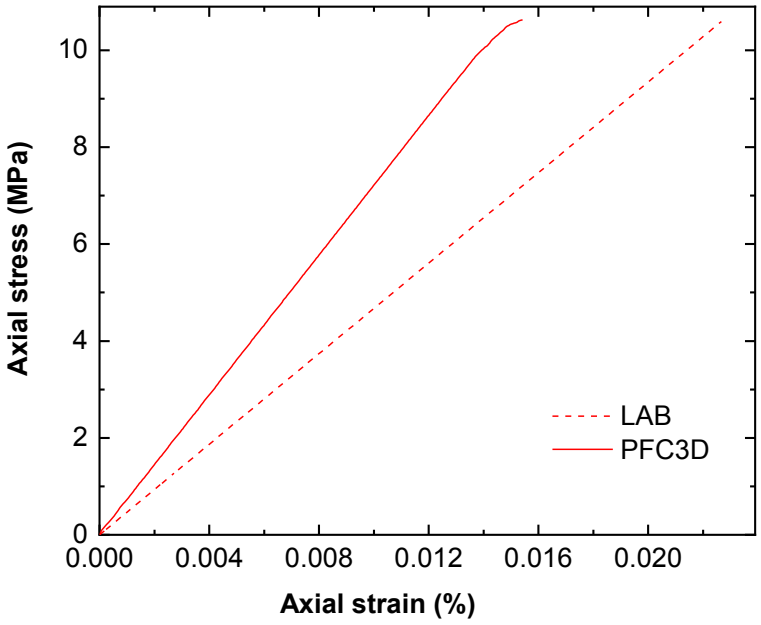

(b)

Figure 5.14: Comparison of Laboratory and PFC3D results (a) UCS (b) direct tension test. Note in direct tension the axial stress and strain are in tension.

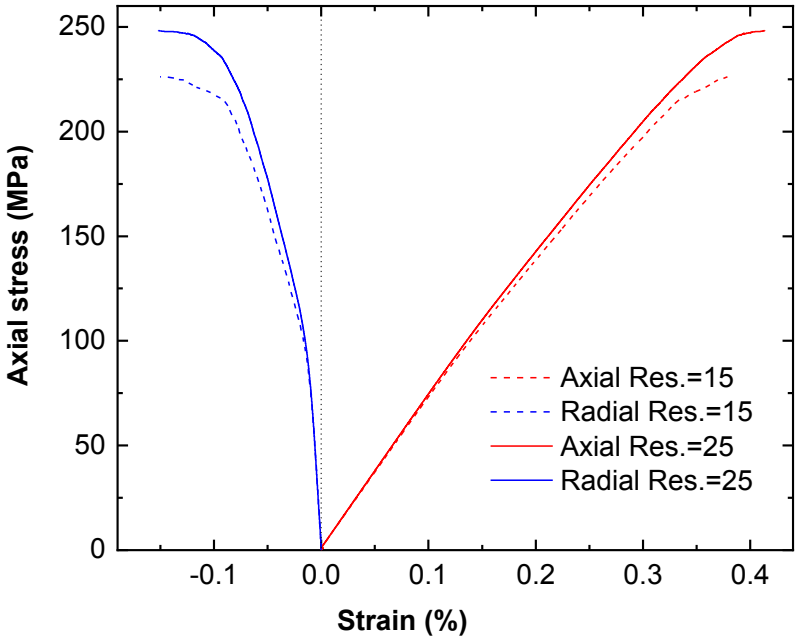

(a)

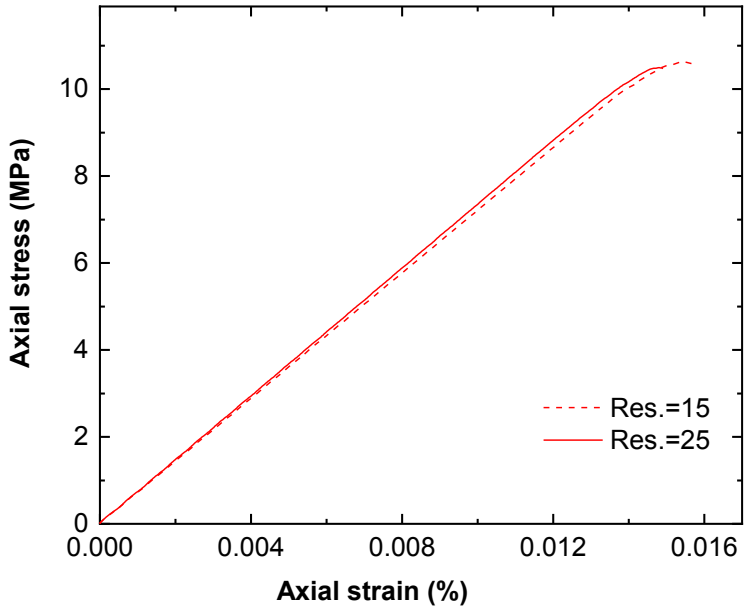

(b)

Figure 5.15: PFC3D results showing the impact of particle resolution (a) UCS test (b) direct tension test. Res. (resolution) = average number of particles along the diameter.

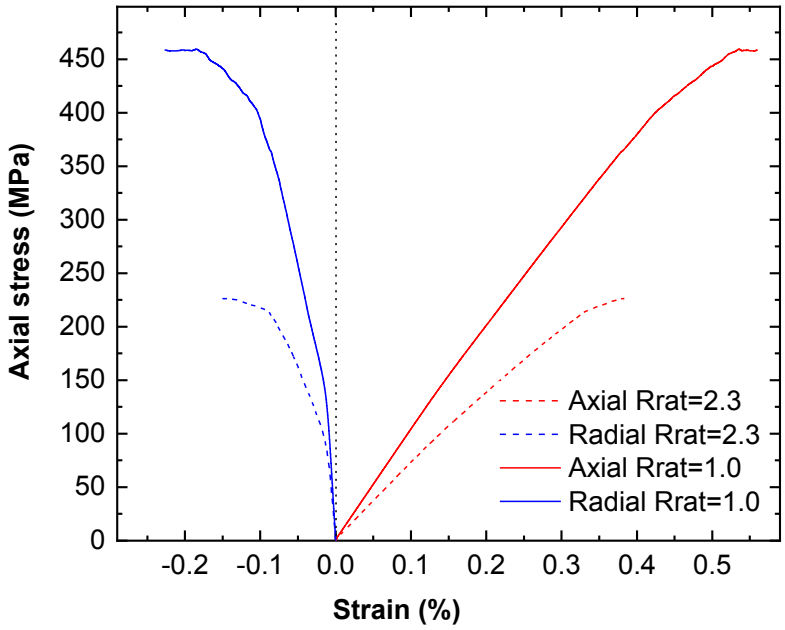

(a)

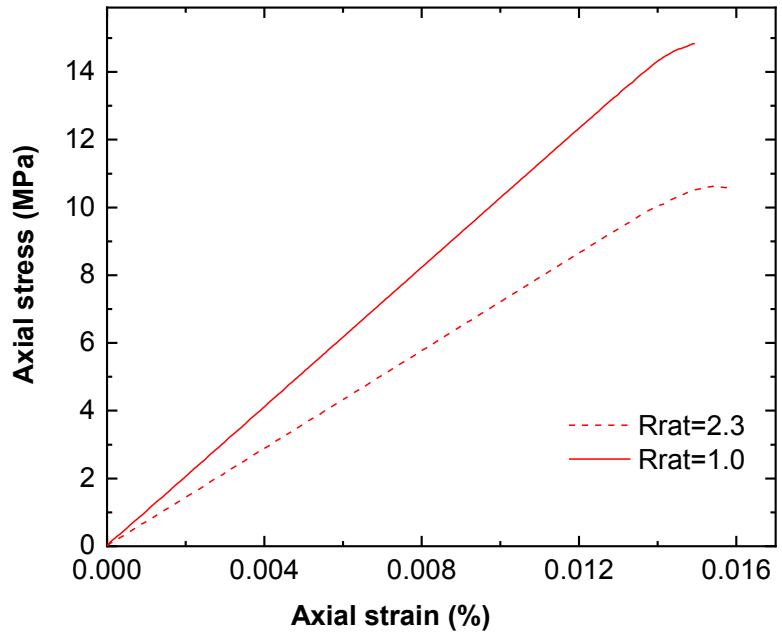

(b)

Figure 5.16: PFC3D results showing the impact of grain size distribution (a) UCS test (b) direct tension test. Rrat=ratio of maximum to minimum particle radius. Note in direct tension the axial stress and strain are in tension.

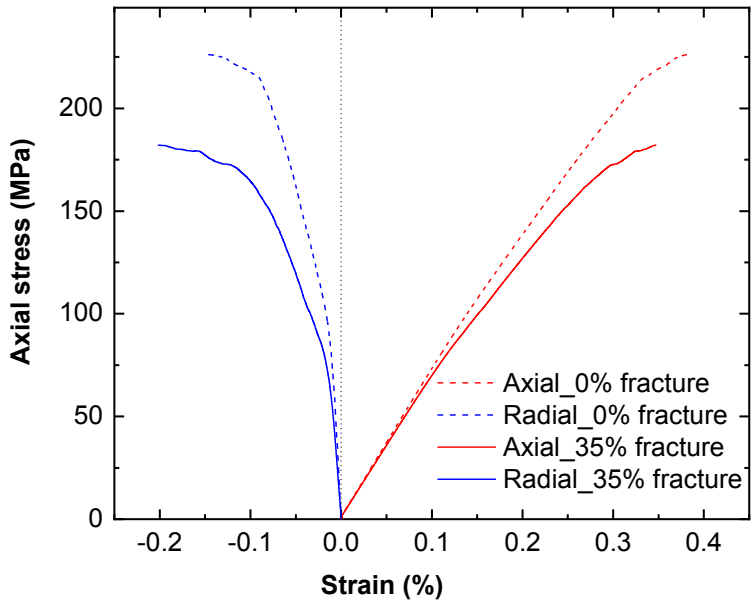

(a)

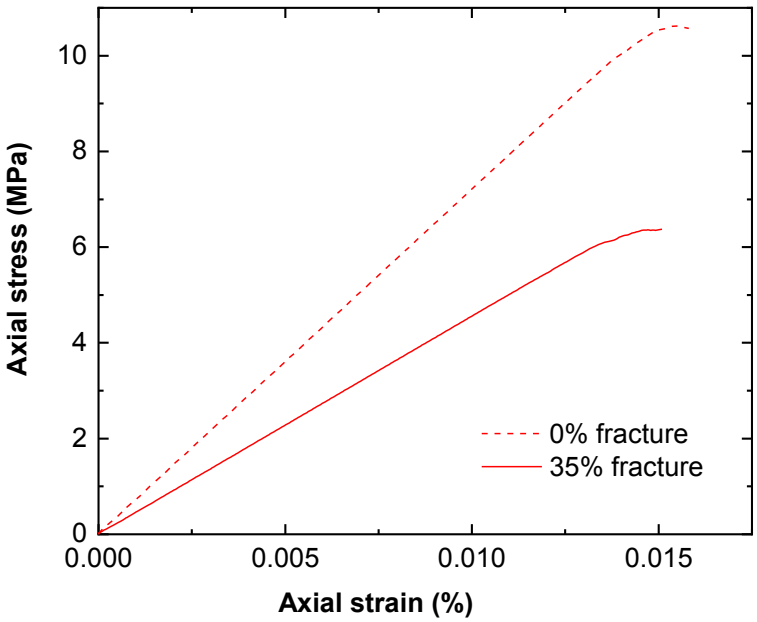

(b)

Figure 5.17: PFC3D results showing the influence of micro fractures in the rock (a) UCS test (b) direct tension test. Note in direct tension the axial stress and strain are in tension.

5.9 Impact of bi-modularity on crack initiation stress

Researcher have identified that the crack initiation in low porosity crystalline rock is a common phenomenon occurring between 40% and 50% of the UCS (Brace et al., 1966; Martin and Chandler, 1994, Nicksiar and Martin 2013). However, when no micro fractures were used in the model, the crack initiation was found to be only 29% of UCS, although the model is calibrated to both the direct tensile strength and UCS.

To examine the impact of micro-fractures present in the rock, the model discussed in previous section (35% micro fracture) was re-calibrated to the UCS and the tensile strength. Figure 5.18a compares the radial strain versus axial stress/UCS and Figure 5.18b compares the crack formation with the increase in axial stress/UCS ratio for no micros fracture and 35% micro fractures. Because of the lower value of E_t the model with bi-modularity (35% fracture) can accomodate more lateral extension between the mineral grains and delay the crack initiation. Hence, the crack initiation stress is increased from 29% to 40% of the UCS.

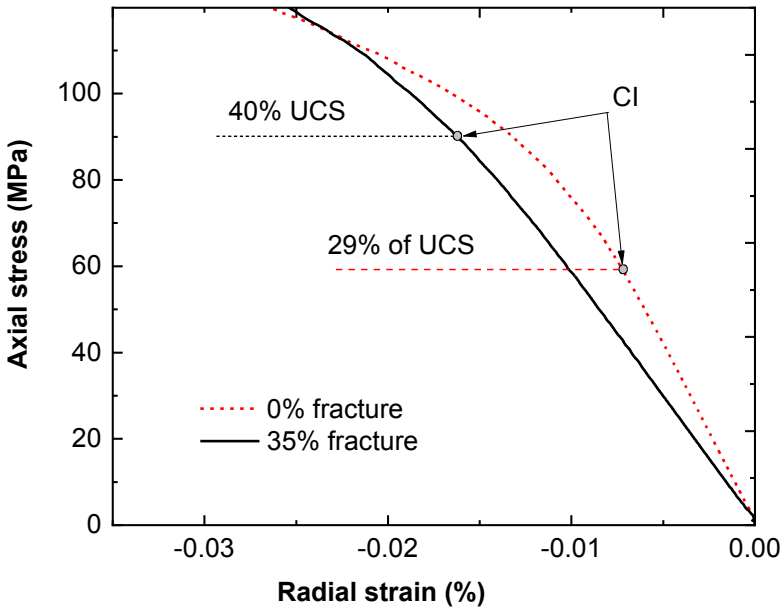

(a)

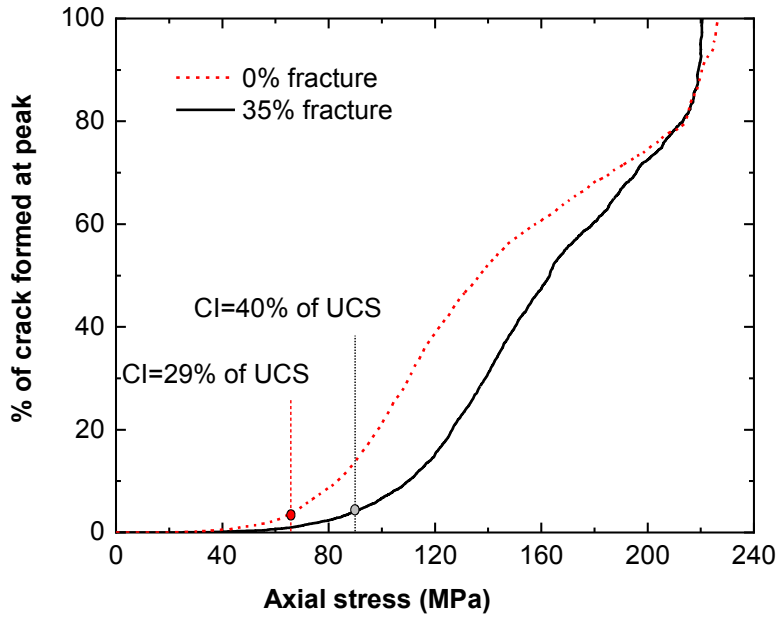

(b)

Figure 5.18: PFC3D results showing the impact of bi-modularity on crack initiation stress (a) change in radial strain with increase in axial stress (note, stress-strain curve shown up to 120 MPa for clarity) (b) cracks formed with increase in axial stress in percentage. Both models were calibrated to same value of tensile strength (10.6 MPa) and UCS (~220 MPa).

5.10 Compressive and tensile failure in FJ bonded particle model

The micro parameters of the model were obtained from the calibration of macro parameters from the laboratory tests. This was done using an iterative procedure. The final set of micro parameters obtained which produced acceptable results are shown in

Table 5-1.

5.10.1 *Tensile failure*

The tensile test is simulated using the same numerical sample generated for the UCS test. The steps followed were: (a) the six walls as shown in Figure 5.3 are removed (b) the top and bottom particles of the sample whose center lies within the face and 5 mm into the sample are held together and (c) a constant strain is applied to the sample until fracture.

Figure 5.19 shows the stress-strain curve obtained for a PFC sample during the direct tensile test whereas Figure 5.20 shows the increase in fracturing with the axial load and the tensile fracture generated just before the peak respectively. Unlike the UCS test, the direct tension test does not show initial non linearity between the axial stress-strain curve. Because in direct tension test the micro fractures present in the sample do not close. The macro Young's modulus obtained (~46 GPa) was results from the particles in the sample which are not cracked. The peak strength obtained for the numerical sample was within 3% of the value obtained in the laboratory. As shown in Figure 5.20, the tensile cracking begins rapidly in the sample at around 85% of the peak load. As expected for a direct tensile test the tensile fractures are localized (in a plane).

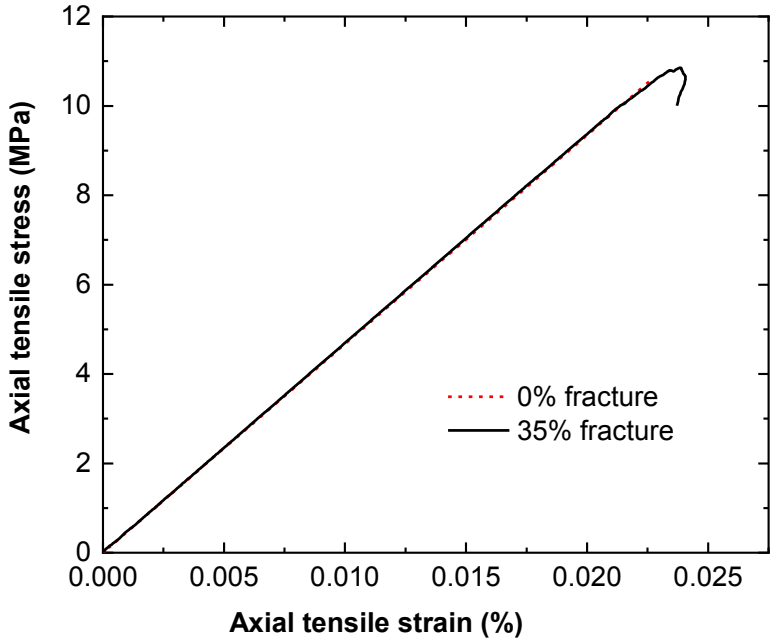

Figure 5.19: Stress-strain curve obtained for direct tensile test

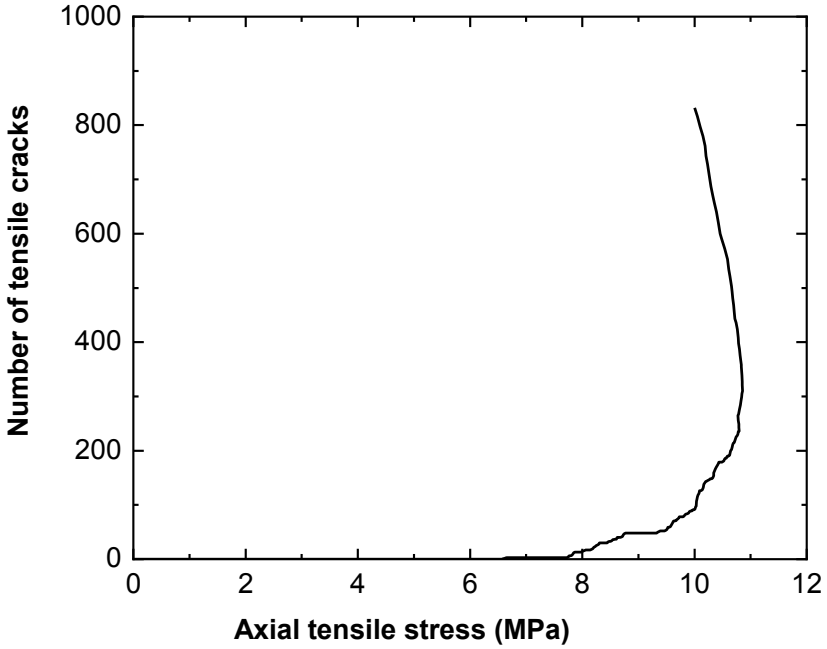

Figure 5.20: Fracture number versus the axial load (fracture generated just before the peak in a numerical sample). Note: for direct tensile test there are no shear fractures in the sample.

5.10.2 *Compressive failure*

The stress-strain plot obtained from the UCS test and direct tension test for the numerical sample and their comparison with laboratory results are shown in Figure 5.22. The macro parameters (Young's modulus in compression, Poisson's ratio in compression, crack initiation stress, crack damage stress, UCS, Young's modulus in tension, direct tensile strength) and the strain values at different stress levels are presented in Table 5-5. With the methodology described in the Section 5.7, it was possible to capture the non-linearity at the initial stage of stress-strain curve in the UCS. By incorporating the stress released micro fractures in the numerical model, the Et/Ec ratio achieved was within 4% of the laboratory value. The Young's modulus in compression, crack initiation stress, crack damage stress, UCS, Young's modulus in tension and direct tensile strength values obtained are within 2%, 1%, 14%, 1.2%, 2.1% and 2.5% of the values obtained in the laboratory respectively. Because of the high porosity (Figure 5.6) and the unavoidable voids in the numerical model (Figure 5.7) which do not allow the sample to expand freely in the lateral direction, the Poisson's ratio obtained was less (0.26 versus 0.12). However, the shape of the axial stress versus the axial strain curve (Figure 5.22) matches perfectly.

As shown in Table 5-5, the crack initiation stress (87.7 MPa) obtained for the PFC3D sample is close to the value of compressive strength suggested by Griffith 1924 (ten times the tensile strength=10*10.6). As shown in Figure 5.21a, all the cracks formed in the sample are random tensile cracks mostly formed at the void tips (Figure 5.7b). The number of cracks formed at the crack initiation stress was 4.4% of the total cracks formed at the peak stress. As the cracks formed in the sample are tensile cracks, the crack initiation stress cannot be captured in an axial strain versus axial stress plot i.e. the plot is linear until the crack damage stress. With increase in the axial

compressive load beyond the crack initiation stress, the random tensile cracks in the sample continue to grow.

Figure 5.21b shows the cracks formed in the sample at the crack damage stress. The total number of cracks formed in the sample at the crack damage stress was found to be 61.2% of the cracks formed at the peak. The cracks grew rapidly between the crack damage stress and the peak stress. As shown in Figure 5.21b, the shear cracks (green) start forming in the sample at the crack damage stress. Due to the shear crack formation the axial stress-strain curve deviates from linearity sharply. Peak stress is the point where enough tensile and shear micro cracks have formed in the sample and join to form macro surfaces such that the sample is unable to take additional load.

As shown in Figure 5.22, the total volumetric strain (Equation (5-8), compression positive), is increased with the increase in the axial load till the crack damage stress. The crack volumetric strain (Equation (5-9)) decreases with the increase in the axial stress (stress released micro crack close) till the crack closure stress. The sample then behaves elastically till the crack initiation stress. The crack volumetric strain increases rapidly after the crack initiation stress.

Figure 5.23 shows the axial stress-strain plots obtained for the samples with increase in confinement (2 MPa, 4 MPa, 6 MPa, 8 MPa and 10 MPa). The macro properties obtained for the triaxial tests are compared in Table 5-6. With increase in confinement, the crack initiation stress and the crack damage stress in the numerical sample increased. The values of the crack damage stresses for the numerical sample were found to be more than the corresponding values in the laboratory tests. As shown in Figure 5.23, the numerical sample showed a strain hardening behavior after a confining stress of 8 MPa. The PFC3D showed an early strain hardening behavior because it uses a rigid wall for application of confinement. A flexible boundary technique as suggested by Patel and Martin (2015) must be used to study the triaxial test at higher confinement.

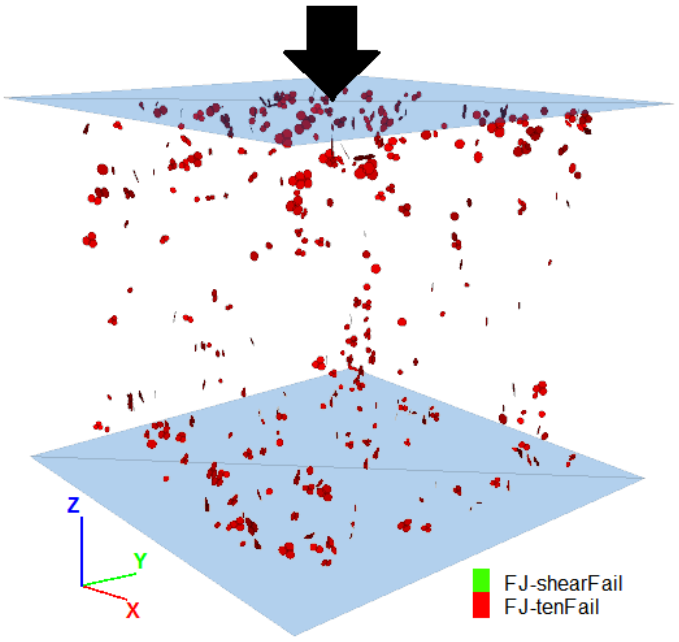

(a)

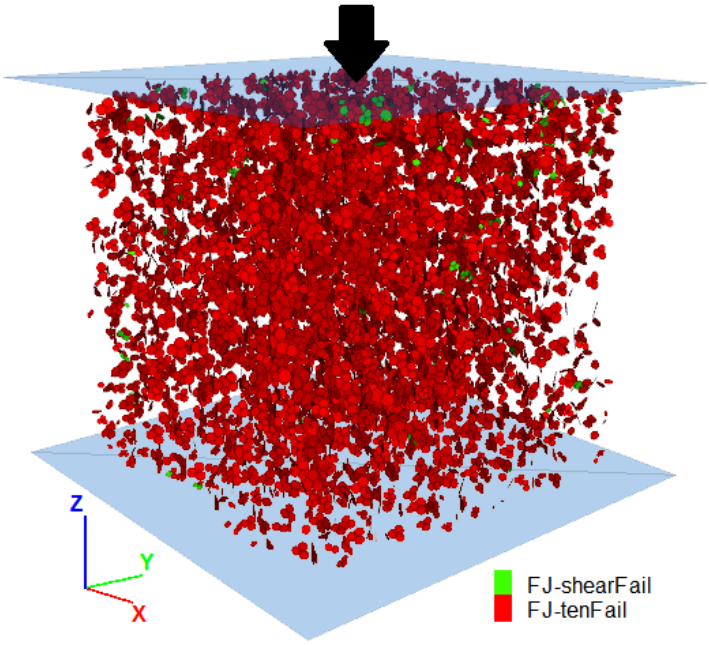

(b)

Figure 5.21: Tensile and shear crack formed in the numerical sample at (a) crack initiation stress (number of cracks= 4.4% of total number of cracks recorded at peak) (b) crack damage stress (number of cracks= 61.2% of total number of cracks recorded at peak)

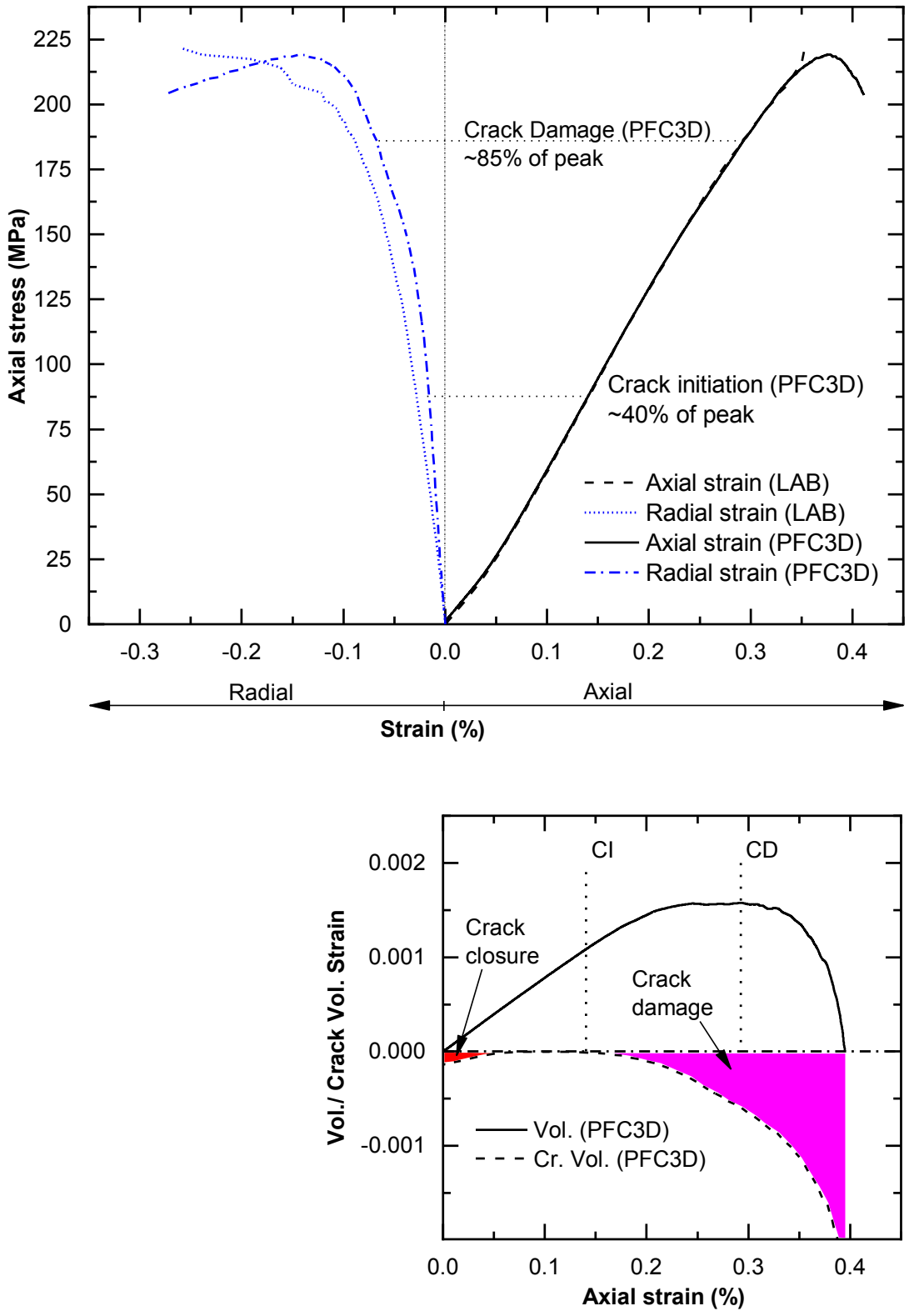

Figure 5.22: Comparison of stress-strain plot obtained for numerical sample of Lac du Bonnet granite with a laboratory sample in UCS test.

Table 5-5: Comparison of direct tension and UCS test results obtained from laboratory and PFC3D tests on Lac du Bonnet granite

Case	UCS test										Direct tension			Et/Ec
	Ec (GPa)	ν_c	Crack initiation stress			Crack damage stress			Peak		Et (GPa)	Peak		
			σ_{CI} (MPa)	ε_{axial} (%)	ε_{radial} (%)	σ_{CD} (MPa)	ε_{axial} (%)	ε_{radial} (%)	σ_{UCS} (MPa)	ε_{axial} (%)		σ_t (MPa)	ε_{axial} (%)	
LAB	69.6	0.24	88.6	0.143	-0.028	163.3	0.252	-0.066	221.7	0.353	45.2	10.6	-	0.65
PFC3D	69.3	0.12	87.7	0.140	-0.016	185.9	0.293	-0.067	219.1	0.377	46.8	10.9	0.024	0.68

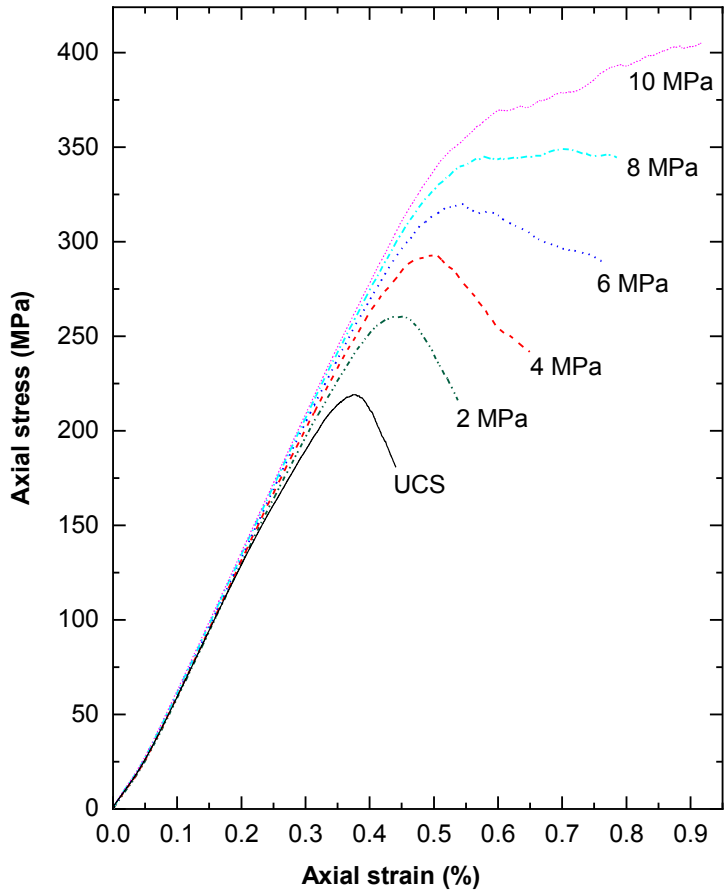

Figure 5.23: Stress-strain plot obtained from PFC3D numerical sample of Lac du Bonnet granite tested in triaxial confinement

Table 5-6: Results of triaxial tests on numerical Lac du Bonnet granite sample

Case		E_c (GPa)	ν_c	Crack Initiation			Crack Damage			Peak	
				σ_{CI} (MPa)	ε_{axial} (%)	ε_{radial} (%)	σ_{CD} (MPa)	ε_{axial} (%)	ε_{radial} (%)	σ_{UCS} (MPa)	ε_{axial} (%)
Triaxial (2MPa)	LAB	70.1	0.31	121.0	0.17	-0.04	157.0	0.22	-0.07	255.0	0.37
	PFC3D	69.3	0.12	110.4	0.17	-0.02	227.0	0.35	-0.07	260.5	0.44
Triaxial (4MPa)	LAB	67.7	0.39	136.0	0.20	-0.06	159.0	0.23	-0.08	298.0	0.45
	PFC3D	70.8	0.12	121.7	0.18	-0.02	263.9	0.39	-0.08	293.0	0.50
Triaxial (6MPa)	LAB	68.9	0.30	168.0	0.23	-0.06	219.0	0.31	-0.09	344.0	0.56
	PFC3D	71.5	0.12	145.7	0.21	-0.02	286.5	0.42	-0.08	320.1	0.53
Triaxial (8MPa)	LAB	75.2	0.36	165.0	0.20	-0.06	199.0	0.25	-0.08	368.0	0.52
	PFC3D	69.3	0.12	153.0	0.21	-0.02	308.6	0.44	-0.08	349.4	0.69
Triaxial (10MPa)	LAB	70.3	0.27	197.0	0.26	-0.06	264.0	0.36	-0.10	391.0	0.61
	PFC3D	72.7	0.12	150.3	0.20	-0.02	330.4	0.47	-0.08	-	0.90

5.11 Parametric PFC3D study

After the PFC3D model was calibrated and a set of parameters obtained which produces a reasonable direct tensile; UCS; and triaxial test results, the influence of major PFC3D input assumptions and parameters were studied. The results of the study is presented below.

5.11.1 *Cylindrical versus prismatic sample*

To apply three major principal stresses with different magnitudes in the X-, Y- and Z-directions to a numerical sample a cubical/rectangular prismatic sample is required. However, the sample generally tested in the laboratory for UCS and triaxial test are cylindrical samples. So, analysis was carried out for cylindrical samples keeping all the micro parameters (

Table 5-1) the same. The results of the UCS and direct tension test are presented in Table 5-8 and Figure C.16. It was found out that even the grain arrangement changes (with random particle generation in two samples), the macro parameters obtained are within 10%.

Table 5-7: Comparison of macro parameters obtained from the direct tension test and the UCS test for rectangular and cylindrical samples (micro parameters for both samples are the same,

Table 5-1)

Case	Ec (GPa)	ν_c	σ_{CI} (MPa)	σ_{CD} (MPa)	σ_{UCS} (MPa)	Et (GPa)	σ_t (MPa)	Et/Ec
LAB	70.5	0.26	88.6	163.3	221.7	45.8	10.6	0.65
Rectangular	69.3	0.12	87.7	185.9	219.1	46.8	10.9	0.68
Cylindrical	67.4	0.13	89.7	179.4	196.7	43.8	10.0	0.65

5.11.2 *Height to width ratio*

With the increase in height of the sample the number of particles in the sample increases. Considering a numerical sample with height to width ratio (H/D) of one decreases the run time significantly compared to a sample with H/D of two. Figure C.17 compares the results for the UCS tests for samples with H/W 1.0 and 2.0. With the increase in H/W ratio the peak strength in UCS

is increased by 6% while the tensile strength is increased by 7%. The crack initiation stress and the crack damage stress for the longer sample was within 9% and 7.7% of the shorter sample respectively. Ideally the strength of the sample should increase with decrease in the sample height (Hudson, Brown, and Fairhurst 1971). As, in this study, the loading platens are made frictionless the sample does not show a significant difference in the peak strength. The difference in the macro parameters are because of the change in grain arrangements. However, a detailed analysis is required changing the random generation of particles to confirm this.

Table 5-8: Comparison of macro parameters obtained from the direct tension test and the UCS test for samples with height and width ratio (W/H) 1.0 and 2.0 (micro parameters for both samples are same,

Table 5-1)

Case	Ec (GPa)	ν_c	σ_{CI} (MPa)	σ_{CD} (MPa)	σ_{UCS} (MPa)	Et (GPa)	σ_t (MPa)	Et/Ec
LAB	70.5	0.26	88.6	163.3	221.7	45.8	10.6	0.65
H/W=1.0	69.3	0.12	87.7	185.9	219.1	46.8	10.9	0.68
H/W=2.0	69.0	0.11	95.6	200.2	232.3	46.9	10.1	0.68

5.11.3 *Grain interaction range*

As described in section 5.4.8, numerical models with different grain interaction values were tested. Figure C.18 shows the results of the UCS tests with grain interaction range 1.3 mm and 0.65 mm. The average number of bonds per particles was decreased from 5.39 to 4.4 when the interaction range was decreased. This increases the voids present in the sample and the sample becomes weaker. As shown in Table 5-9, the peak strength in UCS is decreased by 48.9% when instead of 1.3 mm, a 0.65 mm interaction range was used. Because of the increase in the voids in the sample, other macro parameters also found to decrease significantly when the grain interaction range is reduced.

Table 5-9: Comparison of macro parameters obtained from the direct tension test and the UCS test for samples with grain interaction range (iGap) 1.3 mm and 0.65 mm (other micro parameters for both samples are same,

Table 5-1)

Case	Ec (GPa)	ν_c	σ_{CI} (MPa)	σ_{CD} (MPa)	σ_{UCS} (MPa)	Et (GPa)	σ_t (MPa)	Et/Ec
LAB	70.5	0.26	88.6	163.3	221.7	45.8	10.6	0.65
iGap=1.3 mm	69.3	0.12	87.7	185.9	219.1	46.8	10.9	0.68
iGap=0.65 mm	51.0	0.15	54.3	89.4	112.0	34.9	7.9	0.68

5.11.4 *Grain interface discretization*

The major changes in the present FJ bonded particle model is the introduction of the discretized grain interface. Hence, to see the impact of increased discretization numerical samples were tested in UCS and direct tension keeping all the micro parameters in

Table 5-1 constant. It was observed that the FJs discretized in three elements was enough to produce the required moment resistance for matching the UCS/tensile strength value observed in the laboratory. As shown in Figure C.19 and Table 5-10 there is less than 1% change in the macro parameters when the FJs are discretized in twelve elements compared to three elements. On the other hand increasing the discretization increases the run time significantly. So, for all the analysis the FJs in this investigation were divided in three elements.

Table 5-10: Comparison of macro parameters obtained from the direct tension test and the UCS test for samples when grain interface is discretized wit 3 elements and 12 elements (other micro parameters for both samples are same,

Table 5-1)

Case	Ec (GPa)	ν_c	σ_{CI} (MPa)	σ_{CD} (MPa)	σ_{UCS} (MPa)	Et (GPa)	σ_t (MPa)	Et/Ec
LAB	70.5	0.26	88.6	163.3	221.7	45.8	10.6	0.65
3 elements	69.3	0.12	87.7	185.9	219.1	46.8	10.9	0.68
12 elements	69.3	0.12	87.7	187.9	220.9	47.0	10.6	0.68

5.11.5 *Loading rate*

As described in the material modelling support manual (Potyondy 2017), after each step in a numerical model the particles and the FJs must have enough time to distribute the unbalanced forces. This is done by providing a slow loading rate to the specimen. Figure C.20 shows the results of UCS tests when samples are loaded with two different axial strain rates (1.5 and 0.75). Table 5-11 indicates that the loading rate has higher impact on the crack damage stress and the peak strength while there is a little impact on the crack initiation, and the elastic properties. This indicates that the peak strength is an artifact of the boundary conditions.

Table 5-11: Comparison of macro parameters obtained from the direct tension test and the UCS test for samples with axial strain rate 1.5 and 0.75 (other micro parameters for both samples are same, Table 5-1)

Case	Ec (GPa)	ν_c	σ_{CI} (MPa)	σ_{CD} (MPa)	σ_{UCS} (MPa)	Et (GPa)	σ_t (MPa)	Et/Ec
LAB	70.5	0.26	88.6	163.3	221.7	45.8	10.6	0.65
Strain rate= 1.5	69.3	0.12	87.7	185.9	219.1	46.8	10.9	0.68
Strain rate= 0.75	69.3	0.12	90.3	177.9	211.3	46.9	10.9	0.68

5.11.6 *Insitu stress at which material is created*

Before installing the FJs in a numerical sample the particles are compressed inside the rigid cylindrical walls so that there will be a proper contact between the mineral grains (Potyondy 2017). However, it was observed that after a particular value of confinement (around 1% of UCS), there is no major impact of the confinement on the material behavior. Table 5-12 shows that with an increase in confinement from 10 MPa to 30 MPa, there is a small increase (5.39 to 5.4) in the average number of FJs per particles, a small decrease in porosity (0.3542 to 0.3536) when the insitu stress is increased. Figure C.21 shows the results of direct tension test and UCS test for

confinement 10 MPa and 30 MPa keeping all micro parameters for both cases the same. It was observed that, the macro parameters do not change significantly with the increase in insitu stress.

Table 5-12: Comparison of macro parameters obtained from the direct tension test and the UCS test for samples created at 10 MPa and 30 MPa confinement (other micro parameters for both samples are same,

Table 5-1)

Case	Ec (GPa)	ν_c	σ_{CI} (MPa)	σ_{CD} (MPa)	σ_{UCS} (MPa)	Et (GPa)	σ_t (MPa)	Et/Ec
LAB	70.5	0.26	88.6	163.3	221.7	45.8	10.6	0.65
10 MPa	69.3	0.12	87.7	185.9	219.1	46.8	10.9	0.68
30 MPa	69.3	0.12	88.9	180.9	220.3	47.0	10.8	0.68

5.11.7 *Number of particles along the diameter*

Whether the average number of particles considered in the numerical samples are sufficient can be decided by ensuring the sample reproduces the behavior observed in the laboratory. To determine the impact of number of particles along the diameter of the numerical sample, the particle number was increased from 3618 to 16882 (average number of particles along the diameter from 15 to 25) keeping the micro parameters constant. This increased the peak strength in UCS by 7.6% whereas the crack initiation and the crack damage were increased by 2.3 % and 15.1% respectively. The Young's modulus and the Poisson's ratio were decreased by 6.5% and 7.6% respectively. As shown in Table 5-13 the sample becomes stronger in direct tension by 3.2% with increase in the number of particles. As shown in Figure C.22, the shape of the stress-strain curve in UCS remains same.

Table 5-13: Comparison of macro parameters obtained from the direct tension test and the UCS test for samples with average 15 particles and 25 particles along the width (other micro parameters for both samples are same,

Table 5-1)

Case	Ec (GPa)	ν_c	σ_{CI} (MPa)	σ_{CD} (MPa)	σ_{UCS} (MPa)	Et (GPa)	σ_t (MPa)	Et/Ec
LAB	70.5	0.26	88.6	163.3	221.7	45.8	10.6	0.65
15 particles	69.3	0.12	87.7	185.9	219.1	46.8	10.9	0.68
25 particles	64.8	0.11	89.7	213.9	235.8	48.3	11.1	0.75

5.11.8 *Sample width/diameter*

With the decrease in the sample width/diameter the strength of the rock sample generally increases (Hudson et al. 1971). To confirm whether the 54 mm diameter sample used in the numerical investigation correctly represents the intact and the micro fractures present in the rock sample a 100 mm diameter sample with the same set of micro parameters as in

Table 5-1 was tested. Table 5-14 shows the results of the investigation. Instead of a decrease in the peak strength, there is an increase of 11.6% in UCS and a 5.5% decrease in the direct tensile strength. The crack initiation stress for the 100 mm diameter sample was found to be 39.8% of UCS compared to 40% for 54 mm sample. The crack damage stress increased from 84.8% for 54 mm diameter sample to 91.8% of UCS for the 100 mm diameter sample.

Table 5-14: Comparison of macro parameters obtained from the direct tension test and the UCS test for samples width = 54 mm and 100 mm (other micro parameters for both samples are the same,

Table 5-1). The UCS are compared in Figure C.23.

Case	E_c (GPa)	ν_c	σ_{CI} (MPa)	σ_{CD} (MPa)	σ_{UCS} (MPa)	Et (GPa)	σ_t (MPa)	Et/Ec
LAB	69.6	0.24	88.6	163.3	221.7	45.2	10.6	0.65
54 mm	69.3	0.12	87.7	185.9	219.1	46.8	10.9	0.68
100 mm	69.2	0.1	97.4	224.5	244.5	47.7	10.3	0.7

5.12 Relation between the tensile and compressive Young's modulus and Poisson's ratio in rock

The relationship between the Young's moduli and the Poisson's ratios of rock in tension and compression are given by (Ambartsumyan 1969):

$$\frac{\nu_t}{E_t} = \frac{\nu_c}{E_c} \tag{5-13}$$

Where, ν_t= tensile Poisson's ratio; E_t= tensile Young's modulus; ν_c= compressive Poisson's ratio; E_c= compressive Young's modulus.

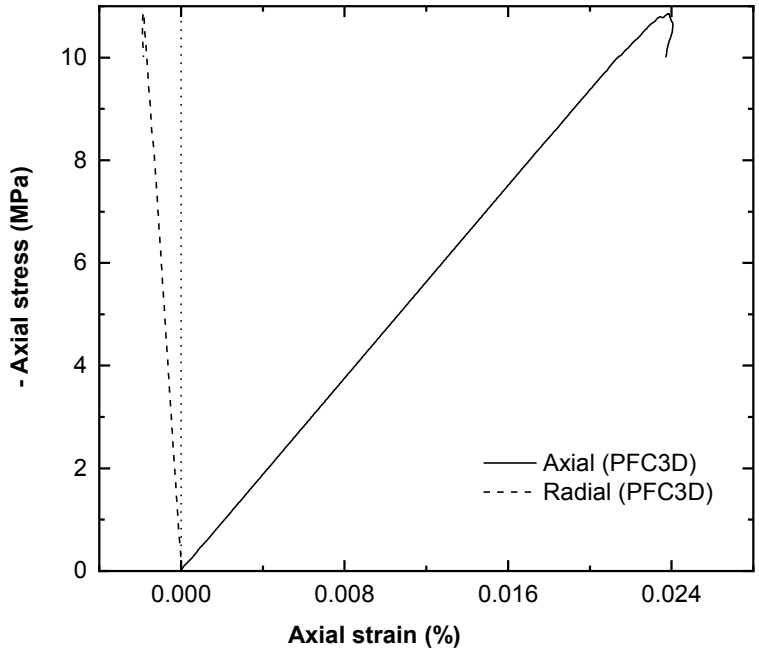

Figure 5.24: Axial stress versus axial and radial strain obtained for FJ model in a direct tension test.

To examine this relationship the results from the FJ numerical investigation were used. Figure 5.24 shows the axial stress versus axial and radial strain obtained for the FJ model. The ratio between the simulated tensile Poisson's ratio and Young's modulus found out was 0.0017 GPa^{-1} (0.077/46.8 GPa). When this value was compared with the value from the UCS test the same ratio was observed (0.0017 GPa^{-1}= 0.12/69.3 GPa, Table 5-5). This validates the Equation (5-13) suggested by Ambartsumyan (1969).

5.13 Micro fracturing in UCS test and the impact of the changes in ratio between the normal and shear stiffness (krat)

The tensile micro fractures in a numerical FJ sample during the UCS test occur at an early stage of loading (around 10% of peak). Figure 5.25 shows the crack formation in the numerical sample (for micro parameters in

Table 5-1) the increase in the axial load. The crack formation is also compared with the laboratory sample of a 300 mm diameter and 161.6 MPa UCS in Figure 5.26.

Although, the FJ model matches most of the macro parameters (Table 5-5), random cracks form at an axial stress of ~10% of UCS while in the laboratory sample those form very close to the crack initiation stress. When numerical models are studied in both compression and tension, it was found out that these cracks have a minor impact on the UCS test but have a major impact on the confined extension tests (discussed in the next section). When sample subjected to compression is tested in tension, the early micro cracks reduce the strength of the rock considerably. To reduce the formation of early cracks and match the laboratory crack formation, the ratio between the normal stiffness and the shear stiffness (krat) was reduced (keeping all other micro parameters constant). This changed most of the macro parameters obtained for the numerical sample. The model was then recalibrated to the direct tensile strength; Young's moduli; crack initiation stress and the peak strength in UCS test. The corresponding set of micro parameters are given in Table C-10. Figure 5.26 compares the formation of random cracks before the crack damage stress for krat value of 1.6 and 1.2 with the laboratory observation. A kratio of 1.2 reduces the crack number considerably and more closely matches the crack formation in the laboratory. Also, this matches the most of the micro parameters observed in the laboratory (Table 5-15). Hence, the parameters given in Table C-10 were used to study the confined extension behavior in rock.

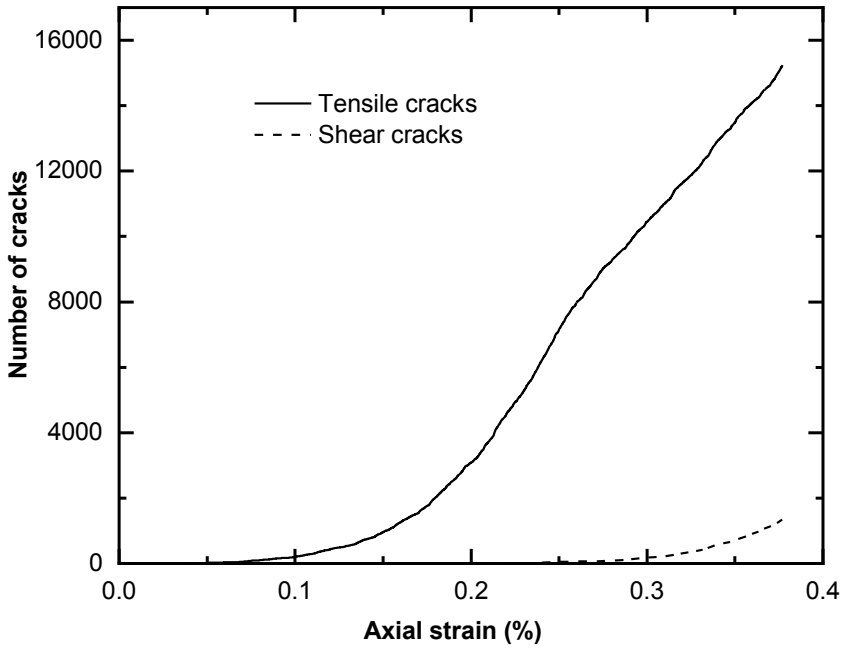

Figure 5.25: Tensile and shear crack formation in the numerical sample for the micro parameters given in Table 5.1.

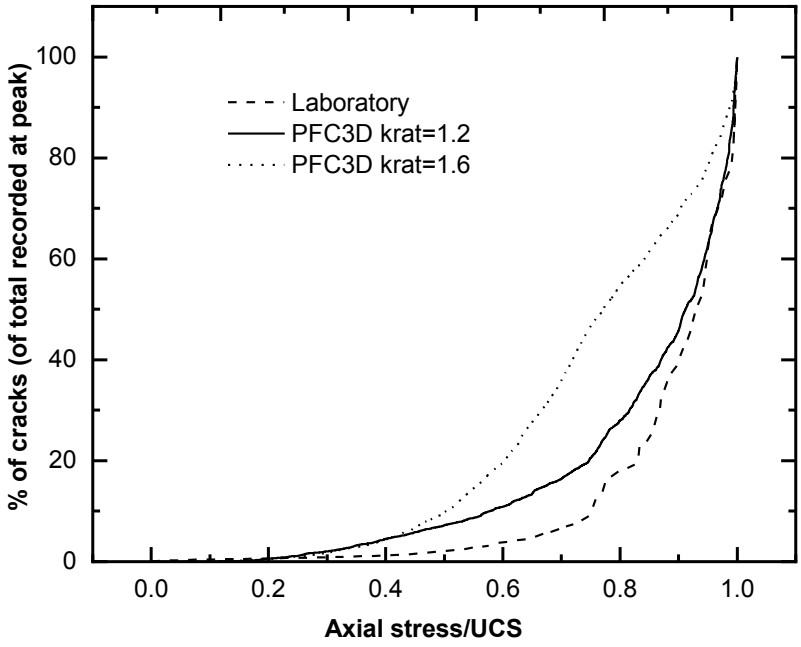

Figure 5.26: Comparison of micro crack formation in the numerical sample for krat=1.6 and krat=1.2 with the laboratory sample (UCS=161.6 MPa) before crack damage stress. Note: both the numerical samples (krat 1.6 and 1.2) are calibrated to the same value of tensile strength and UCS (Table 5-5 and Table 5-15).

Table 5-15: Comparison of micro crack formation in the numerical sample for krat=1.6 and krat=1.2

Case	Ec (GPa)	ν_c	σ_{CI} (MPa)	σ_{CD} (MPa)	σ_{UCS} (MPa)	Et (GPa)	σ_t (MPa)	Et/Ec
LAB	70.5	0.26	88.6	163.3	221.7	45.8	10.6	0.65
kRatio=1.6	69.3	0.12	87.7	185.9	219.1	46.8	10.9	0.68
kRatio=1.2	69.3	0.07	97.7	208.1	219.6	47.7	10.8	0.69

5.14 Summary: Investigation of laboratory response observed in rock using the flat jointed bonded particle model

The flat jointed bonded particle model was used in this study to capture the rock behavior observed in the laboratory during the UCS test; triaxial tests and direct tension test. A methodology was developed to select the values of the micro parameter for the particles and FJs in the numerical sample. Using a single mineral grain type and an average of 15 particles along the width of the sample it was possible to produce reasonable bi-modularity, initial non-linearity during an UCS and triaxial test; match the crack initiation stress, crack damage stress; the ratio between the UCS and direct tension test and the responses of the laboratory sample during the triaxial tests.

The initial non-linearity in the stress-strain curve which is typical of a UCS and a triaxial rock testing was captured by considering micro gaps between the mineral grains present in the laboratory sample. The numerical sample exhibited bi-modularity when stress-released micro fractures were included in the model. The ratio between the simulated tensile and compressive Young's modulus was 0.68 which is within 5% of that obtained from laboratory testing. The tensile Young's modulus is close to the compressive Young's modulus for the rocks with fine grained minerals and grains with uniform particle size. However, the numerical modelling showed that the bi-modularity was independent of the grain size and grain size distribution. When bi-modularity was considered in the model, a crack initiation stress of about 40% of the peak was achieved.

The crack damage stress was found to be mainly a function of micro cohesion, micro friction and the ratio between the normal and shear stiffness of the FJs. The micro friction was found to impact the stress-strain response after the crack damage stress in an UCS test and the triaxial tests. The peak strength in an UCS test can be matched with different combinations of the micro friction and cohesion of the FJs. However, the friction angle can be decided by calibrating the model to the crack damage stress and the triaxial test results. The present rigid boundary technique used in the PFC3D code to apply confinement in a triaxial test was found to capture the triaxial behavior under low confinements while it showed strain hardening at higher confinement (greater than 8 MPa).

5.15 Laboratory confined extension test on rock

Confined tensile fracturing occurs in rock under mixed tensile and compressive stress condition. Such a test was proposed by Brace (1964). As shown in Figure 5.27a, all-around compressive stress (P') and vertical compressive force (F) is initially applied to the model. The load (F) on the top and bottom platens is then gradually reduced till the specimen fractures. The confining stress in the curve part of the sample generates the tensile stress in the central part. The compressive and tensile stress at failure are then calculated from equations (5-14) and (5-15).

$$\sigma_1 = \sigma_2 = P' \tag{5-14}$$

$$\sigma_3 = -\frac{P'(A_h - A_t)}{A_t} + \frac{F}{A_t} \tag{5-15}$$

Where,

C= axial stress (+ve in tension),

F= axial force (-ve F acts towards sample),

P= confining pressure (+ve),

A_h= head area, and

A_t= throat area.

The confined extension test conducted is called the triaxial confined extension test where the intermediate principal stress is same as the major principal stress. Rock tested in triaxial confined extension, and triaxial test in the same range of confinement showed that sample tested in triaxial confined extension fails at a considerably higher peak stress. To test the sample in confined extension with zero intermediate principal stress Patel and Martin (2018a) used the flattened Brazilian test. To test samples with increased confinement flattened Brazilian samples with increased depth of flattening were tested. However, the maximum confinement achieved using

flattened Brazilian test was 37% of UCS. The FJ bonded particle model was therefore used to investigate confined extension.

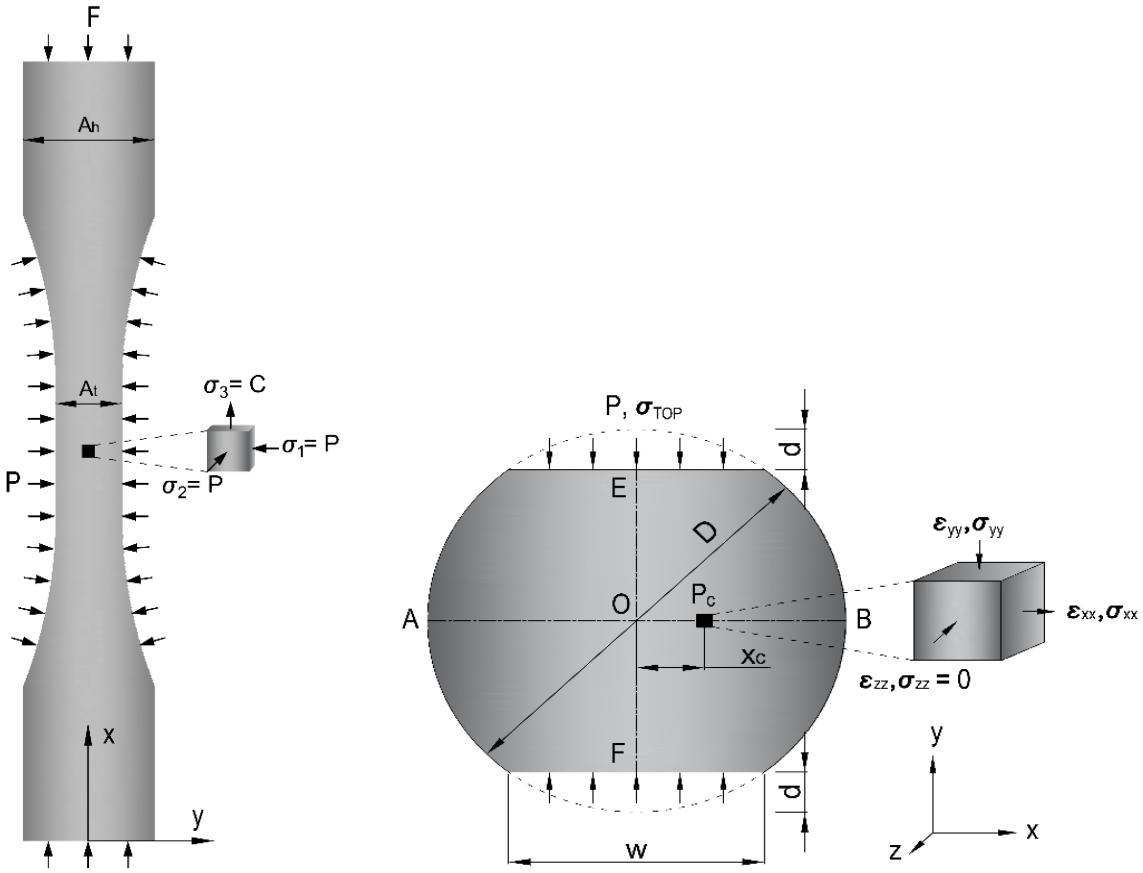

(a) (b)

Figure 5.27: Confined extension test on rock (a) on dog-bone shaped sample (Brace 1964) (b) flattened Brazilian sample (Patel and Martin 2018b)

5.16 Confined Extension PFC3D

The central part of the sample, Figure 5.27a, used in the laboratory testing of rock in confined extension passes through the stress path ODEC as shown in Figure 5.29. The sample at zero confinement (point O) is subjected to a hydrostatic stress (point D). Then the minor principal stress is gradually reduced keeping the major and intermediate principal stress constant till the sample is fractured at point C. Samples failed along such a stress path are influenced by the intermediate principal stress (Mogi 1967). For the investigation of the confined extension on the numerical

sample (Figure 5.28) with no intermediate principal stress, therefore, the following steps were taken:

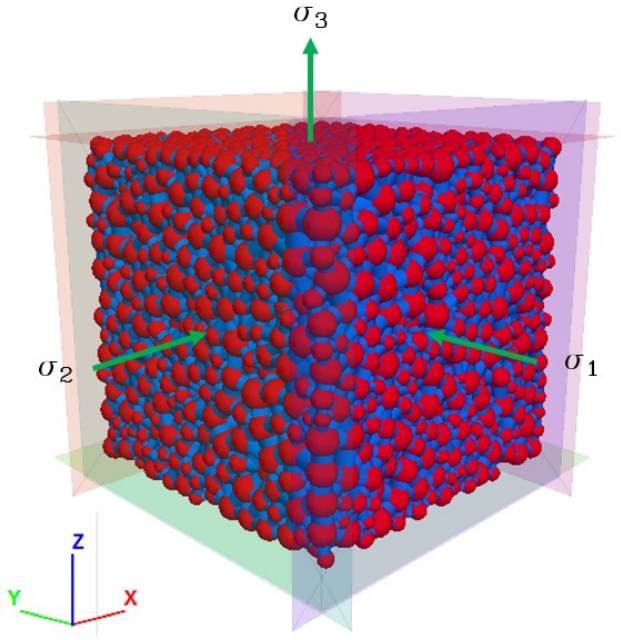

Figure 5.28: Confined extension sample and applied boundary condition

A) The cubical sample shown in Figure 5.28 was hydrostatically confined to a particular magnitude of major principal stress (point D, Figure 5.29).

B) Keeping the major principal stress constant ($\sigma_1 = \sigma_{yy}$), the minor principal stress ($\sigma_3 = \sigma_{zz}$) and the intermediate principal stress ($\sigma_2 = \sigma_{xx}$) was reduced simultaneously to (point E, Figure 5.29).

C) The top and bottom 5mm of the sample were then held and pulled in opposite directions keeping the major principal stress constant and intermediate principal stress at zero till the sample failed at point C (Figure 5.29). The x coordinate gives the magnitude of minor principal stress for the corresponding major principal stress.

D) Steps A-C was then repeated for different magnitudes of major principal stress to obtain different failure points in confined extension.

To undertake this task, the present FJ code was modified. The code written is given in section C.6

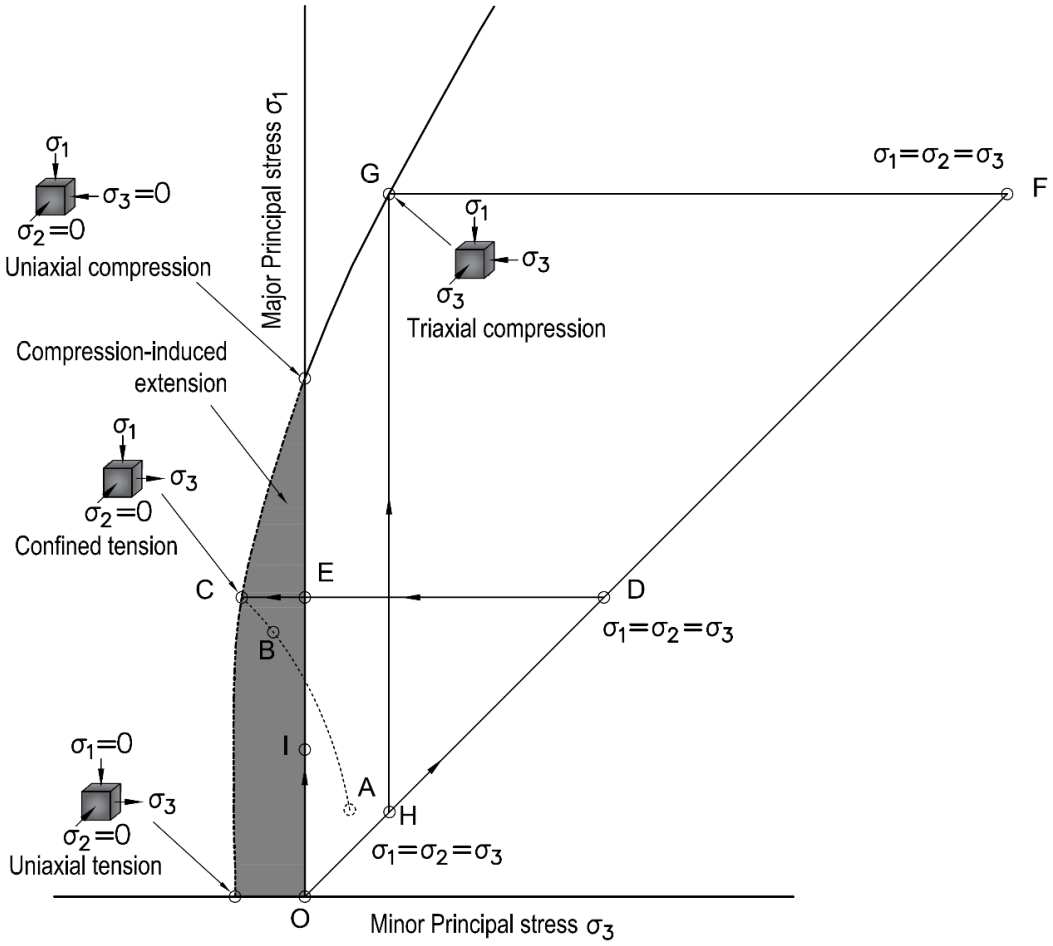

Figure 5.29: A typical failure envelope for rock showing the stress path during: field confined extension failure (ABC); confined extension test (ODEC and OFG); and triaxial test (OHG). Note: the location of the point A depends upon the boundary condition the rock is subjected to in the field.

5.17 Influence of stress path on confined extension

As shown in Figure 5.29, point 'A' represents an insitu stress condition with $\sigma 1 >= \sigma 2 >= \sigma 3$. Due to the excavation i.e change in the boundary condition, the rock at this point may fail in confined extension following the path ABC. However, this stress path is case dependent. The path followed by the conventional confined extension test using the dog-bone shaped geometry is ADEC, Figure 5.29. The micro fracture formation in a rock and its peak strength is path dependent. To compare the impact of the stress path followed the numerical FJ sample tested along stress path ODEC was compared with OEC. As shown in Figure 5.30, more cracks form (533 versus 470) in the sample when it follows the stress path OEC compared to ODEC although the final stress conditions are similar (90 MPa at E). This influences the peak strength obtained from the samples due to the application of tensile load. As shown in Figure 5.31 there is a difference of 3.6% in the peak strength for stress path ODEC compared to OEC.

Figure 5.32a and b compares the tensile and shear crack generated in the sample when it moves from point E to C. The number of shear cracks formed in the numerical sample is greater when the stress path followed in the laboratory is considered in accordance with the results of Ramsey and Chester (2004). To compare the numerical results with the laboratory results stress path ODEC was considered.

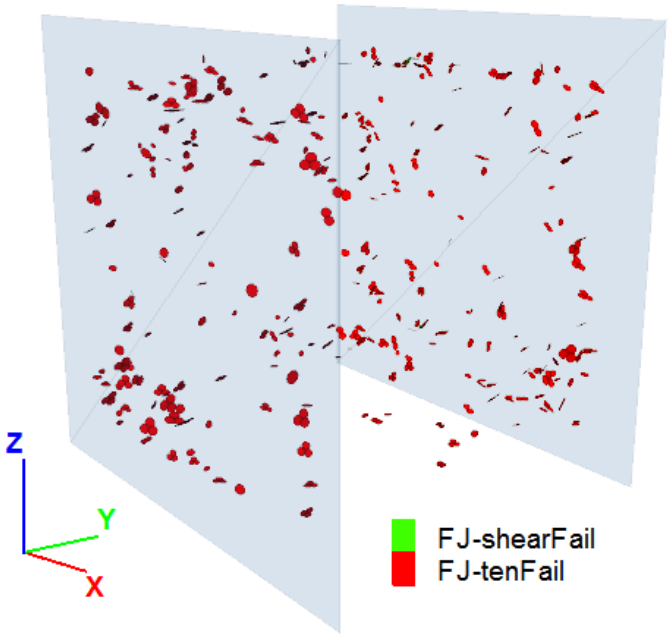

(a) 533 tensile, 3 shear

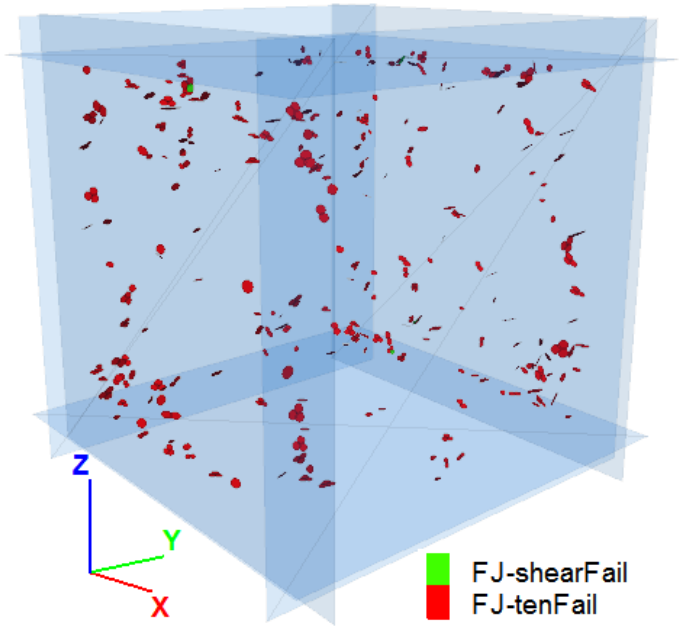

(b) 470 tensile & 5 shear

Figure 5.30: Cracks formed in the sample at point E when the sample follows stress path (a) OEC (b) ODEC.

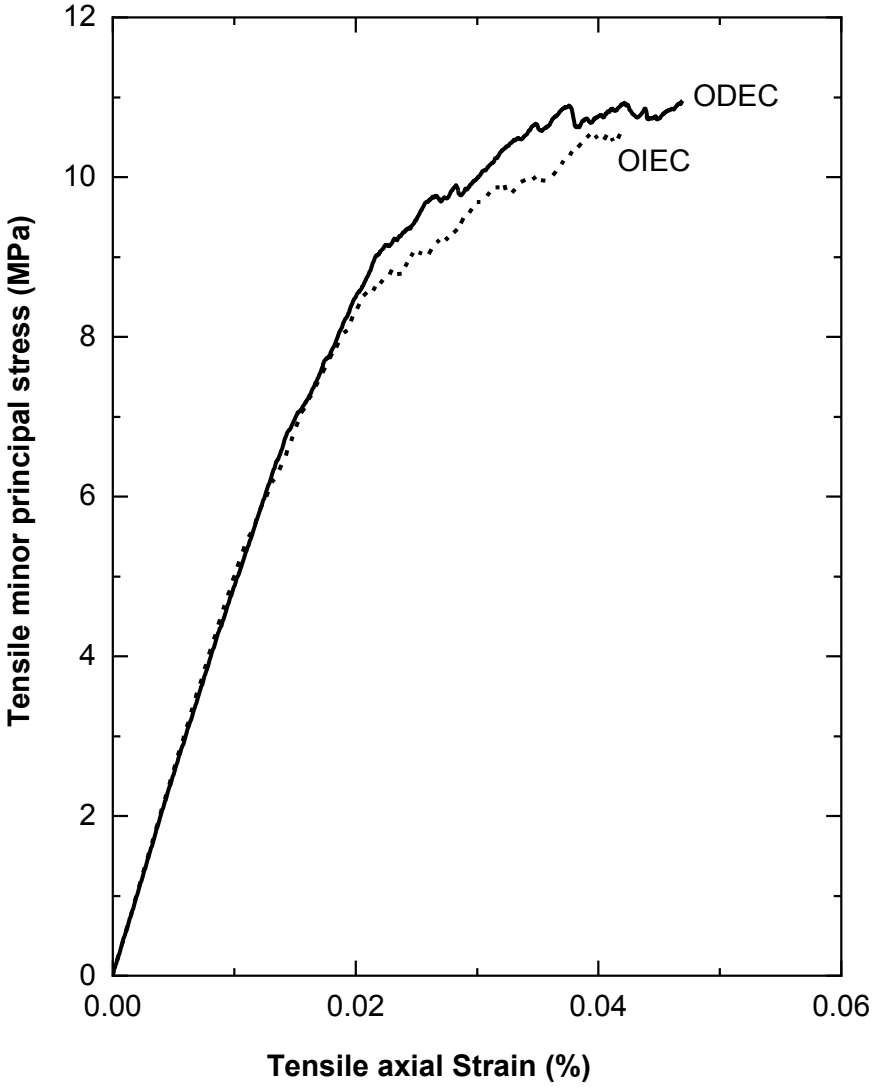

Figure 5.31: Tensile axial stress-strain curve obtained due to application of tensile stress for stress paths ODEC and OEC (from point E to C, Figure 5.29)

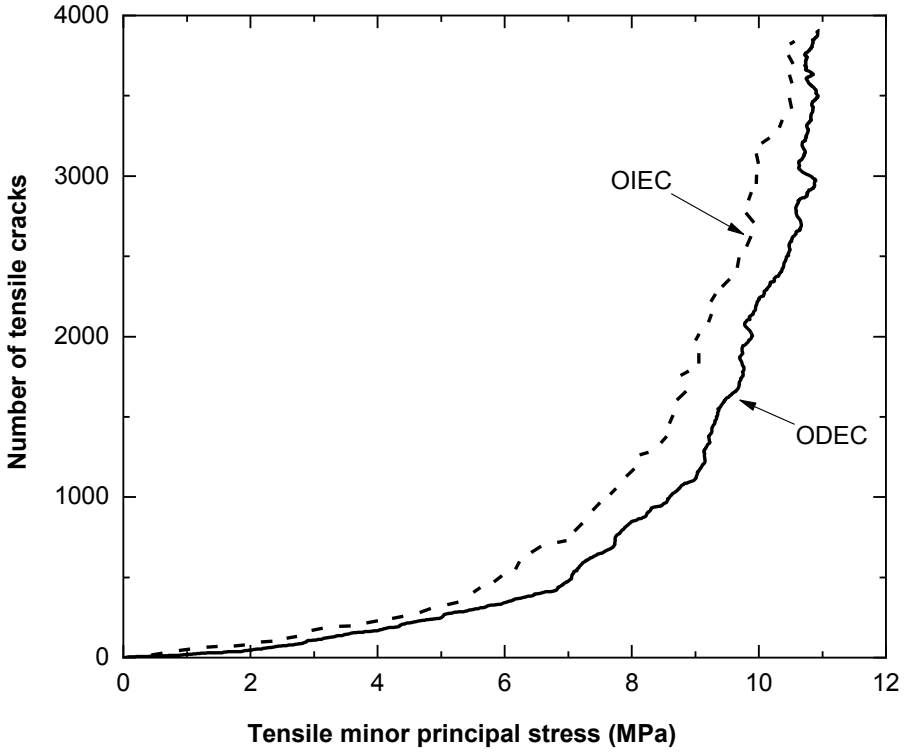

(a)

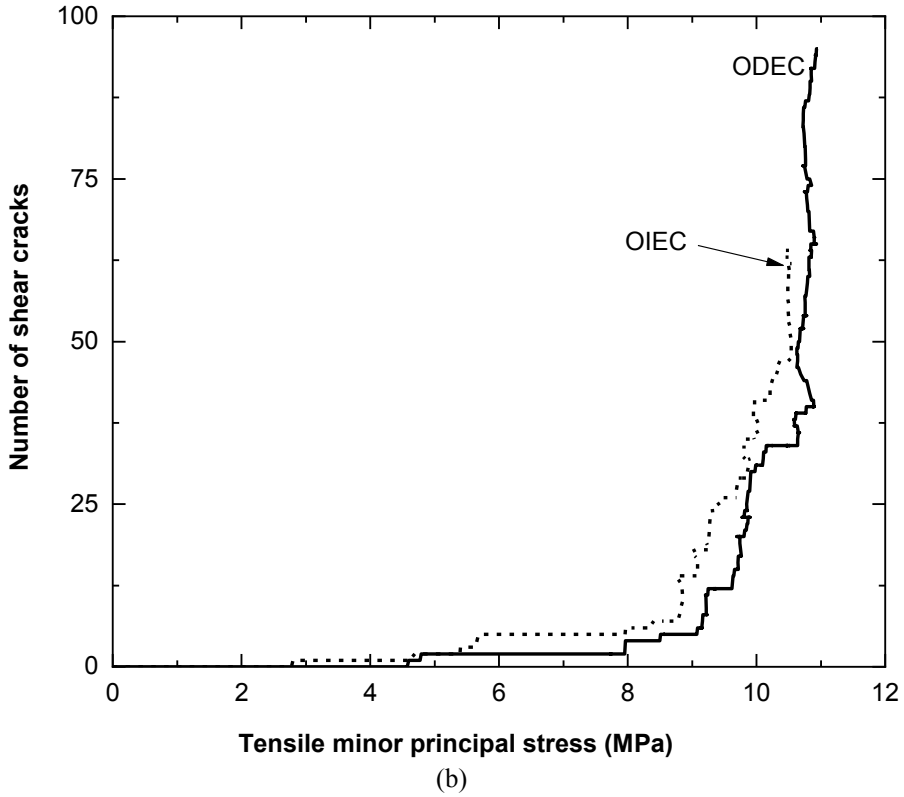

(b)

Figure 5.32: Comparison of crack development in the sample with increase in tensile strain from point E to C for stress paths ODEC and OEC (a) tensile crack (b) shear cracks

5.18 Results of the confined extension test (with zero intermediate principal stress)

Using the steps described in section 5.16, confined extension tests were carried out at different major principal stress magnitudes. The stress-strain results for the tests between points E and C (Figure 5.29) at three stress levels; low (10 MPa), medium (90MPa) and high (150 MPa) are shown in Figure 5.33. At low confinement the sample failed like a direct tension test sample. However, because of the confinement, the sample fails at a higher tensile stress (i.e. similar to the Brazilian tensile strength being greater than the direct tensile strength for Lac du Bonnet granite). With increase in confinement the peak strength of the sample increases (up to around 50% of the UCS value). The sample, however, yields at a lower percentage of the peak stress. As shown in Figure 5.34 and Figure 5.35 tensile cracking is dominant at low confinement while the percentage of shear cracks increases with the increase in confinement. This finding is in agreement with the observation by Brace (1964) and Ramsey and Chester (2004) using confined extension tests on dog-bone shape samples.

The confinement in the sample was increased from 10 MPa to around 80% of the UCS which was around the crack damage stress of Lac du Bonnet granite. When a sample with a confinement more than the crack damage stress was relaxed from point D to E, equilibrium was not reached and the sample failed. This observation indicates that the peak strength obtained after the crack damage stress depends upon the boundary condition applied. The cracks generated in the sample for different confinements at point E on the stress path ODEC are shown in Figure C.24 and at point C in Figure C.25.

The sample was then further confined beyond the UCS (point F) and the minor and intermediate principal stress gradually relaxed till the sample failed at point G (Figure 5.29). The results are

plotted in Figure 5.39 and a discussion is presented in section 5.20. These results are also compared with the conventional triaxial stress (stress path OFG versus OHG) in section 5.20.

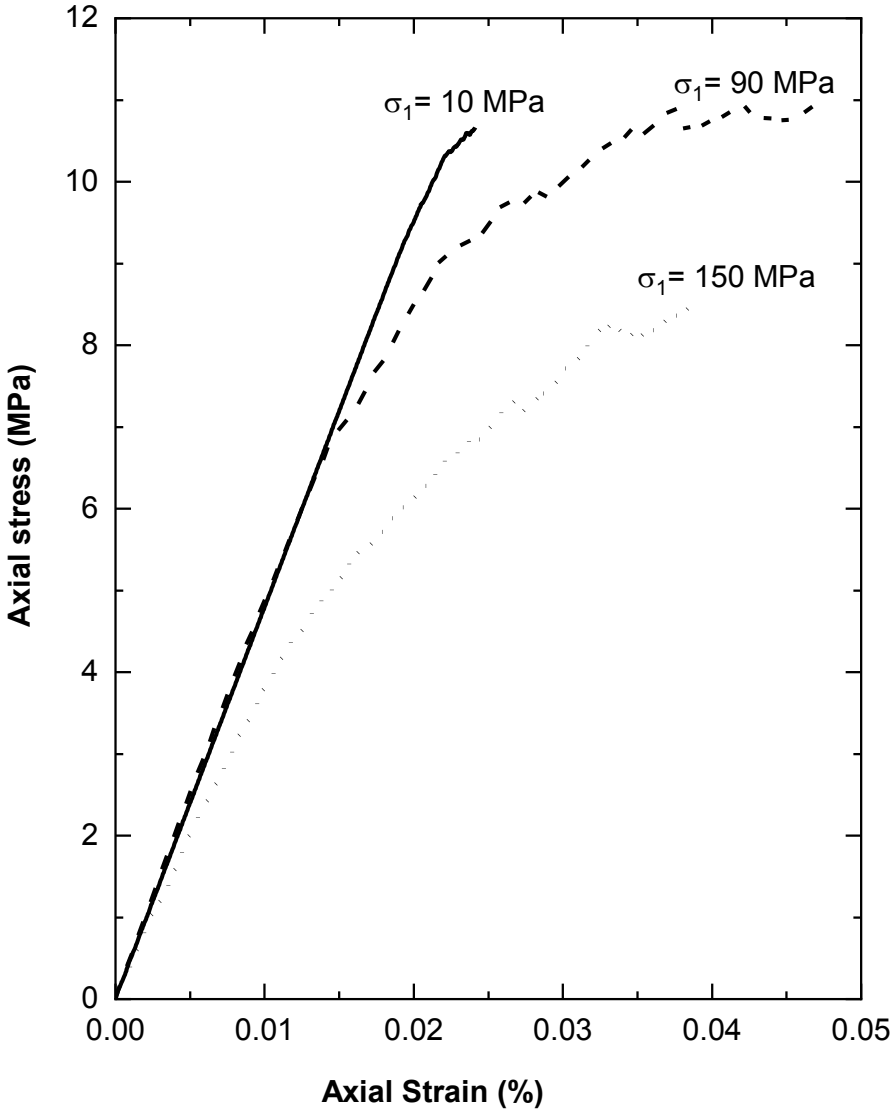

Figure 5.33: Stress-strain curves obtained for numerical confined extension tests at low (10 MPa); mid (90 MPa); and high (150 MPa) confinements (from point E to C Figure 5.29). In all the cases the intermediate principal stress is zero.

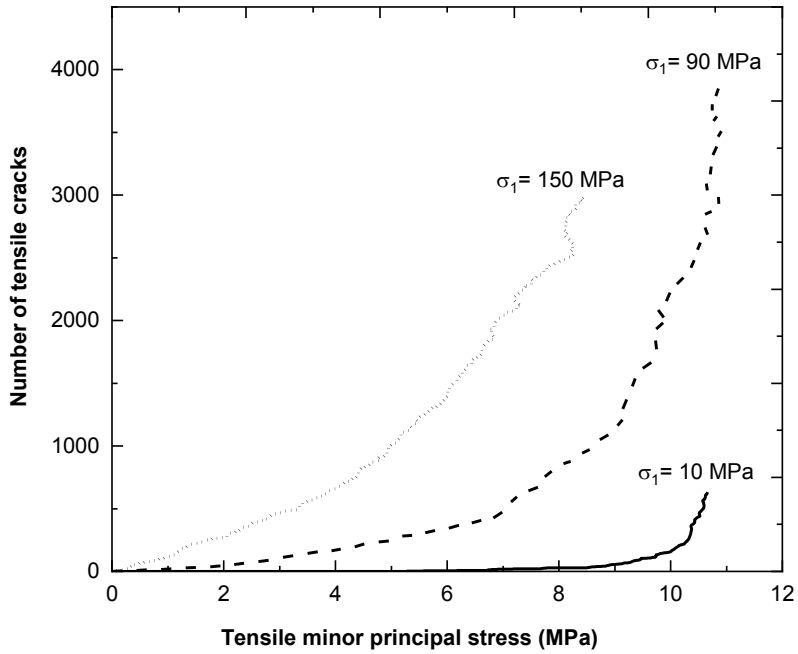

Figure 5.34: Number of tensile cracks formed with increase in minor principal stress for numerical confined extension tests at low (10 MPa); mid (90 MPa); and high (150 MPa) confinements (from point E to C Figure 5.29)

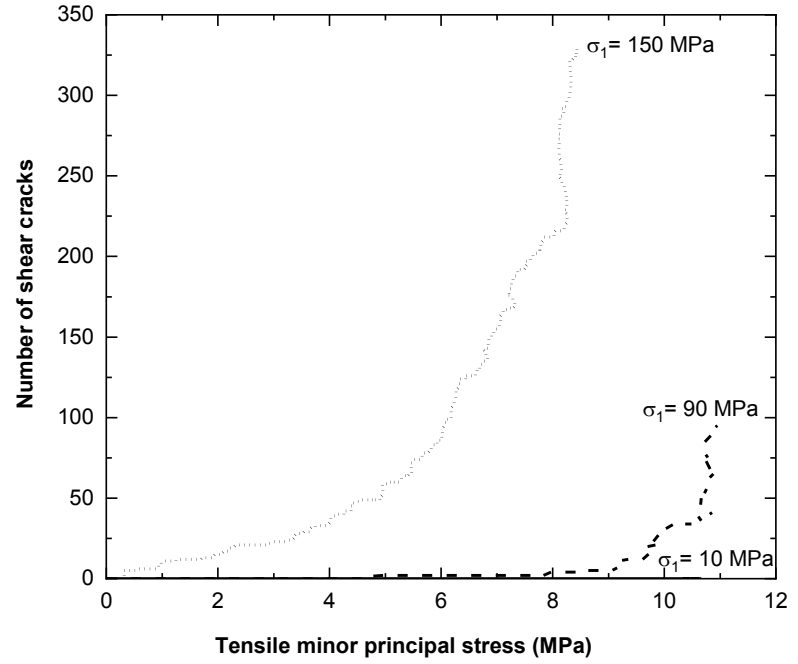

Figure 5.35: Number of shear crack formed with increase in minor principal stress for numerical confined extension tests at low (10 MPa); mid (90 MPa); and high (150 MPa) confinements from point E to C Figure 5.29)

5.19 Impact of intermediate principal stress on confined extension

One of the main objectives of this study is to examine the influence of the intermediate principal stress on the confined extension test of rock. To conduct the confined extension on a numerical sample the sample was loaded hydrostatically to point D (Figure 5.29). After point D the minor principal stress was gradually reduced keeping the major and intermediate principal stress constant. The sample was then extended in axial direction to fail the sample in confined extension. Figure 5.36 compares the formation of cracks in the sample after the minor principal stress is unloaded (point E, Figure 5.29) and the sample is failed in extension (point C, Figure 5.29) at major principal stress of 90 MPa and three intermediate stress levels (90MPa, 45 MPa and 0 MPa). The cracks formed at point E (Figure 5.29) in the samples were random. The number of cracks formed is less when additional confinement was provided by the intermediate principal stress. The intermediate principal stress also prevents the formation of tensile cracks in the model. The shear crack percentage in the case where the intermediate principal stress was equals the major principal stress was found to be greater than when the intermediate principal stress zero. As shown in Figure 5.37 the peak strength increased from 11.0 MPa to 19.2 MPa when the intermediate principal stress is kept the same as the major principal stress. Figure 5.38 compares the crack formation from point E to F (with increase in extensile stress in the numerical sample). The number of shear cracks formed in the sample is greater when there is intermediate principal stress applied to the sample. This is in agreement with the confined extension results on dog-bone shaped Carrara marble (Ramsey & Chester, 2004).

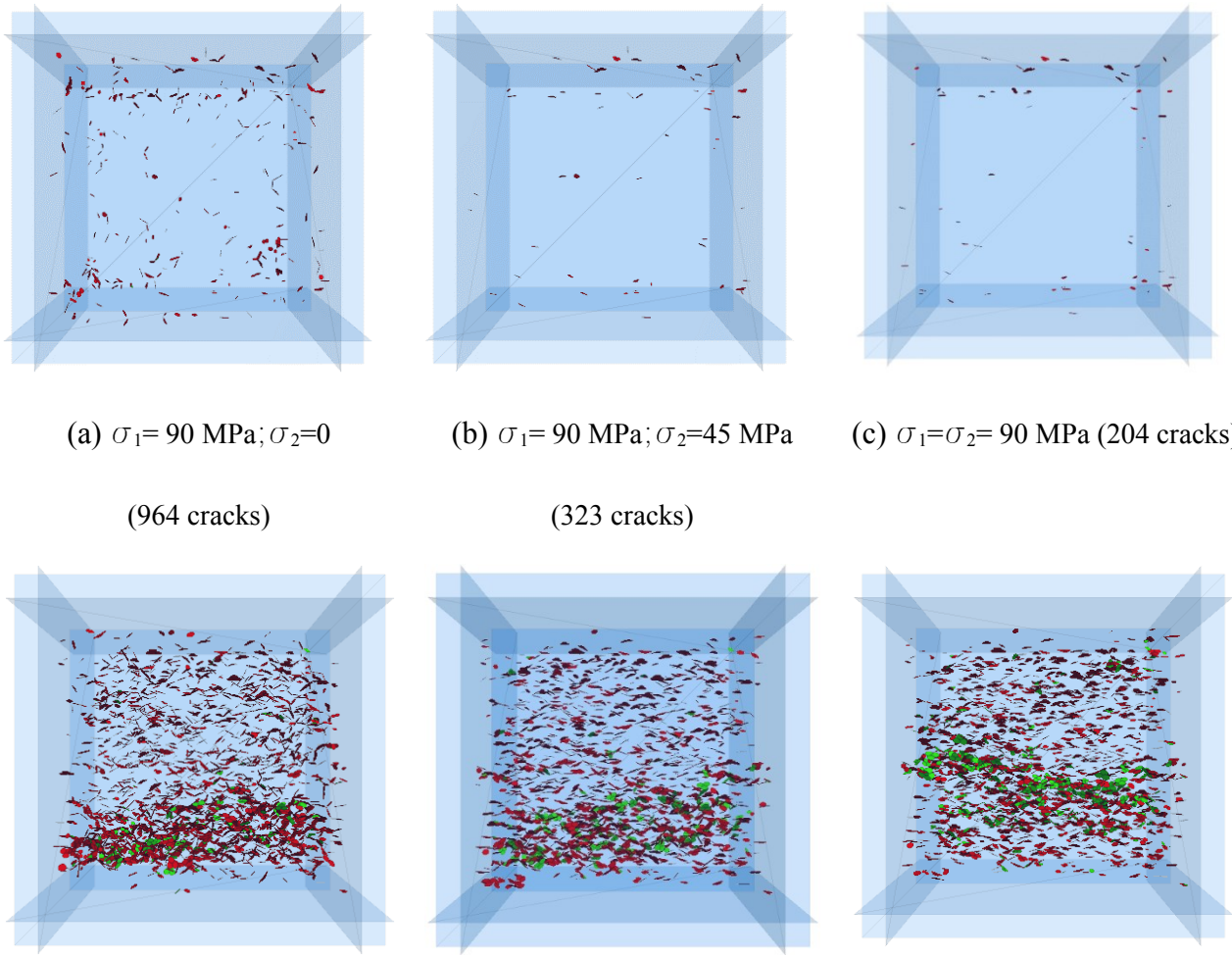

(a) σ_1= 90 MPa; σ_2=0 (964 cracks)

(b) σ_1= 90 MPa; σ_2=45 MPa (323 cracks)

(c) σ_1=σ_2= 90 MPa (204 cracks)

(d) σ_1= 90 MPa; σ_2=0

(e) σ_1= 90 MPa; σ_2=45 MPa

(f) σ_1=σ_2= 90 MPa

Figure 5.36: Comparison of crack formation in numerical sample (a) (b) (c) after the relaxation of minor principal stress (point E, Figure 5.29) and (d) (e) (f) at peak (point C, Figure 5.29) for (i) zero intermediate principal stress (b) intermediate principal stress 50% of major principal stress and (iii) intermediate principal stress same as major principal stress. Red= tensile crack, Green= Shear crack.

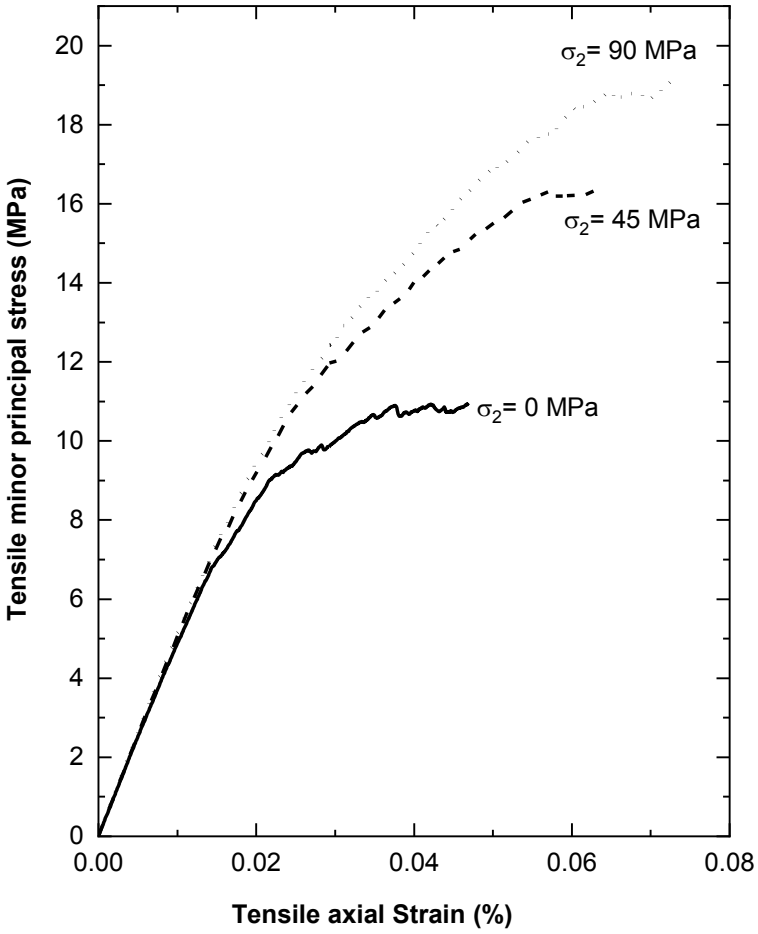

Figure 5.37: Confined extension test at $\sigma_2=\sigma_1$=90MPa, $\sigma_2=\sigma_1/2$=45MPa and σ_2=0 (Stress-strain curve showing the impact of intermediate principal stress in the numerical sample).

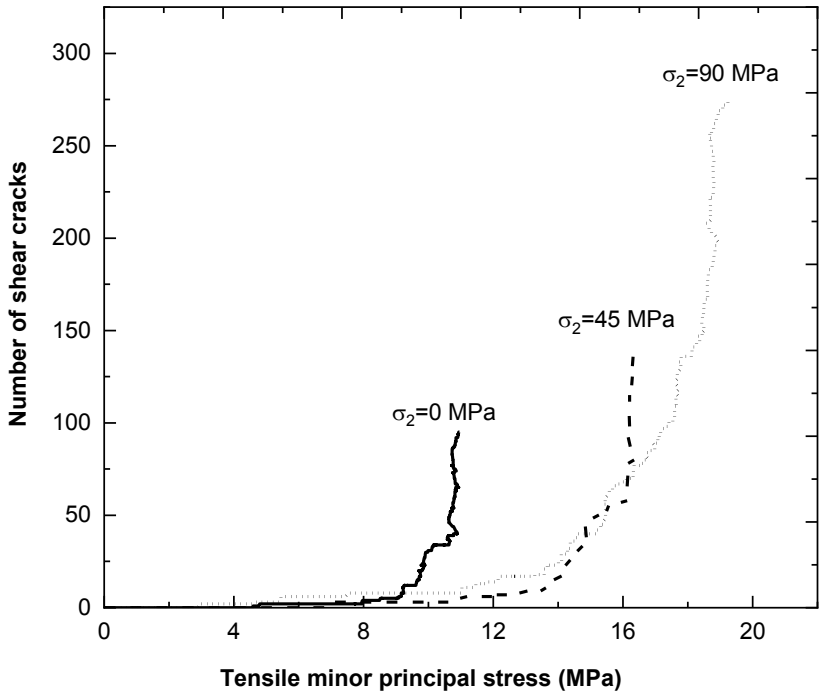

(a)

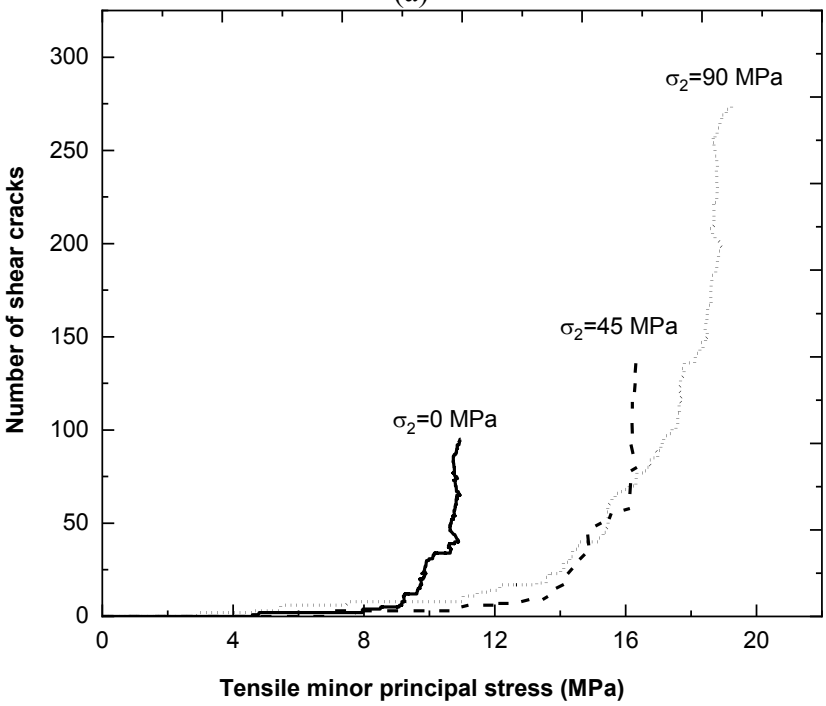

(b)

Figure 5.38: Comparison of crack formation in numerical sample with increase in intermediate principal stress (a) tensile crack (b) shear crack. In all the cases the major principal stress was kept constant at 90 MPa

5.20 Failure envelope for Lac du Bonnet granite

The data points obtained from the direct tension test; Brazilian test (major and minor principal stress at yield); flattened Brazilian tests; UCS and triaxial tests; confined extension tests and triaxial tests on numerical samples along with the Hoek-Brown failure envelope obtained from the triaxial tests on Lac du Bonnet granite are plotted in Figure 5.39. The data points obtained from the confined extension test on numerical sample was found to pass through the laboratory testing on direct tension, Brazilian and flattened Brazilian, UCS and Triaxial samples. The numerical confined extension tests, showed a tension cut-off up to ~50% of the UCS and then the minor principal stress decreases sharply with increase in the major principal stress. However, as shown in Figure 5.39 the confinement in the laboratory sample could not be applied beyond 80% of the UCS which is the crack damage stress for Lac du Bonnet granite. The numerical confined extension test was continued on the compression side (major principal stress compressive, minor principal stress= intermediate principal stress compressive, stress path OFG, Figure 5.29). When these results were compared with the conventional triaxial test on the numerical sample (stress path OAG, Figure 5.29), a good match was found indicating a negligible influence of the stress path. The Hoek-Brown failure envelope when extended into the confined extension region produced conservative values compared to the laboratory direct tension, Brazilian, flattened Brazilian tests and confined extension test results on numerical samples. The laboratory direct tension strength was 10.6 MPa whereas the Hoek-Brown failure gave a value of 6.8 MPa.

In Figure 5.39, the major and minor principal stresses on the PFC3D samples were obtained using two techniques; (a) for the confinement provided, the wall based measurement (section 5.6) was used, and (b) the gradual increase in axial tensile or compressive stress to the samples were from the measurement sphere technique (section 5.6). Figure 5.40 shows the difference in the major

principal stress obtained from the systems when stress path ODEC is applied to the PFC3D sample. The major principal stress applied by the walls to the sample from point D to C (Figure 5.29) was 120 MPa whereas, the measurement sphere technique produced 9% higher stress. Figure 5.41 shows the failure envelope obtained when both major and minor principal stress were obtained using the measurement sphere technique. A minor difference in the principal stresses was found out between the two techniques near the UCS, however, the shape of the failure envelope remains the same. Failure envelopes in confined extension with increase in intermediate principal stress (σ_2=0 MPa, 2MPa and 8MPa) are shown in Figure 5.42. A gradual increase in peak strength with the increase in intermediate principal stress was observed.

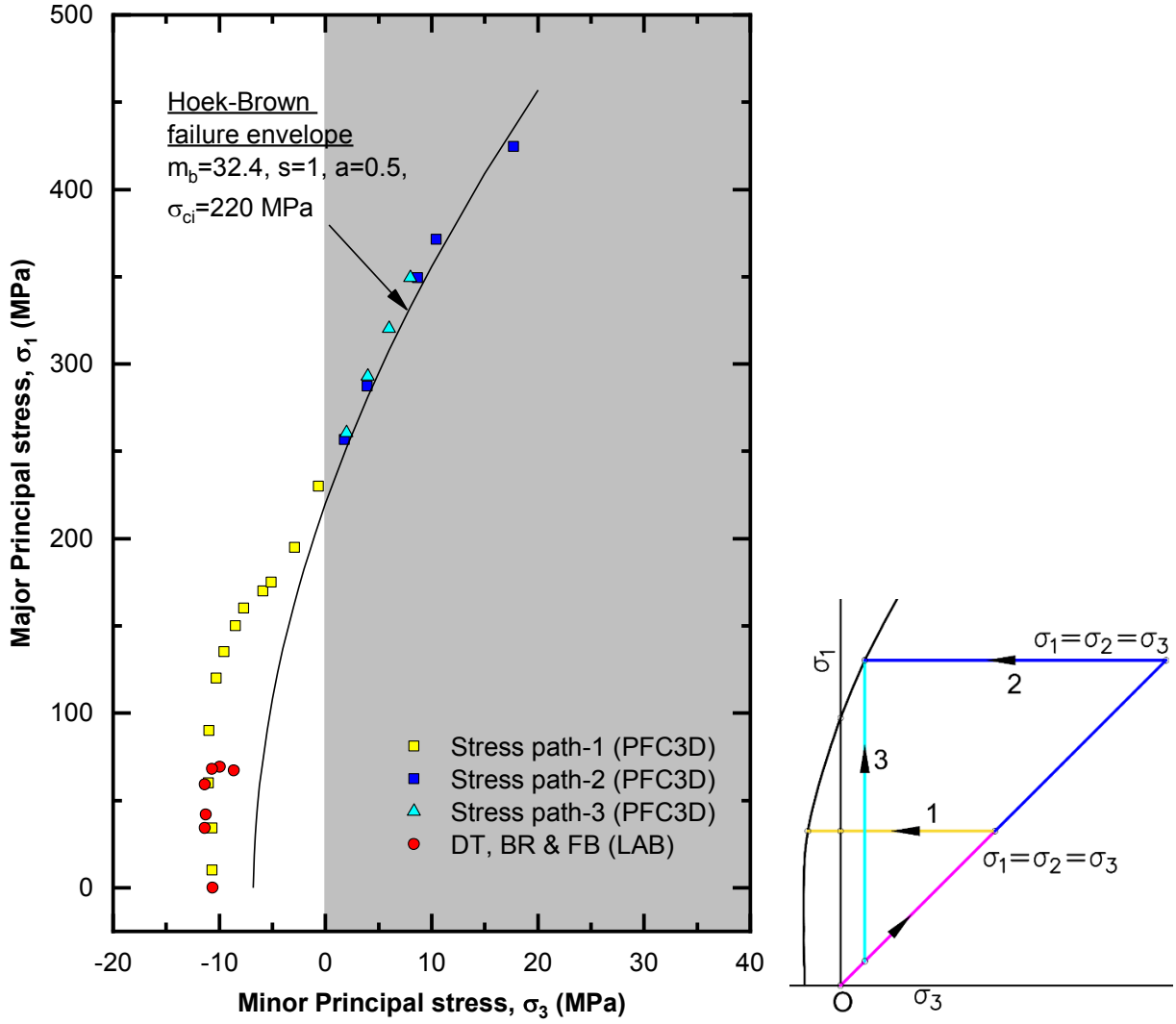

Figure 5.39: Results of laboratory and PFC3D numerical samples on Lac du Bonnet granite. DT= direct tension, BR= Brazilian, FB= Flattened Brazilian

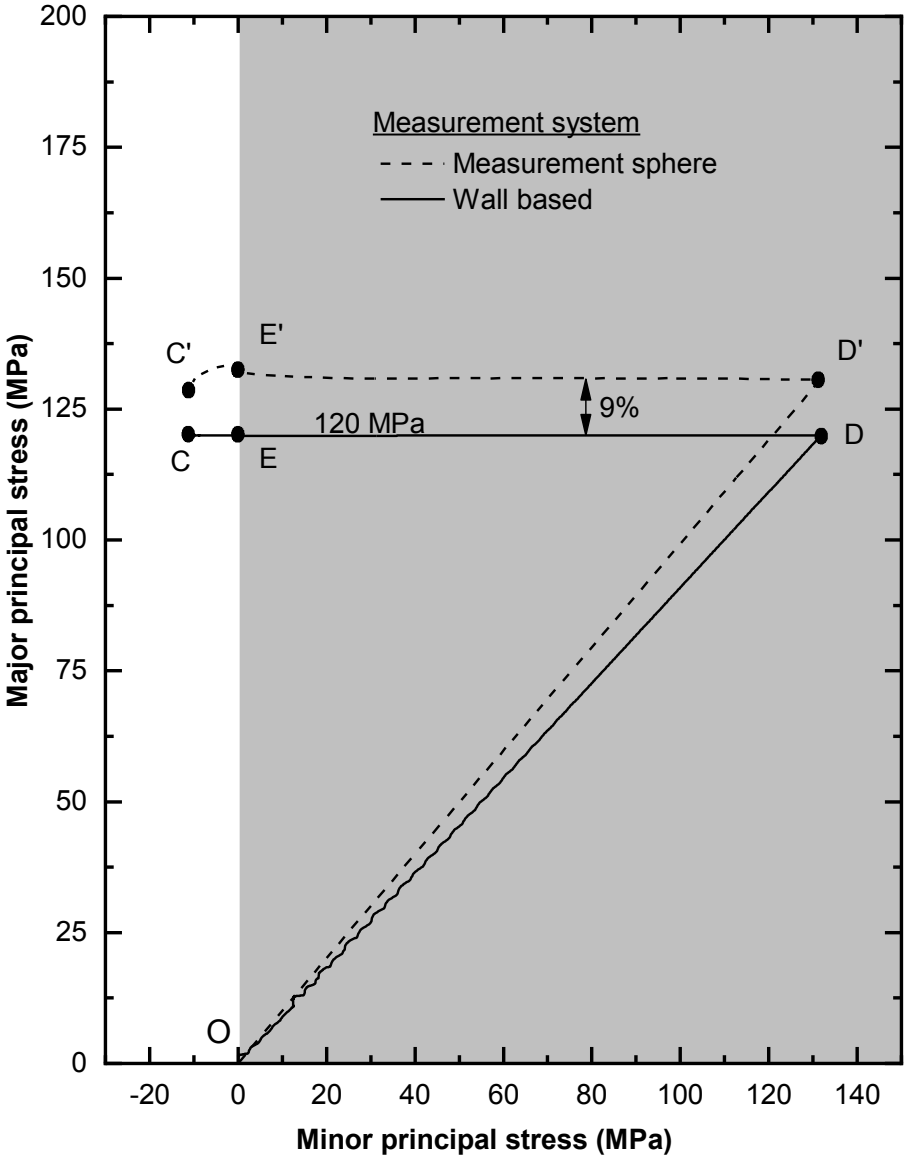

Figure 5.40: Comparison of major principal stress obtained from wall based measurement system with the measurement sphere system when stress path ODEC is applied to the PFC3D sample.

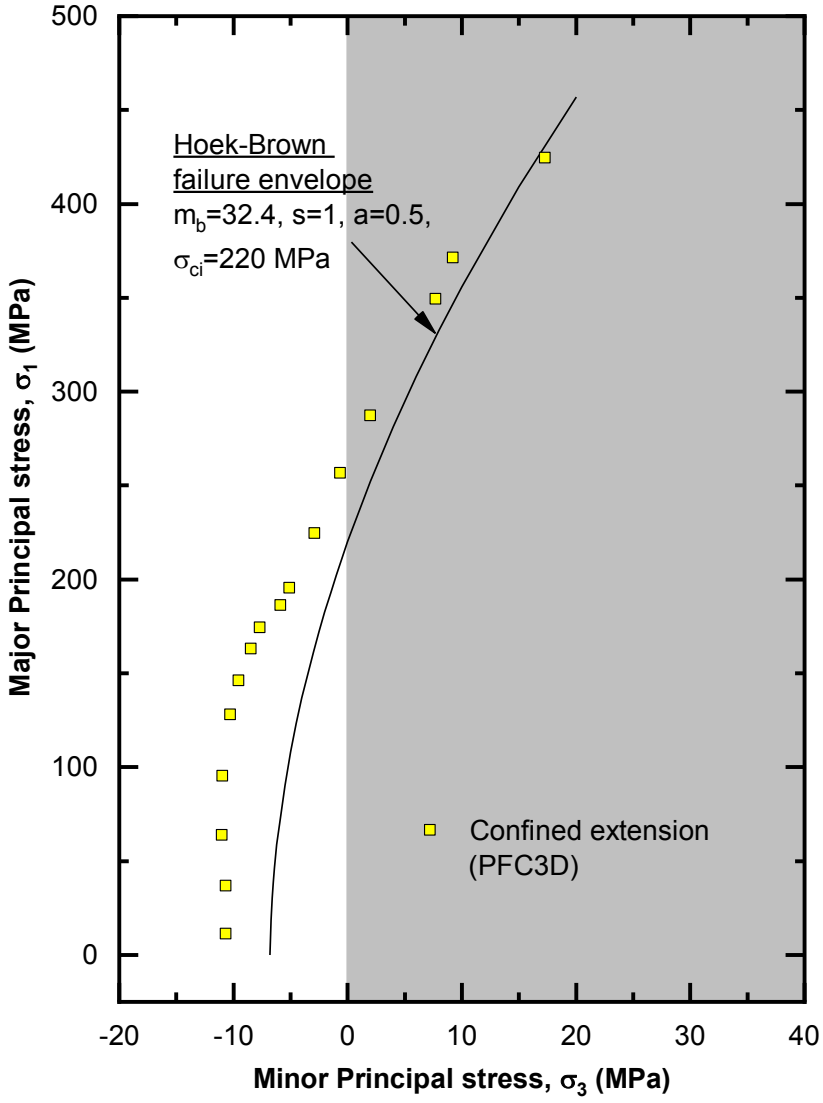

Figure 5.41: PFC3D results on confined extension test (both σ_1 and σ_2 are obtained from the measurement sphere) on Lac du Bonnet granite. Stress path ODEC and OFG (Figure 5.29) were applied to the samples.

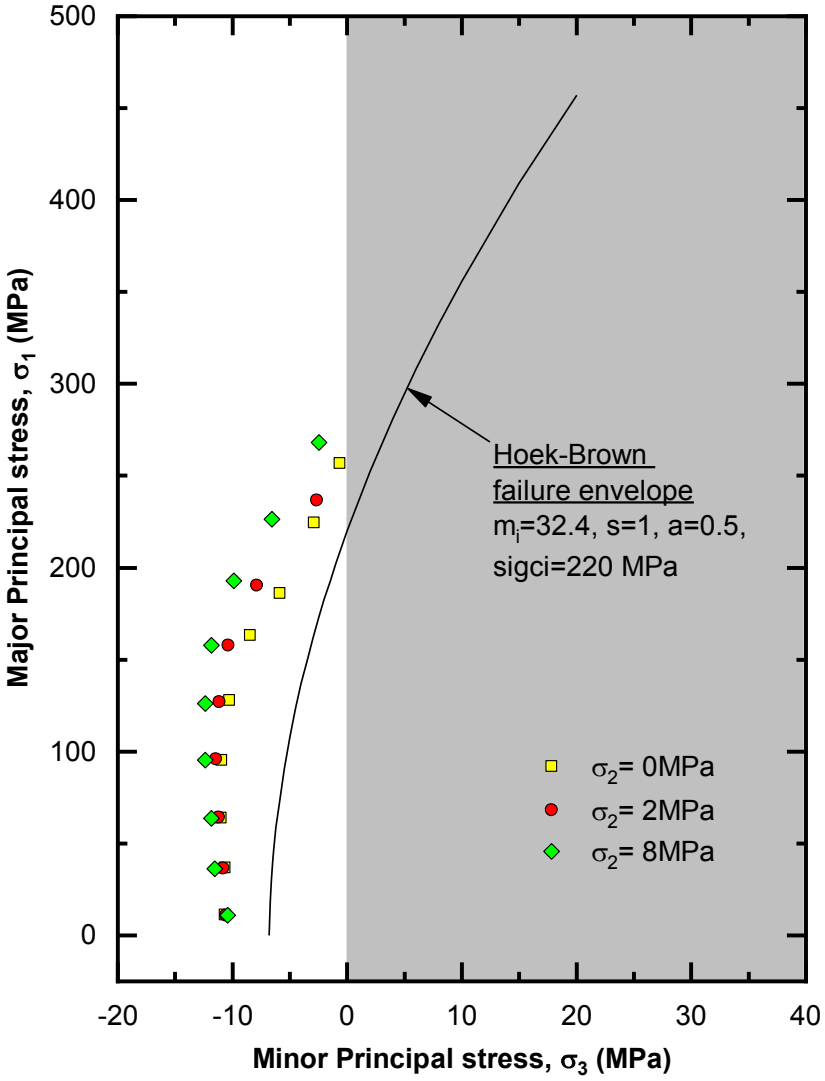

Figure 5.42: PFC3D results on confined extension test (both σ_1 and σ_2 are obtained from the measurement sphere) on Lac du Bonnet granite showing the influence of intermediate principal stress. Stress path ODEC (Figure 5.29) was applied to the samples.

5.21 Summary

The present PFC3D code was modified to study the rock behavior in a confined extension test. By changing the code, it was possible to study the behavior of the rock in confined extension at zero intermediate principal stress. When compared with the Hoek-Brown failure criterion, the data points obtained from the numerical samples in the confined extension were on higher side compared to the data points from the Hoek-Brown criterion. The data points obtained from the Brazilian test and the flattened Brazilian tests were found to be close to the value from the numerical analysis. Limited data available from the laboratory testing (Brazilian and flattened Brazilian tests) and the data from the numerical analysis suggests a tensile cut-off for the material as suggested by Hoek and Martin (2014). The numerical sample shows a clear influence of the intermediate principal stress in the confined extension test. Rock with 90 MPa confinement for both major and intermediate stress produced ~76% higher strength compared to the sample with zero intermediate principal stress. This requires a review of the present methodology to test dog-bone shaped specimen in confined extension.

Chapter 6:

Summary, conclusions and future research

The main objective of this thesis was to investigate the behavior of low-porosity rocks in confined extension with zero intermediate principal stress. The following sections provide the summary of a new laboratory technique developed to obtain the tensile Young's modulus and Poisson's ratio in rock; development of a new technique to test rocks in confined extension; investigating the failure process of rocks in laboratory testing using the flat jointed bonded particle code and the modification of the code to investigate failure envelope of rock in confined extension.

6.1 Validation and application of the digital image correlation technique

The research in the thesis required the application of the digital image correlation (DIC) technique. However, the application of DIC in the rock mechanics application is limited. Hence, it was validated against the strain measured from strain gauges in a Brazilian test. The DIC technique was found useful to map the strain pattern in the Brazilian and the flattened Brazilian tests confirming the uniformity of loading. DIC was also able to monitor the crack growth in the samples.

Using the bi-modular relation between the Young's modulus and Poisson's ratio in compression and tension (Ambartsumyan 1969 and Sundaram and Corrales 2008), new equations relating Young's modulus and Poisson's ratio in tension and the central strain values in a Brazilian test were derived. Brazilian samples of Lac du Bonnet granite taken from the 228 m level of the URL

in southern Manitoba, Canada were tested. The tensile Young's modulus and Poisson's ratio obtained from the strain values at the center of the Brazilian samples were compared with the direct tension test using a dog-bone shaped sample. The difference found was less than 8%. Because the sample preparation and conducting the direct tension test is difficult to carry out, the Brazilian test can be used to estimate the tensile Young's modulus and Poisson's ratio of a rock. However, the measurement of Young's modulus and Poisson's ratio from the central strain values is mainly applicable in case of the fine grained rocks because if the grain size is too big the values obtained will be more representative of the grains than the material itself.

6.2 Evaluation of Tensile Young's modulus and Poisson's ratio of a bi-modular rock from the displacement measurements in a Brazilian test

Since the evaluation of tensile Young's modulus and Poisson's ratio from the strain measurements is mainly applicable for finer grained rocks, it was necessary to develop a new methodology which can provide the Young's modulus and Poisson's ratio for a wide range of rocks using a Brazilian test. The displacements monitored far from the center along the horizontal and vertical diameter during the Brazilian test was used to obtain the Young's modulus and Poisson's ratio in tension. The bi-modularity relationship between the elastic constants (E_c, E_t, ν_c and ν_t) were incorporated in the stress-strain equations of a Brazilian test. New equations were derived to obtain the tensile elastic constants from the displacement measurements along the vertical and horizontal diameter of the Brazilian disk. The DIC technique was used to monitor the displacements on the flat surface of Brazilian disks. The results from the Brazilian tests were found to be in good agreement with the results from direct tensile tests using dog-bone shaped samples. The tensile modulus was found to be 65.4% of the compressive modulus from the Brazilian test while it was 64% of the direct

tensile test. The coefficient of variation in the Brazilian method was 11.9% and from the direct tensile test was 11.2%.

6.3 A new methodology to investigate rock in confined extension

The flattened Brazilian test was used to investigate the confined extension behavior of Lac du Bonnet granite. The flattened Brazilian test was used because in this test the intermediate principal stress is equal to zero, whereas in the conventional confined extension test on a dog bone shaped sample, the intermediate principal stress is equal to the major principal stress. The DIC technique was used to determine the exact location of macro crack formation and to measure the strain values at the crack initiation location on the surface of the samples during the tests.

Flattened Brazilian samples with increasing depth of flattening from 1 mm to 10 mm of Lac du Bonnet granite, were tested. With the increase in the depth of flattening the major principal stress increased from about -33 MPa to -69.2 MPa at 6 mm depth of cut. However a depth of cut beyond 6 mm the does not significantly increase the compressive major principal stress. For the flattened Brazilian samples, it was found that cracking initiates in the samples when the tensile strain reaches around 489 μm/m. With the increase in the major principal stress it was observed that the minor principal stress remains in the range of the Brazilian tensile strength of the material suggesting a tension cut-off for the Lac du Bonnet granite tested. The range of the major principal stress achieved was around 37% of UCS and the data points obtained were used to validate the results from the flat jointed bonded particle model and to investigate the behaviour of Lac du Bonnet granite under a wide range of confinement.

6.4 Investigation of the confined extension behavior of low-porosity rock using the flat jointed bonded particle model

The discrete element code PFC3D was used to investigate the behavior of Lac du Bonnet granite under a wide range of confined extension conditions. A methodology was developed to determine the values of the micro parameter for the particles and flat joints in the numerical sample. A single mineral grain type with an average of 15 particles along the width of the sample was found adequate for simulating (a) bi-modularity, (b) stress-strain non-linearity during initial loading; (c) crack initiation stress, (d) crack damage stress; (e) the ratio between the UCS and direct tension test, and (f) stress-strain response during conventional triaxial testing.

The initial non-linearity in the stress-strain curve which is commonly found in UCS and triaxial test results on cylindrical samples was captured by considering micro gaps between the mineral grains present in the laboratory sample. The numerical sample could reproduce bi-modularity when stress released micro fractures were considered in the model. The ratio between the tensile and compressive Young's modulus obtained was 0.68 which is within 5% obtained of the laboratory test. The numerical modelling showed that the bi-modularity is independent of the grain size and grain size distribution. When bi-modularity was considered in the model, the crack initiation stress was about 40% of the peak strength, which is similar to the values commonly reported for low porosity rocks.

The crack damage stress was found to be mainly a function of micro cohesion, micro friction and the ratio between the normal and shear stiffness of the flat joints. The micro friction was found to influence the stress-strain response after the crack damage stress in an UCS test and the triaxial tests. The peak strength in an UCS test can be matched with different assumed combinations of the micro friction and cohesion of the flat joint. However, the friction angle can be decided by

calibrating the model to the crack damage stress and the triaxial test results. The present rigid boundary technique used in the PFC3D code to apply confinement in a triaxial test was found to capture the triaxial behavior at low confinements while it showed strain hardening at higher confinement greater than 8 MPa. A flexible boundary technique must be used to investigate rocks at high confinement. This was beyond the scope of this research.

The present flat jointed code was modified to study the confined extension of Lac du Bonnet granite samples with and without intermediate principal stress using the appropriate stress path. When compared with the Hoek-Brown failure criterion, the data points obtained from the numerical samples in the confined extension were greater than those predicted using the Hoek-Brown criterion. The data points obtained from the laboratory testing using the Brazilian test and the flattened Brazilian tests were found to be close to the values obtained from the numerical analysis. The laboratory results from the Brazilian and flattened Brazilian tests and the data from the numerical analysis at zero intermediate principal stress, suggest a tension cut-off best fits the data for Lac du Bonnet granite. The numerical results shows a clear influence of the intermediate principal stress on the confined extension test. Rock with 90 MPa compressive stress for both major and intermediate stress produced ~76% higher strength compared to the sample with zero intermediate principal stress.

6.5 Conclusions

The important conclusions and the contributions of this research towards understanding rock failure in confined extension are presented below.

a. Considering an appropriate DIC system and spackle pattern, the digital image correlation technique was found to be capable of capturing the low strain values observed in the testing of low porosity of rock. It has the advantage over the strain gauge measurements

allowing to confirm the uniformity of loading over the entire sample surface and to observe the gradual development of cracks.

b. The displacement and strain produced in a Brazilian test are functions of the load applied; sample dimensions; and the elastic properties in compression and tension. The Brazilian test can be used to evaluate the tensile Young's modulus and Poisson's ratio from the strain and displacement observed, considering the bi-modularity of the sample. The strain method is applicable to fine grained rocks while the displacement technique can be applied to all rocks.

c. The new laboratory technique developed to test Lac du Bonnet granite in confined extension with zero intermediate principal stress can be applied to similar crystalline rocks. However, it has a limitation on the magnitude of the principal stress that can be applied to the sample. Modification in the test methodology is needed to test rocks at a wide range of confinement in the laboratory with zero intermediate principal stress.

d. With some modifications, the flat jointed bonded particle model was able to capture most of the response observed in a rock testing in the laboratory. With a single set of micro parameters and considering one grain type only it could produce (a) the bi-modularity; (b) non-linearity in the initial stress-strain response; (c) crack initiation; (d) crack damage; and (e) the peak strengths in UCS, direct tension and triaxial tests at low confinements.

e. By incorporating the stress released micro fractures in the numerical model, it was possible to capture the bi-modularity behavior observed in the direct tension and the UCS tests. The bi-modularity was found to be the main influencing factor controlling the crack initiation stress. With bi-modularity implemented in the model a crack initiation stress of

approximately 40% of the UCS for Lac du Bonnet granite was obtained. Without bi-modularity the crack initiation stress was only 25% of the UCS.

f. The numerical tests on confined extension samples using the flat jointed bonded particle model produced similar results to that of the Brazilian and flattened Brazilian tests. The laboratory and numerical results obtained for Lac du Bonnet granite suggest a tension cut-off should be used for two-dimensional failure envelopes.

g. To obtain a more reliable Hoek-Brown failure envelope for the confined extension region, the direct tensile strength/ Brazilian strength along with the UCS and triaxial test results should be included when determining the Hoek-Brown parameters.

6.6 Future research

The research conducted here provides a new insight into the behavior of rock in confined extension. Three areas where the additional research can be done for the problem discussed in this thesis are:

a. Continuum modelling typically ignores the bi-modularity of a rock. The impact of this assumption should be investigated.

b. Development of a test technique to conduct confined extension at a wide range of confinement (zero to the UCS of the material).

c. Development of a flexible boundary technique to apply the confinement in confined extension with intermediate principal stress.

d. Improvement in the calculation time and void removal in the flat jointed numerical sample.

The laboratory technique developed in this research tested Lac du Bonnet granite samples up to a confinement of ~37% of the UCS. Although the flat jointed bonded particle was able to capture

the rock behavior observed in the laboratory and was used to investigate a wide range of confinement, a new laboratory technique should be developed to allow further understanding. In the flattened Brazilian testing, acoustic emission technique can also be combined with the DIC to further investigate the fracturing process in the sample.

The present flat jointed PFC3D code uses the rigid boundary technique to apply confinement to a numerical sample. The rigid boundary produces reasonable results while studying the behavior in confined extension with zero intermediate principal stress. However, when a sample with the intermediate principal stress equal to the major principal stress is applied to the model, it produces unreasonable results at high confinement. A flexible boundary approach for confinement application is required to study the behavior in triaxial confined extension.

The run time for the flat jointed numerical sample increases considerably if the number of particles in the model is increased or the flat joints are discretized more. Effort must be given to reduce the run time, so that, the FJ bonded particle can be used to model problems beyond the lab scale in three dimensions. The discrete element sample with spherical particles produces porosity of about 0.35. The interaction range in the model reduces the void in the sample to some extent. However, research should be conducted to reach the porosity of the crystalline rock by the flat jointed model acknowledging its micro structural validity.

Bibliography

Ambartsumyan, S. A. 1969. “Basic Equations and Relations in the Theory of Elasticity of Anisotropic Bodies with Differing Moduli in Tension and Compression.” *Inzh. Zh. Meth. Tverd. Tela. Trans- lation available from Aerospace Corp., El Segundo, Calif., as LRG-70-T-1* 3:51–61.

ASTM Standard D3967-08. 2008. “Standard Test Method for Splitting Tensile Strength of Intact Rock Core Specimens.” *ASTM International, West Conshohocken, PA, DOI: 10.1520/D3967-08.2* 20–23.

ASTM Standard D7012-14. 2014. “Compressive Strength and Elastic Moduli of Intact Rock Core Specimens under Varying States of Stress and Temperatures.” *ASTM International, West Conshohocken, PA 19428-2959*.

Belrhiti, Y. et al. 2017. “Combination of Brazilian Test and Digital Image Correlation for Mechanical Characterization of Refractory Materials.” *Journal of the European Ceramic Society* 37(5):2285–93.

Bieniawski, Z. T. and M. J. Bernede. 1979. “Suggested Methods for Determining the Uniaxial Compressive Strength and Deformability of Rock Materials.” *International Journal of Rock Mechanics and Mining Sciences & Geomechanics Abstracts* 16(2):137–40.

Bobich, Jennifer Kay. 2005. “Experimental Analysis of the Extension to Shear Fracture Transition in Berea Sandstone.” *Texas A&M University* (August):52.

Brace, W. F. 1961. “Dependence of Fracture Strength of Rocks on Grain Size.” *Bull Miner Inds Exp Stn Penn St Univ* 76:99–103.

Brace, W. F. 1964. “Brace1964.Pdf.” Pp. 111–80 in *Brittle failure of rock: State of stress in the earth’s crust*, edited by W. R. Judd. New York: American Elsevier.

Brace, W. F., B. W. Paulding, and C. Scholz. 1966. “Dilatancy in the Fracture of Crystalline Rocks.” *Journal of Geophysical Research* 71(16):3939.

Brady, BHG and ET Brown. 2004. *Rock Mechanics for Underground Mining*. Kluwer Academic Publishers.

Brown, E. T. 1981. *Rock Characterization Testing and Monitoring ISRM Suggested Methods*. Pergamon Press, Oxford.

Collins, D. S. 1997. “Excavation Induced Seismicity in Granitic Rock: A Case Study at the Underground Research Laboratory, Canada.” Keele University.

CorelatedSolutions. 2010a. *CSI Application Note AN-824*. Columbia, SC, USA.

CorelatedSolutions. 2010b. *Vic-3D 2010 Reference Manual*. Columbia, SC, USA.

Cundall, P. A. 2015. “A Discontinuous Future for Numerical Modelling in Geomechanics?” *Proceedings of the Institution of Civil Engineers - Geotechnical Engineering*.

Fairbairn, E. M. R. and F. J. Ulm. 2002. “A Tribute to Fernando L . L . B . Carneiro (1913 - 2001) Engineer and Scientist Who Invented the Brazilian Test.” *Materials and Structures* 35(April):195–96.

Fairhurst, C. 1961. “Laboratory Measurement of Some Physical Properties of Rock.” Pp. 106–17 in *The 4th U.S. Symposium on Rock Mechanics (USRMS), 30 March-1 April, University Park, Pennsylvania*.

Fairhurst, Charles. 1972. “Fundamental Considerations Relating to the Strength of Rock Colloquium on Rock Fracture.” Pp. 1–41 in *Ruhr Universitat, Bochum, Germany*.

Fredrich, Joanne T., Brian Evans, and Teng-Fong Wong. 1990. “Effect of Grain Size on Brittle and Semibrittle Strength: Implications for Micromechanical Modelling of Failure in Compression.” *Journal of Geophysical Research* 95(B7):10907.

Fuenkajorn, Kittitep and Sippakorn Klanphumeesri. 2011. “Laboratory Determination of Direct Tensile Strength and Deformability of Intact Rocks.” *Geotechnical Testing Journal* 34(1):1–6.

Griffith, A. 1921. “The Phenomena of Rupture and Flow in Solids.” *Philosophical Transactions of the Royal Society A: Mathematical, Physical and Engineering Sciences* 221(582–593):163–98.

GrifIith, A. 1924. “Theory of Rupture.” Pp. 55–63 in *Intern. Congr. Appl. Mech., Delft*.

Haimson, B. C. and T. M. Tharp. 1974. “Stresses Around Boreholes in Bilinear Elastic Rock.” *Society of Petroleum Engineers Journal* 14(02):145–51.

Hedayat, A. and G. Walton. 2017. “Laboratory Determination of Rock Fracture Shear Stiffness Using Seismic Wave Propagation and Digital Image Correlation.” *Geotechnical Testing Journal* 40(1):20160035.

Hijazi, A. and C. J. Kähler. 2017. “Contribution of the Imaging System Components in the Overall Error of the Two-Dimensional Digital Image Correlation Technique.” *Journal of Testing and Evaluation* 45(2):20150437.

Hoek, E. and Z. T. Bieniawski. 1965. “Brittle Fracture Propagation in Rock under Compression.” *International Journal of Fracture* 26(4):276–94.

Hoek, E. and E. T. Brown. 1980. *Underground Excavations in Rock*. Institution of Mining and Metallurgy.

Hoek, E. and C. D. Martin. 2014a. “Fracture Initiation and Propagation in Intact Rock - A Review.” *Journal of Rock Mechanics and Geotechnical Engineering* 6(4):287–300.

Hoek, E. and C. D. Martin. 2014b. “Fracture Initiation and Propagation in Intact Rock e A Review.” *Journal of Rock Mechanics and Geotechnical Engineering*.

Hoek, Evert. 1966. “Rock Mechanics - an Introduction for the Practical Engineer.” *Mining Magazine* (July).

Hondros, G. 1959. “The Evaluation of Poisson’s Ratio and the Modulus of Materials of Low Tensile Resistance by the Brazilian (Indirect Tensile) Test with Particular Reference to Concrete.” *Australian Journal of Applied Science* 10:243–68.

Hudson, John A., Edwin T. Brown, and Charles Fairhurst. 1971. “Shape of the Complete Stress-

Strain Curve for Rock." Pp. 773–95 in *13th Symposium Rock Mechanics*. Illionis: University of Illionis Urban.

Irani, Fersheed K. and Akhtar S. Khan. 1987. "Failure Behavior of Rocks at Ambient Temperature." *Mechanics of Materials* 6:271–83.

ISRM. 1978. "Suggested Methods for Determining Tensile Strength of Rock Materials." *Int. J. Rock Mech. Min. Sci. & Geomech. Abstr.* 15:99–103.

Itasca. 2015. *Particle Flow Code (PFC) Version 5.0 User's Guide*. Minneapolis, Minnesota 55401 USA.

Itasca.. 2011. *FLAC 2D 7.0 User's Guide*. Minneapolis, Minnesota 55401 USA.

Itasca. 2013. *FLAC3D 5.0 User's Guide*. Minneapolis, Minnesota 55401 USA.

Jaeger, J. C. and E. R. Hoskins. 1966. "Rock Failure under the Confined Brazilian Test." *Journal of Geophysical Research* 71(10):2651–59.

Labuz, JF. 1985. "A Study of the Fracture Process Zone in Rock." PhD Thesis. Northwestern University, Evanston, Illinois, USA.

Lan, Hengxing, C. Derek Martin, and Bo Hu. 2010. "Effect of Heterogeneity of Brittle Rock on Micromechanical Extensile Behavior during Compression Loading." *Journal of Geophysical Research* 115(B1):B01202.

Lau, J. S. O. and R. Jackson. 1992. *Uniaxial and Triaxial Compression Tests on URL Rock Samples from Boreholes 207-045-GC3 and 209-069-PH3*.

Martin, C. D. and N. A. Chandler. 1994. "The Progressive Fracture of Lac Du Bonnet Granite." *International Journal of Rock Mechanics and Mining Sciences and* 31(6):643–59.

Martin, CD. 1993. "The Strength of Massive Lac Du Bonnet Granite around Underground Openings." PhD Thesis. University of Manitoba, Winnipeg, Canada.

Mogi, Kiyoo. 1967. "Effect of the Intermediate Principal Stress on Rock Failure." *Journal of Geophysical Research* 72(20):5117–31.

Murrell, S. A. F. 1958. “The Strength of Coal under Tri-Axial Compression.” Pp. 123–45 in *Mechanical properties of non-metallic brittle materials*, edited by W. H. Walton. London: Butterworth Scientific Publications.

Nicksiar, Mohsen and C. D. Martin. 2013. “Crack Initiation Stress in Low Porosity Crystalline and Sedimentary Rocks.” *Engineering Geology* 154:64–76.

Park, G. and M. Piasecki. 1993. *Petrofabric Assessment of Samples from the Lac Du Bonnet Batholith*. Retrieved (Keele University Internal Report, Canada.).

Patel, S. and C. D. Martin. 2015. “A New Approach for Applying Confining Stress to a Bonded-Particle Model.” *13th International Congress of Rock Mechanics*.

Patel, S. and C. D. Martin. 2018a. “Application of Digital Image Correlation Technique for Measurement of Tensile Elastic Constants in Brazilian Tests on a Bi-Modular Crystalline Rock.” *Geotechnical Testing Journal*. https://doi.org/10.1520/GTJ20170208. ISSN 0149-6115.

Patel, S. and C. D. Martin. 2018b. “Application of Flattened Brazilian Test to Investigate Rocks under Confined Extension.” *Rock Mechanics and Rock Engineering (Accepted)*.

Patel, S. and C. D. Martin. 2018c. “Evaluation of Tensile Young’s Modulus and Poisson’s Ratio of a Bi-Modular Rock from the Displacement Measurements in a Brazilian Test.” *Rock Mechanics and Rock Engineering* 51(2):361–73.

Paul, Dalim K. and Carthigesu T. Gnanendran. 2016. “Determination of Stiffness Modulus and Poisson’s Ratio of Lightly Stabilized Granular Materials From Indirect Diametral Tensile Testing.” *Geotechnical Testing Journal* 39(4):20150087.

Potyondy, D. O. 2012. “A Flat-Jointed Bonded-Particle Material For Hard Rock.” *46th U.S. Rock Mechanics/Geomechanics Symposium*.

Potyondy, D. O. and P. A. Cundall. 2004. “A Bonded-Particle Model for Rock.” *International Journal of Rock Mechanics and Mining Sciences* 41(8):1329–64.

Potyondy, David. 2017. *Material-Modeling Support in PFC [FistPkg25]*. 111 Third Avenue

South, Suite 450 / Minneapolis, MN 55401.

Ramsey, J. M. 2003. “Experimental Study of the Transition from Brittle Shear Fractures to Joints.” Texas A&M University.

Ramsey, J. M. and M. F. Chester. 2004. “Hybrid Fracture and the Transition from Extension Fracture to Shear Fracture.” *Nature* 428:63–66.

RocLab. 2008. *RocLab Users Guide*. https://www.rocscience.com/

Stirling, Ross A., David J. Simpson, and Colin T. Davie. 2013. “The Application of Digital Image Correlation to Brazilian Testing of Sandstone.” *International Journal of Rock Mechanics and Mining Sciences* 60:1–11.

Sundaram, P. N. and J. M. Corrales. 1980. “Brazilian Tensile Strength of Rocks with Different Elastic Properties in Tension and Compression.” *International Journal of Rock Mechanics and Mining Sciences & Geomechanics Abstracts* 17(2):131–33.

Sundaram, P. N. and J. M. Corrales. 2008. “Brazilian Tensile Strength of Rocks with Different Elastic Properties in Tension and Compression.” *Int. J. Rock Mech. Min. Sci. & Geomech. Abstr.* 62(March):15–18.

Sutton, Michael A., Jean-José Orteu, and Hubert Schreier. 2009. *Image Correlation for Shape, Motion and Deformation Measurements*. Boston, MA: Springer US.

Timoshenko, S. and J. N. Goodier. 1951. *Theory of Elasticity*. New York: McGraw-Hill Book Company, Inc.

Wang, Q. Z. and Lei Xing. 1999. “Determination of Fracture Toughness KIC by Using the Flattened Brazilian Disk Specimen for Rocks.” *Engineering Fracture Mechanics* 64(2):193–201.

Wawersik, Wolfgang Rudolf. 1968. “Detailed Analysis of Rock Failure in Laboratory Compression Tests.” PhD Thesis. University of Minnesota, Minneapolis, USA.

Yang, Diansen, Weizhong Chen, Jianping Yang, and Guojun Wu. 2012. “Application of Digital Image Correlation Technique in Experimental Study of the Creep Behavior and Time

Dependent Damage of Natural Rock Salt." *Journal of Testing and Evaluation* 40(2):220–26.

Ye, J. H., F. Q. Wu, and J. Z. Sun. 2009. "Estimation of the Tensile Elastic Modulus Using Brazilian Disc by Applying Diametrically Opposed Concentrated Loads." *International Journal of Rock Mechanics and Mining Sciences* 46(3):568–76.

Ye, J. H., F. Q. Wu, Y. Zhang, and H. G. Ji. 2012. "Estimation of the Bi-Modulus of Materials through Deformation Measurement in a Brazilian Disk Test." *International Journal of Rock Mechanics and Mining Sciences* 52:122–31.

Appendix A

Derivations for the tensile Young's modulus and Poisson's ratio from the Brazilian test considering the bi-modularity of rock

A.1 Displacement along horizontal and vertical line in a Brazilian test

Figure A.1 shows the Brazilian disk loaded along its vertical diameter EF. For a particular value of load (*P*), the horizontal displacement (*u(x)*) along the horizontal diameter (AB) and the vertical displacement (*v(y)*) along the vertical diameter (EF) are functions of x, y, E_c, E_t, ν_c and ν_t (due to symmetry, the vertical displacement along AB and the horizontal displacement along EF are zero). The derivations for *u(x)* and *v(y)* here follow the methodology that is adopted by Ye et al. (2012). However, the bi-modularity relation between the elastic constants as given by Ambartsumyan (1969) and Sundaram and Corrales (2008) is considered in the Brazilian stress-strain equations.

The horizontal and vertical stress along the horizontal diameter AB are:

$$\sigma_{xx} = \frac{2P}{\pi Dt}\left[1 - \frac{16D^2x^2}{(D^2 + 4x^2)^2}\right] \tag{A-1}$$

$$\sigma_{yy} = \frac{2P}{\pi Dt}\left[1 - \frac{4D^4}{(D^2 + 4x^2)^2}\right] \tag{A-2}$$

and the horizontal and vertical stress along the vertical diameter EF are:

$$\sigma_{xx} = \frac{2P}{\pi Dt} \tag{A-3}$$

$$\sigma_{yy} = \frac{2P}{\pi Dt}\left[1 - \frac{4D^2}{(D^2 - 4y^2)^2}\right] \quad \text{(A-4)}$$

(Hondros 1959 and Ye et al. 2012).

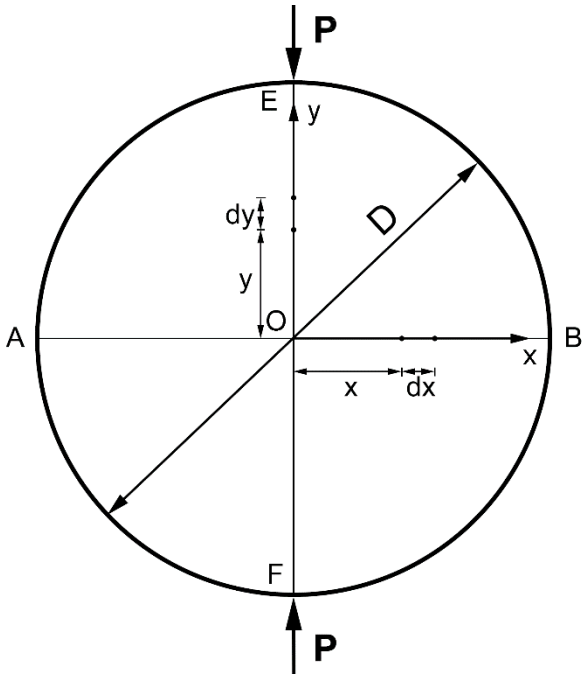

Figure A.1: Brazilian sample loaded along the diameter.

According to Ambartsumyan (1969) and the model adopted by Sundaram and Corrales (2008), the strain-stress relationships for a plane stress condition (σ_{zz}=0) with bi-modularity can be written as:

$$\varepsilon_{xx} = \frac{\sigma_{xx}}{E_t} - C_0\sigma_{yy} \quad \text{(A-5)}$$

and

$$\varepsilon_{yy} = \frac{\sigma_{yy}}{E_c} - C_0\sigma_{xx} \quad \text{(A-6)}$$

where:

$$C_0 = \frac{\nu_t}{E_t} = \frac{\nu_c}{E_c} \tag{A-7}$$

Considering a small segment *dx* at a distance *x* from the center of the disk along the horizontal diameter AB (Figure A.1), the small displacement of this segment is:

$$du = \varepsilon_{xx} dx$$

$$du = \left[\frac{\sigma_{xx}}{E_t} - \frac{\nu_c \sigma_{yy}}{E_c}\right] dx$$

and the total horizontal displacement of the point at distance x is:

$$u(x) = \int_0^x \left[\frac{\sigma_{xx}}{E_t} - \frac{\nu_c \sigma_{yy}}{E_c}\right] dx$$

Substituting the value of σ_{xx} and σ_{yy} from Equations (A-1) and (A-2), *u(x)* can be written as:

$$u(x) = \frac{2P}{\pi D t E_t}\int_0^x dx - \frac{2PD}{\pi t E_t}\int_0^x \frac{16x^2}{(D^2+4x^2)^2}\,dx$$

$$- \frac{2\nu_c P}{\pi D t E_c}\int_0^x dx + \frac{2\nu_c P D^4}{\pi D t E_c}\int_0^x \frac{4}{(D^2+4x^2)^2}\,dx$$

$$\Rightarrow u(x) = \frac{2Px}{\pi D t E_t} - \frac{2PD}{\pi t E_t}\int_0^x \frac{16x^2}{(D^2+4x^2)^2}\,dx - \frac{2\nu_c Px}{\pi D t E_c}$$

$$+ \frac{2\nu_c P D^4}{\pi D t E_c}\int_0^x \frac{4}{(D^2+4x^2)^2}\,dx$$

$$\Rightarrow u(x) = \frac{2Px}{\pi D t E_t} - \frac{2PD}{\pi t E_t} I_1]_0^x - \frac{2\nu_c Px}{\pi D t E_c} + \frac{2\nu_c P D^4}{\pi D t E_c} I_2]_0^x$$

where,

$$I_1 = \int \frac{16x^2}{(D^2 + 4x^2)^2}\,dx$$

and

$$I_2 = \int \frac{4}{(D^2 + 4x^2)^2}\,dx$$

$$I_1 = \int \frac{16x^2}{(D^2 + 4x^2)^2}\,dx = 4\int \frac{4x^2}{(D^2 + 4x^2)^2}\,dx$$

$$\Rightarrow I_1 = 4\int \frac{D^2 + 4x^2 - D^2}{(D^2 + 4x^2)^2}\,dx$$

$$\Rightarrow I_1 = 4\int \frac{dx}{(D^2 + 4x^2)} - 4D^2\int \frac{dx}{(D^2 + 4x^2)^2}$$

$$\Rightarrow I_1 = \frac{4}{D^2}\int \frac{dx}{\left(1 + \frac{4x^2}{D^2}\right)} - 4D^2\int \frac{dx}{(D^2 + 4x^2)^2}$$

Let's assume $w = 2x/D$ for the first part and $x = \frac{D}{2}\ tan\ z$ for the second part.

i.e. $dw = \frac{2}{D}dx$; $(D^2 + 4x^2)^2 = D^4 sec^2 z$ and $dx = \frac{1}{2}D\ sec^2 z$ dz

$$\Rightarrow I_1 = \frac{2}{D}\int \frac{dw}{(1 + w^2)} - \frac{2}{D}\int cos^2 z\ dz$$

$$\Rightarrow I_1 = \frac{2}{D}tan^{-1}\,w - \frac{\sin 2z}{2D} - \frac{z}{D}$$

substituting the values of w and z

$$\Rightarrow I_1 = \frac{2}{D} tan^{-1}\ \frac{2x}{D} - \frac{1}{D}\frac{\left({}^{2x}/_{D}\right)}{\left({}^{2x}/_{D}\right)^2 + 1} - \frac{1}{D} tan^{-1}\ \frac{2x}{D}$$

$$\Rightarrow I_1 = \frac{1}{D} tan^{-1}\ \frac{2x}{D} - \frac{2x}{4x^2 + D^2}$$

$$I_2 = \int \frac{4}{(D^2 + 4x^2)^2} dx$$

Assuming $x = \frac{D}{2} \tan w$

i.e. $(D^2 + 4x^2)^2 = D^4 sec^2 w$ and $dx = \frac{1}{2} D\ sec^2 w\ dw$

$$\Rightarrow I_2 = \frac{2}{D^3} \int cos^2 w\ dw$$

$$\Rightarrow I_2 = \frac{1}{D^3} \int (\cos 2w + 1)\ dw$$

$$I_2 = \frac{1}{D^3}\left(\frac{\sin 2w}{2} + w\right)$$

Substituting the value of *w,*

$$I_2 = \frac{1}{D^2} tan^{-1} \frac{2x}{D} + \frac{2x}{D^2(4x^2 + D^2)}$$

Hence,

$$u(x) = \frac{2Px}{\pi Dt}\left(\frac{1}{E_t} - \frac{\nu_c}{E_c}\right) - \frac{2PD}{\pi t E_t} I_1]_0^x + \frac{2\nu_c PD^4}{\pi Dt E_c} I_2]_0^x$$

Substituting the vales for I_1 and I_2 and rearranging u(x) can be written as:

$$u(x) = \frac{2P}{\pi t}\left[\left(\frac{x}{D} - tan^{-1}\frac{2x}{D}\right)\left(\frac{1}{E_t} - \frac{\nu}{E_c}\right) + \frac{2Dx}{4x^2 + D^2}\left(\frac{1}{E_t} + \frac{\nu_c}{E_c}\right)\right] \quad \text{(A-8)}$$

or in terms of *du/dP*

$$du/dP = \frac{1}{m_x} = \frac{2}{\pi t}\left[\left(\frac{x}{D} - tan^{-1}\frac{2x}{D}\right)\left(\frac{1}{E_t} - \frac{\nu}{E_c}\right) + \frac{2Dx}{4x^2 + D^2}\left(\frac{1}{E_t} + \frac{\nu_c}{E_c}\right)\right] \quad \text{(A-9)}$$

where,

$m_x = dP/du$ (slope of *u-P* plot, Figure 3.7)

Similarly, considering a small segment *dy* at a distance *y* from the center of the disk along the vertical diameter EF (Figure A.1), the small displacement of this segment is:

$$dv = \left[\frac{\sigma_{yy}}{E_c} - \frac{\nu_t \sigma_{xx}}{E_t}\right] dy = \left[\frac{\sigma_{yy}}{E_c} - \frac{\nu_c \sigma_{xx}}{E_c}\right] dy$$

and the total vertical displacement of the point at distance *y* is:

$$v(y) = \int_0^y \left[\frac{\sigma_{yy}}{E_c} - \frac{\nu_c \sigma_{xx}}{E_c}\right] dy$$

$$\Rightarrow v(y) = \frac{1}{E_c}\int_0^y \sigma_{yy} dy - \frac{\nu_c}{E_c}\int_0^y \sigma_{xx} dy$$

substituting the value of σ_{xx} and σ_{yy} from Eqs. (A-3) and (A-4), $v(x)$ can be written as:

$$v(y) = \frac{1}{E_c}\int_0^y \frac{2P}{\pi D t}\left(1 - \frac{4D^2}{D^2 - 4y^2}\right) dy - \frac{\nu_c}{E_c}\int_0^y \frac{2P}{\pi D t} dy$$

$$\Rightarrow v(y) = \frac{2P}{\pi D t E_c}\int_0^y dy - \frac{8DP}{\pi t E_c}\int_0^y \left(\frac{1}{D^2 - 4y^2}\right) dy - \frac{2P\nu_c}{\pi D t E_c}\int_0^y dy$$

$$\Rightarrow v(y) = \frac{2Py}{\pi D t E_c}(1 - \nu_c) - \frac{8DP}{\pi t E_c} I_3]_0^y$$

where,

$$I_3 = \int \frac{dy}{(D^2 - 4y^2)}$$

Assuming *2y=t* i.e. *2dy=dt*

$$I_3 = \frac{1}{2}\int \frac{dt}{(D^2 - t^2)}$$

$$\Rightarrow I_3 = \frac{1}{2}\left(\frac{1}{2D} ln\left[\frac{D + t}{D - t}\right]\right)$$

$$\Rightarrow I_3 = \frac{1}{4D} ln\left[\frac{D+2y}{D-2y}\right]$$

substituting the value of I_3

$$\Rightarrow v(y) = \frac{2Py}{\pi DtE_c}(1-\nu_c) - \frac{8DP}{\pi tE_c}\left(\frac{1}{4D} ln\left[\frac{D+2y}{D-2y}\right]\right)$$

$$\Rightarrow v(y) = \frac{2Py}{\pi DtE_c}(1-\nu_c) - \frac{2P}{\pi tE_c} ln\left[\frac{D+2y}{D-2y}\right]$$

$$v(y) = -\frac{2P}{\pi tE_c}\left[ln\frac{D+2y}{D-2y} + \frac{y}{D}(1-\nu_c)\right] \quad \text{(A-10)}$$

or in terms of *dv/dP*

$$\frac{dv}{dP} = \frac{1}{m_y} = -\frac{2}{\pi tE_c}\left[ln\frac{D+2y}{D-2y} + \frac{y}{D}(1-\nu_c)\right] \quad \text{(A-11)}$$

where,

$m_y = dP/dv$ (slope of *v*-*P* plot, Figure 3.7)

A.2 Calculation of tensile modulus from the displacement measurements

The horizontal displacement equation

$$u(x) = \frac{2P}{\pi t}\left[\left(\frac{x}{D} - tan^{-1}\frac{2x}{D}\right)\left(\frac{1}{E_t} - \frac{\nu}{E_c}\right) + \frac{2Dx}{4x^2+D^2}\left(\frac{1}{E_t} + \frac{\nu_c}{E_c}\right)\right]$$

can be written as:

$$C = \mathrm{A}\left(\frac{1}{E_t} - \frac{\nu_c}{E_c}\right) + B\left(\frac{1}{E_t} + \frac{\nu_c}{E_c}\right) \quad \text{(A-12)}$$

where,

$$A = \left(\frac{x}{D} - tan^{-1}\frac{2x}{D}\right);\ B = \frac{2Dx}{4x^2+D^2}\ and\ C = \frac{\pi ut}{2P} = \frac{\pi t}{2m_x} \quad \text{(A-13)}$$

The vertical displacement equation

$$v(y) = -\frac{2P}{\pi t E_c}\left[ln\frac{D+2y}{D-2y} + \frac{y}{D}(1-\nu_c)\right]$$

can be written as:

$$F = \frac{1}{E_c}[G + H(1-\nu_c)]$$

where,

$$F = -\frac{\pi v t}{2P} = -\frac{\pi t}{2m_y}; G = ln\frac{D+2y}{D-2y}\ and\ H = \frac{y}{D} \tag{A-14}$$

$$\frac{1}{E_c} = \frac{F}{[G + H(1-\nu_c)]} \tag{A-15}$$

substituting the value of $\frac{1}{E_c}$ in Equation (A-12) and rearranging, E_t can be expressed as:

$$E_t = \frac{A+B}{C + \frac{(A-B)E\nu_c}{F + G(\nu_c - 1)}} \tag{A-16}$$

The elastic constants are related by the equation (Ambartsumyan 1969):

$$\frac{\nu_t}{E_t} = \frac{\nu_c}{E_c}$$

Substituting the value of $1/E_c$ and E_t, ν_t can be written as:

$$\nu_t = \frac{(A+B)F\nu_c}{[G + H(1-\nu_c)]\left[C + \frac{(A-B)F\nu_c}{G + H(\nu_c - 1)}\right]} \tag{A-17}$$

A.3 Sample calculation for Young's modulus and Poisson's ratio in tension form the displacement measurements

The typical value obtained for a sample and the parameters A, B, C, F, G, H, E_c, E_t and ν_t as per the (A-13), (A-14), (A-15), (A-16) and (A-17) are shown in Table A-1. The coefficient of variation for the tensile Young's modulus and Poisson's ratio are 6.0% and 3.7% respectively. These variations within the sample are acceptable considering the different kinds of mineral grains present in the sample as discussed in section 3.3 and because some plastic strain may have developed in the sample even at 50% of the peak load.

Table A-1: Typical values measured and the tensile modulus and Poisson's ratio obtained for a sample

Parameters	*(P1 & P6) vs (P1′ & P6′)*	*(P2 & P5) vs (P2′ & P5′)*	*(P3 & P4) vs (P3′ & P4′)*	*Average*	*SD*	*CoV (%)*
P (kN)	16.02	16.02	16.02	-	-	-
m_x (kN/mm)	5.9E+06	6.1E+06	3.9E+06	-	-	-
m_y (kN/mm)	2.0E+06	2.8E+06	4.6E+06	-	-	-
x (m)	0.022	0.016	0.011	-	-	-
y (m)	0.023	0.017	0.011	-	-	-
u (m)	2.7E-06	2.5E-06	2.1E-06	-	-	-
v (m)	8.1E-06	5.6E-06	3.5E-06	-	-	-
A	-0.26	-0.22	-0.16	-	-	-
B	0.47	0.41	0.31	-	-	-
C (m^2/kN)	0.01	0.01	0.01	-	-	-
F (m^2/kN)	0.02	0.02	0.01	-	-	-
G	1.81	1.20	0.75	-	-	-
H	0.36	0.27	0.18	-	-	-
E_t (GPa)	42.3	41.0	37.6	40.3	2.4	6.0
ν_t	0.16	0.17	0.16	0.16	0.01	3.7
E_c (GPa)	67.6	63.4	62.7	64.6	2.7	4.1

Appendix B

Additional Figures and results on Brazilian and flattened Brazilian testing

B.1 Sample preparation

Figure B.2: Lac du Bonnet cores taken from 228 level of URL in southern Manitoba, Canada

Figure B.3: Cutting a Lac du Bonnet granite core using a diamond saw

Figure B.4: Grinding a Lac du Bonnet granite sample using a surface grinder

Figure B.5: Inspecting the flatness of a Lac du Bonnet granite sample

Figure B.6: Preparing a Lac du Bonnet granite sample for DIC measurement. A layer of white paint was sprayed first and then using an ultra fine sharpie black spackle pattern was made

B.2 Results of flattened Brazilian test on Lac du Bonnet granite

The results of 1mm, 4 mm, 6mm, 8 mm and 10 mm depth of flattening are presented in Figure B.7 to Figure B14 and Table B-2 to Table B-7. The average value, standard deviation and the coefficient of variation of all specimens are given in Table B-7.

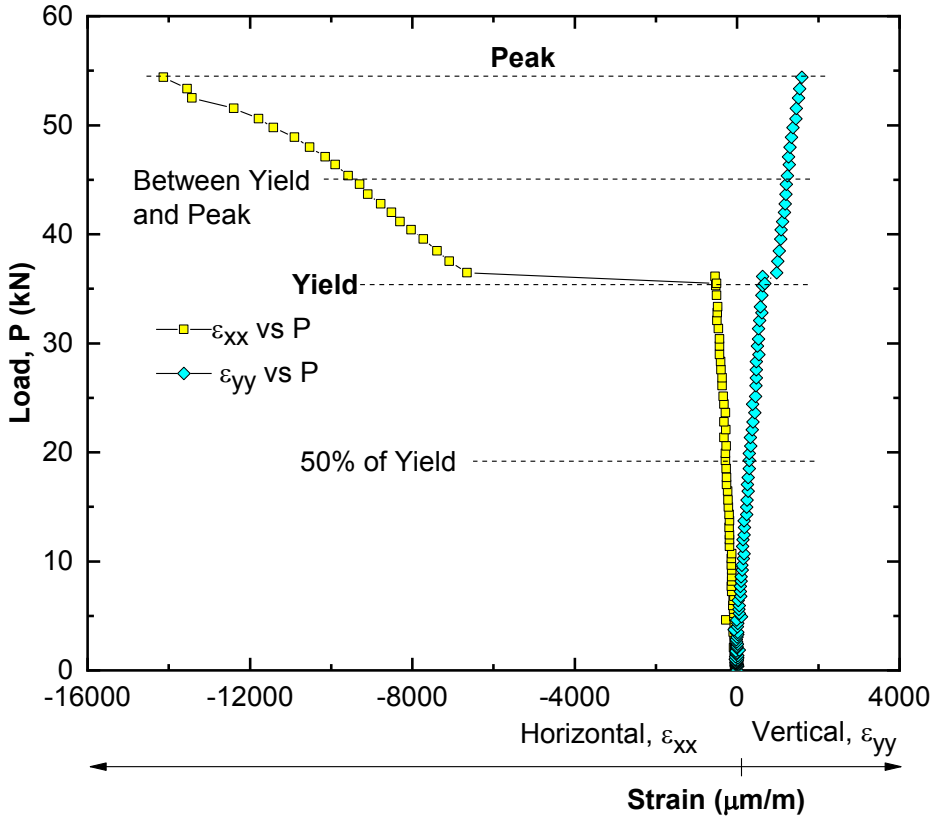

Figure B.7:Typical load strain plot obtained from DIC measurements (depth of flattening 1mm) showing yield and peak and other load levels at which strain values are compared in Figure B.8

Figure B.8: Typical strain contours obtained from the DIC analysis at different load levels (depth of flattening 1mm, see Figure B.7 for the load levels). (a), (b), (c) and (d) Horizontal strain (ε_{xx}) at 50% of yield, at yield, between yield and peak and at peak respectively. (e), (f), (g) and (h) Vertical strain (ε_{yy}) at 50% of yield, at yield, between yield and peak and at peak respectively.

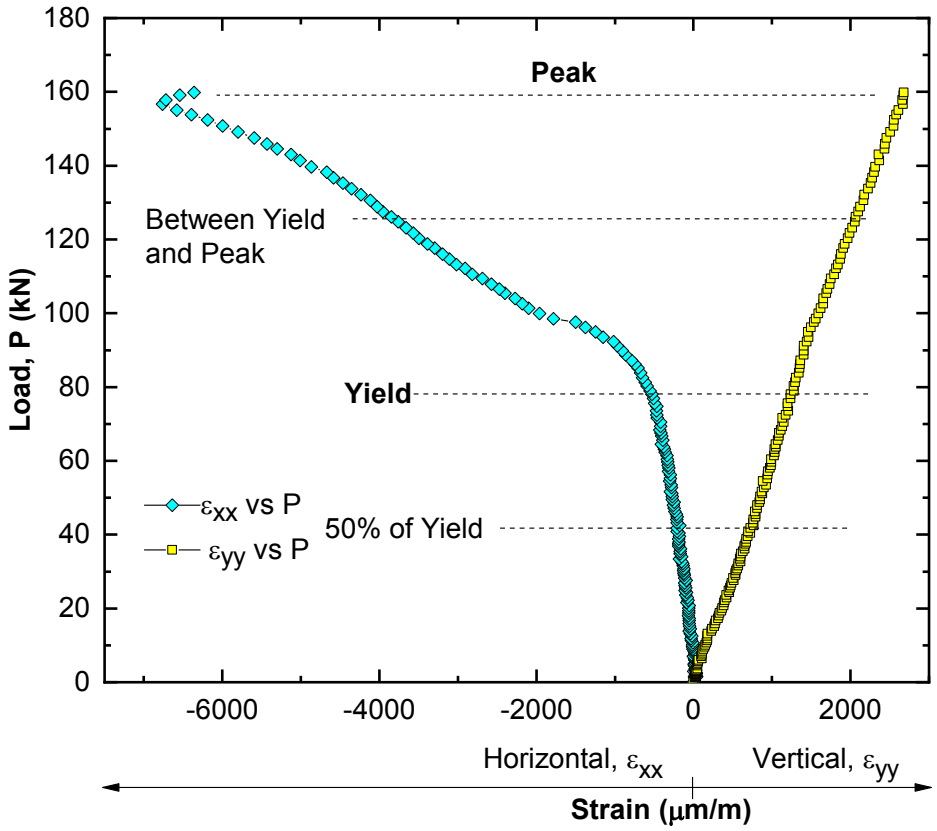

Figure B.9: Typical load strain plot obtained from DIC measurements (depth of flattening 6mm) showing yield and peak and other load levels at which strain values are compared in Figure B.10

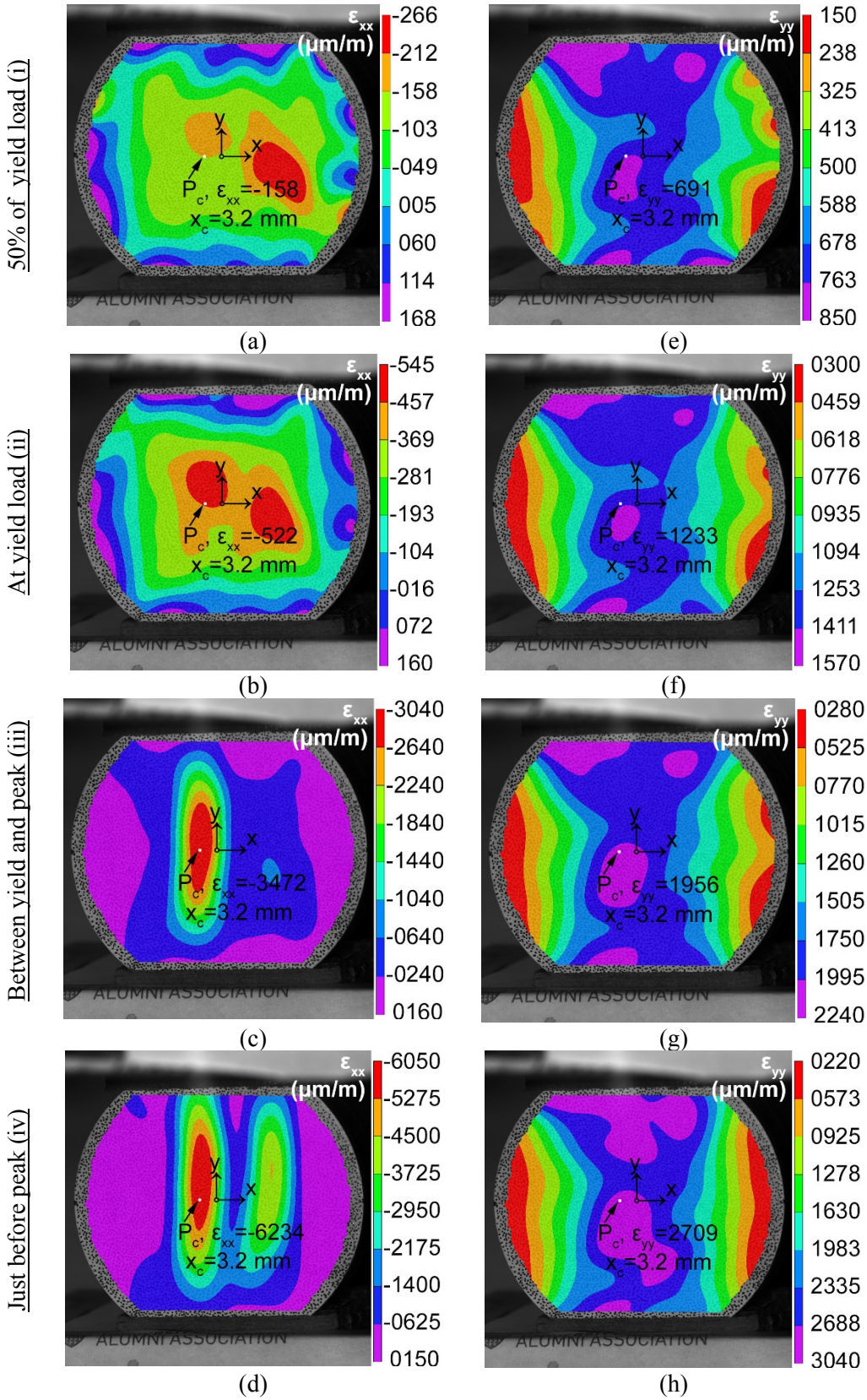

Figure B.10: Typical strain contours obtained from the DIC analysis at different load levels (depth of flattening 6mm, see Figure B.9 for the load levels). (a), (b), (c) and (d) Horizontal strain (ε_{xx}) at 50% of yield, at yield, between yield and peak and at peak respectively. (e), (f), (g) and (h) Vertical strain (ε_{yy}) at 50% of yield, at yield, between yield and peak and at peak respectively.

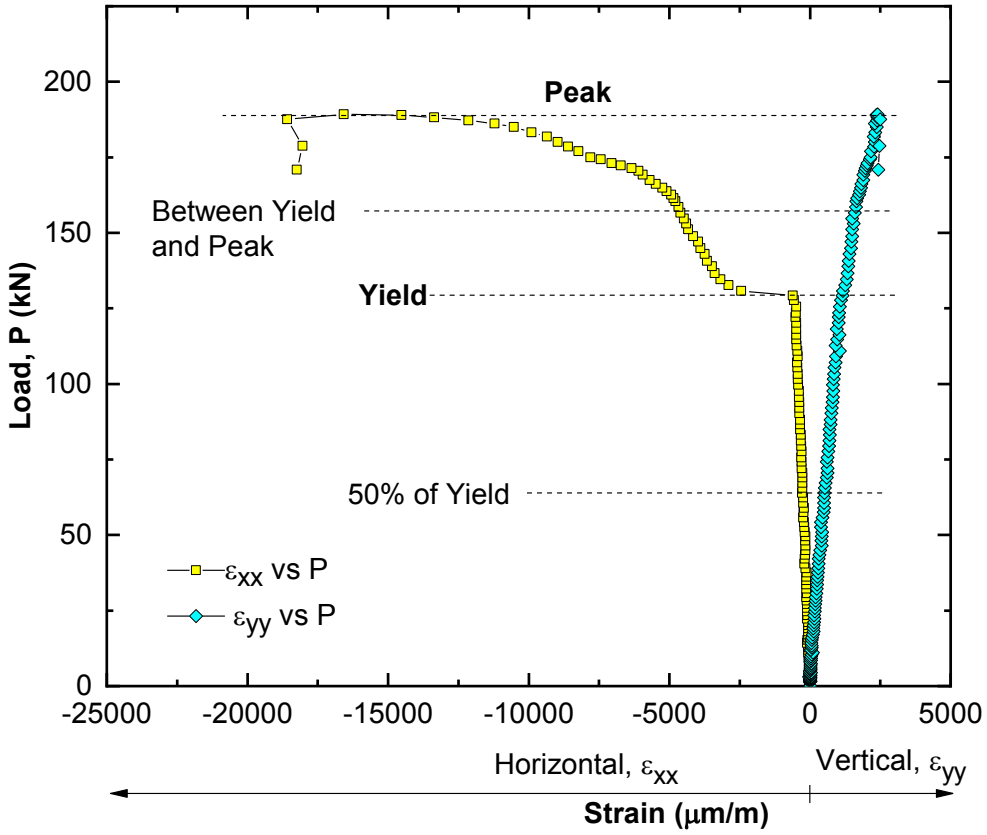

Figure B.11: Typical load strain plot obtained from DIC measurements (depth of flattening 8mm) showing yield and peak and other load levels at which strain values are compared in Figure B.12

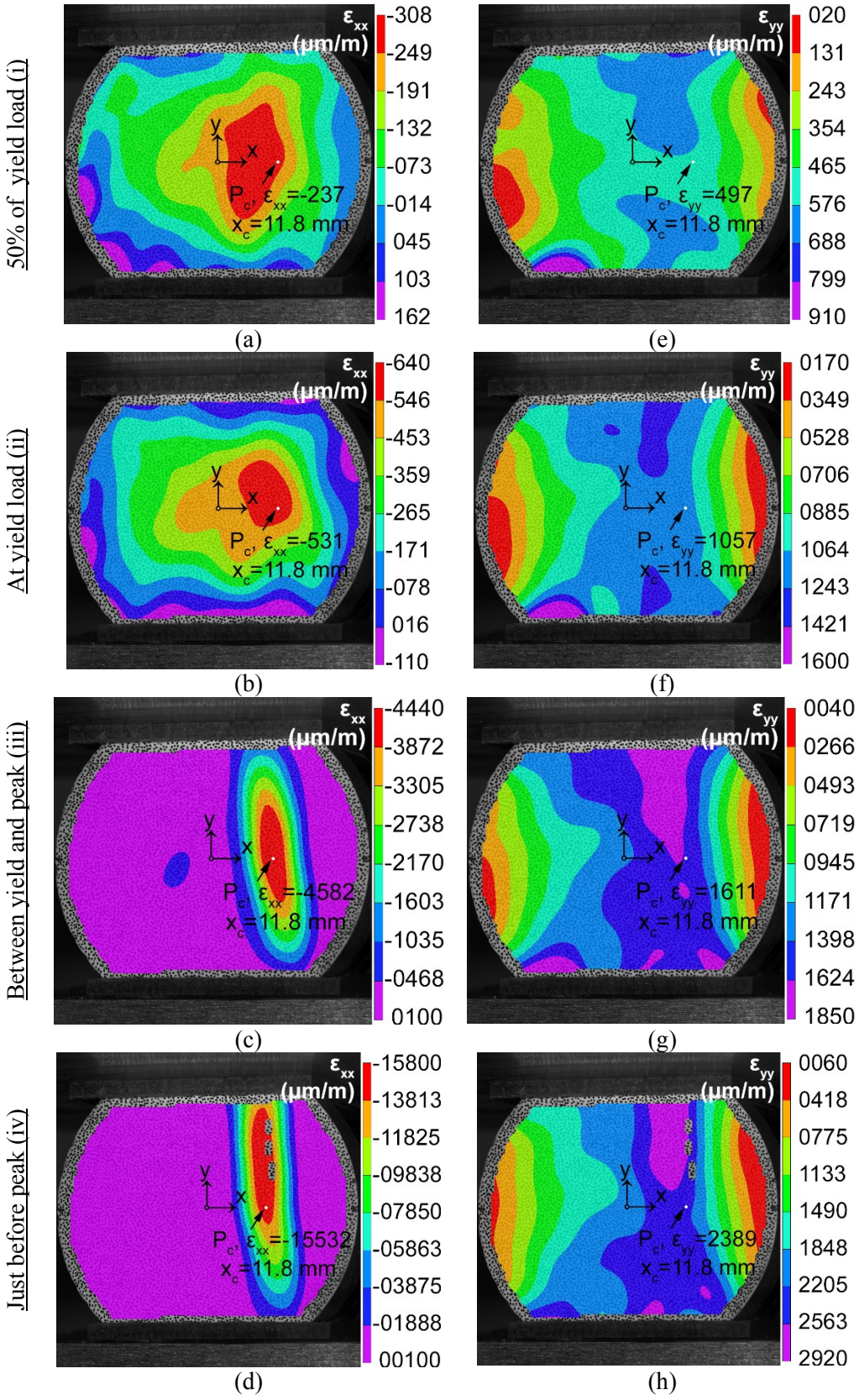

Figure B.12: Typical strain contours obtained from the DIC analysis at different load levels (depth of flattening 8mm, see Figure B.11 for the load levels). (a), (b), (c) and (d) Horizontal strain (ε_{xx}) at 50% of yield, at yield, between yield and peak and at peak respectively. (e), (f), (g) and (h) Vertical strain (ε_{yy}) at 50% of yield, at yield, between yield and peak and at peak respectively.

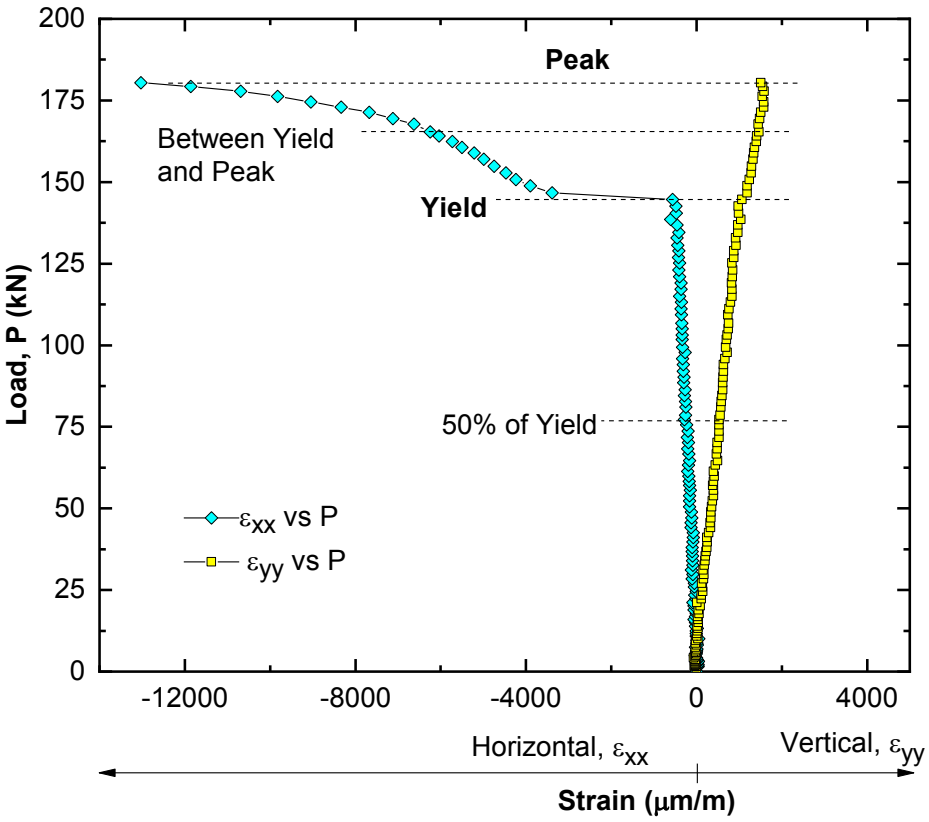

Figure B.13: Typical load strain plot obtained from DIC measurements (depth of flattening 10mm) showing yield and peak and other load levels at which strain values are compared in Figure B.14

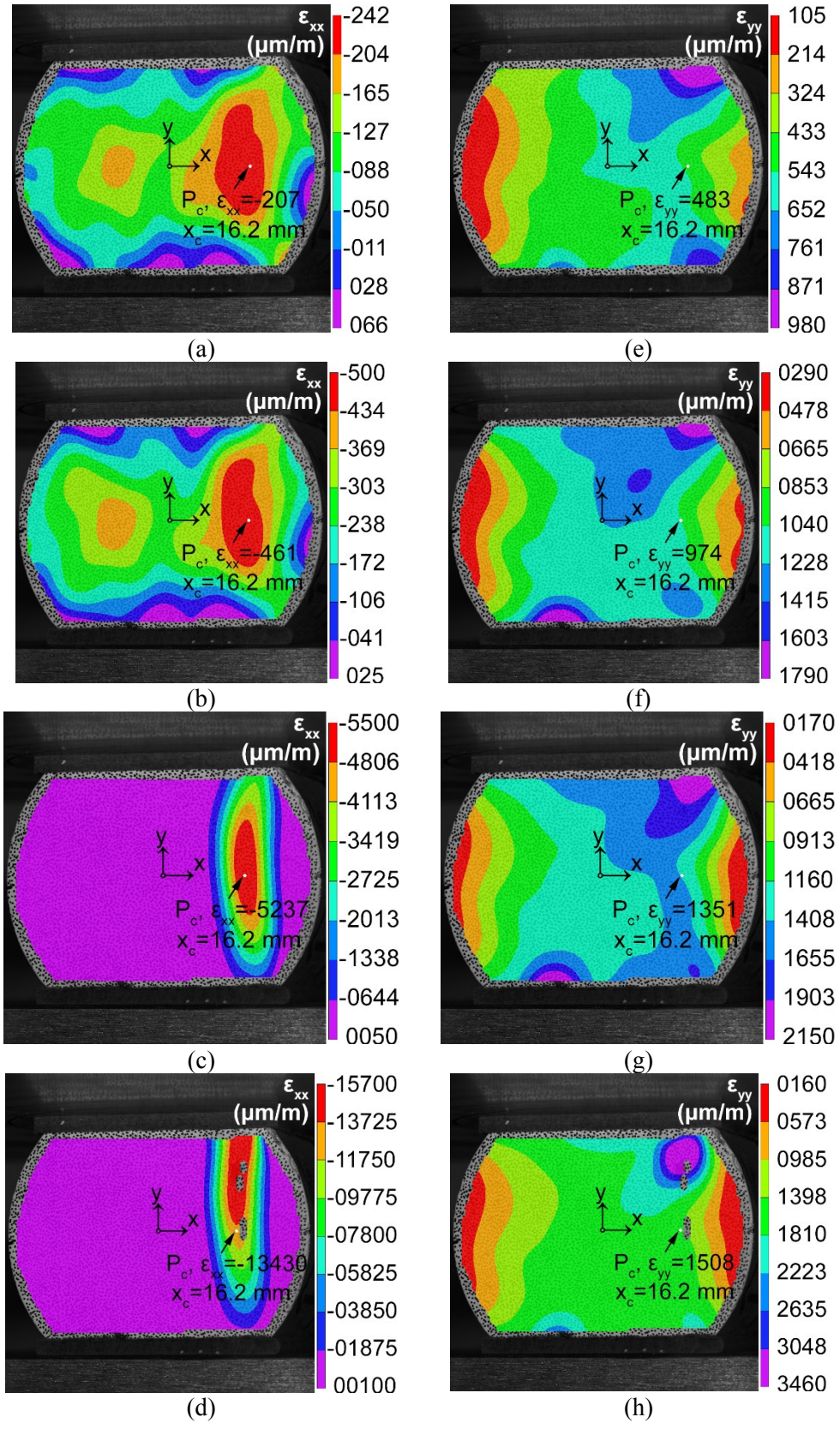

Figure B.14: Typical strain contours obtained from the DIC analysis at different load levels (depth of flattening 10mm, see Figure B.13 for the load levels). (a), (b), (c) and (d) Horizontal strain (ε_{xx}) at 50% of yield, at yield, between yield and peak and at peak respectively. (e), (f), (g) and (h) Vertical strain (ε_{yy}) at 50% of yield, at yield, between yield and peak and at peak respectively.

Table B-2: Results of flattened Brazilian test on 1 mm depth of flattening of Lac du Bonnet granite (see Figure 4.7, $_Y$= yield, $_P$=peak)

Specimen	t (mm)	w (mm)	$\varepsilon_{xx,y}$ µm/m	$\varepsilon_{yy,y}$ µm/m	x_c (mm)	$\sigma_{TOP,Y}$ (MPa)	$\sigma_{TOP,P}$ (MPa)	σ_3 (MPa)	σ_1 (MPa)
LdB-1-1	24.5	7.8	-432.2	783.1	4.1	124.5	206.3	-10.1	48.1
LdB-1-2	26.1	7.8	-417.1	662.0	0.2	148.3	296.9	-10.9	40.1
LdB-1-3	24.9	7.9	-448.0	645.2	1.3	122.6	231.8	-12.4	38.6
LdB-1-4	29.9	7.9	-503.6	791.8	1.8	154.8	234.6	-13.2	47.9
LdB-1-5	30.0	7.6	-363.1	568.9	0.0	127.2	278.5	-9.5	34.4
Mean	***27.1***	***7.8***	***-432.8***	***690.2***	***1.5***	***135.5***	***249.6***	***-11.2***	***41.8***
SD	***2.7***	***0.1***	***50.9***	***95.5***	***1.7***	***15.0***	***37.0***	***1.5***	***6.0***
CoV	***10.0***	***1.2***	***11.8***	***13.8***	***110.3***	***11.0***	***14.8***	***13.7***	***14.4***

Table B-3: Results of flattened Brazilian test on 4 mm depth of flattening of Lac du Bonnet granite (see Figure 4.7, $_Y$= yield, $_P$=peak)

Specimen	t (mm)	w (mm)	$\varepsilon_{xx,y}$ µm/m	$\varepsilon_{yy,y}$ µm/m	x_c (mm)	$\sigma_{TOP,Y}$ (MPa)	$\sigma_{TOP,P}$ (MPa)	σ_3 (MPa)	σ_1 (MPa)
LdB-4-1	29.8	15.4	-474.0	910.5	61.5	133.6	267.7	-10.5	56.3
LdB-4-2	29.8	15.4	-508.1	1040.0	75.8	164.7	299.9	-10.5	64.6
LdB-4-3	30.4	15.4	-497.4	861.0	59.9	127.6	273.7	-12.1	52.6
LdB-4-4	30.0	15.5	-534.3	1034.4	60.0	129.3	271.1	-11.8	64.0
LdB-4-5	30.0	15.4	-508.6	944.0	59.0	127.8	264.6	-11.7	58.1
Mean	***30.0***	***15.4***	***-504.5***	***958.0***	***63.2***	***136.6***	***275.4***	***-11.3***	***59.1***
SD	***0.2***	***0.0***	***21.8***	***78.1***	***7.1***	***15.9***	***14.1***	***0.7***	***5.1***
CoV	***0.8***	***0.2***	***4.3***	***8.2***	***11.2***	***11.7***	***5.1***	***6.6***	***8.7***

Table B-4: Results of flattened Brazilian test on 6 mm depth of flattening of Lac du Bonnet granite (see Figure 4.7, $_Y$= yield, $_P$=peak)

Specimen	t (mm)	w (mm)	$\varepsilon_{xx,y}$ µm/m	$\varepsilon_{yy,y}$ µm/m	x_c (mm)	$\sigma_{TOP,Y}$ (MPa)	$\sigma_{TOP,P}$ (MPa)	σ_3 (MPa)	σ_1 (MPa)
LdB-6-1	41.9	18.5	-472.2	1068.3	11.8	136.1	260.8	-8.6	67.0
LdB-6-2	40.0	18.6	-484.8	1057.5	8.1	126.1	266.0	-9.3	66.1
LdB-6-3	41.4	18.6	-576.2	1302.9	5.0	182.9	272.6	-10.5	81.7
LdB-6-4	29.9	18.6	-507.1	859.4	7.0	120.9	291.2	-12.6	52.4
LdB-6-5	29.9	18.6	-516.9	1247.3	3.2	137.9	272.5	-8.7	78.6
Mean	***36.6***	***18.6***	***-511.4***	***1107.1***	***7.0***	***140.8***	***272.6***	***-10.0***	***69.2***
SD	***6.1***	***0.0***	***40.3***	***175.6***	***3.3***	***24.6***	***11.5***	***1.7***	***11.6***
CoV	***16.8***	***0.2***	***7.9***	***15.9***	***46.9***	***17.4***	***4.2***	***16.6***	***16.8***

Table B-5: Results of flattened Brazilian test on 8 mm depth of flattening of Lac du Bonnet granite (see Figure 4.7, $_Y$= yield, $_P$=peak)

Specimen	t (mm)	w (mm)	$\varepsilon_{xx,y}$ µm/m	$\varepsilon_{yy,y}$ µm/m	x_c (mm)	$\sigma_{TOP,Y}$ (MPa)	$\sigma_{TOP,P}$ (MPa)	σ_3 (MPa)	σ_1 (MPa)
LdB-8-1	35.1	21.1	-516.7	1183.0	13.1	164.4	276.7	-9.3	74.2
LdB-8-2	35.0	21.1	-501.0	1002.5	14.0	173.7	243.0	-10.7	62.2
LdB-8-3	35.0	21.1	-514.5	923.1	13.3	173.0	270.7	-12.2	56.7
LdB-8-4	35.0	21.1	-543.0	1213.7	7.8	186.3	285.2	-10.1	76.0
LdB-8-5	35.0	21.1	-544.4	1135.3	11.8	175.6	256.5	-11.1	70.7
Mean	***35.0***	***21.1***	***-523.9***	***1091.5***	***12.0***	***174.6***	***266.4***	***-10.7***	***68.0***
SD	***0.1***	***0.0***	***19.0***	***124.0***	***2.5***	***7.8***	***16.8***	***1.1***	***8.3***
CoV	***0.2***	***0.0***	***3.6***	***11.4***	***20.6***	***4.5***	***6.3***	***10.2***	***12.2***

Table B-6: Results of flattened Brazilian test on 10 mm depth of flattening of Lac du Bonnet granite (see Figure 4.7, $_Y$= yield, $_P$=peak)

Specimen	t (mm)	w (mm)	$\varepsilon_{xx,y}$ µm/m	$\varepsilon_{yy,y}$ µm/m	x_c (mm)	$\sigma_{TOP,Y}$ (MPa)	$\sigma_{TOP,P}$ (MPa)	σ_3 (MPa)	σ_1 (MPa)
LdB-10-1	35.1	23.1	-514.6	1089.3	17.0	186.0	245.3	-10.3	67.9
LdB-10-2	35.0	23.1	-463.2	1183.9	17.4	181.0	248.9	-6.9	74.9
LdB-10-3	34.1	23.1	-455.1	951.2	16.2	173.4	229.2	-9.2	59.2
LdB-10-4	34.9	23.1	-490.3	915.5	16.3	142.6	239.2	-11.2	56.4
LdB-10-5	35.0	23.1	-440.3	1212.2	13.1	145.7	267.4	-5.5	77.1
Mean	***34.8***	***23.1***	***-472.7***	***1070.4***	***16.0***	***165.8***	***246.0***	***-8.6***	***67.1***
SD	***0.4***	***0.0***	***29.7***	***133.8***	***1.7***	***20.2***	***14.1***	***2.3***	***9.2***
CoV	***1.1***	***0.0***	***6.3***	***12.5***	***10.5***	***12.2***	***5.7***	***27.3***	***13.7***

Table B-7: Mean, standard deviation and coefficient of variation of the results obtained for all Lac du Bonnet granite specimens tested in flattened Brazilian (see Figure 4.7, $_Y$= yield, $_P$=peak)

Depth of flattening (mm)		1	4	6	8	10
Number of specimens tested		5	5	5	5	5
$\varepsilon_{xx,Y}$ (μm/m)	Mean	-432.8	-504.5	-511.4	-523.9	-472.7
	StDev	50.9	21.8	40.3	19.0	29.7
	CoV	11.8	4.3	7.9	3.6	6.3
$\varepsilon_{yy,Y}$ (μm/m)	Mean	690.2	958.0	1107.1	1091.5	1070.4
	StDev	95.5	78.1	175.6	124.0	133.8
	CoV	13.8	8.2	15.9	11.4	12.5
x_c (mm)	Mean	1.5	3.9	7.0	12.0	16.0
	StDev	1.7	2.7	3.3	2.5	1.7
	CoV	110.3	69.2	46.9	20.6	10.5
$\sigma_{TOP,Y}$ (MPa)	Mean	135.5	136.6	140.8	174.6	165.8
	StDev	15.0	15.9	24.6	7.8	20.2
	CoV	11.0	11.7	17.4	4.5	12.2
$\sigma_{TOP,P}$ (MPa)	Mean	249.6	275.4	272.6	266.4	246.0
	StDev	37.0	14.1	11.5	16.8	14.1
	CoV	14.8	5.1	4.2	6.3	5.7
σ_3 (MPa)	Mean	-11.2	-11.3	-10.0	-10.7	-8.6
	StDev	1.5	0.7	1.7	1.1	2.3
	CoV	13.7	6.6	16.6	10.2	27.3
σ_1 (MPa)	Mean	41.8	59.1	69.2	68.0	67.1
	StDev	6.0	5.1	11.6	8.3	9.2
	CoV	14.4	8.7	16.8	12.2	13.7
P_P (kN)	Mean	28.8	73.4	96.9	129.0	133.3
	StDev	5.2	3.3	28.7	5.7	16.3
	CoV	18.2	4.4	29.7	4.4	12.2

Appendix C

Additional results on PFC3D modeling and FISH code for confined extension

C.1 Impact of bond cohesion/friction angle on the crack damage stress

To see the impact of friction angle on the failure envelope, the friction angle was changed from 30^0 to 56^0. The micro cohesion value was decreased to produce the same value of UCS. Figure C.15a shows the Impact of friction angle on triaxial test while Figure C.15b shows the relation between the cohesion and friction angle to produce same value of direct tension and UCS for the numerical sample.

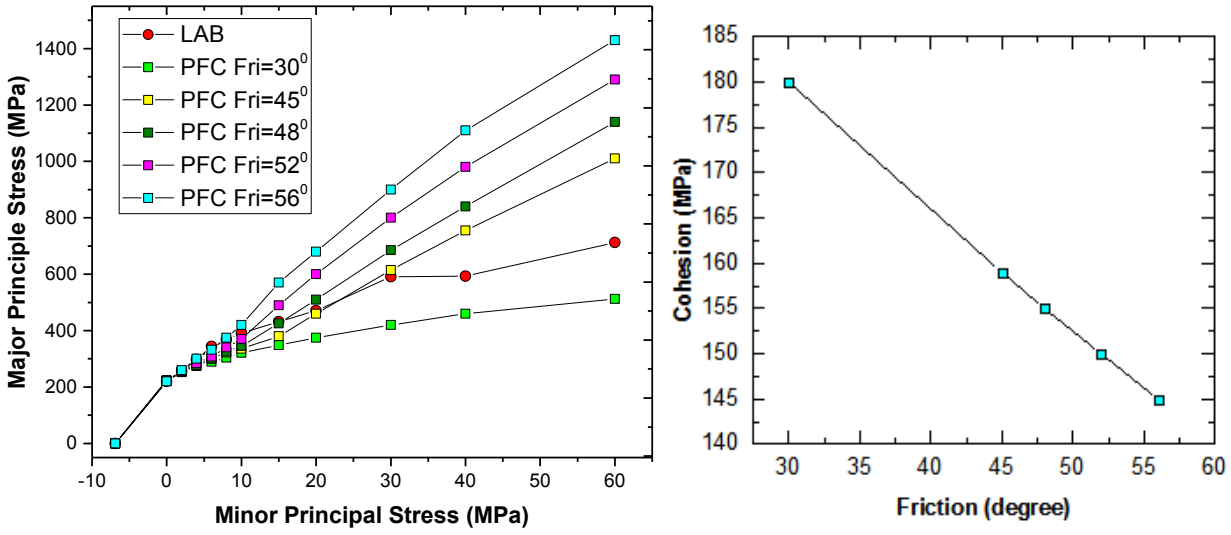

(a) (b)

Figure C.15: (a) Impact of friction angle on triaxial test (b) Plot showing the relation between the cohesion and friction angle to produce same value of UCS for the numerical sample

C.2 List of micro properties used for the investigation of bi-modularity

Table C-8: List of micro properties used for the investigation of bi-modularity

Parameter	Value
Associated with particle size distribution:	
Minimum particle radius	1.1 mm
Particle-size ratio	2.3
Associated with material genesis:	
Width of sample	54 mm
Height width ratio	1
Associated with particles:	
Particle density	2600
Particle modulus	70.0 GPa
Particle stiffness ratio	1.6
Particle friction coefficient	1
Associated with flat joints:	
Bonded fraction ($0 \leq F_B \leq 1$)	1
Gapped fraction ($0 \leq F_G \leq 1$)	0
Initial-gap	0.45*Rmin
Number of elements in radial and circumferential directions, respectively	{2,4}
Fixed or maximum radius multiplier	1
Modulus	70.0 GPa
Stiffness ratio	1.6
Friction coefficient	1
Bond tensile-strength distribution	(12.76 MPa,0)
Bond cohesion distribution	(126.6 MPa,0)
Bond friction angle	45

C.3 Results of the parametric study

Table C-9: Results of parametric study on numerical sample

Case	UCS test										Direct tension			Et/Ec
	Ec (Gpa)	ν_c	Crack Initiation			Crack Damage			Peak		Et (GPa)	Peak		
			σ_{CI} (MPa)	ε_{axial} (%)	ε_{radial} (%)	σ_{CD} (MPa)	ε_{axial} (%)	ε_{radial} (%)	σ_{UCS} (MPa)	ε_{axial} (%)		σ_t (MPa)	ε_{axial} (%)	
LAB	69.6	0.24	88.6	0.143	-0.028	163.3	0.252	-0.066	221.7	0.353	45.2	10.6	-	0.65
Base	69.3	0.12	87.7	0.140	-0.016	185.9	0.293	-0.067	219.1	0.377	46.8	10.9	0.024	0.68
Cyllindrical	67.4	0.13	89.7	0.147	-0.017	179.4	0.290	-0.066	196.7	0.335	43.8	10.0	0.024	0.65
H/W=1.5	68.5	0.12	91.0	0.146	-0.016	205.1	0.325	-0.074	216.3	0.360	46.6	10.5	0.023	0.68
H/W=2.0	68.9	0.11	93.1	0.148	-0.016	212.8	0.334	-0.075	225.8	0.372	46.9	10.0	0.022	0.68
H/W=3.0	69.4	0.11	91.6	0.146	-0.016	208.5	0.324	-0.069	221.5	0.354	46.1	9.4	0.021	0.66
iGap=0.65mm	51.0	0.15	54.3	0.118	-0.015	89.4	0.191	-0.037	112.0	0.278	34.9	7.9	0.024	0.68
iGap=0.975mm	59.2	0.12	64.6	0.120	-0.014	134.0	0.246	-0.055	161.0	0.322	41.3	9.3	0.023	0.70
12 elements	69.3	0.12	87.7	0.140	-0.016	187.9	0.296	-0.069	220.9	0.388	47.0	10.6	0.023	0.68
Loading rate= 50%	69.3	0.12	90.3	0.144	-0.017	177.9	0.280	-0.063	211.3	0.366	46.9	10.9	0.024	0.68
Loading rate= 10%	69.3	0.12	88.8	0.142	-0.016	157.0	0.244	-0.045	206.8	0.344	46.9	10.8	0.024	0.68
30 MPa	69.3	0.12	88.9	0.142	-0.016	180.9	0.283	-0.063	220.3	0.378	47.0	10.8	0.024	0.68
2 MPa	69.3	0.12	92.6	0.147	-0.017	159.8	0.248	-0.046	217.3	0.375	46.9	10.9	0.024	0.68
25 particles	64.8	0.11	89.7	0.152	-0.016	213.9	0.345	-0.075	235.8	0.406	48.3	11.1	0.024	0.75
100 mm sample	69.2	0.1	97.4	0.2	0.0	224.5	0.4	-0.1	244.5	0.4	47.7	10.3	0.0	0.7

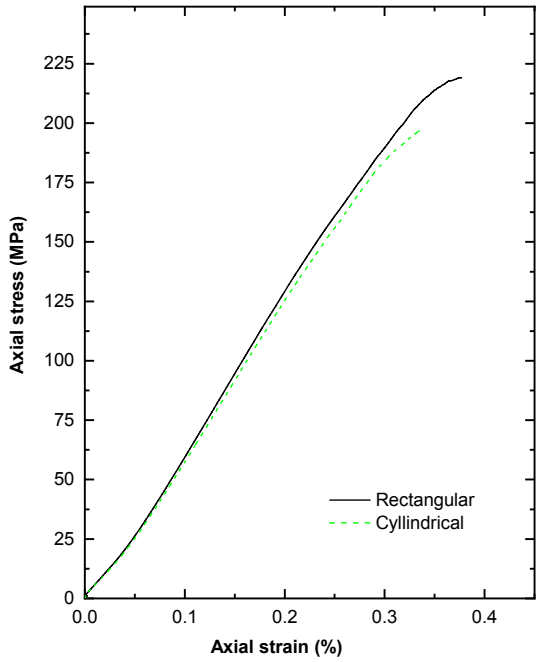

Figure C.16: Comparison of stress-strain curve obtained for rectangular and cylindrical samples (micro parameters for samples are same)

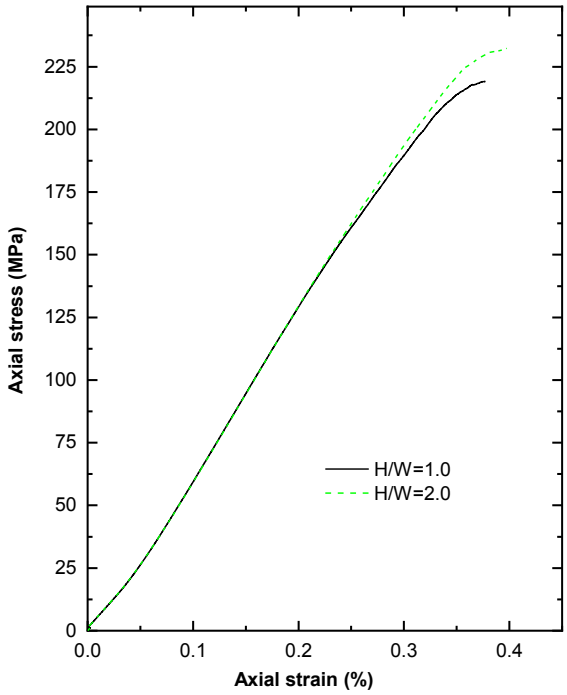

Figure C.17: Comparison of stress-strain curve obtained for samples with height and width ratio (W/H) 1.0 and 2.0 (micro parameters for samples are same)

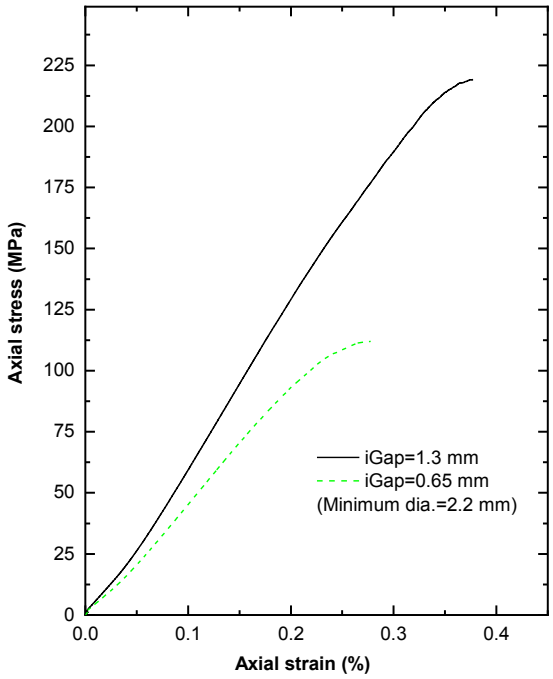

Figure C.18: Comparison of stress-strain curve obtained for samples with grain interaction range (iGap) 1.3 mm and 0.65 mm (micro parameters for samples are same)

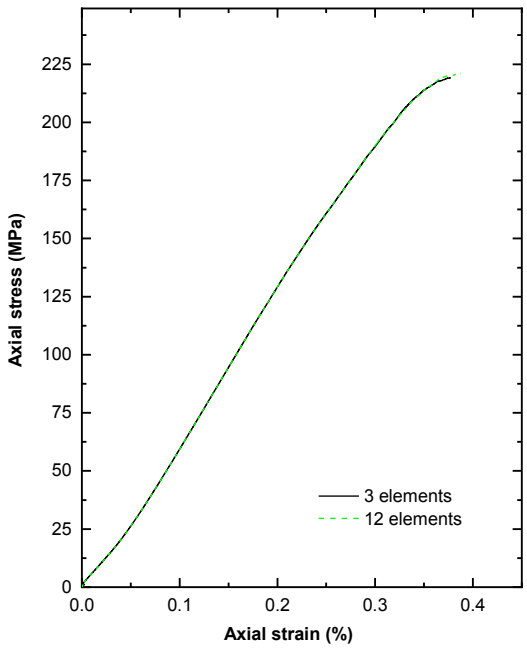

Figure C.19: Comparison of stress-strain curve obtained for samples when grain interface is discretized with 3 elements and 12 element (micro parameters for samples are same)

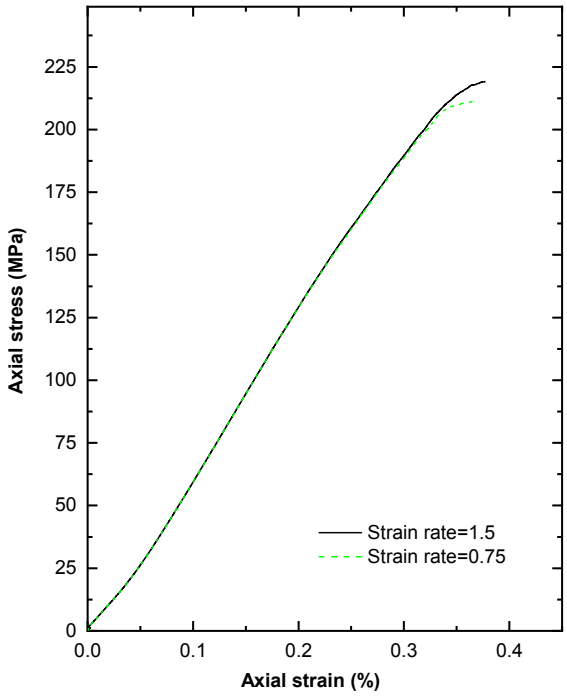

Figure C.20: Comparison of stress-strain curve obtained for samples with axial strain rate 1.5 and 0.75 (micro parameters for samples are same)

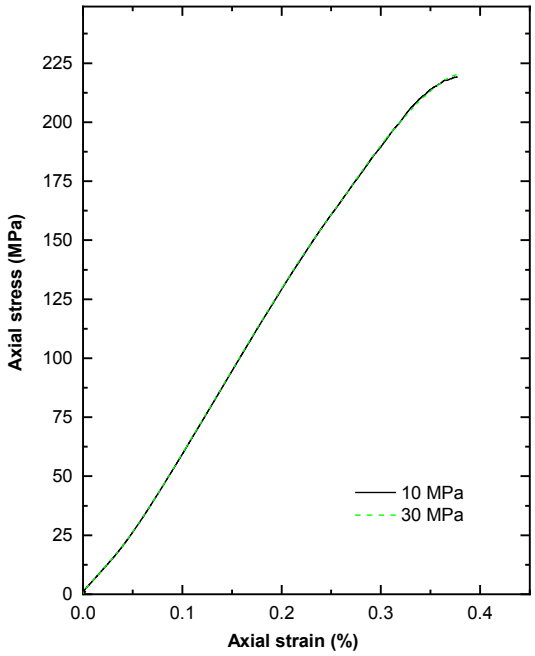

Figure C.21: Comparison of stress-strain curve obtained for samples created at 10 MPa and 30 MPa confinement (micro parameters for samples are same)

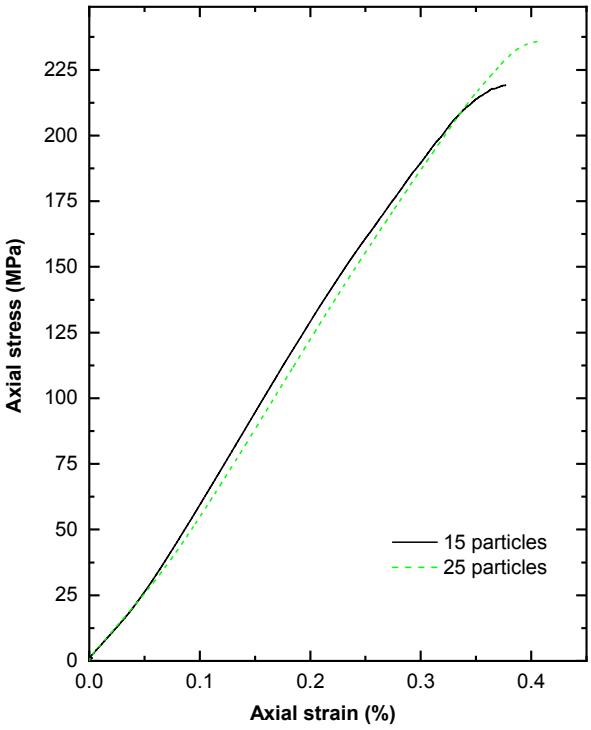

Figure C.22: Comparison of stress-strain curve obtained for samples with average 15 particles and 25 particles along the width (micro parameters for samples are same)

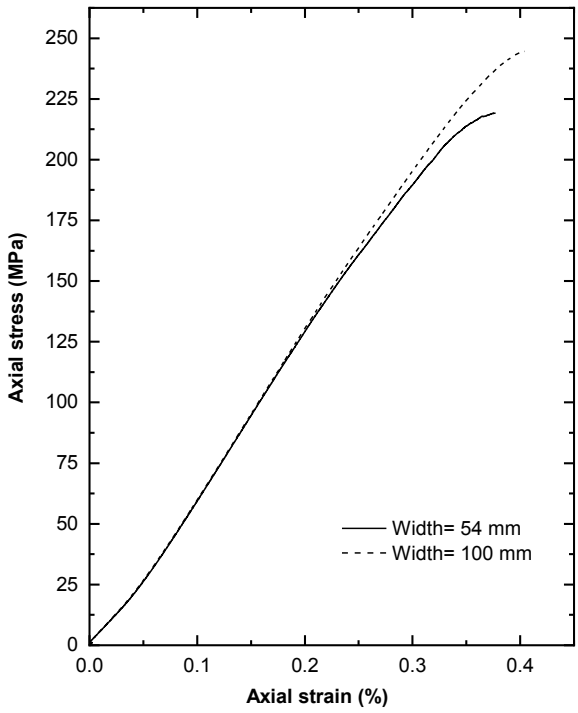

Figure C.23: Comparison of stress-strain curve obtained for samples with width = 54 mm and 100 mm (micro parameters for samples are same)

C.4 Micro parameters for confined extension test

The Micro parameters used for the confined extension test are given in Table C-10.

Table C-10: Micro parameters used for the confined extension test

Parameter	Value
Associated with particle size distribution:	
Minimum particle diameter (R_{min})	2.2 mm
Particle-size ratio (R_{max}/R_{min})	2.3
Associated with material genesis:	
Width of sample (W)	54 mm
Height width ratio (H/W)	1
Associated with Flat-jointed material group:	
fjm_igap (installation gap):	1.309 mm
fjm_B_frac (bonded fraction):	0.65
fjm_G_frac (gapped fraction):	0.35
fjm_S_frac (slit fraction, derived):	0
fjm_G_m (initial surface-gap distribution, mean):	0.002mm
fjm_G_sd (initial surface-gap distribution, standard deviation):	0
fjm_Nr (elements in radial direc.)	1
fjm_Nal (elements in circumferential direc.)	3
fjm_rmulCode (radius-multiplier code): 0 (fixed)	0
fjm_rmulVal (radius-multiplier value):	0.577
fjm_emod (effective modulus):	135.8 GPa
fjm_krat (stiffness ratio):	1.2
fjm_fric (friction coefficient):	1.37752
fjm_ten_m (tensile-strength distribution, mean):	41.6 MPa
fjm_ten_sd (tensile-strength distribution, standard deviation):	0
fjm_coh_m (cohesion distribution, mean):	203 MPa
fjm_coh_sd (cohesion distribution, standard deviation):	0
fjm_fa (friction angle [degrees]):	43.2
Associated with Linear material group:	
lnm_emod (effective modulus):	135.8 GPa
lnm_krat (stiffness ratio):	1.2
lnm_fric (friction coefficient):	1.10201

C.5 Formation of cracks in confined extension test

The Tensile and shear cracks at different confinement before application of tensile load (point E, Figure 5.29) and at peak(point C, Figure 5.29) are given in Figure C.24 and Figure C.25 respectively.

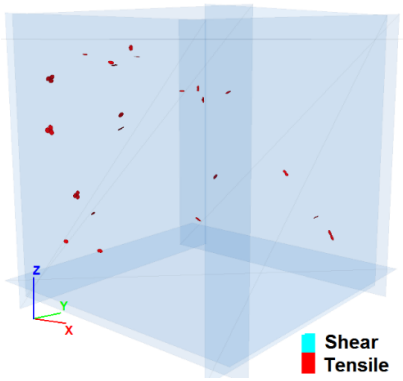

(a) Low confinement (34 MPa)

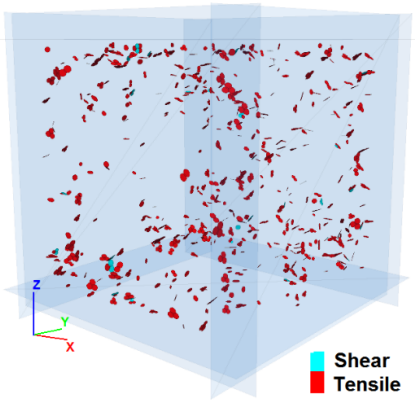

(b) Medium confinement (120 MPa)

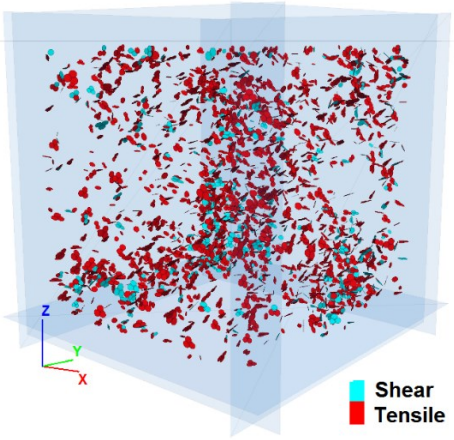

(c) High confinement (175 MPa)

Figure C.24: Tensile and shear cracks at different confinement before application of tensile load (point E, Figure 5.29)

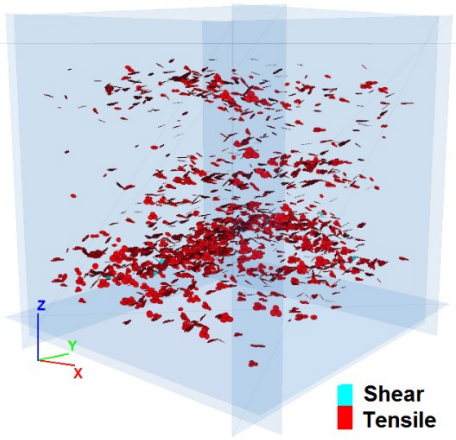

(a) Low confinement (34 MPa)

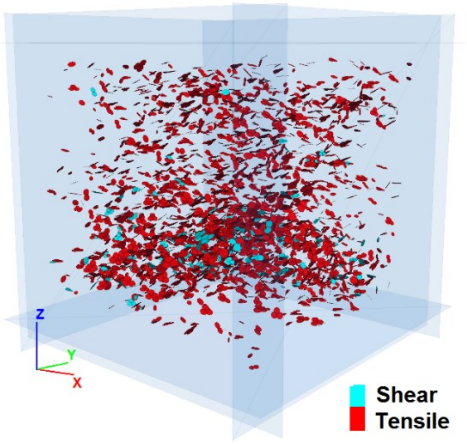

(b) Medium confinement (120 MPa)

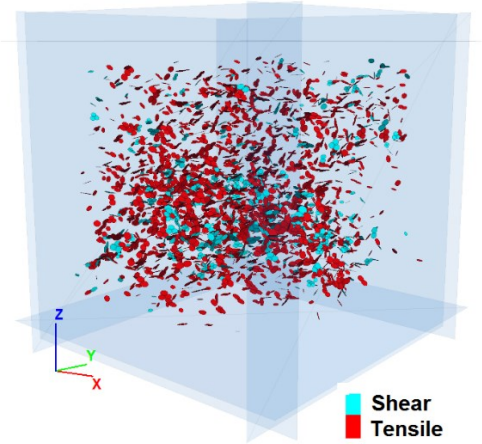

(c) High confinement (175 MPa)

Figure C.25: Tensile and shear cracks at different confinement at peak (point C, Figure 5.29). Note amount of shear cracks is increased with increase in confinement

C.6 Fish code for conducting confined extension test in PFC3D

The FISH code written to conduct the confined extension test on the FJ numerical sample is given below. Refer PFC3D fish tank (Potyondy 2017) for the .fis files.

```
;#########################################################
Stage 1: Cubical, numerical sample generated in the material generation phase was used for the confined extension test
;#########################################################
;fname: myCETest.p3dvr
;
;  IN:  ctParams.p3dat
;       Saved State (with corresponding model title):
;         <cm_matName>-matV : specimen in material vessel
;  OUT: myCETest.p3log
;
;=========================================================================
set logfile myCETest.p3log
set log     on truncate
set echo    on
;#########################################################
restore ..\CG_FlatJointed-matV.p3sav
call ..\..\fistSrc\ck.fis   suppress
call ..\..\fistSrc\ct.fis   suppress

;*********************************************
call ctParams.p3dat suppress
@ckInit
@ctSeatingPhase
@ctLoadingPhase
@ckListCrackData
;#########################################################
step 1000
```

```
save ConfExTen0.p3sav
call ConfExTen1.p3dat


;#########################################################
Stage 2: sample was brought to the hydrostatic state
;#########################################################
;Restore ConfExTen0.p3sav
def ctSetParams
; Set Compression-Test Parameters.
  ct_testType = 0
  Pxxn=11e6 ; initial stress in x-direction
  Pyyn=11e6 ; initial stress in y-direction
  Pzzn=11e6 ; initial stress in z-direction
  Pyynf=90e6 ; Hydrostatic confining stress
  ryy=(Pyynf-Pyyn)/20
  ct_Pc = (Pcx+Pcy+Pcz)/3
  ;ct_Pc = 1e6
  ct_eRate = 0.15
  ct_loadCode = 0
  ct_loadFac = 0.2
end
@ctSetParams
;*********************************************************
; Increase confining stress to the sample gradually in 20 increments
def Grad_Red_Conf
    loop for (local i=1, i <=20, i+=1)
        ;Pcx=Pxxn*(1-i/21.0)
        Pcy=Pyyn+i*ryy
        ;Pcz=Pzzn*(1-i/21.0)
        Pcx=Pyyn+i*ryy
```

```
      Pcz=Pyyn+i*ryy
      ct_Pc=(Pcx+Pcy+Pcz)/3
    command
      @_ctCheckParams
      @ctListProps
      ;@ckInit
      @ctSeatingPhase
    endcommand
  endloop
end
@Grad_Red_Conf
step 1000
save ConfExTen1.p3sav
call ConfExTen3.p3dat


;#########################################################
Stage 3: Intermediate and minor principal stress gradually reduced to ~0
;#########################################################
;Reduce zz and xx confining stress to ~0
def Grad_Red_Conf2
      Pcx=2e6
      Pcy=Pyynf
      Pcz=.1e6
      ct_Pc=(Pcx+Pcy+Pcz)/3
    command
      @_ctCheckParams
      @ctListProps
      ;@ckInit
      @ctSeatingPhase
    endcommand
```

```
end
@Grad_Red_Conf2
save ConExTen3.p3sav
call ConfExTen4.p3dat


;#########################################################
```

Stage 4: gradual application of tensile minor principal stress keeping Intermediate and major principal stress constant

```
;#########################################################
;Apply axial tension to the sample till failure
call ..\..\fistSrc\ck.fis suppress
call ..\..\fistSrc\tt.fis suppress
;***********************************************
  call ttParams.p3dat suppress
  ; Servo pressures and strains:
  history add id=11 fish mv_wPx
  history add id=12 fish mv_wPy
  history add id=13 fish mv_wPz
  history add id=14 fish mv_wPr
  history add id=21 fish mv_wex
  history add id=22 fish mv_wey
  history add id=23 fish mv_wez
  ; Measurement sphere stress
  history add id=24 fish mv_msxx
  history add id=25 fish mv_msyy
  history add id=26 fish mv_mszz
;
@ckInit
@ttSetupPhase
@ttLoadingPhase
```

@ckListCrackData

;**********

save ConExTen.p3sav

;##########

NOTE:

The *ct.fis* file was modified to apply principal stresses of different magnitudes to the cubical sample.